Simulation of Premixed Hydrocarbon Flames at High Turbulence Intensities

Thesis by

Simon Lapointe

In Partial Fulfillment of the Requirements

for the Degree of

Doctor of Philosophy

California Institute of Technology

Pasadena, California

2016

(Defended May 11, 2016)

Acknowledgements

First of all, I would like to thank my research advisor, Professor Guillaume Blanquart, for his constant support, availability, motivation, and comic relief. I would also like to thank my committee members, Professors Joanna Austin, Joseph Shepherd, and Tim Colonius for their comments on this thesis.

I would like to thank all past and present members of The FORCE. In particular, I acknowledge Bruno Savard for many fruitful discussions. This work also benefited from collaborations with Jennifer Smolke, Laurel Paxton, and Professor Fokion Egolfopoulos at University of Southern California.

Financial funding from Air Force Office of Scientific Research (FA9550-12-1-0472 and FA9550-12-1-0144) under supervision of Dr. Chiping Li and Fonds de Recherche du Québec - Nature et Techonologies is gratefully acknowledged. This research used resources of the National Energy Research Scientific Computing Center, a DOE Office of Science User Facility supported by the Office of Science of the U.S. Department of Energy under Contract No. DE-AC02-05CH11231. This work used the Extreme Science and Engineering Discovery Environment (XSEDE), which is supported by National Science Foundation grant number ACI-1053575.

Abstract

Turbulent premixed hydrocarbon flames in the thin and distributed reaction zones regimes are simulated using both Direct Numerical Simulations (DNS) and Large Eddy Simulations (LES). A series of DNS is performed to study the transition from the thin reaction zones regime to the distributed reaction zones regime. Differential diffusion effects, distributed burning, and local extinctions are quantified. Different fuels, chemical mechanisms, and equivalence ratios are considered. The fuel Lewis number significantly influences the chemical source terms and turbulent flame speeds. More precisely, simulations with differential diffusion effects exhibit lower mean fuel consumption and heat release rates than their unity Lewis number counterparts. However, the differences are reduced as the reaction zone Karlovitz number is increased. The turbulent reaction zone surface areas increase with the turbulence intensity but aren't strongly affected by fuel, equivalence ratio, chemical mechanism, or differential diffusion. Unsurprisingly, changes in the integral length at a fixed Karlovitz number do not affect the chemical source terms but lead to an increase in flame surface area. Assumptions behind closure models for the filtered source term are then studied *a priori* using the DNS results. Using the concept of optimal estimators, it is shown that a tabulation approach using a progress variable and its variance can predict accurately the filtered progress variable source term. The filtered source terms are compared to predictions from two common presumed sub-filter Probability Density Functions (PDF) models. Both models show deviations from the filtered DNS source terms but predict accurately the mean turbulent flame speed. Finally, LES of experimentally-studied piloted premixed jet flames are performed using tabulated chemistry. Velocity and flame height measurements from simulations and experiments are compared. The LES are in good agreement with the experimental results for the four different hydrocarbon fuels and three different Reynolds

numbers simulated. This corroborates that fuel and chemistry effects in turbulent flames are limited to effects present in laminar flames.

Published Content and Contributions

- Chapter 3 is based on: S. Lapointe, B. Savard, and G. Blanquart. Differential diffusion effects, distributed burning, and local extinctions in high Karlovitz premixed flames. *Combust. Flame*, 162:3341 – 3355, 2015

  The author of this thesis performed seven of the nine simulations, analyzed the data, made the figures, and wrote the manuscript.

- Chapter 4 is based on: S. Lapointe and G. Blanquart. Fuel and chemistry effects in high Karlovitz premixed flames. *Combust. Flame*, 167:294–307, 2016

  The author of this thesis performed twenty-two of the twenty-four simulations, analyzed the data, made the figures, and wrote the manuscript.

- Chapter 7 is based partly on: J. Smolke, S. Lapointe, L. Paxton, G. Blanquart, F. Carbone, A.M. Fincham, and F.N. Egolfopoulos. Experimental and numerical studies of fuel and hydrodynamic effects on piloted turbulent premixed jet flames. *Proc. Combust. Inst.*, accepted, 2016

  The author of this thesis performed the simulations and participated in the writing.

- The code presented in Appendix B is briefly described in: L.R. Boeck, S. Lapointe, J. Melguizo-Gavilanes, and G. Ciccarelli. Flame propagation across an obstacle: OH-PLIF and 2-D simulations with detailed chemistry. *Proc. Combust. Inst.*, accepted, 2016

  The author of this thesis implemented and validated the numerical framework, performed the simulations, and participated in the writing.

Contents

List of Figures

List of Tables

Chapter 1

Introduction

1.1 Background

Combustion of fossil fuels is the main source of energy for power generation and transportation and will remain so for decades to come. Other energy sources account for less than 20% of the world's total energy consumption [1]. Liquid fuels composed of large hydrocarbons are usually preferred for their high energy density. Unfortunately, combustion of hydrocarbons produces pollutants such as NO_x, soot, unburnt hydrocarbons, and carbon dioxide.

Combustion in practical devices primarily takes place in a turbulent flow. Turbulence increases mixing, thus enhancing combustion processes and therefore power output. Combustion processes are typically divided into premixed, non-premixed, and partially premixed combustion. In premixed flames, the fuel and oxidizer are fully mixed prior to combustion. In non-premixed flames (also called diffusion flames), the fuel and oxidizer are originally separated and mix and subsequently burn through diffusion. In partially-premixed flames, the fuel and oxidizer partially mix before combustion occurs. Non-premixed and partially premixed combustion processes are typically found in diesel engines and furnaces. On the other hand, premixed combustion is found in homogeneous compression charge ignition (HCCI) engines and lean-burn gas turbines [117]. Lean premixed combustion is increasingly common in modern devices since lean conditions prevent soot production and the lower temperature reduces NO_x emissions [80]. Highly turbulent premixed flames are also used in ramjets and scramjets.

The design of efficient combustion devices relies more and more on numerical simulations. Direct numerical simulations of practical devices remain beyond current computational capabilities due to the extreme range of scales and complex chemical kinetics. Combustion and turbulence models are thus required for accurate predictive simulations.

While premixed flames burning heavy hydrocarbons at high turbulence intensities are favored in recent designs to reduce pollutants and increase performance, most experimental and numerical studies are performed with simple fuels at low turbulence intensities. There is thus a need for assessing modeling assumptions for premixed flames under intense turbulence with large hydrocarbon fuels.

1.2 Premixed Combustion

This thesis focuses on numerical simulations of premixed turbulent flames. In this section, basic concepts of premixed flames and turbulent combustion are reviewed.

1.2.1 Laminar Premixed Flames

In premixed flames, the reactants (fuel and oxidizer, typically air) are mixed prior to combustion. They are characterized by the unburnt conditions: the type of fuel and oxidizer, the temperature T_u, the pressure, and the equivalence ratio ϕ (ratio of fuel/air ratio to stoichiometric fuel/air ratio). Lean mixtures have below unity equivalence ratios and rich mixtures have above unity equivalence ratios. The two main characteristics of laminar premixed flames are the flame speed and flame thickness. The propagation speed, or flame speed, is labelled S_L and defined as the speed at which the flame front moves with respect to the unburnt gas. The laminar flame thickness, or thermal width, can be defined as

$$l_F = \frac{T_b - T_u}{|\nabla T|_{\max}}, \tag{1.1}$$

where T_b and T_u are the burnt and unburnt temperatures and $|\nabla T|_{\max}$ is the maximum temperature gradient.

The laminar flame structure of a n-heptane/air flame is shown in Fig. 1.1. It was computed using the FlameMaster code [85] and a 35 species reduced chemical mechanism [11]. It is representative of most laminar flames burning heavy hydrocarbons. The equivalence ratio is $\phi = 0.9$, unburnt temperature $T_u = 298$ K, and pressure 1 atm. Mass fractions of fuel, CO_2, and C_2H_4 are plotted in physical space (distance normalized by the laminar flame thickness) in Fig. 1.1a. As typical with heavy hydrocarbon fuels, fuel is consumed early, intermediate species are produced then consumed (such as C_2H_4 here), and then combustion products are formed (such as CO_2 here). Fuel consumption rate and heat release rate are shown in Fig. 1.1b. The fuel consumption layer is thinner and its location is shifted from that of the heat release layer. Temperature, density, and kinematic viscosity of the fluid are plotted in Fig. 1.2, all normalized by their peak values. Temperature increases through the flame while density decreases. Viscosity has a strong dependence on temperature and thus presents an even larger increase.

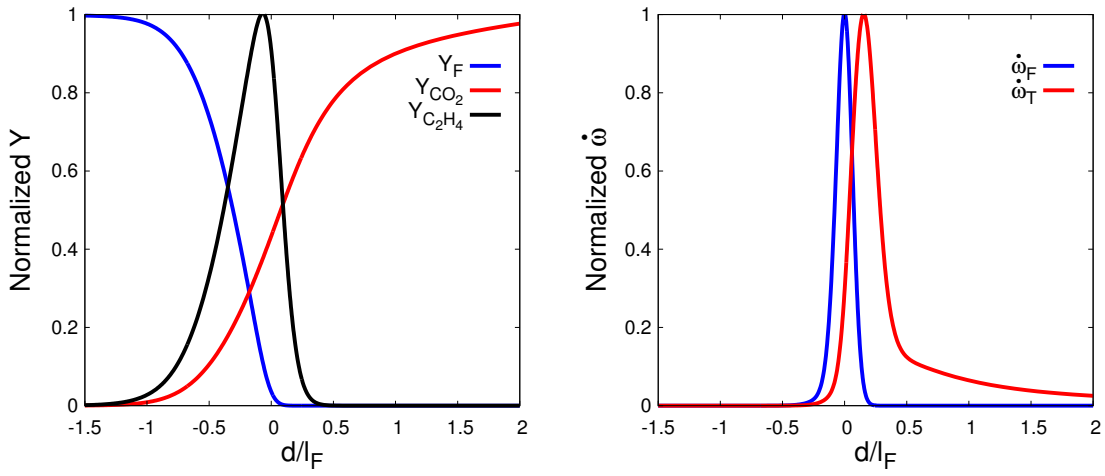

(a) Normalized mass fractions

(b) Normalized chemical source terms

Figure 1.1: Laminar flame structure as a function of distance from the peak fuel consumption. Taken from an n-heptane flame at $T_u = 298$ K.

It is common and often more insightful to represent the species mass fractions and chemical source terms profiles in temperature space. This allows, for example, to easily illustrate the effects of differential diffusion. Differential diffusion occurs when heat and species diffuse at different rates

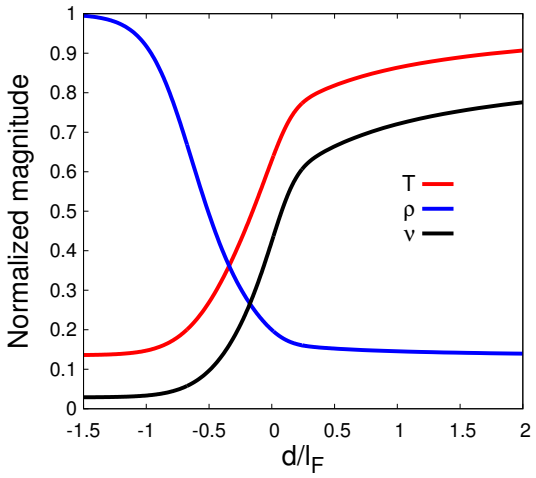

Figure 1.2: Normalized fluid properties as a function of distance from the peak fuel consumption. Taken from a laminar n-heptane flame at $T_u = 298$ K.

and is characterized by different, non-unity, Lewis numbers for each species:

$$\mathrm{Le}_i = \frac{\alpha}{D_i}, \tag{1.2}$$

where α is the thermal diffusivity, D_i is the mass diffusivity of species i, and Le_i is the Lewis number of species i. Figure 1.3 shows the fuel mass fraction profiles in temperature space for three fuels with different Lewis numbers. The effect of differential diffusion on species with non-unity Lewis numbers (such as n-heptane and hydrogen) is significant. Differential diffusion also affects the laminar flame speed. For example, the computed laminar flame speeds of the n-heptane, methane, and hydrogen flames shown in Fig. 1.3 are 0.36, 0.29, and 0.22 m/s with non-unity Lewis numbers and, respectively, 0.29, 0.26, and 0.41 m/s with unity Lewis numbers. Furthermore, depending on the Lewis number of the limiting reactant, premixed flames may be thermo-diffusively unstable [63]. Thermo-diffusively unstable flames exhibit cells and cusps which affect the burning rate [28].

In laminar flames, the initial decrease in the fuel mass fraction is mostly due to diffusion, not chemical reactions. In the preheat zone of a premixed flame, species evolution is a balance of convection and diffusion. In the reaction zone, diffusion is balanced by chemical reactions.

Figure 1.4 compares the different terms in the transport equation of the fuel mass fraction in

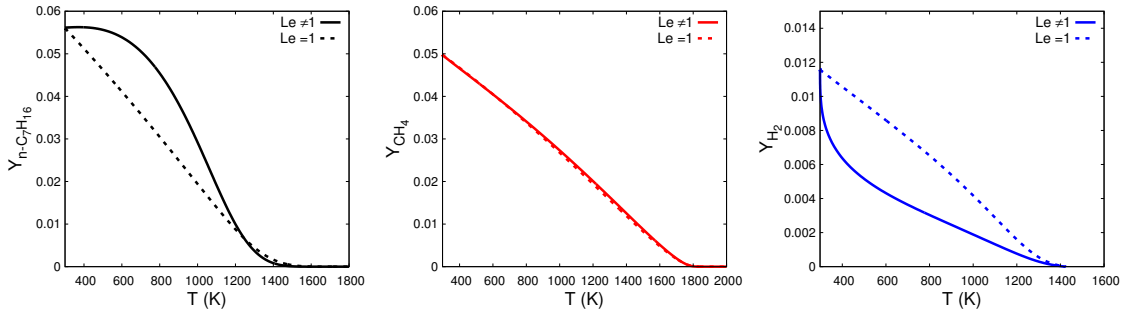

(a) n-heptane (b) methane (c) hydrogen

Figure 1.3: Fuel mass fraction profile in temperature space for different fuels. n-Heptane/air at $\phi = 0.9$ ($\mathrm{Le}_F \approx 2.8$), methane/air at $\phi = 0.9$ ($\mathrm{Le}_F \approx 1$), and hydrogen/air at $\phi = 0.4$ ($\mathrm{Le}_F \approx 0.3$).

the $\phi = 0.9$ n-heptane/air laminar flame. At low temperatures ($T < 1000$ K), the chemical source term is negligible but there is significant diffusion. This is the cause of the change in the fuel mass fraction. The fuel reaction rate is maximum where diffusion is maximum. In other words, chemical reactions are most important where the second derivative of Y_F is the largest.

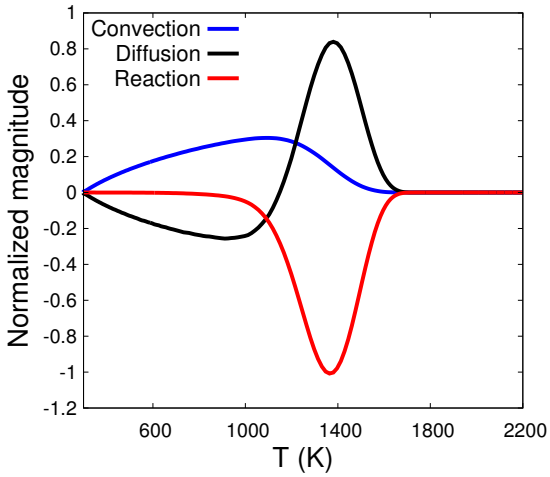

Figure 1.4: Normalized magnitude of the terms in the fuel transport equation. Taken from a laminar n-heptane flame.

1.2.2 Turbulence

As turbulence is a vast subject, this section briefly covers some basic aspects that are most relevant to the physical analysis and numerical simulations performed in this thesis. Turbulent scales are reviewed in this section and their effects on premixed combustion are discussed in Section 1.2.3.

Turbulence can be considered to be composed of eddies of different sizes or scales. The larger eddies are the most energetic ones, containing most of the kinetic energy created by the velocity gradients of the mean turbulent motion, and their size is of the order of the dimension of the flow feature itself or the turbulent region studied. This size is often given by the integral length scale l and the largest eddies are also characterized by the rms turbulence intensity u'. The energy contained in those large eddies is then transferred to smaller scales by a cascade process where the large eddies break down to form smaller eddies which, when small enough, succeed to dissipate the energy by the action of molecular viscosity [94].

The Turbulent Kinetic Energy (TKE) is defined as

$$k = \frac{3}{2}u'^2, \tag{1.3}$$

the eddy turnover time is defined as

$$\tau = \frac{k}{\epsilon}, \tag{1.4}$$

where ϵ is the dissipation rate, and the turbulent Reynolds number is defined as

$$\mathrm{Re}_t = \frac{u'l}{\nu}, \tag{1.5}$$

where ν is the kinematic viscosity.

The scales distribution in the turbulence cascade can be described by Kolmogorov's theory [57], expressed as three hypotheses.

1. Hypothesis of local isotropy: At high Reynolds number, the small-scale motions are isotropic. This suggests that the smallest-scale motions have a universal character.

2. First similarity hypothesis: At high Reynolds number, the universal character of the small-scale motions is determined by the kinematic viscosity, ν, and the dissipation rate, ϵ, uniquely. The Kolmogorov length, velocity and time scales, associated with the smallest eddies, are thus expressed as:

$$\eta \equiv \left(\frac{\nu^3}{\epsilon}\right)^{1/4}, \tag{1.6}$$

$$u_\eta \equiv (\epsilon\nu)^{1/4}, \tag{1.7}$$

$$\tau_\eta \equiv \left(\frac{\nu}{\epsilon}\right)^{1/2}. \tag{1.8}$$

It is revealing to compare the ratios of the Kolmogorov scales to those of the largest scales as a function of the Reynolds number [109]:

$$\frac{\eta}{l} \sim \mathrm{Re}^{-3/4}, \tag{1.9}$$

$$\frac{u_\eta}{u} \sim \mathrm{Re}^{-1/4}, \tag{1.10}$$

$$\frac{\tau_\eta}{\tau} \sim \mathrm{Re}^{-1/2}, \tag{1.11}$$

which show the wide ranges of the length scales at high Reynolds number making Direct Numerical Simulations of turbulent flows a formidable challenge.

3. Second similarity hypothesis: At high Reynolds number, there exists a motion within a range of scales λ in the range $l_\eta \ll \lambda \ll l$ which has a universal form depending only on ϵ. This means that in this certain range of length scales (referred to as the inertial sub-range), turbulence is independent of the generation mechanism. This is associated with the constant slope portion on the turbulent energy spectrum, as depicted in Fig. 1.5, and expressed by:

$$E(k) = C_k \epsilon^{2/3} k^{-5/3}. \tag{1.12}$$

1.2.3 Regimes of Turbulent Premixed Combustion

Turbulent combustion regimes are typically defined in terms of length and velocity scale ratios [17, 78] with u'/S_L the ratio of rms turbulent intensity to laminar flame speed and l/l_F the ratio of integral

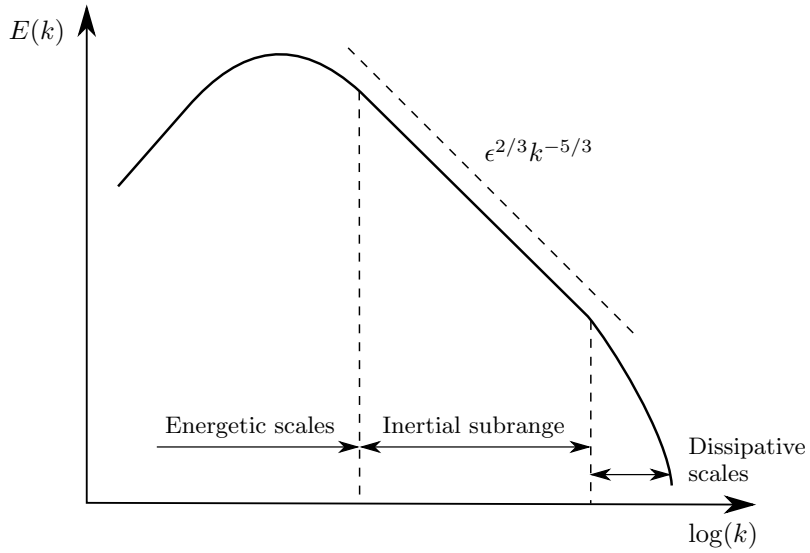

Figure 1.5: The turbulence energy spectrum.

length scale to laminar flame thickness.

For scaling purposes, a unity Schmidt number is assumed ($\mathrm{Sc} = \nu/D$) and the flame thickness is approximated as

$$l_F \approx \frac{D}{S_L} = \frac{\nu}{S_L}, \tag{1.13}$$

and the flame time defined as

$$\tau_F = \frac{l_F}{S_L}. \tag{1.14}$$

The turbulent Reynolds number can then be written as

$$\mathrm{Re}_t = \frac{u' l_0}{l_F S_L}, \tag{1.15}$$

and the Karlovitz number as

$$\mathrm{Ka} = \frac{\tau_F}{\tau_\eta} = \frac{l_F^2}{\eta^2} = \frac{u_\eta^2}{S_L^2}. \tag{1.16}$$

A reaction zone Karlovitz number may be defined using the reaction zone thickness, δ, instead of the flame thickness

$$\mathrm{Ka}_\delta = \frac{\delta^2}{\eta^2}. \tag{1.17}$$

The ratios u'/S_L and l/l_F are thus related through the Reynolds and Karlovitz numbers:

$$\begin{aligned} \frac{u'}{S_L} &= \mathrm{Re}_t \left(\frac{l}{l_F}\right)^{-1} \\ &= \mathrm{Ka}^{-2/3} \left(\frac{l}{l_F}\right)^{1/3}. \end{aligned} \tag{1.18}$$

Following Eq. 1.18, the Reynolds and Karlovitz numbers can be used to delimit the different regimes of premixed turbulent combustion. The regime diagram proposed by Peters [80] is shown in Fig. 1.6. The $\mathrm{Re}_t = 1$ line separates turbulent flames from laminar flames. The wrinkled and corrugated flamelet regimes are separated by the $u' = S_L$ line. The $\mathrm{Ka} = 1$ line (Klimov-Williams criterion) separates the thin reaction zone regime from the corrugated flamelet regime. In the thin reaction zone regime, the smallest eddies (of size η) are smaller than the flame thickness and are thus expected to thicken the preheat zone. The $\mathrm{Ka}_\delta = 1$ line separates the thin reaction zone regime from the distributed/broken reaction zone regime. In the latter regime ($\mathrm{Ka}_\delta = 1$ and $\mathrm{Ka} \gg 1$), the smallest eddies are smaller than the reaction zone thickness and may thus thicken (distribute) or disrupt (break) the reaction zone. It should be noted that the regime diagram intends to draw only a qualitative picture of the effect of turbulence on the flame. Turbulence is characterized by a spectrum of length scales and thus considering that a single length scale will affect the flame is a simplification.

Though turbulent premixed combustion has been widely studied, few numerical and experimental studies have assessed finite-rate chemistry or fuel effects, especially in the distributed/broken reaction zones regime. This is illustrated in Fig. 1.6 by two comprehensive surveys of turbulent premixed flames experiments and simulations.

Two main observations may be drawn from these surveys. First, the vast majority of the experimental investigations have been carried out for either hydrogen or methane flames, with very limited data on heavy hydrocarbons despite their omnipresence in practical combustion engines [26, 36]. Second, there is a scarcity of data for any fuels (and especially for high carbon number fuels) in the distributed/broken reaction zone regime.

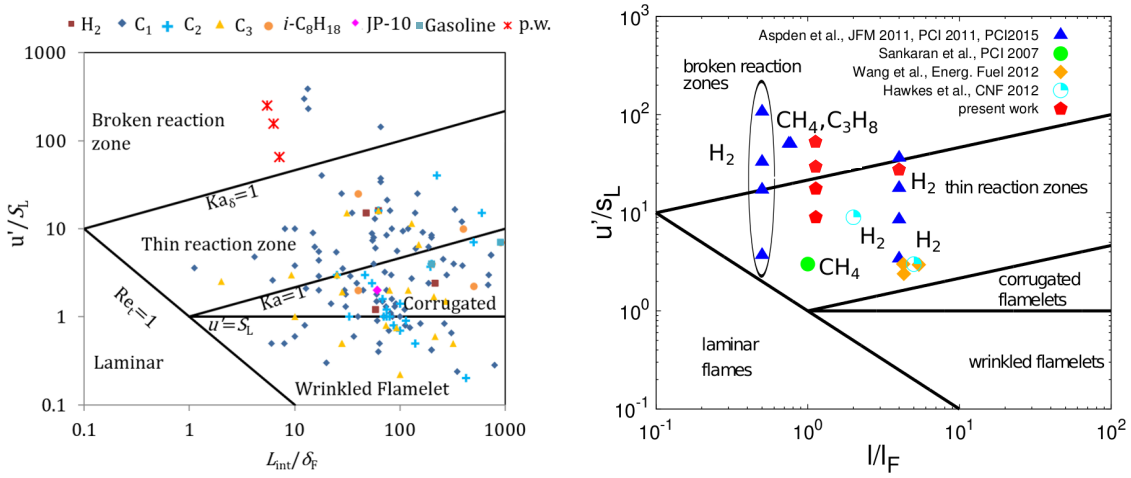

(a) Experiments (b) Simulations

Figure 1.6: Regime diagram showing experimentally and numerically investigated fuels. a) Survey of turbulent premixed flames experiments, from Smolke *et al.* [107]. b) Survey of turbulent premixed flames simulations with detailed chemistry, adapted from Savard [99]. Red symbols indicate conditions investigated in the present work (p.w.) through LES (left) and DNS (right).

Practical premixed combustion devices operate at elevated unburnt temperatures and pressures under high turbulence intensities, and use heavy hydrocarbon-based fuels. These applications typically fall in the thin or broken/distributed reaction zones regimes, which are characterized by a large Karlovitz number [86]. One of the overarching goals of the present work is to provide much needed data for heavy hydrocarbons at high Karlovitz numbers.

More specifically, this thesis has two main objectives. First, understand and describe the physics of high Karlovitz number flames burning heavy hydrocarbons. This is introduced in Sections 1.3, 1.4, and 1.5. Second, use these insights for efficient and accurate modeling of premixed flames. This is introduced in Sections 1.6 and 1.7.

1.3 Broken/Distributed Reaction Zone

Only a limited number of experiments at high Karlovitz numbers are available in the literature [25, 48, 31, 32, 21]. Similarly, few Direct Numerical Simulations (DNS) of turbulent premixed flames with detailed chemistry have been performed in the thin and broken/distributed reaction zones regimes [4, 5, 7, 8, 114, 6, 97]. In an effort to reduce computational costs, studies have been

performed with simplified chemistry, such as one-step chemical models [90, 91]. However, detailed kinetic modeling remains necessary to study the impact of high-speed turbulence on the chemistry, especially in the thin and broken/distributed reaction zones regimes.

High Karlovitz number flames are fundamentally different from low Karlovitz number flames because the turbulence penetrates inside and disturbs the reaction zone. From a theoretical and modeling point of view, three aspects need to be investigated: the impact of differential diffusion, the distributed nature of the reaction zone, and possible local extinction events. The present numerical work will focus on these three critical aspects by considering heavy hydrocarbon fuels. In contrast, previous numerical simulations at high Karlovitz numbers using detailed chemistry considered mostly simple fuels such as hydrogen [7, 8, 114, 22], methane [6, 97, 22], and propane [6].

Aspden *et al.* [7] studied the interaction of lean premixed hydrogen flames with turbulence over a wide range of Karlovitz numbers. Distributed burning was observed at high Karlovitz numbers ($\mathrm{Ka} \approx 4200$) and global extinction did not occur. The distributed flame was characterized by a broad mixing region, similar to turbulent mixing of a passive scalar. Turbulent mixing was dominant over molecular mixing and differential diffusion effects were again significantly reduced. Aspden *et al.* [6] investigated Lewis number effects in distributed hydrogen ($\mathrm{Le_{fuel}} < 1$), methane ($\mathrm{Le_{fuel}} \sim 1$), and propane flames ($\mathrm{Le_{fuel}} > 1$). It was shown that distributed burning led to an enhanced burning rate in low Lewis number flames while the burning rates of methane and propane flames remained closer to their laminar values.

DNS of premixed n-heptane-air turbulent flames close to the transition between the thin/broken reaction zones were recently presented in Savard *et al.* [102, 101]. To better analyze differential diffusion effects, two simulations were performed, one with unity Lewis numbers and one with non-unity Lewis numbers. The flame structure (defined as the dependence of species mass fractions on temperature) of the unity Lewis number flame was shown to be very similar to that of a one-dimensional, flat flame, suggesting that turbulence has a very limited impact on the flame in temperature space, in the absence of differential diffusion. On the other hand, the structure of the non-unity Lewis number flame was affected more substantially by turbulence. It was argued that turbulence affects the flame

structure through an effective Lewis number [80, 100]. At high turbulence levels (i.e. high Karlovitz number) turbulence reduces differential diffusion effects consistently with the results of Aspden *et al.* [7, 6]. These effects were almost suppressed in the preheat zone, but were still present at the reaction zone while the reaction zone remained thin. The fuel consumption rate exhibited significant fluctuations (both for the unity and non-unity Lewis number simulations) and local extinctions were observed in the non-unity Lewis number case.

These studies provided valuable, yet still qualitative, insight in the behavior of flames in the distributed burning regime. There is still a need for quantifying the impact of differential diffusion effects and distributed burning on chemical source terms fluctuations and local extinctions.

In addition, it is important to underline that most of these studies have been performed at ambient temperatures while most combustion devices operate at higher unburnt temperatures. An increase in the unburnt temperature will lead to a reduction in the viscosity ratio across the flame. As the Kolmogorov length scale depends on the viscosity, small-scale turbulent structures are then expected to penetrate further in the reaction zone. Considering a fixed velocity ratio u'/S_L and length ratio l/l_F, the change in viscosity ratio will lead to an increased Karlovitz number at the reaction zone while the Karlovitz number in the unburnt gases would not change. To take these effects into account, it is more adequate to use the reaction zone Karlovitz number [79]:

$$\mathrm{Ka}_\delta = \frac{\delta_{F,\mathrm{lam}}^2}{\eta_\delta^2}, \tag{1.19}$$

where $\delta_{F,\mathrm{lam}}$ is the laminar reaction zone thickness of the fuel and η_δ denotes the value of the Kolmogorov length scale *at the reaction zone* (taken at T_{peak}, the temperature corresponding to the peak value of the fuel consumption rate in the flame). Equation (1.19) is preferred in the present work to distinguish between the different unburnt temperatures.

The present study builds upon previous studies by Savard *et al.* [102, 101] and aims at investigating the transition from the thin to broken/distributed reaction zone regimes in premixed flames with engine-relevant, heavy hydrocarbon fuels. In contrast to [102, 101], turbulent flames are

studied over a range of Karlovitz numbers, covering the thin reaction zone and the distributed burning regimes. More precisely, the Karlovitz number at the reaction zone is increased incrementally using different turbulence intensities and unburnt temperatures. The focus is placed on three main objectives.

- Understand and quantify differential diffusion effects on burning rate and heat release.
- Identify the transition to distributed burning and characterize the resulting reaction zone.
- Quantify and explain the occurence of local extinctions at increasing turbulence intensities.

1.4 Fuel and Chemistry Effects

As mentioned, previous numerical simulations at high Karlovitz numbers using detailed chemistry considered mostly simple fuels such as hydrogen [7, 8, 114, 22], methane [6, 97, 22], and propane [6]. Since most transportation fuels are composed of alkane and aromatic species [26], there is a need to assess the effect of turbulence on the flame for linear alkane, cyclic alkane, and aromatic fuels. Additionally, typical turbulent combustion regime diagrams [79] use only a few laminar flame properties such as S_L and l_F, implicitly assuming no significant chemical effects beyond those global properties. This raises an important question: what is the impact of fuel and chemistry on the turbulence-flame interaction?

The present study also aims at investigating the role of fuel chemistry in premixed flames at the transition from the thin to broken/distributed reaction zone regimes with engine-relevant, heavy hydrocarbon fuels. In the present work, n-heptane/air, toluene/air, iso-octane/air, and methane/air turbulent flames are studied. n-heptane, toluene, and iso-octane are characterized by large fuel Lewis numbers ($\mathrm{Le}_F \approx 2.8$, 2.5, and 2.8, respectively) while methane has a close to unity Lewis number ($\mathrm{Le}_F \approx 1$). Only fuels with Lewis numbers at and above unity are considered. Additionally, different chemical mechanisms of various sizes, from 35 to 207 species, are compared. The focus is placed on the effect of turbulence and differential diffusion on the turbulent flame speeds, the geometry of the reaction zone, and the chemical source terms. The objective of the present study is

not to compare high Karlovitz flames to low Karlovitz flames, but rather to compare the effects of fuel and chemistry within high Karlovitz number flames.

1.5 Integral Length Scale Effects

Accurate knowledge of the burning velocity of turbulent premixed flames is of importance for many combustion devices. In order to model the turbulent flame speed, premixed flames are often treated as a surface separating reactants and products. Based on this concept, a commonly used model for the turbulent burning velocity was proposed by Bray [18] and Candel and Poinsot [20]:

$$\frac{S_T}{S_L} = I_0 \frac{A_T}{A}, \tag{1.20}$$

where A_T is the turbulent flame surface area, A is the surface area of a flat flame, and I_0 is the burning efficiency. This equation distinguishes the local effects of turbulence on the chemistry (represented by I_0) from the global propagation of the flame into incoming turbulence (represented by A_T). While this model was originally intended for flames interacting with large-scale turbulence (flamelet regime) [27], it has been used successfully in multiple studies of turbulent flames in the thin reaction zones regime [91, 89, 98]. There is, however, no concensus on a general expression for I_0 applicable to flames interacting with intense turbulence. Furthermore, the effects of turbulence intensity and integral length scale on the flame surface area are not fully understood.

Unfortunately, DNS of turbulent flames at high Reynolds number using detailed, finite-rate chemistry remain beyond current computational resources. That is why studies of high Karlovitz number flames are often performed at low/moderate Reynolds numbers by reducing l/l_F [7, 6, 102, 101, 59] following the scaling

$$\mathrm{Re}_t \propto \left(\frac{l}{l_F}\right)^{4/3} \mathrm{Ka}^{2/3}. \tag{1.21}$$

For instance, in a previous study [101], the effects of small-scale turbulence on the flame chemistry at high Karlovitz numbers were investigated. Given that purpose and computational cost

considerations, a small integral length scale (roughly equal to the laminar flame thickness) was used. The validity of such an approach relies on two main assumptions. First, the small turbulent scales are universal (even at these low Reynolds numbers). Second, turbulent scales larger than the flame thickness do not impact the chemical processes.

Typical premixed turbulence scalings suggest that only scales smaller than the flame thickness can affect its structure [80]. However, it is sometimes argued that large scales can produce high strain rates which would quench the flame [87, 66]. This is investigated in this work. More precisely, the objectives are to identify the possible effects of l/l_F on the chemistry, and in doing so to investigate the dependence of the flame surface area and chemical source terms on Ka, Re_t, and l/l_F. These objectives are met by performing simulations with varying integral length scales at a fixed Karlovitz number, and using simulations at a fixed l/l_F with varying Ka.

1.6 Sub-filter Combustion Modeling

While Direct Numerical Simulations (DNS) are an extremely valuable research tool, they are currently limited to canonical configurations and low Reynolds numbers. This is due to the extreme range of length and time scales separating the large, energy-containing eddies, and the small, energy-dissipating eddies. At high Reynolds numbers, the resolution of all the scales of a turbulent flow requires computing resources well beyond current capabilities.

As an alternative, Large Eddy Simulations (LES) resolve the larger eddies while the effects of the smaller eddies are modeled. Depending on where the resolution threshold is set, the range of resolved scales can be drastically reduced, making LES of practical geometries at relevant conditions computationally feasible. The reduction in the range of resolved scales is often accompanied by the use of reduced-order chemistry models [86]. This helps reduce computational cost and simplify the sub-filter closure of non-linear terms.

Among such chemistry reduction methods, chemistry tabulation [110, 42] is an appealing approach as it requires the transport of only a few controlling variables (usually one or two). All thermodynamic and flame properties are tabulated against these controlling variables using infor-

mation obtained from detailed chemistry simulations of laminar flames. Commonly used tabulated chemistry modeling approaches for LES include the G-equation [72], PCM-FPI [30], and physical-space filtered flamelets [40, 75, 68]. While these models have been used with success in LES of low Karlovitz number flames, only a very limited number of studies have targeted premixed flames at high Karlovitz numbers [24, 34].

Most tabulated chemistry approaches rely on the assumption that the turbulent flame behaves locally like a one-dimensional laminar flame (flamelet regime). At high Karlovitz numbers, small turbulent eddies broaden the preheat zone and disturb the reaction zone [102, 98], causing significant fluctuations in the chemical source terms and local extinctions due to differential diffusion in high curvature regions [101]. Tabulated chemistry simulations using a single progress variable do not capture these phenomena [52]. Therefore, it is unclear if current sub-filter closure models, often validated using tabulated chemistry results [71, 73] at low to moderate Karlovitz numbers, are still valid under such conditions.

In this work, the assumptions behind typical sub-filter closures for tabulated chemistry are assessed using Direct Numerical Simulations of high Karlovitz number flames.

1.7 Large Eddy Simulations of High Karlovitz Flames

As mentioned previously, there is a lack of experimental studies of turbulent premixed flames at high Karlovitz numbers (see Fig. 1.6). Furthermore, very few Large Eddy Simulations of experimentally-studied turbulent premixed flames have been performed in the broken/distributed reaction zones regimes [24, 34] and these studies only considered methane/air combustion.

Since DNS of practical devices remain well beyond current computational capabilities, there is a need to assess the potential of LES to accurately predict high Karlovitz number flames with heavy hydrocarbon fuels.

In this work, fuel and hydrodynamic effects are studied by performing Large Eddy Simulations of a modified piloted premixed jet burner (PPJB) [31, 32] with matching experimental data. Any possible fuel effects are isolated by conducting the experiments with fuel/air mixtures with the same

S_L and by performing LES with models purposely assuming the same structure as laminar flames.

1.8 Objectives and Outline

In summary, the overarching goal of this thesis is to further the understanding of the physics of high Karlovitz number premixed flames, gain insight into their modeling, and perform simulations of experimentally-studied flames.

The specific objectives are as follows:

1. investigate the effects of the transition from the thin reaction zone regime to the distributed reaction zone regime on the flame structure and reaction zone;
2. investigate fuel and chemistry effects in those regimes;
3. investigate integral length scale or Reynolds number effects;
4. gain insight into modeling of the filtered chemical source term for LES;
5. perform simulations of experimentally-studied flames.

The governing equations and the numerical solver used are presented in Chapter 2. Objectives 1 through 4 are achieved by performing and analyzing a series of DNS with detailed chemistry using a canonical flow configuration and are presented in Chapters 3, 4, 5 and 6. Objective 5 is achieved through Large Eddy Simulations presented in Chapter 7. Conclusions and avenues of future work are presented in Chapter 8.

Chapter 2

Governing Equations and Computational Methodology

In the present thesis, both direct numerical simulations and large eddy simulations are performed. Both DNS and LES are performed with a low-Mach number code. Additionally, a compressible formulation is implemented to investigate compressibility effects and assess the validity of the low-Mach number assumption for the high Karlovitz number flames considered in this work.

The governing equations and computational methodology for DNS and LES with the low-Mach number code are presented here. The equations and methodology used in the compressibe code are described in Appendix B along with a few validation cases.

2.1 Direct Numerical Simulations

2.1.1 Governing equations

The governing equations for the unsteady, chemically reacting, low-Mach number Navier-Stokes equations are solved with both detailed kinetic modeling and tabulated chemistry. In detailed kinetic modeling, a transport equation is solved for each species and a chemical mechanism is used to compute the chemical source terms. The governing equations are

$$\frac{\partial \rho}{\partial t} + \nabla \cdot (\rho \mathbf{u}) = 0, \tag{2.1}$$

$$\frac{\partial \rho \mathbf{u}}{\partial t} + \nabla \cdot (\rho \mathbf{u}\mathbf{u}) = -\nabla p + \nabla \cdot \tau + \mathbf{f}, \tag{2.2}$$

$$\frac{\partial \rho Y_i}{\partial t} + \nabla \cdot (\rho \mathbf{u} Y_i) = -\nabla \cdot \mathbf{j_i} + \rho \dot{\omega}_i, \tag{2.3}$$

$$\frac{\partial \rho T}{\partial t} + \nabla \cdot (\rho \mathbf{u} T) = \nabla \cdot (\rho \alpha \nabla T) + \rho \dot{\omega}_T - \frac{1}{c_p} \sum_i c_{p,i} \mathbf{j_i} \cdot \nabla T + \frac{\rho \alpha}{c_p} \nabla c_p \cdot \nabla T. \tag{2.4}$$

In those equations, $\mathbf{u}$ is the velocity vector, ρ is the fluid density, τ is the viscous stress tensor,

$$\tau = \mu \left[\nabla \mathbf{u} + (\nabla \mathbf{u})^T \right] - \frac{2}{3} \mu (\nabla \mathbf{u}) \mathbf{I}, \tag{2.5}$$

$\mathbf{f}$ is a forcing term, Y_i is the species mass fraction, $\dot{\omega}_i$ is the species production rate, $\mathbf{j_i}$ is the species diffusion mass flux, T is the temperature, $c_{p,i}$ is the species heat capacity, c_p is the mixture heat capacity, $\alpha = \lambda/(\rho c_p)$ is the mixture thermal diffusivity, λ is the mixture thermal conductivity, and $\dot{\omega}_T = -\frac{1}{c_p} \sum h_i \dot{\omega}_i$ is the temperature production term (heat release). The species diffusion term is defined as:

$$\mathbf{j_i} = -\rho D_i \frac{Y_i}{X_i} \nabla X_i - \rho Y_i \mathbf{u_c}, \tag{2.6}$$

where $\mathbf{u_c}$ is the correction velocity to ensure conservation of mass:

$$\mathbf{u_c} = -\sum_i \rho D_i \frac{Y_i}{X_i} \nabla X_i. \tag{2.7}$$

The fluid is treated as a perfect gas with the equation of state

$$P_0 = \rho R T \sum_i \frac{Y_i}{W_i}, \tag{2.8}$$

where P_0 is the thermodynamic pressure, R is the universal gas constant, and W_i is the species molecular weight. Soret and Dufour effects, body forces, and radiative heat transfer are ignored. Soret and Dufour effects are not expected to be significant in slightly lean hydrocarbon flames. It should also be noted that there is no viscous heating term in the temperature equation. This is equivalent to the addition of a cooling term to the internal energy equation and it ensures that the

internal energy (and the temperature) can reach a stationary state [81].

In addition to detailed chemistry simulations, simulations are performed with tabulated chemistry. In tabulated chemistry, all thermodynamic and flame properties (ρ, ν, D, $\dot{\omega}$) are tabulated against one progress variable using the solutions of one-dimensional, unstretched, laminar premixed flames [42, 110, 53]. For all fuels considered, the progress variable is defined as the sum of H_2O, H_2, CO, and CO_2 mass fractions and is governed by the transport equation:

$$\frac{\partial \rho c}{\partial t} + \nabla \cdot (\rho \mathbf{u} c) = \nabla \cdot (\rho D \nabla c) + \rho \dot{\omega}_c. \tag{2.9}$$

In tabulated chemistry, this equation is used in place of Eqs. (2.3) and (2.4) and thus reduces significantly the computational cost.

The species viscosities μ_i are computed from standard gas kinetic theory [46] and the mixture-averaged viscosity is calculated using a modified form of Wilke's formula [115] (see Appendix A.2). The species thermal conductivities, λ_i, are computed using Eucken's formula [38] and the mixture-averaged thermal conductivity λ is obtained following Mathur *et al.* [64]. The species diffusivities are computed as $D_i = \alpha / Le_i$, with the Lewis numbers Le_i assumed to be constant throughout the flame.

2.1.2 Numerical framework

The governing equations 2.1 to 2.8 are solved using the energy conservative, finite difference code NGA designed for the simulation of variable density, low Mach number, turbulent flows [29]. The simulations use second-order accurate spatial and temporal discretizations. A semi-implicit Crank-Nicolson time integration is used [82]. A preconditioning strategy based on a diagonal approximation of the chemical Jacobian [103] is used to integrate the chemical source terms. The diagonal elements are approximated as the inverse of the chemical consumption timescales. The preconditioning is applied within an iterative procedure for each time step, allowing suitable reduction of the residuals in unsteady reacting flows. The numerical integration method has been thoroughly valided in 0D,

1D, and 3D cases (including the present turbulent flames). The third-order Bounded QUICK scheme, BQUICK [45], is used as the transport scheme of the species and temperature to ensure that the scalars remain within their physical bounds.

2.2 Large Eddy Simulations

The combustion modeling used in the present LES relies on chemistry tabulation with presumed sub-filter PDF. The governing equations are described first, followed by the chemistry tabulation.

2.2.1 Governing equations and LES closure

The filtered (LES) equations are as follows:

$$\frac{\partial \overline{\rho}}{\partial t} + \nabla \cdot (\overline{\rho}\tilde{\mathbf{u}}) = 0, \tag{2.10}$$

$$\frac{\partial \overline{\rho}\tilde{\mathbf{u}}}{\partial t} + \nabla \cdot (\overline{\rho}\tilde{\mathbf{u}}\tilde{\mathbf{u}}) = -\nabla \overline{p} + \nabla \cdot \overline{\tau} + \nabla \cdot \overline{\tau}_{\mathbf{u}}, \tag{2.11}$$

$$\frac{\partial \overline{\rho}\tilde{c}}{\partial t} + \nabla \cdot (\overline{\rho}\tilde{\mathbf{u}}\tilde{c}) = \nabla \cdot \left(\overline{\rho}\widetilde{D_c}\nabla \tilde{c}\right) + \nabla \cdot \overline{\tau}_c + \overline{\rho}\tilde{\dot{\omega}}_c, \tag{2.12}$$

$$\frac{\partial \overline{\rho}\tilde{Z}}{\partial t} + \nabla \cdot \left(\overline{\rho}\tilde{\mathbf{u}}\tilde{Z}\right) = \nabla \cdot \left(\overline{\rho}D_Z\nabla \tilde{Z}\right) + \nabla \cdot \overline{\tau}_Z, \tag{2.13}$$

where the density, $\overline{\rho}$, velocity vector, $\tilde{\mathbf{u}}$, progress variable, $\tilde{c}$, and mixture fraction, $\tilde{Z}$, are the resolved quantities. All sub-filter stresses ($\overline{\tau}_{\mathbf{u}}$) and scalar fluxes ($\overline{\tau}_{\phi}$) are closed using dynamic Smagorinsky models [41, 69, 61] with Lagrangian averaging techniques [65, 93]. A bar denotes Reynolds averaging while a tilde denotes Favre averaging.

The filtered thermochemical quantities $\overline{\rho}$, $\tilde{\nu}$, $\tilde{D}$, $\tilde{\dot{\omega}}$ are expressed as

$$\tilde{\phi} = \tilde{\phi}(\tilde{c}, \widetilde{c''^2}, \tilde{Z}) \tag{2.14}$$

and looked up from a table using the progress variable, its variance ($\widetilde{c''^2}$), and the mixture fraction. The validity of a tabulated chemistry approach for LES of high Karlovitz number flames will be

assessed in this thesis (Chapter 6).

The governing equations are solved using the energy conservative, finite difference code NGA designed for the simulation of variable density, low Mach number, turbulent flows [29]. The simulations use second-order accurate spatial and temporal discretizations. The third-order Bounded QUICK scheme, BQUICK [45], is used as the transport scheme for the scalars to ensure they remain within their physical bounds.

2.2.2 Sub-filter modeling

In the filtered equations, all sub-filter stresses are closed using a dynamic Smagorinsky model [41, 69, 61]. This model introduces an artificial eddy viscosity to represent the effects of turbulence. Kinetic energy dissipation at sub-filter scales is modeled as increased molecular diffusion. The sub-filter stresses are modeled as

$$\tau_{ij}^{\mathrm{SGS}} - \frac{1}{3}\tau_{i,j}^{\mathrm{SGS}}\delta_{ij} = -2\nu_t\widetilde{S}_{ij}, \tag{2.15}$$

where ν_t is the turbulent eddy viscosity and

$$\widetilde{S}_{ij} = \frac{1}{2}\left(\frac{\partial\widetilde{u}_i}{\partial x_j} + \frac{\partial\widetilde{u}_j}{\partial x_i}\right) \tag{2.16}$$

is the rate-of-strain tensor. In the Smagorinsky model, the turbulent eddy viscosity is computed as

$$\nu_t = (C_s\Delta)^2\left|\widetilde{S}\right|, \tag{2.17}$$

where $\widetilde{S} = \sqrt{2\widetilde{S}_{ij}\widetilde{S}_{ij}}$, Δ is the filter width, and C_s is a constant. While C_s is fixed in the static Smagorinsky model, a dynamic procedure is used to determine its value in the dynamic Smagorinsky model. The constant is computed as

$$C_s^2 = \frac{\mathcal{L}_{ij}\mathcal{M}_{ij}}{\mathcal{M}_{ij}\mathcal{M}_{ij}}, \tag{2.18}$$

where

$$\mathcal{M}_{ij} = 2\Delta^2\left(\widehat{\left|\widetilde{S}\right|\widetilde{S}_{ij}} - \alpha^2\left|\widehat{\widetilde{S}}\right|\widehat{\widetilde{S}}_{ij}\right), \tag{2.19}$$

and

$$\mathcal{L}_{ij} = \widehat{\widetilde{u}_i \widetilde{u}_j} - \widehat{\widetilde{u}}_i \widehat{\widetilde{u}}_j, \tag{2.20}$$

where $\widehat{\ }$ is a filtering operation with filter width $\widehat{\Delta}$ (larger than Δ) and $\alpha = \widehat{\Delta}/\Delta$.

To avoid numerical instabilities, an averaging procedure is used leading to

$$C_s^2 = \frac{\langle \mathcal{L}_{ij} \mathcal{M}_{ij} \rangle}{\langle \mathcal{M}_{ij} \mathcal{M}_{ij} \rangle}. \tag{2.21}$$

In the current work, Lagrangian averaging [65, 93] is used. The average of a variable ϕ at time t and location $x(t)$ is computed as

$$\langle \phi \rangle (t, x(t)) = \xi \phi(t, x(t)) + (1 - \xi) \phi(t - \Delta t, x(t - \Delta t)), \tag{2.22}$$

where Δt is the time step size and ξ is a weighting function defined as

$$\xi = \frac{\frac{2 \Delta t \psi^{\frac{1}{8}}}{3\Delta}}{1 + \frac{2 \Delta t \psi^{\frac{1}{8}}}{3\Delta}}, \tag{2.23}$$

where $\psi = \langle \mathcal{L}_{ij} \mathcal{M}_{ij} \rangle \langle \mathcal{M}_{ij} \mathcal{M}_{ij} \rangle$.

2.2.3 Sub-filter variance modeling

A scalar-gradient scaling law is used to obtain an algebraic equation for the sub-filter variance [83, 9]

$$\widetilde{c''^2} = C_v \Delta^2 |\nabla \widetilde{c}|^2, \tag{2.24}$$

where C_v is determined with a dynamic approach

$$C_v = \frac{\langle LM \rangle}{\langle MM \rangle}, \tag{2.25}$$

where

$$L = \widehat{\widehat{c}c} - \widehat{\widehat{\widehat{c}c}}, \tag{2.26}$$

and

$$M = \widehat{\Delta}^2 \nabla\widehat{\widehat{c}} \cdot \nabla\widehat{\widehat{c}}. \tag{2.27}$$

Chapter 3

Karlovitz Number Effects

In this chapter, DNS are performed to investigate the transition from the thin to broken/distributed reaction zone regimes in premixed flames with an engine-relevant, heavy hydrocarbon fuel, namely n-heptane. In contrast to [102, 101], turbulent flames are studied over a range of Karlovitz numbers, covering the thin reaction zone and the distributed burning regimes. More precisely, the Karlovitz number at the reaction zone is increased incrementally using different turbulence intensities and unburnt temperatures. The focus is placed on three main objectives.

- Understand and quantify differential diffusion effects on burning rate and heat release.
- Identify the transition to distributed burning and characterize the resulting reaction zone.
- Quantify and explain the occurence of local extinctions at increasing turbulence intensities.

In Section 3.1, the computational methodology is reviewed. An overview of the results is presented in Section 3.2. The three objectives are addressed in Sections 3.3, 3.4, and 3.5. Section 3.3 focuses on the role of differential diffusion on the fuel consumption and heat release rates; the transition to distributed burning is quantified in Section 3.4; and Section 3.5 describes local extinctions and their connection with differential diffusion effects. Section 3.6 highlights the importance of the Karlovitz number definition. Finally, the results are summarized and their implications for combustion modeling are discussed in Section 3.7.

3.1 Computational methodology

The direct numerical simulations performed in this study follow the methodology presented in Savard *et al.* [102] and Savard and Blanquart [101]. For completeness, the numerical framework is briefly reviewed here. A total of nine simulations have been performed. The parameters for each simulation are provided in Table 3.1.

3.1.1 Flow configuration

The same flow configuration is used for all the simulations and is illustrated in Fig. 3.1. It was chosen to achieve statistically-planar, three-dimensional, freely propagating flames without mean shear and mean curvature effects. The simulations can be run for an unbounded time, allowing a statistically-stationary state to be reached. Different configurations, where turbulence is sustained through mean shear in the flow, have been used in DNS studies of premixed turbulent combustion [98, 33, 56]. However, these configurations require directing computational resources towards large domains to contain the mean shear. Additionally, these flows develop in space or time which increases the complexity of isolating the effects of the flame on turbulence. Therefore, the present configuration was chosen in order to study the effect of turbulence on the chemical source terms at a reasonable computational cost.

Inflow/outflow boundary conditions are used in the x direction and periodic boundary conditions are used in the y and z directions. To avoid negative inlet velocities, the unburnt gases are introduced with a low turbulent kinetic energy (TKE). The domain size is $11L \times L \times L$ in x, y, and z respectively. The relation of the domain width, L, to the integral length scale is discussed in Section 3.1.4.

Since the flow configuration lacks generation of turbulence due to large scale flow straining, turbulence forcing is necessary [4, 5, 7, 8, 6, 90, 91, 89]. The forcing magnitude is increased $0.5L$ downstream of the inlet to reach the desired TKE value. The velocity field forcing is stopped after a distance of $8L$ and the velocity fluctuations decay rapidly, such that there are no negative axial velocities at the outlet. The forcing method used is briefly described in subsection 3.1.4. For each simulation, the mean inlet velocity is constant throughout the simulation and selected to

match approximately the turbulent flame speed of that simulation. This inflow velocity is obtained by performing a first simulation with an approximate inflow velocity and computing the mean turbulent flame speed (from Eq. (6.9)) over approximately 10 eddy turnover times. The simulation is then restarted with this new inflow velocity. In practice, the flames drift slightly, but the drift is negligible compared to the domain length. The simulations are performed for at least 50 eddy turnover times, $\tau = k/\epsilon$, and statistics are computed using the last 30 τ to remove any initial transient effects. While a turnover time is shorter than a flame time ($\tau_F = l_F/S_L$) at high Ka, using 30τ was verified to be sufficient by running one of the simulations for approximately ten flame times. The authors have found that only a few eddy turnover times were sufficient to remove the effect of the initial conditions on quantities controlled by small turbulent scales such as chemical source terms, curvature, and strain rate.

All simulations are performed on uniform grids with constant Δx spacing in all three directions and offer sufficient resolution of the small-scale turbulence ($\Delta x \leq 2\eta$) [92] and sufficient resolution of the flame ($\Delta x \leq l_F/20$) [15]. Grid resolution is discussed further in Appendix A.1 and the time accuracy (timestep size and associated errors) was also previously investigated [99, 103] and found to be sufficient.

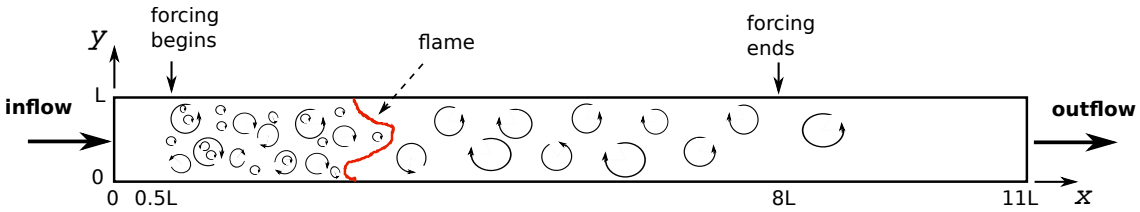

Figure 3.1: Schematic diagram of the flow configuration, from Savard *et al.* [102]. The domain is three-dimensional and periodic boundary conditions are used in the y and z directions.

3.1.2 Simulation parameters

The unburnt gas is a lean n-C_7H_{16}/air mixture at standard pressure ($P_0 = 1$ atm) and varying temperatures. The equivalence ratio ($\phi = 0.9$) is the same for all simulations and air is 23.2% O_2 and 76.8% N_2 by mass. The unburnt temperatures (T_u) and turbulent intensities (u') are changed to cover a range of reaction zone Karlovitz numbers clustered around the thin to broken/distributed

reaction zones regimes. Figure 3.2 shows where the simulations stand on a typical regime diagram, and Table 3.1 summarizes the simulation parameters. For most cases, two simulations are performed: one with non-unity Lewis numbers and one with unity Lewis numbers (subscript 1). Simulations with unity Lewis numbers are not expected to reproduce realistic, experimentally observed flames and are not computationally cheaper than non-unity Lewis number simulations. They are used for comparison purposes as they allow the systematic isolation of differential diffusion effects. Simulations A and A_1 are expected to be representative of the thin reaction zones regime. Simulations B and B_1 were previously reported in Savard *et al.* [102] and were selected to fall close to the transition from thin to broken/distributed reaction zones. They have the same unburnt temperature as case A with an increased turbulence intensity. The turbulence intensity ratio (u'/S_L) and length scale ratio (l/l_F) of simulations C are held approximately the same as for case B, while the unburnt temperature is increased. The unburnt Karlovitz numbers (Ka) are thus similar, but the reaction zone Karlovitz numbers (Ka_δ) are different. Finally, simulations D and D_1 use the same unburnt temperature as C with a further increase in turbulence intensity, increasing further the Karlovitz numbers. Those simulations are expected to be representative of the distributed burning regime.

Due to intense turbulence conditions and high unburnt temperatures, the turbulent Mach number, $Ma_t = u'/c$, reaches approximately 0.25 for case D_1. The maximum instantaneous Mach number in the domain due to turbulent fluctuations is around 0.9. It is unclear *a priori* if the low-Mach number assumption is still valid for such flames. This was assessed by developing a compressible formulation of the NGA code and performing the simulation of flame D_1 with both flow solvers. The code description, validation, and results are presented in Appendix B. It is found that compressibility effects remain negligible for case D. Therefore, only results obtained with the low-Mach number code are presented in this Chapter.

Simulation C$'$ uses an intermediate unburnt temperature of 500 K with a turbulence intensity ratio resulting in the same reaction zone Karlovitz number as case C (albeit at an higher unburnt Karlovitz number). This simulation is used to highlight the importance of using the reaction zone Karlovitz number (with the Kolmogorov length scale at the reaction zone) to investigate the influence

of turbulence on the chemical sources terms in simulations at different unburnt temperatures.

The objective of the present study is to investigate the effects of small-scale turbulence on the flame chemistry at high Karlovitz numbers. Given that purpose and computational cost considerations, a small integral length scale (roughly equal to the laminar flame thickness) is used. It is important to note that the domain width imposes a length scale and the simulations may be missing large scale effects. However, the focus of this chapter is on the reaction zone, whose thickness is significantly smaller than the domain size ($L \sim 15\delta_F$). This way, the effects of small-scale turbulence on the flame can be isolated from large-scale effects (not specific to high Karlovitz number flames and already present in low Karlovitz number flames). Effects of integral length scale will be assessed in Chapter 5.

Case	A	A_1	B [102]	B_1 [102]	C	C_1	C′	D	D_1
T_u (K)	298		298		800		500	800	
ϕ	0.9		0.9		0.9		0.9	0.9	
S_L (m/s)	0.36	0.29	0.36	0.29	2.3	1.71	0.86	2.3	1.71
l_F (mm)	0.39	0.43	0.39	0.43	0.25	0.27	0.32	0.25	0.27
u'/S_L	9.0	10	18	21	19	25	38	45	60
l/l_F	1.1	1.0	1.1	1.0	1.2	1.1	1.0	1.2	1.1
Ka_u	78	91	220	280	204	280	648	740	1050
Ka_δ	1.9	1.6	7.0	5.0	73	64	70	256	237
Re_t	83		190		170		290	380	
η_u (m)	1.6×10^{-5}		9.0×10^{-6}		7.0×10^{-6}		4.6×10^{-6}	3.5×10^{-6}	
Δx (m)	1.8×10^{-5}		1.8×10^{-5}		1.2×10^{-5}		1.0×10^{-5}	7.0×10^{-6}	
Domain	$11L \times L \times L$		$11L \times L \times L$		$11L \times L \times L$		$11L \times L \times L$	$11L \times L \times L$	
Grid	11×128^3		11×128^3		11×128^3		11×146^3	11×220^3	
$T_{\mathrm{peak,lam}}$	1240	1365	1240	1365	1345	1482	1290	1345	1482
T_{ad}	2188		2188		2447		2298	2447	

Table 3.1: Parameters of the simulations. Subscript 1 denotes simulations with unity Lewis numbers. ϕ is the equivalence ratio, S_L is the laminar flame speed, $l_F = (T_b - T_u)/|\nabla T|_{\max}$ is the laminar flame thickness, $l = u'^3/\epsilon$ is the integral length scale, Ka_u is the Karlovitz number in the unburnt gas, Ka_δ is the reaction zone Karlovitz number, $\mathrm{Re}_t = u'l/\nu$ is the turbulent Reynolds number in the unburnt gas, η_u is the Kolmogorov length scale in the unburnt gas, Δx is the grid spacing, L is the domain width and corresponds to $\sim 5l$, $T_{\mathrm{peak,lam}}$ is the temperature of peak fuel consumption rate in the corresponding laminar flame, and T_{ad} is the adiabatic temperature in the corresponding laminar flame.

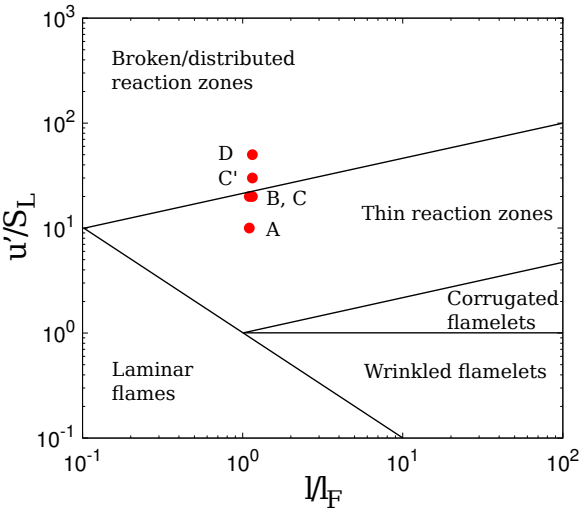

Figure 3.2: Regime diagram showing current simulations.

3.1.3 Chemical and transport models

All nine simulations use the same Lewis numbers as the increase in unburnt temperature does not significantly change the Lewis numbers. The species Lewis numbers are taken from the simulation of one-dimensional, laminar, premixed flames using full transport properties computed with FlameMaster [85]. They are listed in Table 3.2. Soret and Dufour effects were neglected. It was shown by Savard and Blanquart [101] that, in the one-dimensional laminar heptane flame considered, differences in species mass fractions and chemical source terms were negligible between mixture-averaged formulation for transport properties (including Soret effects) and constant Lewis numbers. The impact of these limitations in 3D turbulent flames is still unknown and is beyond the scope of the present work.

The present study uses a reduced n-heptane chemical mechanism. The mechanism developed in Bisetti *et al.* [11] was further reduced from 47 species and 290 reactions to 35 species and 217 reactions. Species produced under rich conditions (mostly aromatic species) were removed. The mechanism used in this study does not contain low temperature chemistry (such as the formation of peroxide species RO_2). While low temperature chemistry is known to be relevant to ignition studies, it is not expected to play a significant role in the present study on turbulent premixed flames.

N_2	0.99	1-CH_2	0.94	3-CH_2	0.94
O	0.69	H_2	0.28	H	0.16
OH	0.70	H_2O	0.79	O_2	1.06
HO_2	1.07	CH	0.64	CO	1.07
HCO	1.22	CH_2O	1.23	CH_3	0.96
CO_2	1.37	CH_4	0.97	C_2H_3	1.28
C_2H_4	1.28	C_2H_5	1.39	C_2H	1.25
HCCO	0.86	C_2H_2	1.27	C_3H_3	1.60
A-C_3H_5	1.79	n-C_3H_7	1.81	C_2H_6	1.40
P-C_3H_4	1.68	A-C_3H_4	1.68	C_3H_6	1.80
1-C_4H_8	1.99	1-C_5H_{10}	2.27	1-C_5H_{11}	2.08
2-C_7H_{15}	2.84	n-C_7H_{16}	2.84		

Table 3.2: Species Lewis numbers used in the turbulent flame simulations.

3.1.4 Turbulence forcing

The canonical flow configuration used in the present study lacks generation of turbulence due to large scale flow straining. Consequently, the turbulence is expected to decay. In the present simulations, the characteristic time scale for the decay of turbulent kinetic energy is smaller than the laminar flame time scale. The ratio of these two is in fact the inverse of the Karlovitz number. Velocity field forcing is thus necessary to maintain a constant turbulence intensity and achieve a statistically-stationary state.

Linear velocity forcing [96, 23] was chosen for its physical nature and good stability properties. Linearly forced turbulent fields under comparable Reynolds numbers were analyzed in Ref. [23] and it was shown that the second- and third-order structure functions and the energy spectrum are self-consistent and in agreement with experimentally obtained data [74] of decaying grid turbulence. One advantage of the present linear forcing method is that an isotropic field is not imposed via the forcing and any physically-relevant anisotropy generated by the flame will be preserved. The forcing method is implemented through the addition of a source term to the momentum equation

$$\mathbf{f}(x,y,z,t) = \frac{\epsilon_0}{2k(x,t)} \left(\rho\mathbf{u}(x,y,z,t) - \overline{\rho\mathbf{u}}(x,t)\right), \tag{3.1}$$

where ϵ_0 is the desired dissipation rate and k is the planar Favre-averaged TKE

$$k = \frac{1}{2}\left(\widetilde{u''^2} + \widetilde{v''^2} + \widetilde{w''^2}\right). \tag{3.2}$$

Planar Favre averages are defined as

$$\widetilde{\xi} = \frac{\overline{\rho\xi}}{\overline{\rho}}, \tag{3.3}$$

with the standard (Reynolds) planar average

$$\overline{\xi}(x,t) = \frac{1}{L^2}\int_0^L\int_0^L \xi(x,y,z,t)\,\mathrm{d}y\,\mathrm{d}z. \tag{3.4}$$

As demonstrated in previous studies, the present forcing technique imposes a fixed integral length of approximately 1/5 of the domain width and a constant dissipation rate throughout the flame [101, 96, 23]. Hence, the turbulent rms velocity ($u' = (\epsilon_0 l)^{1/3}$) is fixed by l and ϵ_0. Under these conditions, the turbulent kinetic energy was found to be almost constant [101]. Additionally, in recent work by Bobbitt *et al.* [14], the present configuration with forced turbulence was found to produce similar vorticity characteristics as the slot Bunsen flames of Sankaran *et al.* [98]. This suggests that the turbulence characteristics of the present flames are relevant to practical configurations where turbulence is generated through intense mean shear.

Figure 3.3 shows the energy and dissipation spectra taken at a fixed plane in the unburnt gases and averaged over time. These correspond to two-dimensional three components velocity spectra computed in a y-z plane. When normalized by their respective Kolmogorov scales, all spectra collapse to a single curve. This confirms that, even in the absence of an inertial subrange in the present low Reynolds number simulations, the dissipation scales in the incoming turbulence are universal. Since the turbulence at the scale of the reaction zone is in the viscous dissipation range, the small scales interacting with the flame are expected to be the same whether the Reynolds number is high or low. Nevertheless, assessing Reynolds number effects in high Karlovitz number flames is the subject of Chapter 5.

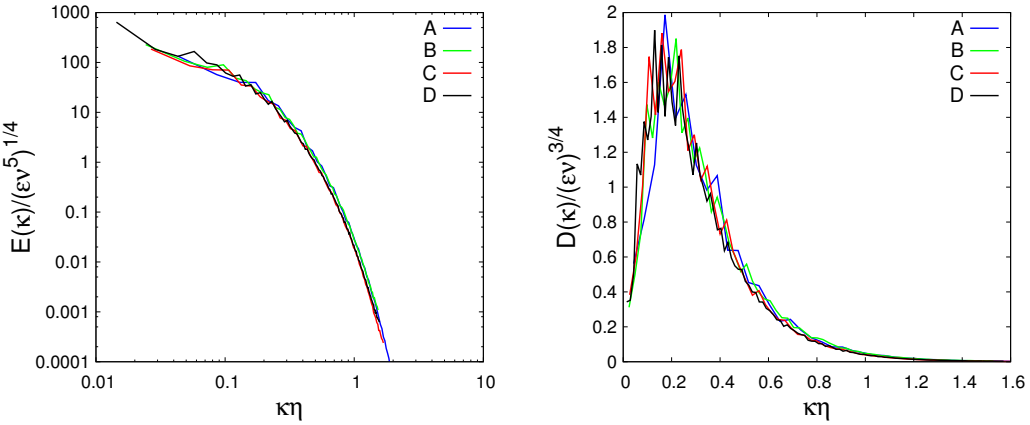

(a) Energy spectra

(b) Dissipation spectra

Figure 3.3: Normalized energy and dissipation spectra for the different simulations. Two-dimensional three components spectra taken in a y-z plane in the unburnt gases.

3.2 Results overview

This section presents a qualitative overview of the simulations performed. The differential diffusion effects on the species mass fractions dependence on temperature are highlighted, and the influence of turbulence on the main chemical reactions contributing to fuel consumption and heat release rates is investigated.

3.2.1 Global properties

Figure 3.4 shows two-dimensional slices of vorticity magnitude and temperature for simulations A, B, C, and D using non-unity Lewis numbers (results of simulation C$'$ are very similar to C and will be discussed in Section 3.6). The slices were taken at arbitrary spatial and temporal locations (after the initial transient) and are representative of each simulation.

Increasingly smaller scales are observed from cases A to D. This is due to the decreasing Kolmogorov length scale. In all cases, smaller turbulent structures are observed in the preheat zone than in the reaction zone and in the burnt gases. As viscosity increases through the flame, the Kolmogorov length scale (defined as $\eta = (\nu^3/\epsilon)^{1/4}$) increases too. The vorticity contours also highlight the fact that, as the reaction zone Karlovitz number is increased, small-scale turbulent structures become more prominent in the burnt gases. In comparison to the respective incoming turbulence,

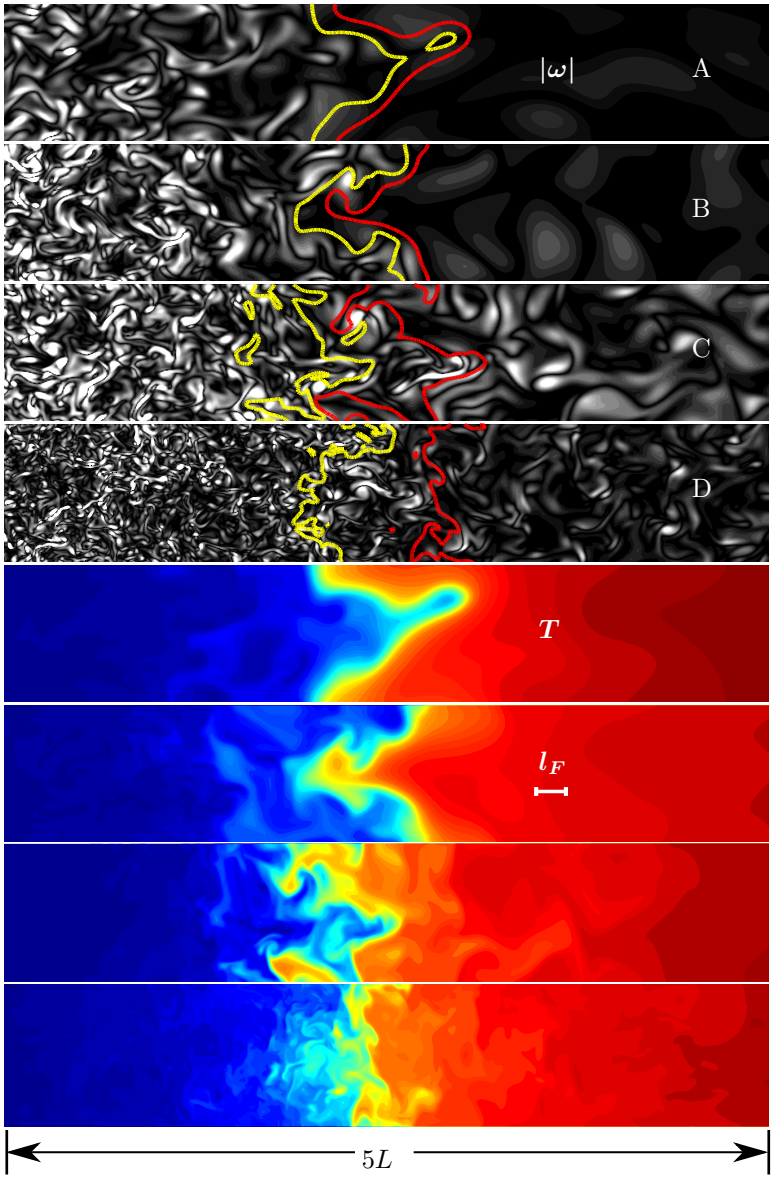

Figure 3.4: Two-dimensional slices of a $5L \times L$ region centered around the flame showing magnitude of vorticity and temperature for the non-unity Lewis number cases, respectively. The yellow line indicates the $T_{\text{peak}} - 300\text{K}$ isocontour and the red line indicates the $T_{\text{peak}} + 300\text{K}$ isocontour. The vorticity ranges are satured at [0, 8e4] (s^{-1}), [0, 1.6e5] (s^{-1}), [0, 1.6e6] (s^{-1}), and [0, 8e6] (s^{-1}). The temperature ranges are [298, 2200] K for A and B and [800, 2400] K for C and D.

smaller structures are observed in the burnt gases in cases C and D than cases A and B. This is again an effect of the different viscosity ratios across the flame due to the change in unburnt temperature. Finally, the yellow and red lines indicate isocontours of temperature at 300K below and above the corresponding temperature of peak fuel consumption rate in the turbulent flame. They illustrate the broadening of the reaction zone with increased Karlovitz number. The distributed nature of the reaction zone will be further analyzed in Section 3.4.

The temperature contours indicate that, in all cases, the flame appears thicker than the laminar flame but to a different extent. In case A, there is only a slight broadening of the preheat zone. The flame resembles a locally one-dimensional laminar flame. Signs of increased turbulent mixing are noticeable in cases B and C. The flame surface appears more wrinkled and the preheat zone is further broadened. Case D presents more small-scale turbulent structures and enhanced turbulent mixing.

Table 3.3 summarizes the average turbulent flame speed (S_T), its standard deviation, and the fuel effective reaction zone thickness, all normalized by their respective laminar flame values. The turbulent flame speed is defined here as:

$$S_T = \frac{1}{(\rho Y_F)_u L^2} \int_V \rho \dot{\omega}_F \, \mathrm{d}V. \tag{3.5}$$

The effective reaction zone thickness (equivalent to the turbulent flame brush thickness of the whole flame) is defined here as the volume where the fuel burning rate is greater than 5% of the laminar value divided by the cross-sectional area of the $y-z$ plane,

$$\delta_T = \frac{\mathrm{Vol}(\dot{\omega}_F > 0.05 \dot{\omega}_{F,\mathrm{lam}})}{L^2}. \tag{3.6}$$

As expected, the turbulent flame speed increases with Ka_δ and significant fluctuations are present. The effective reaction zone thickness also increases with Ka_δ, showcasing the broadening and increase in surface area of the flame with increased turbulence intensity. Note that the reaction zone can still be thin despite $\delta_T > 1$. The effective reaction zone thickness is affected by the increase in surface area and thus does not represent the local reaction zone thickness. There is also a clear difference between non-unity Lewis number and unity Lewis number simulations. The ratio of turbulent to laminar flame speed is always lower when differential diffusion is included, although the difference is reduced as Ka_δ is increased.

Case	$\overline{S_T}/S_L$		$\mathrm{std}(S_T)/S_L$		$\overline{\delta_T}/\delta_{F,\mathrm{lam}}$	
	Le$\neq$1	Le=1	Le$\neq$1	Le=1	Le$\neq$1	Le=1
A	1.6	3.0	0.4	0.8	2.3	3.1
B	2.2	3.4	0.6	0.6	3.0	3.3
C	3.3	4.6	0.7	0.9	4.4	5.5
C′	3.4		0.6		4.5	
D	4.7	6.7	1.2	1.7	6.4	7.0

Table 3.3: Time average and standard deviation of the turbulent flame speed as well as fuel effective reaction zone thickness for the different cases.

3.2.2 Turbulent flame structure

Following the qualitative overview and global quantities presented in Section 3.2.1, the local flame structure is now investigated. As mentioned earlier, cases B and B_1 have already been investigated by Savard *et al.* [102]. They reported that, in case B_1 with unity Lewis numbers, the conditional mean profiles of species mass fractions with respect to temperature followed very closely the profiles of a one-dimensional, unstretched laminar flame at the same conditions. In contrast, in case B, the turbulent flame structure lay between that of a full transport and a unity Lewis number flamelet. This is a consequence of the increased effective species diffusivity due to turbulent mixing [80, 100]. It is thus expected that, as the turbulence intensity is increased, differential diffusion effects would be reduced. This is verified in the present study by examining the conditional mean with respect to temperature of two representative species.

Figures 3.5 and 3.6 present conditional means of n-C_7H_{16} and C_2H_4 mass fractions from simulations A (lowest Ka_δ) through D (highest Ka_δ). In all unity Lewis number cases (subscript 1), the conditional mean of the fuel mass fractions follows closely the unity Lewis laminar flame. The fuel mass fraction exhibits small differences between cases A and A_1 and B and B_1. No noticeable differences are observed between cases C and C_1 and D and D_1. The same trends are observed for the mass fraction of C_2H_4, a key chemical intermediate in the cracking of the fuel, shown in Fig. 3.6.

For both species, the profiles from the non-unity Lewis number turbulent simulations are closer to the unity Lewis number laminar flame than the non-unity Lewis number laminar flame. It should be noted that case A presents the largest departure from the unity Lewis number 1D profiles and that departure is reduced as the turbulence level is increased. This is consistent with the reduction

of differential diffusion effects with increased turbulent mixing [100]. While differential diffusion effects appear negligible for flames C and D, they still play an important role on chemical source terms (as will be shown in Section 3.3).

Finally, one might expect that fuel cracking (i.e. fuel being consumed at lower temperatures than in the laminar flame) may occur in turbulent flames due to a thicker flame and thus longer residence time. Such early fuel cracking would result in a mean fuel mass fraction profile below that of the corresponding laminar flame. This was not observed here despite the high unburnt temperature of 800K.

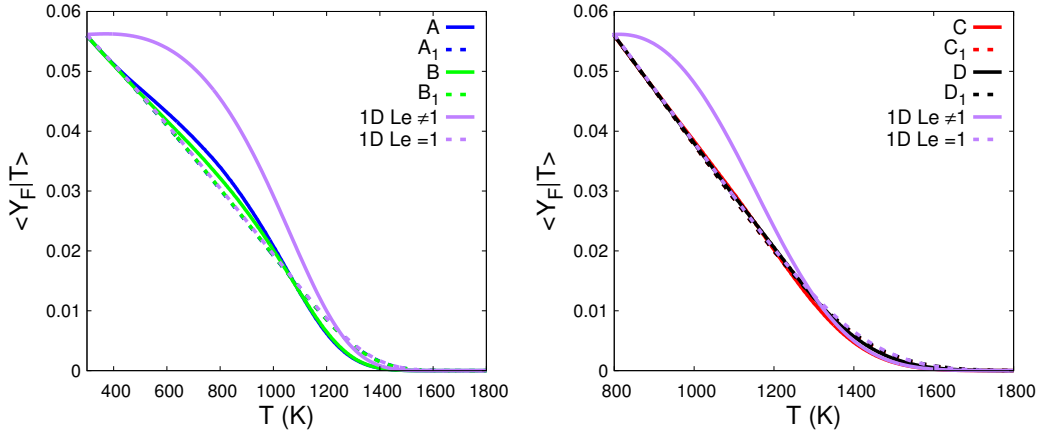

(a) Cases A and B ($T_u = 298$K) (b) Cases C and D ($T_u = 800$K)

Figure 3.5: Conditional means of fuel mass fractions.

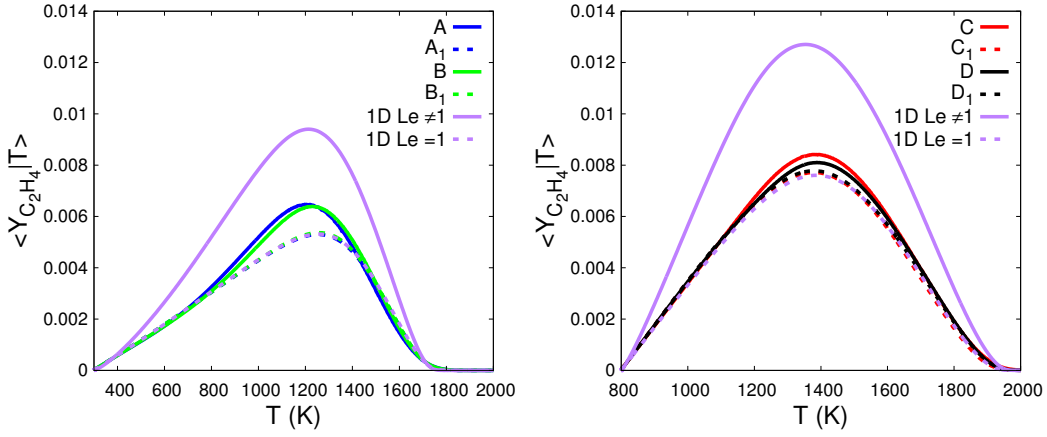

(a) Cases A and B ($T_u = 298$K) (b) Cases C and D ($T_u = 800$K)

Figure 3.6: Conditional means of C_2H_4 mass fractions.

3.2.3 Chemical pathways

Since the present study is focused on the effects of turbulence on the fuel consumption and heat release rates, it is of interest to examine if the chemical pathways are affected by changes in the turbulence intensity. In this subsection, the main contributing reactions to fuel consumption and heat release rates are compared between the laminar and turbulent simulations.

In the laminar simulations, the following three reactions account for more than 95% of the overall fuel consumption rate

$$\begin{aligned} n\text{-}C_7H_{16} + H &\rightarrow 2\text{-}C_7H_{15} + H_2, \\ n\text{-}C_7H_{16} + OH &\rightarrow 2\text{-}C_7H_{15} + H_2O, \\ n\text{-}C_7H_{16} + O &\rightarrow 2\text{-}C_7H_{15} + OH. \end{aligned} \tag{3.7}$$

Table 3.4 lists the contributions (in percentage) of the three reactions to the overall fuel consumption rate of the corresponding flame. The contribution of the different reactions is very similar between laminar flames and turbulent flames. Cases A and D are selected as they have the lowest and highest reaction zone Karlovitz numbers, respectively. The percentage of contribution of each reaction is essentially unchanged from laminar to highly turbulent flames, with or without differential diffusion. In other words, turbulence and differential diffusion effects do not change the balance between the different fuel consumption reactions.

Considering the present mechanism, a large number of reactions present non-negligible heat release rates (above 5% of the total). Among them, the following two reactions contribute significantly to the overall heat release rate:

$$\begin{aligned} CH_3 + O &\rightarrow CH_2O + H, \\ HCO + H &\rightarrow CO + H_2. \end{aligned} \tag{3.8}$$

The contributions to the overall heat release rate from these two reactions are shown for the different

Reaction/Case		298K		800K	
		1D	Case A	1D	Case D
n-C_7H_{16}+H	Le$\neq$1	59	56	65	68
	Le$=$1	52	55	55	56
n-C_7H_{16}+OH	Le$\neq$1	32	34	26	28
	Le$=$1	33	31	29	28
n-C_7H_{16}+O	Le$\neq$1	8	10	8	12
	Le$=$1	12	13	12	14
CH_3 + O	Le$\neq$1	12	13	12	13
	Le$=$1	13	13	13	14
HCO + H	Le$\neq$1	7	6	9	9
	Le$=$1	9	9	10	10

Table 3.4: Percentage of contribution of different reactions to the overall fuel consumption rate (first three reactions) and heat release rate (last two reactions) of the corresponding flame.

laminar flames and turbulent cases A and D in Table 3.4. The heat release rate of each reaction is normalized by the peak overall heat release rate of the corresponding flame. For both reactions, the contribution to the total heat release rate remains largely unchanged between the laminar and turbulent cases. The fuel consumption reactions are not among the main contributors to heat release. This is because n-heptane breaks down into small C_2 and C_3 fragments (mostly C_2H_4 and C_3H_6) before the heat release layer.

In summary, for both fuel consumption and heat release rates, there is no significant effect of turbulence intensity on the main contributing reactions. The important reactions in the laminar flames remain the most important in the turbulent flames and their relative contributions are largely unchanged. Differences in absolute magnitudes will be discussed in the following sections.

3.3 Differential diffusion effects

In this section, the effects of differential diffusion on the fuel consumption and heat release rates are investigated.

Contour plots of the fuel consumption rate for the eight different cases are presented in Fig. 3.7. A white line is superimposed to show the location of the peak fuel consumption rate. It is defined as the isocontour $T = T_{\text{peak}}$, the temperature of peak source term in the corresponding turbulent flame. In cases A and B, the reaction zone remains thin but signs of local extinctions are observed

for the non-unity Lewis number simulations. This was already observed by Savard *et al.* [102]. The Kolmogorov length scale in the unburnt gas is smaller than the laminar reaction zone thickness in all cases (A through D). However, it increases significantly through the flame due to the large increase in kinematic viscosity. In fact, for cases A and B, the Kolmogorov length scale at the reaction zone ($\eta_\delta = 1.2\times10^{-4}$ m and 7×10^{-5} m), evaluated as $\eta_\delta = (\nu_\delta^3/\epsilon)^{1/4}$, is not significantly smaller than the laminar reaction zone thickness ($\delta_{F,\text{lam}} = 1.5\times10^{-4}$ m). As a result, turbulence does not significantly broaden the reaction zone.

As mentioned previously, there is a distinct change from case B to case C. The Karlovitz number in the unburnt gases is the same in cases B and C but noticeable differences are observed since the Karlovitz number at the reaction zone is larger in case C. As Ka_δ is increased, the source terms exhibit larger fluctuations and local broadening of the reaction zone is observed. Finally, the fuel consumption rate contours of case D appear to be more diffused as chemical reactions occur further away from the iso-surface. This is characteristic of distributed burning.

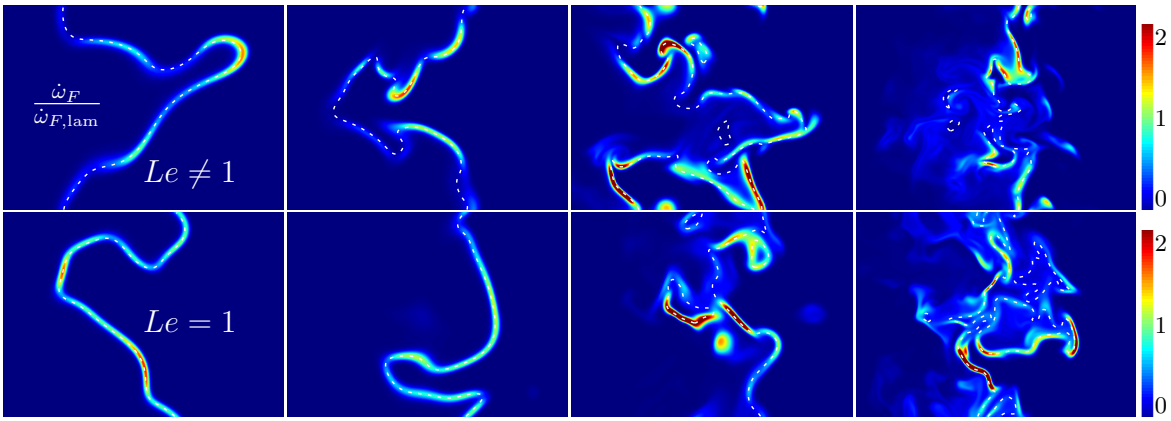

(a) Case A (b) Case B (c) Case C (d) Case D

Figure 3.7: Two-dimensional slices of the fuel consumption rate (normalized by the peak value of the corresponding laminar flame). The fuel consumption rate range is satured at [0,2] in each case. The isotherm of peak source term is also shown (white). The top figures correspond to the non-unity Lewis number simulations while the bottom figures correspond to the unity Lewis number cases.

Figures 3.8 and 3.9 present conditional means in temperature space of the normalized fuel consumption and heat release rates for the different non-unity Lewis number cases. Only the mean source terms are shown but it should be noted that, as turbulence intensity at the reaction is increased, the fluctuations of the fuel consumption rate are enhanced significantly. A characterization

and quantification of these fluctuations will be provided later in Section 3.5. For both fuel and heat release, simulations including differential diffusion exhibit a lower mean source term than the corresponding laminar flame with differential diffusion, but the conditional mean approaches that of the laminar flame without differential diffusion as Ka_δ is increased. It is interesting to evaluate quantitatively these effects with increasing Ka_δ.

Figure 3.10a shows the shift in temperature of the peak fuel consumption rate for the non-unity and unity Lewis number turbulent flames. The peak temperature corresponds to the location of the maximum of the conditional means, shown in Fig. 3.8. Note that the peak temperature of heat release rate is not shown as it does not change significantly between non-unity and unity laminar and turbulent flames. For cases A and B, the peak fuel source term in the turbulent flame occurs at the same temperature as the 1D laminar flame with differential diffusion. In case C, the peak fuel consumption rate is observed at a slightly higher temperature than in the laminar non-unity Lewis number flame. This effect is more pronounced in case D as the temperature of peak source term approaches that of the laminar unity Lewis number flame. This is one of many indications that, as turbulent mixing is enhanced, differential diffusion effects are reduced. It should be noted that, while the dependence of species mass fractions on temperature showed relatively small Lewis number effects even in case A (Section 3.2.2), differential diffusion effects on the chemical source terms are more pronounced and still present at high Karlovitz numbers.

The change in peak temperature can be explained by a change in the effective Lewis numbers due to enhanced turbulent mixing. To quantify this change, the semi-empirical model of Savard and Blanquart [100] is considered

$$Le_{i,\mathrm{eff}} = \frac{1 + a_1 \mathrm{Ka}_\delta}{\frac{1}{Le_i} + a_1 \mathrm{Ka}_\delta}. \tag{3.9}$$

As the focus is placed on the reaction zone and not the preheat zone, the unburnt Karlovitz number Ka was replaced by Ka_δ. Similarly to [100], the proportionality coefficient is adjusted to best fit the data ($a_1 = 0.01$). One-dimensional laminar flames are computed with these effective Lewis numbers and the predictions of the peak temperature of the fuel consumption rate are shown in Fig. 3.10a. The change in peak temperature of the laminar flames at both 298K and 800K are similar and thus

a single curve is shown for clarity. A good agreement between the model and the turbulent flames simulations is found.

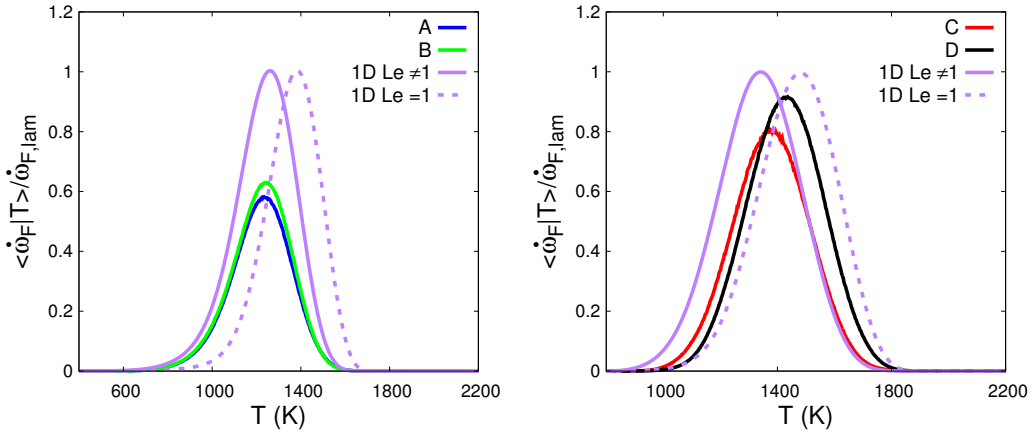

(a) Cases A and B (b) Cases C and D

Figure 3.8: Conditional means of normalized fuel consumption rate for non-unity Lewis number simulations. The fuel consumption rates are normalized by the peak value in the corresponding laminar flame.

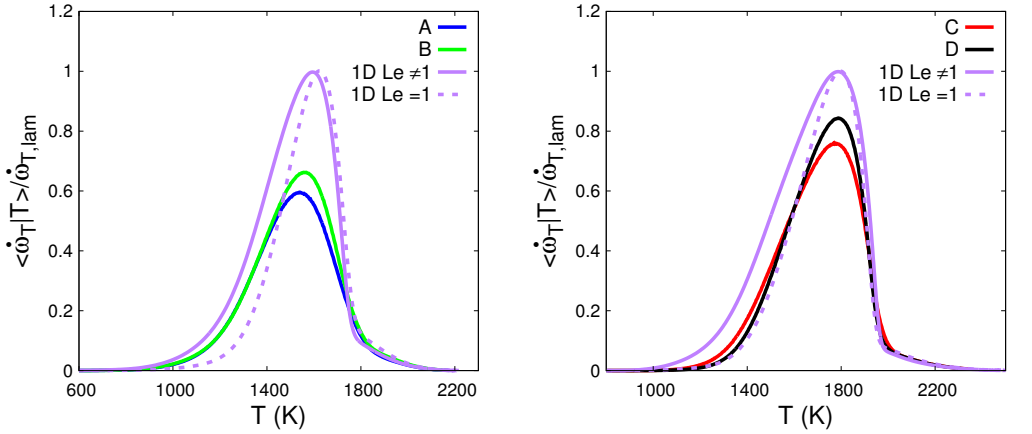

(a) Cases A and B (b) Cases C and D

Figure 3.9: Conditional means of normalized heat release rate for non-unity Lewis number simulations. The heat release rates are normalized by the peak value in the corresponding laminar flame.

Figure 3.10b presents the maximum values of the conditional means of $\dot{\omega}_F$ and $\dot{\omega}_T$ as a function of the reaction zone Karlovitz numbers for the different simulations using both non-unity and unity Lewis numbers. The conditional means were computed using at least 30 data files (to ensure converged statistics) and the standard deviations of the means are negligible. There are, however,

large fluctuations of the chemical source terms around the mean values, as will be discussed in Section 3.5. The mean fuel consumption rates of the unity Lewis number cases are all close to the laminar values. While this had been observed in previous studies [102, 101] for the fuel consumption in case B_1, it is of interest to note that there is no Karlovitz number effect on the mean fuel consumption and heat release rates in the unity Lewis number cases. On the other hand, the mean fuel consumption rate is smaller than that of the corresponding laminar flame in all non-unity Lewis number cases. As Ka_δ is increased, the conditional means of the non-unity flames get closer to those of the corresponding unity Lewis number flame. It appears that, in the limit of high Karlovitz numbers, the fuel consumption rate approaches the laminar value without differential diffusion. Once again, this is consistent with previous observations that differential diffusion effects appear to weaken as turbulence intensity increases. In previous studies of distributed flames [7, 6], it was observed that the fuel consumption rate was enhanced in low Lewis number hydrogen flames and remained close to the laminar values in methane and propane flames. This is consistent with the present observations.

The lower mean fuel consumption and heat release rates in the present non-unity Lewis number simulations can be attributed to curvature effects. It was shown by Savard and Blanquart [101], in case B, that low fuel consumption rates are correlated with regions of high curvature, suggesting the presence of focusing/defocusing effects. As differential diffusion effects are diminished, the chemical source terms are less sensitive to curvature. This difference in fuel consumption rates can explain the differences in the flame speeds reported in Table 3.3. As discussed in Savard and Blanquart [101], the ratio of turbulent to laminar flame speeds (S_T/S_L) can be explained by the turbulent flame surface area (A_T/A, where A is the cross-sectional area) and the mean turbulent to laminar chemical source term ratio $\dot{\omega}/\dot{\omega}_{\text{lam}}$. For the unity Lewis number simulations, A_1 through D_1, since the source term ratio is unity, the change in flame speeds is due to an increase in flame surface area A_T/A with increasing Ka_δ. Finer turbulent structures within the flame (due to the larger Ka_δ) lead to an enhanced area. The difference between the non-unity and unity Lewis number simulations at the same Ka_δ are due to the difference in $\dot{\omega}/\dot{\omega}_{\text{lam}}$ since, for a given Ka_δ, the flame surface area is roughly

constant. Thus, the increase in S_T/S_L with Ka_δ for the non-unity Lewis number cases (A through D) is due to both an increase in $\dot{\omega}/\dot{\omega}_{\mathrm{lam}}$ and an increase in A_T/A. This is summarized in Table 3.5. The link between the turbulent flame speed, the flame surface area, and the chemical source term will be discussed in more detail in Chapter 4.

Case	$\overline{S_T}/S_L$		$\langle \dot{\omega} \vert T_{\mathrm{peak}} \rangle / \dot{\omega}_{\mathrm{lam}}$		$\overline{A_T}/A$	
	$\mathrm{Le} \neq 1$	$\mathrm{Le} = 1$	$\mathrm{Le} \neq 1$	$\mathrm{Le} = 1$	$\mathrm{Le} \neq 1$	$\mathrm{Le} = 1$
A	1.6	3.0	0.58	1.00	2.5	2.8
B	2.2	3.4	0.63	0.98	3.1	3.3
C	3.3	4.6	0.80	1.06	4.3	4.2
D	4.7	6.7	0.91	1.09	5.7	5.8

Table 3.5: Time average of the normalized turbulent flame speeds, mean fuel consumption rates at T_{peak}, and turbulent flame surface area at T_{peak} for the different cases.

Heat release rate shows similar trends as the fuel consumption rate, namely: the conditional means of unity Lewis number simulations are close to the corresponding laminar value; and simulations with differential diffusion show a lower mean but a noticeable increase in $\langle \dot{\omega}_T \vert T \rangle$ with Ka_δ, getting closer to the unity Lewis number simulations. Note that the maximum values of the conditional means of heat release (Fig. 3.10b) are computed at the temperature of peak heat release rate of the corresponding flame. This temperature being larger than the temperature of peak fuel consumption rate, there is a reduction in the Kolmogorov length scale at the corresponding T_{peak}. Additionally, the width of the heat release layer is slightly larger than that of the fuel consumption layer. Hence, the reaction zone Karlovitz number for heat release differs from that of the fuel. That being said, the difference is small and does not change any of the trends presented here or in following sections. Thus, for simplicity, both fuel and heat release quantities are plotted against the fuel's Ka_δ.

3.4 Distributed burning

In this section, the transition towards distributed burning is investigated. Figures 3.4 and 3.7 seem to indicate that a transition towards distributed burning is observed as Ka_δ is increased. Distributed burning is characterized by a widening of the reaction zone, and is due to increased turbulent mixing

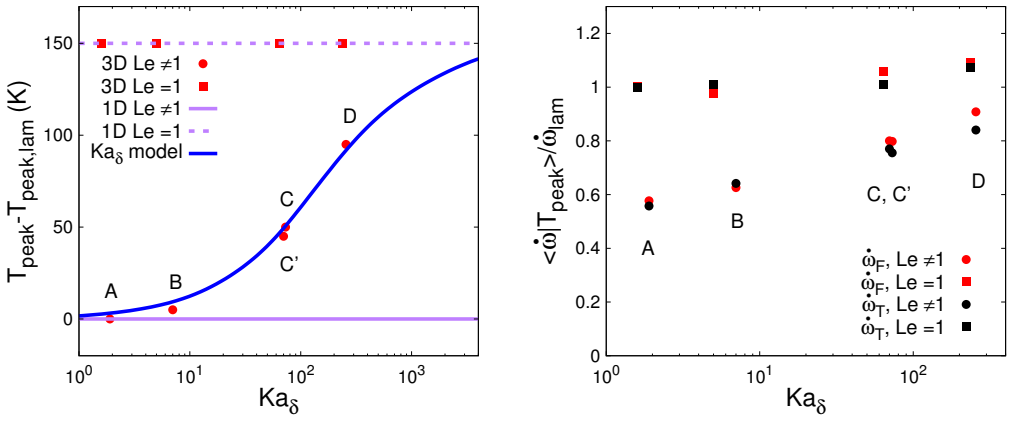

(a) T_{peak} (b) Conditional means

Figure 3.10: Temperature at which the peak burning rate is observed for all cases in (a). Conditional means of the normalized fuel consumption and heat release rates at the corresponding temperature of peak source term in (b). Values are normalized by the corresponding laminar flame.

in that region of the flame [7]. The first step is to quantify the widening of the reaction zone in physical space by evaluating the mean fuel consumption rate conditional to the normal distance to the isosurface of T_{peak}. This post-processing step is performed using a level set method [104]. A level set function is first created as $d(x,y,z) = T(x,y,z) - T_{\text{peak}}$. It is then reinitialized into a signed distance function using a Fast Marching Method (FMM) algorithm. The conditional mean of the burning rate as a function of distance from the peak temperature is shown in Figs. 3.11a and 3.11b. The distance has been normalized by the laminar reaction zone thickness, defined as the distance over which the fuel burning rate is above 5% of the peak laminar value. In cases A and B, the fuel source term follows a similar profile as the laminar flame (albeit with a smaller magnitude). This is an evidence that cases A and B fall in the thin reaction zone regimes. A slight widening of the reaction zone is observed at small values of $\dot{\omega}_F$. In cases C and D, this widening is more noticeable, and non-negligible fuel consumption rates are observed at distances greater than the laminar reaction zone thickness. To quantify the widening of the reaction zone as the turbulence level is enhanced, Fig. 3.11c presents the percentage of the total burning rate occuring outside the laminar reaction zone thickness for the different cases:

$$\frac{\int_{|d|>\delta_{F,\text{lam}}/2} \dot{\omega}_F \mathrm{d}V}{\int_V \dot{\omega}_F \mathrm{d}V}. \tag{3.10}$$

The percentage of reactions occuring outside of the laminar reaction zone thickness varies from 8% in cases A and B to 20% in case D. It is important to note that similar trends are observed in both non-unity and unity Lewis number simulations. In other words, the widening of the reaction zone is not an effect of differential diffusion.

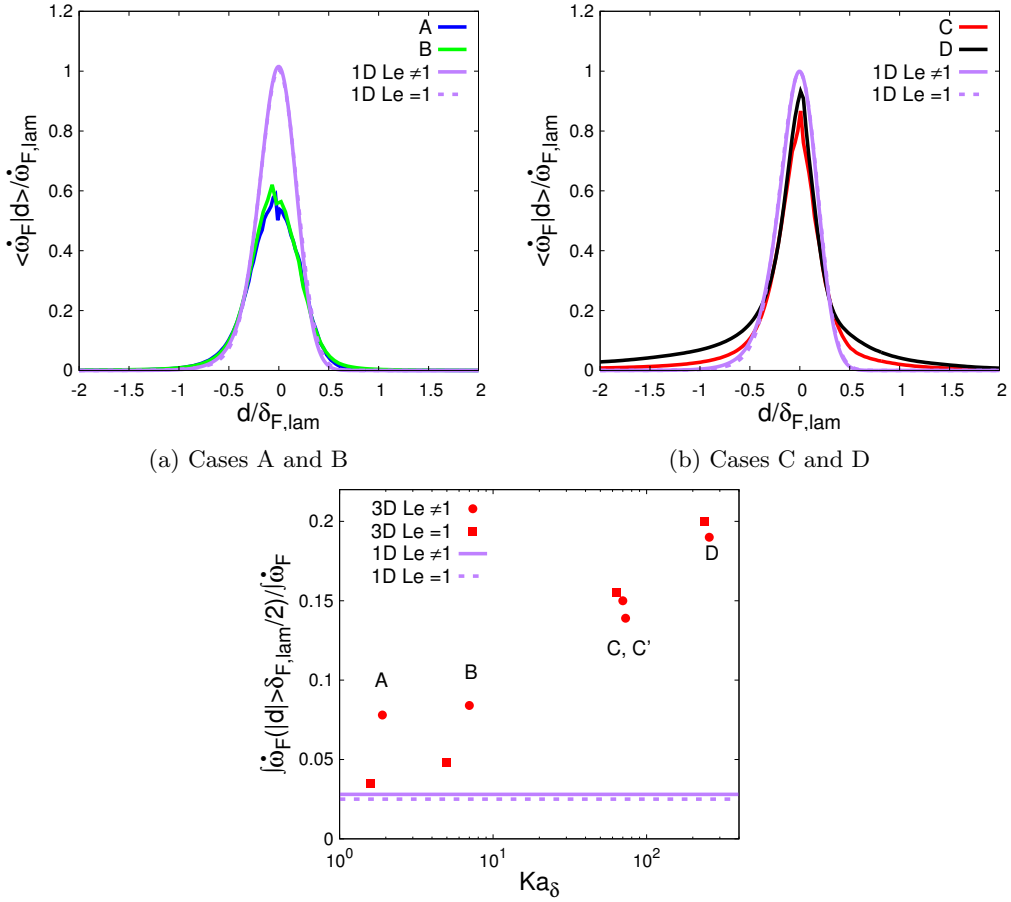

(a) Cases A and B

(b) Cases C and D

(c) $\%\,\dot{\omega}_F(|d| > \delta_{F,\mathrm{lam}}/2)$

Figure 3.11: Conditional mean of normalized fuel consumption rate as a function of distance from the peak temperature for the non-unity Lewis number simulations in (a) and (b) and fraction of the total burning rate occuring at $|d| > \delta_{F,\mathrm{lam}}/2$ for all cases in (c).

The broadening of the reaction zone in physical space can have two different causes. First, in phase space, the chemical reactions may be occuring over a wider temperature range. Second, it could be the consequence of a change in local temperature gradients. Table 3.6 presents the average fuel reaction zone thickness in temperature space $\overline{\Delta T_F}$ and the average reaction zone thickness in physical space $\overline{\delta_F}$, both normalized by the corresponding laminar values. The thickness in temperature space

corresponds to the temperature range where the mean fuel consumption rate (see Fig. 3.8) is above 5% of the laminar value. The physical thickness of the reaction zone corresponds to the local distance around the peak source term where its value is above 5% of the laminar value (see Fig. 3.11). The main observation is that the reaction zone is not wider than the laminar flame in temperature space. Consistent with the results of Section 3.2.3, reactions occur in the same temperature range as the laminar flames. Hence, the widening of the reaction zone is due to a change in the local temperature profile. To better illustrate this conclusion, Fig. 3.12 presents the conditional mean of temperature as a function of the distance from the peak temperature for the turbulent and laminar flame simulations. It is seen that, as the reaction zone Karlovitz number is increased, the temperature profile is flattened. Temperatures close to the peak temperature are observed over a larger distance away from the peak temperature.

Case	$\overline{\Delta T_F}/\Delta T_{F,\mathrm{lam}}$		$\overline{\delta_F}/\delta_{F,\mathrm{lam}}$	
	$\mathrm{Le}\neq 1$	$\mathrm{Le}=1$	$\mathrm{Le}\neq 1$	$\mathrm{Le}=1$
A	0.89	1.1	1.1	1.1
B	0.89	1.1	1.1	1.1
C	0.90	1.0	1.3	1.6
C′	0.91		1.4	
D	0.92	1.0	2.2	2.5

Table 3.6: Normalized fuel reaction zone thickness in temperature space and physical space. $\Delta T_{F,\mathrm{lam}} =$ 679K for cases A and B and 690K for cases C and D. $\delta_{F,\mathrm{lam}} = 1.5 \times 10^{-4}$m for cases A and B and 1.2×10^{-4}m for cases C and D.

The widening of the reaction zone can be explained (once again) by the enhanced turbulent diffusivity. First, let us assume that the reaction zone thickness scales as the square root of the product of the diffusivity and the chemical time scale

$$\delta_F \propto \sqrt{D t_c}. \tag{3.11}$$

Consider again the semi-empirical model of Savard and Blanquart [100] for the turbulent diffusivity

$$\frac{D_T}{D} \propto a_2 \mathrm{Ka}_\delta. \tag{3.12}$$

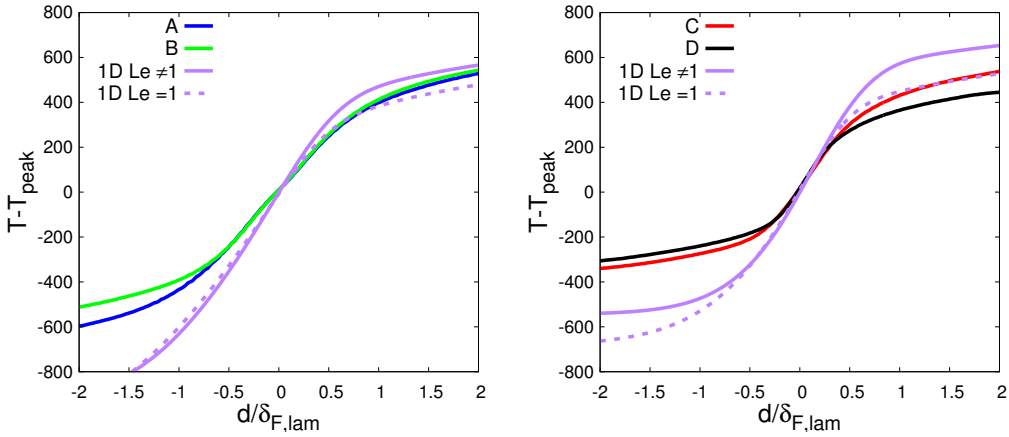

(a) Cases A and B (b) Cases C and D

Figure 3.12: Conditional mean of temperature as a function of distance from the peak temperature for the non-unity Lewis number simulations.

Assuming that the chemical time scales are essentially unchanged between laminar and turbulent cases, a model for the turbulent reaction zone thickness follows

$$\frac{\overline{\delta_F}}{\delta_{F,lam}} \propto \sqrt{1 + a_2 \mathrm{Ka}_\delta}. \tag{3.13}$$

The proportionality coefficient is adjusted to best fit the data ($a_2 = 0.02$) and remains close to that obtained for Eq. (3.9) ($a_1 = 0.01$). The functional form of the empirical models presented here should be applicable to other fuels and conditions. However, the exact numerical values of the proportionality coefficients might change. The prediction from the model is compared with the results in Fig. 3.13. A good agreement between the model and the turbulent flames simulations is found. This is the final evidence that the broadening of the reaction zone is due to reduced temperature gradients because of enhanced turbulent mixing. It should be noted that, in addition to enhanced turbulent diffusivity, increased occurence of high curvatures could lead to the observed widening of the reaction zone. It is, however, difficult to differentiate these effects.

In previous studies [7, 6], distributed burning was related to an exponential distribution in the probability density function (pdf) of $|\nabla\rho|$, characteristic of turbulent scalar mixing. It was shown that in low Karlovitz number (non-distributed) flames, the pdf presented a more rapid decay than

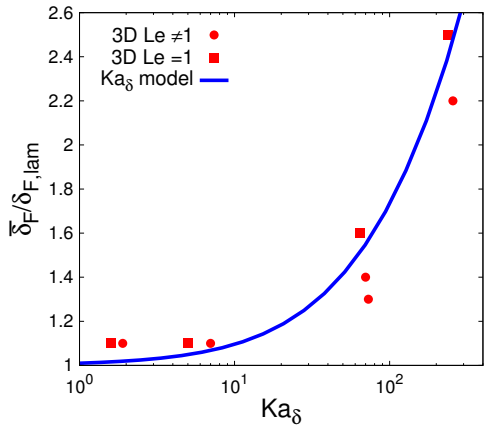

Figure 3.13: Normalized fuel reaction zone thickness in physical space.

exponential for large gradients. An exponential decay of the pdf of $|\nabla\rho|$ is equivalent to a log-normal distribution for $\chi = 2\alpha|\nabla T|^2$. This is characteristic of turbulent mixing of a passive scalar [37, 3, 77]. While it is a consequence of turbulent eddies penetrating the reaction zone, it is not evidence of distributed burning. Again, the widening of the reaction zone is due to smaller density/temperature gradients (Fig. 3.12).

Finally, it is important to note that despite the clear widening of the reaction zone most of the reactions still occur in a thin reaction zone. Additionally, the structure of the reaction zone above $\sim$20% of the peak laminar value is very similar to that of the laminar flame (Figs. 3.12a and 3.12b). These observations, combined with the previous observation of Savard and Blanquart [101] that the fuel consumption locally scales like its value at T_{peak}, justify considering a flame isosurface at the peak temperature as will be done in the following section.

3.5 Local extinction

This section focuses on the third and final objective, namely the occurence of local extinctions in the fuel consumption and heat release rates. Figure 3.14a presents standard deviations of the fuel consumption and heat release rate at the corresponding peak temperatures as a function of the reaction zone Karlovitz numbers. Both series of flames (unity and non-unity Lewis numbers) present similar fuel consumption rate standard deviations. The amplitudes of fluctuations increase

from cases A to D, consistently with the increase in small-scale turbulence at the reaction zone. This is also in agreement with the fluctuations in turbulent flame speeds reported in Table 3.3. In all cases, the magnitude of the standard deviation is comparable to that of the mean. In the case of heat release, the standard deviations are slightly larger with differential diffusion effects and increase with higher reaction zone Karlovitz number in the unity Lewis number simulations. It is interesting to note that differential diffusion effects have a clear influence on the mean chemical source terms (Fig. 3.10b) but show a much smaller effect on the standard deviations. Chemical source term fluctuations are primarily caused by the intense turbulence and only show little impact on heat release rates.

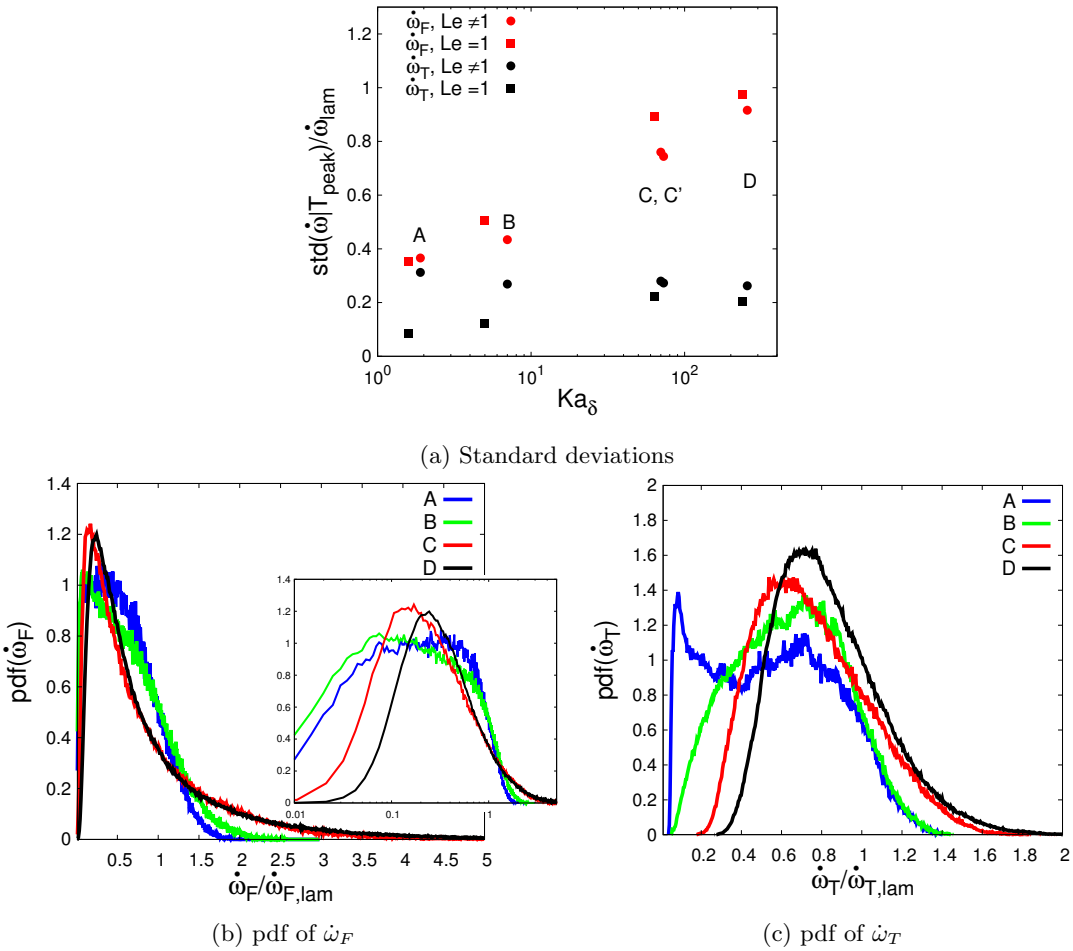

(a) Standard deviations

(b) pdf of $\dot{\omega}_F$

(c) pdf of $\dot{\omega}_T$

Figure 3.14: Standard deviations of the normalized fuel consumption and heat release rates in (a). Probability density function of the normalized fuel consumption rate in (b). Probability density function of the normalized heat release rate in (c). All taken at the corresponding peak temperature.

Figure 3.14b presents the probability density of $\dot{\omega}_F$ (taken at the corresponding isosurface $T = T_{\text{peak}}$) for the different cases using non-unity Lewis numbers. All simulations exhibit smaller fuel consumption rates compared to the laminar value of 1. This is consistent with the mean burning rates reported earlier in Section 3.3 (Fig. 3.10b). As turbulence intensity is increased, the peak of the distribution is followed by a sharper decrease. The long tails (for large values) in cases C and D correspond to the increased fluctuations in burning rate mentioned earlier. The insert with a logarithmic scale illustrates the change in distribution with increased turbulence intensity. The pdfs of the burning rate are approaching a log-normal distribution in cases C and D.

Figure 3.14c presents the probability density of $\dot{\omega}_T$ (taken at the corresponding T_{peak} of heat release) for the different cases using non-unity Lewis numbers. Higher probability of small heat release rates are found at lower turbulence intensities. As Ka_δ is increased, the peak of the pdf shifts towards larger values. This shift occurs to a greater extent than for the fuel consumption rate. The shape of the pdf also changes significantly. Once again, case D is approaching a log-normal distribution.

Local extinctions are defined here as the fuel consumption rate being smaller than 5% of the laminar value on the isosurface $T = T_{\text{peak}}$ [101, 28] (similar trends are observed with thresholds of 1 and 10 %). They are observed with similar probability in cases A (2%) and B (3%) and lower probability in cases C ($< 1\%$) and D ($< 0.1\%$) as shown in Fig. 3.15. This decrease in probability of extinction events with increasing Ka_δ is interesting as it was shown in Fig. 3.14a that source term fluctuations increased with higher Ka_δ. The decrease in extinctions and increase in fluctuations can be attributed to the transition to a distributed burning regime. The reaction zone is uniformized by enhanced turbulent mixing, thus reducing the probability of local extinction. This also illustrates that extinction events are only present for the non-unity Lewis number cases, over the present range of Karlovitz numbers.

These observations, at different Karlovitz numbers, are consistent with the previous observation [101] in case B that local extinctions (in non-unity Lewis number flames) are correlated with regions of high curvature (i.e. curvature of the size of the reaction zone thickness). Intense turbu-

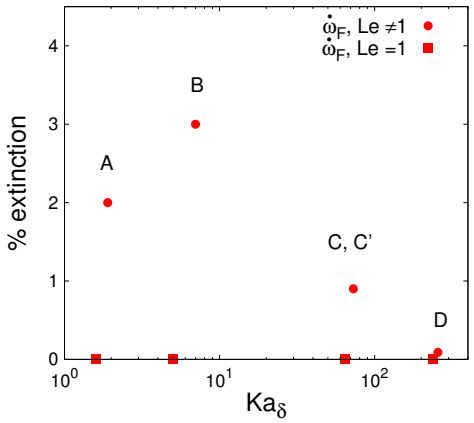

Figure 3.15: Probability of local extinction for the different cases.

lence is required to produce such high curvatures in thermo-diffusively stable flames. More precisely, the fuel mass fraction is correlated with curvature [101], illustrating the defocusing/focusing effect observed in laminar and turbulent flames [43]. Extinction events are thus caused by a combination of intense turbulence and differential diffusion effects.

In summary, the probability of local extinction (or very low fuel consumption rate) increases as Ka_δ is increased from a laminar flame to case B due to the larger curvatures. As Ka_δ is further increased the probability of extinction decreases. This is a consequence of the transition towards unity effective Lewis numbers. The gradual suppression of differential diffusion effects reduces the probability of extinction in regions of high curvature. In the present high Karlovitz number flames, no global extinction was observed and local extinctions were associated with differential diffusion effects. This is consistent with the observations of Aspden *et al.* [7, 6].

3.6 Karlovitz number definition

It is common practice to classify turbulent premixed flames with respect to global, governing quantities evaluated in the unburnt gases, such as the unburnt Karlovitz number [80]. The simulations presented here highlight the fact that the Karlovitz number at the reaction zone (Eq. (1.19)) is the meaningful parameter to characterize the influence of small-scale turbulence on the chemical source terms. More precisely, simulations B and C are qualitatively and quantitatively different while hav-

ing very similar values of the unburnt Karlovitz number Ka_u (220 and 204). On the other hand, simulations C and C′, with a similar Ka_δ (73 and 70) but different Ka_u (204 and 648), have very similar average turbulent flame speeds as well as standard deviations (see Table 3.3). Additionally, their fuel consumption and heat release rates distributions, shown in Figs. 3.16a and 3.16b, are very close.

The reaction zone Karlovitz number is affected by the change in viscosity across the flame and does not take into account the density ratio. Under these conditions, the fact that simulations with the same reaction zone Karlovitz number but different density ratios (C and C') present very similar reaction zone characteristics is an illustration that the change in viscosity has a much greater impact on the small scales than the change in density. The dependence on the reaction zone Karlovitz number may have been expected, but it emphasizes that care has to be exercised when comparing simulations performed at the same u'/S_L and l/l_F but using different unburnt temperatures. While Ka_u is appropriate to quantify the influence of turbulence on the preheat zone, Ka_δ (with the Kolmogorov length scale evaluated at the reaction zone) should be used to describe the effect of the turbulence on the reaction zone.

In the present analysis, the reaction zone Karlovitz number is defined in terms of laminar flame properties and incoming turbulence quantities, similarly to the commonly used Karlovitz number evaluated in the unburnt gases. This is possible since ϵ is constant through the present flames (as a result of the forcing technique). It should be noted that the dissipation rate was also found to be approximately constant across the flame in turbulent slot Bunsen flames [14]. However, this may not be the case in general and thus an accurate estimation of Ka_δ would require knowledge of ϵ at the reaction zone.

3.7 Summary

Three main observations were made from the analysis presented in this Chapter.

First, the increase in turbulence intensity suppressed differential diffusion effects on the flame structure; the species mass fractions dependence on temperature was similar to that of a one-

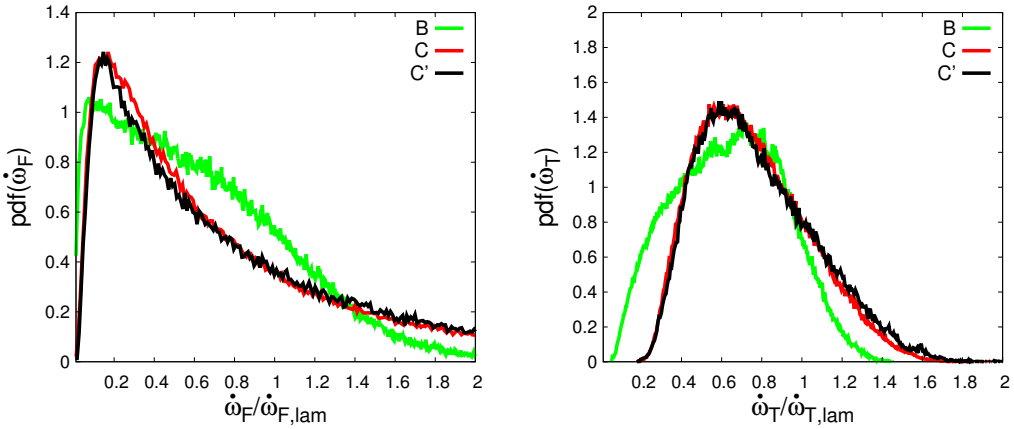

(a) pdf of $\dot{\omega}_F$ (b) pdf of $\dot{\omega}_T$

Figure 3.16: Probability density function of the normalized fuel consumption and heat release rates at the corresponding T_{peak}.

dimensional, unity Lewis number flame. However, differential diffusion effects on the chemical source terms were still present even at high Karlovitz numbers. The consequences were lower mean fuel consumption and heat release rates in the non-unity Lewis number simulations. As turbulence intensity at the reaction zone was increased (i.e. increase in Ka_δ), these rates are ultimately approaching the respective unity Lewis number values. This first set of observations has multiple implications for modeling. In the scope of LES, it indicates that mean quantities (Y_i, ω_i, etc) for unity Lewis number turbulent flames, such as methane flames, could be adequately modeled without detailed chemistry. Tabulated chemistry approaches based on laminar flames would be sufficient. However, this is not the case when significant differential diffusion effects are present, as for heavy hydrocarbon fuels. Thus, there is a need for reduced order models capable of predicting accurately the mean chemical source terms in non-unity Lewis number high Karlovitz flames.

Second, the transition to distributed burning was highlighted by measuring the width of the reaction zone in physical and temperature space. It was shown that the reaction zone's physical width increases with the reaction zone Karlovitz number. However, even at high Karlovitz numbers ($\text{Ka}_\delta \sim 100$), most of the reactions still occur in a thin reaction zone of a thickness comparable to that of a laminar flame.

Third, local extinctions and chemical source terms fluctuations were investigated and quantified

through probability density functions at the temperature of peak reactions. Large fluctuations in fuel consumption rate were observed for both non-unity and unity Lewis number simulations, increasing with the reaction zone Karlovitz number. However, it is unclear, especially in the context of LES filtering, if these chemical source term fluctuations need to be incorporated in low-order models. This will be assessed in Chapter 6. These large fluctuations only lead to local extinction events in the non-unity Lewis number flames, and the probability of these events decreased at high Karlovitz numbers. In fact, less than 1% of the flame surface underwent extinction at $\mathrm{Ka}_\delta > 10$. This was explained by the competing effects of increased curvatures and decreased differential diffusion effects as the reaction zone Karlovitz number was increased.

Throughout the analysis, it was shown that the reaction zone Karlovitz number (evaluated with the appropriate Kolmogorov length scale) was the relevant parameter to characterize the interaction of small-scale turbulence on the chemical source terms. Simulations with similar unburnt Karlovitz numbers but different reaction zone Karlovitz numbers showed distinct fuel consumption and heat release rates.

Chapter 4

Fuel and Chemistry Effects

In this chapter, DNS are performed to investigate the role of fuel chemistry in premixed flames at the transition from the thin to broken/distributed reaction zone regimes with engine-relevant, heavy hydrocarbon fuels. n-heptane/air, toluene/air, iso-octane/air, and methane/air turbulent flames are studied. n-heptane, toluene, and iso-octane are characterized by large fuel Lewis numbers ($\mathrm{Le}_F \approx$ 2.8, 2.5, and 2.8, respectively) while methane has a close to unity Lewis number ($\mathrm{Le}_F \approx 1$). Only fuels with Lewis numbers above unity are considered. Additionally, different chemical mechanisms of various sizes, from 35 to 207 species, are compared. The focus is placed on the effect of turbulence and differential diffusion on the turbulent flame speed, the geometry of the reaction zone, and the chemical source terms. The objective of the present chapter is to compare the effects of fuel and chemistry within high Karlovitz number flames.

In Section 4.1, the computational methodology is reviewed. An overview of the results is presented in Section 4.2. Section 4.3 analyzes the effects of turbulence, differential diffusion, and fuel chemistry on the strain rate and curvature distributions at the reaction zone surface. Section 4.4 compares the chemical fuel consumption rates between the different cases. Finally, the results are summarized in Section 4.5.

4.1 Computational methodology

The direct numerical simulations performed in this study follow the methodology presented in Section 3.1. A total of twenty four simulations are used. The parameters for each simulation are

provided in Tables 4.1, 4.2, 4.3, and 4.4. Table 4.1 lists simulations from Chapter 3 while Tables 4.2 to 4.4 list new simulations performed to study fuel and chemistry effects.

4.1.1 Flow configuration

The flow configuration described in Section 3.1 is used for the simulations presented in this chapter. Again, the objective is to investigate the effects of small-scale turbulence on the flame chemistry at high Karlovitz numbers. Given that purpose and computational cost considerations, a small integral length scale (roughly equal to the laminar flame thickness) is used. It is important to note that the simulations may be missing large scale effects. However, the focus of the study is on the reaction zone, whose thickness is significantly smaller than the domain size ($L \sim 15\delta_{F,\mathrm{lam}}$). This way, the effects of small-scale turbulence on the flame can be isolated from large-scale effects (not specific to high Karlovitz number flames and already present in low Karlovitz number flames). Effects of integral length scale will be studied in Chapter 5.

4.1.2 Simulation parameters

For each simulation, the unburnt gas is a fuel/air mixture at standard pressure ($P_0 = 1$ atm) and varying temperatures. The unburnt temperature (T_u) is changed to cover a range of reaction zone Karlovitz numbers clustered around the thin to broken/distributed reaction zones regimes. Table 4.1 summarizes the simulation parameters of the n-heptane simulations. For each case, two simulations were performed: one with non-unity Lewis numbers and one with unity Lewis numbers (subscript 1). Simulations with unity Lewis numbers are not expected to reproduce realistic, experimentally observed flames. They are used for comparison purposes as they allow the systematic isolation of effects of differential diffusion from those of turbulence. Simulations $\mathrm{A_{NC7}}$ through $\mathrm{D_{NC7}}$ were previously reported in Chapter 3. In this chapter, cases B and C are simulated again with different fuels, equivalence ratios, and chemical mechanisms.

First, the equivalence ratio is varied by performing case B at $\phi = 0.7$ and $\phi = 1.3$ (cases $\mathrm{B_{NC7,\phi=0.7}}$ and $\mathrm{B_{NC7,\phi=1.3}}$) (see Table 4.2). Compared to the baseline case ($\phi = 0.9$), leaner condi-

tions ($\phi = 0.7$) are selected to determine if differential diffusion is enhanced, and richer conditions ($\phi = 1.3$) are chosen to determine if the fuel Lewis number Le_F is still a controlling variable even if the fuel is not the limiting reactant. Case B is chosen since it presents strong differential diffusion effects, namely a significant reduction in the chemical source terms compared to the corresponding one-dimensional laminar flame [101, 59].

Four different fuels are considered: *n*-heptane (abbreviated NC7), iso-octane (abbreviated iC8), toluene (abbreviated ACH3), and methane (CH4). Toluene and iso-octane are chosen because they have similar fuel Lewis numbers to *n*-heptane but have distinct and complex fuel decomposition chemistry. Methane is chosen for comparison purposes because of its close to unity fuel Lewis number and simpler chemistry. The fuel Lewis numbers used in the non-unity Lewis number simulations are $\mathrm{Le}_{n\mathrm{C7}}$=2.84, $\mathrm{Le}_{\mathrm{ACH3}}$=2.45, $\mathrm{Le}_{i\mathrm{C8}}$=2.81, and $\mathrm{Le}_{\mathrm{CH4}}$=0.99. Simulations $\mathrm{B}_{\mathrm{CH4}}$ and $\mathrm{B}_{\mathrm{ACH3}}$ present similar turbulence conditions and laminar flame properties as case B but use different fuels. Similarly, simulations $\mathrm{C}_{\mathrm{ACH3}}$ and $\mathrm{C}_{\mathrm{iC8}}$ are performed at the same turbulent conditions as simulations C and C_1 to investigate fuel effects (see Table 4.3).

Finally, simulations $\mathrm{B}_{\mathrm{NC7,CM}}$ and $\mathrm{C}_{\mathrm{NC7,JSF}}$ present similar conditions as cases B and C but use larger, more detailed chemical mechanisms (see Table 4.4). Cases B and C are chosen to compare fuel and chemical models since they use different unburnt temperatures, present significant differential diffusion effects, and are at the transition between thin and distributed reaction zones.

4.1.3 Chemical and transport models

As mentioned earlier, simulations with four different fuels are performed. Methane/air simulations use the GRI 3.0 mechanism [106] without nitrogen chemistry with 36 species and 420 reactions (forward and backward reactions are counted separately). Cases $\mathrm{B}_{\mathrm{NC7,CM}}$ use the full CaltechMech (172 species, 1853 reactions) [12]. Cases $\mathrm{C}_{\mathrm{NC7,JSF}}$ use the JetSurF 2.0 mechanism [113] (207 species, 2477 reactions). Iso-octane/air simulations use CaltechMech without soot and linear alkane decomposition pathways (74 species, 976 reactions). Toluene/air simulations use the 47 species and 290 reactions mechanism developed in Bisetti *et al.* [11]. The baseline *n*-heptane simulations use a fur-

Case	A_{nC7}	$A_{nC7,1}$	B_{nC7}	$B_{nC7,1}$	$C_{nC7,1}$	$C_{nC7,1}$	D_{nC7}	$D_{nC7,1}$
T_u (K)	298		298		800		800	
ϕ	0.9		0.9		0.9		0.9	
S_L (m/s)	0.36	0.29	0.36	0.29	2.3	1.71	2.3	1.71
l_F (mm)	0.39	0.43	0.39	0.43	0.25	0.27	0.25	0.27
u'/S_L	9.0	10	18	21	19	25	45	60
l/l_F	1.1	1.0	1.1	1.0	1.2	1.1	1.2	1.1
Ka_u	78	91	220	280	204	280	740	1050
Ka_δ	1.9	1.6	7.0	5.0	73	64	256	237
Re_t	83		190		170		380	
η_u (m)	1.6×10^{-5}		9.0×10^{-6}		7.0×10^{-6}		3.5×10^{-6}	
Δx (m)	1.8×10^{-5}		1.8×10^{-5}		1.2×10^{-5}		7.0×10^{-6}	
Grid	11×128^3		11×128^3		11×128^3		11×220^3	
L (mm)	2.30		2.30		1.54		1.54	
T_{peak} (K)	1240	1365	1240	1365	1390	1482	1440	1482

Table 4.1: Parameters of the simulations previously reported in Chapter 3 (Lapointe *et al.* [59]). Subscript 1 denotes simulations with unity Lewis numbers. ϕ is the equivalence ratio, S_L is the laminar flame speed, $l_F = (T_b - T_u)/|\nabla T|_{\max}$ is the laminar flame thickness, $l = u'^3/\epsilon$ is the integral length scale, Ka_u is the Karlovitz number in the unburnt gas, Ka_δ is the reaction zone Karlovitz number, $\mathrm{Re}_t = u'l/\nu$ is the turbulent Reynolds number in the unburnt gas, η_u is the Kolmogorov length scale in the unburnt gas, Δx is the grid spacing, L is the domain width and corresponds to $\sim 5l$, and T_{peak} is the temperature of peak fuel consumption rate in the turbulent flame.

Case	$B_{nC7,\phi0.7}$	$B_{nC7,\phi0.7,1}$	$B_{nC7,\phi1.3}$	$B_{nC7,\phi1.3,1}$
T_u (K)	298		298	
ϕ	0.7		1.3	
S_L (m/s)	0.22	0.20	0.343	0.24
l_F (mm)	0.52	0.53	0.37	0.47
u'/S_L	20.0	22	16	23
l/l_F	1.0	1.0	1.1	0.9
Ka_u	260	280	180	326
Ka_δ	6.3	5.1	6.7	5.3
Re_t	166		166	
η_u (m)	1.1×10^{-5}		9.0×10^{-6}	
Δx (m)	2.1×10^{-5}		1.8×10^{-5}	
Grid	11×128^3		11×128^3	
L (mm)	2.69		2.30	
T_{peak} (K)	1213	1308	1332	1472

Table 4.2: Parameters of the simulations with different equivalence ratios. See Table 4.1 for the definitions of the various parameters.

ther reduced version of that mechanism consisting of 35 species and 217 reactions. Species produced under rich conditions (mostly aromatic species) were removed.

Given the size of the chemical models used (up to 207 species), several simplifications are made in evaluating mixture-averaged transport coefficients. The species viscosities, μ_i, are computed from standard gas kinetic theory [46] and the mixture-averaged viscosity is calculated using a modified

Case	B_{CH4}	$B_{CH4,1}$	B_{ACH3}	$B_{ACH3,1}$	C_{ACH3}	$C_{ACH3,1}$	C_{iC8}	$C_{iC8,1}$
T_u (K)	298		298		800		800	
ϕ	0.9		0.9		0.9		0.9	
S_L (m/s)	0.33	0.26	0.35	0.27	2.2	1.6	2.1	1.6
l_F (mm)	0.47	0.41	0.41	0.49	0.26	0.32	0.24	0.28
u'/S_L	16	20	17	22	18	25	20	27
l/l_F	1.1	0.9	1.1	0.9	1.1	0.9	1.2	1.0
Ka_u	190	270	205	324	200	331	210	324
Ka_δ	6.8	5.4	3.5	3.1	63	60	66	58
Re_t	160		175		160		156	
η_u (m)	9.0×10^{-6}		9.1×10^{-6}		6.8×10^{-6}		6.8×10^{-6}	
Δx (m)	1.8×10^{-5}		1.8×10^{-5}		1.2×10^{-5}		1.2×10^{-5}	
Grid	11×128^3		11×128^3		11×128^3		11×128^3	
L (mm)	2.30		2.30		1.54		1.54	
T_{peak} (K)	1622	1649	1420	1527	1600	1680	1447	1510

Table 4.3: Parameters of the simulations with different fuels. See Table 4.1 for the definitions of the various parameters.

Case	$B_{nC7,CM}$	$B_{nC7,CM,1}$	$C_{nC7,JSF}$	$C_{nC7,JSF,1}$
T_u (K)	298		800	
ϕ	0.9		0.9	
S_L (m/s)	0.36	0.29	2.3	1.71
l_F (mm)	0.39	0.43	0.25	0.27
u'/S_L	18	21	19	25
l/l_F	1.1	1.0	1.2	1.1
Ka_u	220	280	204	280
Ka_δ	7.0	5.0	73	64
Re_t	190		170	
η_u (m)	9.0×10^{-6}		7.0×10^{-6}	
Δx (m)	1.8×10^{-5}		1.2×10^{-5}	
Grid	11×128^3		11×128^3	
L (mm)	2.30		1.54	
T_{peak}	1250	1370	1400	1490

Table 4.4: Parameters of the simulations with different chemical mechanisms. See Table 4.1 for the definitions of the various parameters.

form of Wilke's formula [115, 59]. The species thermal conductivities, λ_i, are computed using Eucken's formula [38] and the mixture-averaged thermal conductivity λ is obtained following Mathur *et al.* [64]. The species diffusivities are computed as $D_i = \alpha/\mathrm{Le}_i$, with the species Lewis numbers Le_i assumed to be constant throughout the flame. The species Lewis numbers are taken from simulations of one-dimensional, laminar, premixed flames using a mixture-averaged formulation for transport properties computed with FlameMaster [85]. It was shown by Savard [99] and Burali *et al.* [19] that, in the turbulent heptane flame considered (case B_{NC7}), differences in species mass fractions and

chemical source terms were negligible between mixture-averaged formulation for transport properties and constant Lewis numbers. Soret and Dufour effects are neglected. The impact of neglecting Soret and Dufour effects in 3D turbulent flames is still unknown and is beyond the scope of the present work. Using these simplifications, the computational time required to evaluate transport properties scales linearly with the number of species. This allows the use of large, detailed chemical models at reasonable computational costs.

4.2 Turbulent flame speed

The reader is referred to Section 3.2 for a qualitative overview of the n-heptane simulations including instantaneous vorticity contours. At a given reaction zone Karlovitz number (similar turbulent conditions), the instantaneous fields from the present simulations with different fuels, equivalence ratios, and mechanisms are qualitatively (visually) similar to the previous n-heptane simulations performed and are thus not shown here. Instantaneous temperature and fuel consumption rate contours for all cases presented in this chapter are provided in Appendix C.2. In this section, the effects of fuel, chemistry, and transport effects on the turbulent flame speeds are quantified.

4.2.1 Evaluating the mean turbulent flame speed

The mean turbulent flame speed may be evaluated in different ways from the previous simulation results. The *instantaneous* turbulent flame speed is defined here as the volume integral of the fuel consumption rate:

$$S_T = \frac{1}{(\rho Y_F)_u L^2} \int_V -\rho \dot{\omega}_F \, \mathrm{d}V. \tag{4.1}$$

The instantaneous flame speed is computed for each snapshot (data file) saved (approximately one eddy turnover time apart) and then averaged (over time) to obtain the mean turbulent flame speed $\overline{S_T}$. As the differences between the various fuels, equivalence ratios, and chemical mechanisms may be small, it is important to ensure that the statistical error on the quantities of interest is small. In order to reduce the error on $\overline{S_T}$ and other mean quantities, data is collected over 30 eddy turnover

times. This allows multiple cycles of the lower frequency phenomena to be captured and provides a sufficient number of snapshots to constitute a representative sample.

As mentioned in Section 3.1, the inlet bulk velocity is constant and differs slightly from the turbulent flame speed. Therefore, the flame drifts from its initial position. In all cases, the drift is negligible compared to the domain size. The flame drift can be computed as in Savard and Blanquart [101]

$$\Delta x_f = x_f - x_0, \tag{4.2}$$

where x_0 is the position of the flame at time $t = 0$ and x_f is the instantaneous position of the flame, computed as

$$x_f = 11L - \frac{1}{L^2 c_b} \int_V c \, \mathrm{d}V, \tag{4.3}$$

where $c = Y_{\mathrm{H_2}} + Y_{\mathrm{H_2O}} + Y_{\mathrm{CO}} + Y_{\mathrm{CO_2}}$ is used as a progress variable [67] and takes the value c_b in the burnt gas. Then, the mean turbulent flame speed can be evaluated from the change in flame position as

$$\overline{S_T}_{\mathrm{drift}} = \frac{\Delta x_f}{\Delta t} + U_{\mathrm{inlet}}. \tag{4.4}$$

Figure 4.1 shows the instantaneous flame speed plotted against time for case $\mathrm{B}_{n\mathrm{C7},\phi 1.3,1}$. Large fluctuations around the mean value are observed. As will be shown later (Section 4.2.3), these fluctuations are due to changes in the topology of the reaction zone surface. The mean and standard deviations of the turbulent flame speeds computed from the instantaneous flame speed (using Eq. 4.1) at every timestep (black line) and the instantaneous flame speed from the snapshots used for the statistics (red dots) are virtually the same (0.75 ± 0.20 m/s and 0.76 ± 0.21 m/s, respectively). The agreement suggests that the mean flame speeds computed from a limited number of data files are accurate estimates over the data collection period. Additionally, the mean turbulent flame speed computed from the flame drift (Eq. 4.4) over the same period is 0.72 m/s, which confirms that both methods yield very similar mean flame speeds.

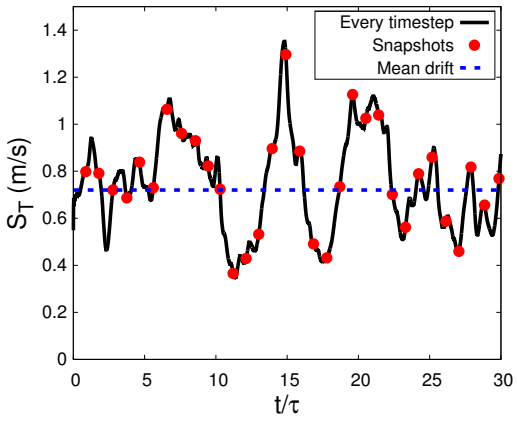

Figure 4.1: Turbulent flame speed for case $\mathrm{B}_{n\mathrm{C7},\phi 1.3,1}$. Solid black line is the instantaneous flame speed (Eq. 4.1), red dots indicate snapshots used for the statistics (Eq. 4.4).

4.2.2 Chemistry and transport effects

Figure 4.2 presents the mean turbulent flame speeds normalized by the corresponding unstretched laminar flame speeds. Filled symbols correspond to the non-unity Lewis number cases while empty symbols correspond to the unity Lewis number cases. The dashed lines represent power law fits of the form $\overline{S_T}/S_L = 1 + a\mathrm{Ka}_\delta^b$.

Since simulations at different unburnt temperatures are used, the flame speeds are plotted against the reaction zone Karlovitz number:

$$\mathrm{Ka}_\delta = \frac{\delta_{F,\mathrm{lam}}^2}{\eta_\delta^2}, \tag{4.5}$$

where $\delta_{F,\mathrm{lam}}$ is the laminar reaction zone thickness and η_δ denotes the value of the Kolmogorov length scale *at the reaction zone* (taken at T_{peak}, the temperature corresponding to the peak value of the fuel consumption rate in the flame). The laminar reaction zone thickness is defined here as the distance over which the fuel burning rate is greater than 5% of the maximum laminar value. For the flames considered here, δ_F varies from 1/3 to 1/2 of the laminar flame thickness (l_F). An increase in the unburnt temperature leads to a reduction in the viscosity ratio across the flame. As the Kolmogorov length scale depends on the viscosity, small-scale turbulent structures penetrate further in the reaction zone at higher unburnt temperatures. Considering a fixed velocity ratio u'/S_L and length ratio l/l_F, the change in viscosity ratio leads to an increased Karlovitz number at

the reaction zone while the Karlovitz number in the unburnt gases does not change. To take these effects into account, it was shown in Chapter 3 that it is more adequate to use the reaction zone Karlovitz number [79, 80] when comparing reaction rates. It is important to note that the turbulent flame speed is expected to depend also on the ratio of integral length scale to flame thickness. This ratio was intentionally kept around unity for all flames.

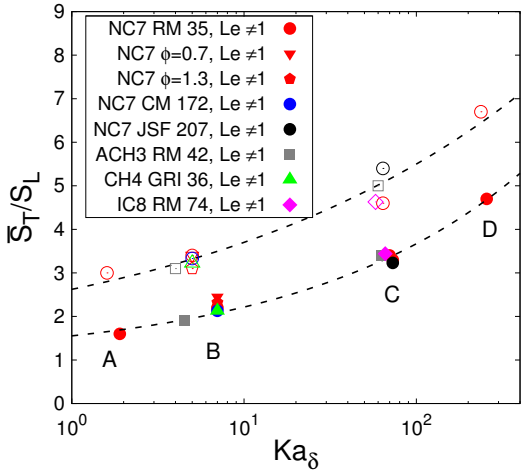

Figure 4.2: Mean turbulent flame speeds. Filled and empty symbols correspond to non-unity and unity Lewis number simulations, respectively. Dashed lines represent power law fits (see text).

As expected, the turbulent flame speed increases with Ka_δ [79]. There is also a clear difference between non-unity Lewis number simulations and unity Lewis number simulations. The ratio of turbulent to laminar flame speed is always lower when differential diffusion is included although both flames are subjected to the same incoming turbulent flow. This is typical of heavy fuels with above unity Lewis numbers. The opposite behavior is expected for lighter fuels with $\mathrm{Le}_F < 1$. More specifically for the present objectives, very similar mean turbulent flame speeds are obtained with the different equivalence ratios, fuels, and chemical mechanisms. This suggests that equivalence ratios, fuels, and chemical mechanisms have only limited effects on the present turbulent flames.

4.2.3 Global *vs.* local effects

Dating back to Damköhler [27], turbulence-flame interactions have been described conceptually by considering two limiting regimes of large-scale and small-scale turbulence. In the large-scale regime

(corrugated flamelet regime), Damköhler proposed that the turbulent flame speed is proportional to the turbulent flame surface area A_T, or $S_T/S_L \approx A_T/A$ where A is the cross-section area ($A = L^2$). In contrast, for a flame interacting with small-scale turbulence (thin reaction zone regime), as for all present flames, Damköhler proposed that the turbulent flame speed should be proportional to the turbulent diffusivity, $S_T \sim \sqrt{D_T/\tau_c}$, where D_T is the turbulent diffusivity and τ_c is the chemical time scale. Substituting the chemical time scale by the inverse of the fuel burning rate ($\dot{\omega}_F$) would yield the following expression:

$$\frac{S_T}{S_L} \approx \sqrt{\frac{D + D_T}{D} \frac{\langle \dot{\omega}_F | T_{\text{peak}} \rangle}{\dot{\omega}_{F,\text{lam}}}}, \tag{4.6}$$

where D is the laminar diffusivity in the unburnt gases.

However, this expression has not yet been verified in simulations of high Karlovitz number premixed flames. For instance, it was shown by Poludnenko and Oran [91], for a turbulent flame close to the transition between the thin reaction zone and distributed burning regimes, that a strong correlation could be found between the turbulent flame speed and the surface area at the reaction zone. Additionally, as was discussed in Savard and Blanquart [101], even if the present flames are not in the corrugated flamelet regime, the reaction zones remain thin and are only weakly corrugated.

Following these observations, a similar approach to that used by Damköhler for the corrugated flamelet regime is taken here considering a reaction zone surface ($T = T_{\text{peak}}$). By rewriting Eq. 4.1 as a surface integral along the isocontour $T = T_{\text{peak}}$ and an integral in the normal direction and using the observation of Savard and Blanquart [101] that the fuel consumption locally scales like its value at $T = T_{\text{peak}}$, the turbulent flame speed can be approximated as:

$$\frac{S_T}{S_L} \approx \frac{A_T}{A} \frac{\langle \dot{\omega}_F / |\nabla T| | T_{\text{peak}} \rangle}{\dot{\omega}_{F,\text{lam}} / |\nabla T_{\text{lam}}|}. \tag{4.7}$$

More details on the derivation can be found in Appendix C.1. It is important to note that, as opposed to Savard and Blanquart [101], it is not assumed that the temperature gradient at the reaction zone is equal to its laminar counterpart. This equation stresses that the local flame propagation speed is not the same as the laminar flame speed and thus changes need to be made to modeling approaches

based on unstretched laminar flames. Note that Eq. 4.7 is equivalent to the burning velocity model proposed by Bray [18] and Candel and Poinsot [20]:

$$\frac{S_T}{S_L} = \frac{A_T}{A} I_0, \tag{4.8}$$

if the burning efficiency factor is replaced by the ratio of the turbulent to laminar burning rate (divided by the local temperature gradient) at the reaction surface.

The validity of Eq. 4.7 is first verified by plotting the instantaneous turbulent flame speed, surface area, Eq. 4.7, and the burning efficiency factor ($I_0 = \frac{S_T/S_L}{A_T/A}$), for cases $\mathrm{C_{ACH3}}$ (non-unity and unity Le), as shown in Fig. 4.3. The turbulent flame surface area, defined as the area of an isotherm, is computed using a marching cubes algorithm [62]. The turbulent flame speed and surface area both exhibit very similar temporal evolutions and are characterized by large fluctuations of the order of their mean values. Eq. 4.7 is very close to S_T/S_L. On the other hand, the burning efficiency factor presents much smaller fluctuations. These observations lead to two main conclusions. First, Eq. 4.7 holds, or equivalently:

$$I_0 \approx \frac{\langle \dot{\omega}_F / |\nabla T| \big| T_{\mathrm{peak}} \rangle}{\dot{\omega}_{F,\mathrm{lam}} / |\nabla T_{\mathrm{lam}}|}. \tag{4.9}$$

Second, the large fluctuations in S_T are mostly due to A_T since the chemical source terms present much smaller fluctuations. The strong correlation between S_T and A_T was also reported in other studies of high Karlovitz number flames [91, 98].

Equation 4.7 is further tested by plotting the instantaneous $A_T \langle \dot{\omega}_F / |\nabla T| \big| T_{\mathrm{peak}} \rangle / (A \dot{\omega}_{F,\mathrm{lam}} / |\nabla T_{\mathrm{lam}}|)$ against the instantaneous turbulent flame speed for each snapshot used for the statistics from all simulations. As shown in Fig. 4.4, most points fall along a straight line, indicating that Eq. 4.7 holds for the present flames. It is important to note that the instantaneous turbulent flame speed varies by about an order of magnitude across all simulated flames. Equation 4.7 is expected to hold for light fuels ($\mathrm{Le}_F < 1$) under thermo-diffusively stable conditions. It is unclear if it holds for thermo-diffusively unstable conditions, such as lean hydrogen/air flames. This is beyond the scope of the present study and should be the subject of future work.

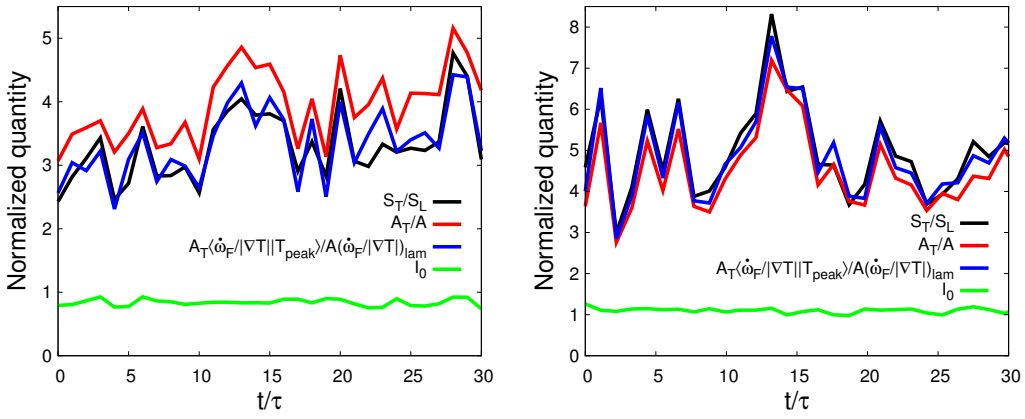

(a) C_{ACH3} (b) $C_{ACH3,1}$

Figure 4.3: Normalized turbulent flame speed (S_T/S_L), surface area (A_T/A), Eq. 5.2, and burning efficiency factor (I_0) plotted against time for cases C_{ACH3}. Quantities are shown for every snapshot used for the statistics ($\sim \tau$ apart).

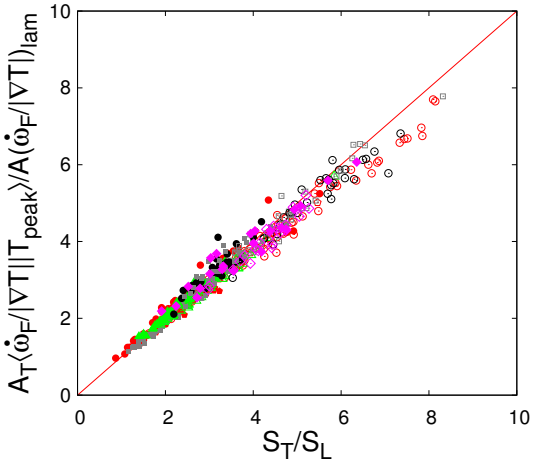

Figure 4.4: Scatter plot of the instantaneous $A_T\langle\dot{\omega}_F/|\nabla T||T_{\rm peak}\rangle/(A\dot{\omega}_{F,\rm lam}/|\nabla T_{\rm lam}|)$ plotted against the instantaneous normalized turbulent flame speed for each snapshot used for all simulations. Filled and empty symbols correspond to non-unity and unity Lewis number simulations, respectively. The colors refer to different fuels and chemistry models (see Fig. 4.2).

Equation 4.7 distinguishes the local effects of turbulence on the chemistry (represented by $\langle\dot{\omega}_F/|\nabla T||T_{\rm peak}\rangle$) from the global propagation of the flame into incoming turbulence (represented by A_T). The flame surface area responds to the large turbulent scales while the chemical source terms are mostly affected by small scales (smaller than the reaction zone thickness δ_F). These two factors are analyzed separately below.

The ratio of flame surface area to domain cross-section area (A_T/A) is computed at the temper-

ature of peak fuel consumption rate, T_{peak}, for the different cases and plotted against the reaction zone Karlovitz number in Fig. 4.5a. As mentioned earlier, changes in the flame surface area are investigated here at a fixed l/l_F. As discussed in previous studies [79, 89], these large scales are also expected to influence A_T. This will be investigated in Chapter 5. In the present cases, the turbulent flame surface area increases with increasing Ka_δ, suggesting increased small-scale wrinkling.

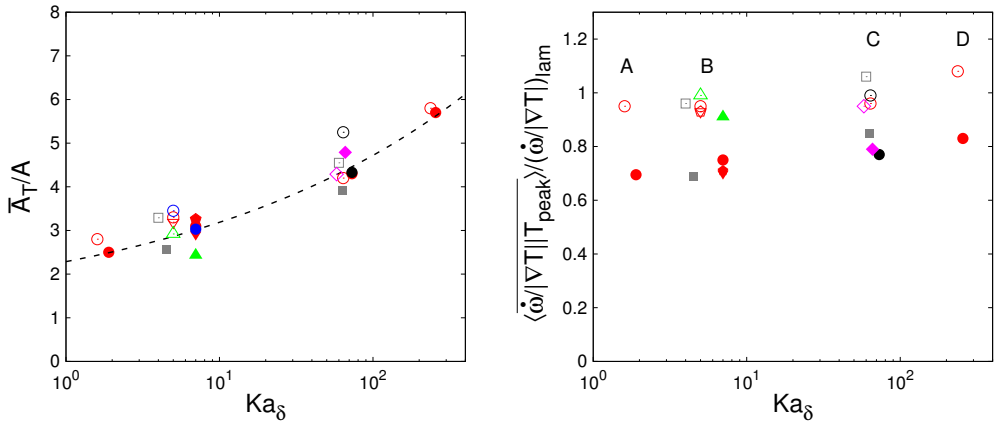

(a) Surface area

(b) Fuel consumption rate

Figure 4.5: Mean turbulent flame surface areas and normalized fuel consumption rates at the corresponding temperature of peak source term. Filled and empty symbols correspond to non-unity and unity Lewis number simulations, respectively. Filled and empty symbols correspond to non-unity and unity Lewis number simulations, respectively. The colors refer to different fuels and chemistry models (see Fig. 4.2).

Figure 4.5b presents the conditional means of $\dot{\omega}_F/|\nabla T|$ at T_{peak} as a function of the reaction zone Karlovitz number for the different simulations using both non-unity and unity Lewis numbers. The mean fuel consumption rates of the unity Lewis number cases are close to the laminar values (with deviations less than 10%). This holds for all fuels used here as well as the different mechanisms and equivalence ratios. On the other hand, in the non-unity Lewis number cases, the mean fuel consumption rate is lower than its unity Lewis number counterpart in all cases. As Ka_δ is increased, the conditional means get closer to the corresponding unity Lewis number flame as turbulent mixing takes over molecular mixing. It is important to note that the conditional means of n-heptane, toluene, and iso-octane (which have similar fuel Lewis numbers) are very similar. Despite the different chemical pathways of the heavy hydrocarbon fuels considered, there are no large differences in their

normalized fuel consumption rates at T_{peak} at a given Ka_δ. The differences in fuel consumption rates between the different heavy fuels are small but the differences between unity and non-unity Lewis numbers are significant. Unsurprisingly, the methane case, which has a fuel Lewis number close to unity, presents a larger conditional mean, closer to the unity Lewis number methane flame. Additionally, the mean fuel consumption rate for case $\text{B}_{n\text{C7},\phi 1.3}$ is very close to cases $\text{B}_{n\text{C7}}$ and $\text{B}_{n\text{C7},\phi 0.7}$. The Lewis number of oxygen (the limiting reactant) being close to unity, $\text{Le}_{\text{O}_2} = 1.06$, it appears that the fuel Lewis number is still the controlling parameter for $\phi > 1$.

In summary, together with the burning efficiency ($I_0 \approx \langle\dot{\omega}/|\nabla T|\rangle/(\dot{\omega}/|\nabla T|)_{\text{lam}}$), the flame surface area explains the differences in turbulent flame speeds seen earlier in Fig. 4.2. First, for the unity Lewis number simulations, since the turbulent to laminar source term ratio is close to unity for all cases, the change in flame speeds can be attributed entirely to a change in flame surface area. Second, the difference between the non-unity and unity Lewis number simulations at the same Ka_δ are due to the difference in $\langle\dot{\omega}/\dot{\omega}_{\text{lam}}\rangle$ since, for a given Ka_δ, the flame surface area is roughly constant.

In order to understand and explain the differences and similarities in turbulent flame speeds reported in Fig. 4.2, the geometry of the reaction zone and the mean fuel consumption rate $\dot{\omega}_F$ are investigated in detail in the next sections.

4.3 Geometry of reaction zone

In this section, the effects of fuel chemistry, equivalence ratio, and differential diffusion on the distributions of tangential strain rate and curvature at the reaction surface are studied. These quantities are related to both the turbulent flame surface area and chemical source terms as stretching, straining, and curvature can affect the chemical source terms and cause small-scale wrinkling of the flame surface.

The strain rate tangential to the reaction surface is computed as

$$a_t = \nabla \cdot \mathbf{u} - \mathbf{n} \cdot \nabla \mathbf{u} \cdot \mathbf{n}, \tag{4.10}$$

where $\mathbf{n} = -\nabla T/|\nabla T|$. The strain rate fields are computed over the entire domain. The conditional probability density functions taken on the isotherm $T = T_{\text{peak}}$ for all cases are presented in Fig. 4.6a. The stain rate distributions are normalized by the respective Kolmogorov time scales at the reaction zone. Another possible normalization would use the flame time scale ($\tau_F = l_F/S_L$). However, at high Karlovitz numbers, it was shown by Bobbitt *et al.* [14] that the enstrophy scaled with the local Kolmogorov time scale, τ_η. Hence, a similar scaling is expected for the tangential strain rate. Once normalized, very similar distributions of strain rate are observed for the different cases independent of the reaction zone Karlovitz numbers, chemistry, and transport effects. This indicates that the strain rate is only affected by the local turbulent conditions and the choice of isotherm does not affect the normalized distributions. It should be noted that τ_η varies by orders of magnitude between the different cases (from $\tau_\eta = 4.6 \cdot 10^{-5}$ s^{-1} in case $\text{A}_{n\text{C7}}$ to $\tau_\eta = 2.5 \cdot 10^{-7}$ s^{-1} in case $\text{D}_{n\text{C7}}$). It is also important to note that approximately 80% of the strain rate is positive, as previously reported by Savard and Blanquart [101]. This is consistent with the analysis of Yeung *et al.* [118] who reported that, when the propagation speed is much smaller than the Kolmogorov speed ($S_L/u_\eta \ll 1$), propagating and material surfaces present the same strain rate distribution where 80% of the strain rate is positive.

The curvature is defined as:

$$\kappa = -\nabla \cdot \mathbf{n}. \tag{4.11}$$

It is taken to be positive when the center of curvature is in the burnt gases. Probability density functions of curvature at the reaction zone, normalized by their respective standard deviations, are shown in Fig. 4.6b. The means of all distributions are close to zero and the normalized distributions have very similar shapes approaching symmetry around $\kappa = 0$. The standard deviations of all cases, normalized by the fuel reaction zone thickness and by the Kolmogorov length scale, are shown in Figs. 4.7a and 4.7b respectively. When normalized by the reaction zone thickness, σ_κ increases by a factor of 10 between the lowest and highest Karlovitz numbers and radii smaller than the laminar reaction zone thicknesses are observed in all cases. Such small curvatures are typical of flames in the thin and distributed reaction zone regimes. As noted by Peters [79], a scaling of the curvature with

the Gibson scale is expected in the corrugated flamelet regime but not in the thin and distributed reaction zones regimes since the Gibson scale would be smaller than the Kolmogorov length scale. A scaling of κ with η may thus be expected as it is the smallest length scale. This is shown in Fig. 4.7b and the change in σ_κ with Ka_δ is much less (a factor of two at most). This indicates that the curvature is mostly influenced by the Kolmogorov length scale. There may still be residual effects of the reaction zone thickness due to the fact the the reaction zone is broadened in cases C and D. Regardless of the dependence of κ on the Karlovitz number, at a given reaction zone Karlovitz number there are no chemistry, equivalence ratio, or differential diffusion effects observed on the distributions of curvature.

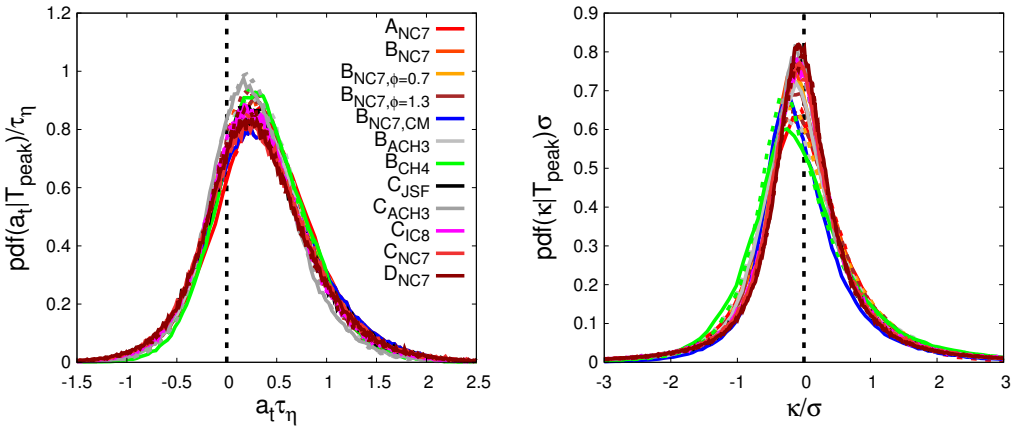

(a) strain rate (b) curvature

Figure 4.6: Probability density functions of the strain rate and curvature taken on the isosurface of the corresponding temperature of peak source term. The strain rates are normalized by the corresponding Kolmogorov time scales and the curvatures are normalized by their standard deviations.

These results clearly underscore that, in the present detailed chemistry simulations, fuel, chemical mechanisms, equivalence ratios, and differential diffusion do not affect the reaction zone geometry as the distributions of strain rate and curvature are essentially unchanged. This is consistent with the results of Savard and Blanquart [101] and the analysis of Yeung *et al.* [118]. At high Karlovitz numbers, the reaction zone surfaces behave as material surfaces. This explains why, at a given reaction zone Karlovitz number and integral length scale, similar flame surface areas are observed despite the differences in chemistry and transport (Fig. 4.5a).

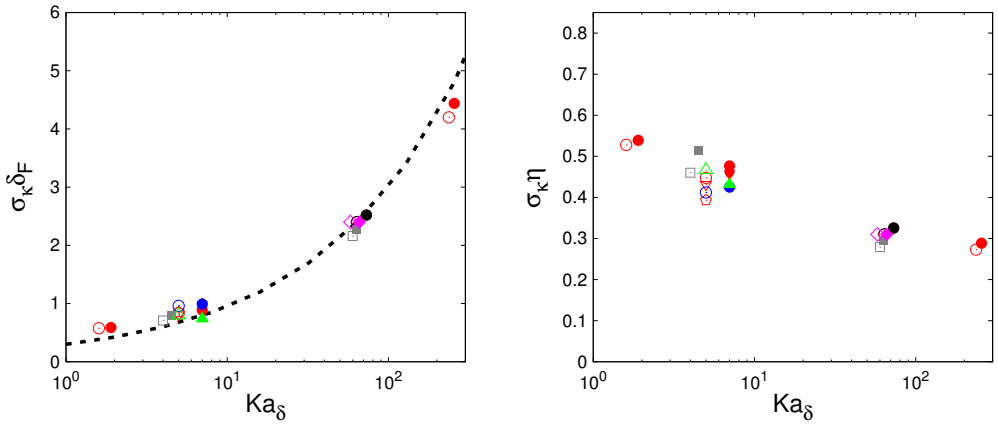

(a) Normalized by reaction zone thickness (b) Normalized by Kolmogorov length scale

Figure 4.7: Standard deviations of curvature on the reaction zone surface, normalized by the fuel reaction zone thickness and by the Kolmogorov length scale, plotted against the reaction zone Karlovitz number. The dashed line on Fig. 4.7a represents $\sigma_\kappa \delta_F = 0.3\sqrt{\mathrm{Ka}_\delta}$. Filled and empty symbols correspond to non-unity and unity Lewis number simulations, respectively. The colors refer to different fuels and chemistry models (see Fig. 4.2).

4.4 Chemical source terms

In this section, the effects of fuel chemistry, equivalence ratio, and differential diffusion on the fuel consumption rates are investigated. Only the fuel consumption rates are studied, but it should be noted that heat release rates present very similar trends, as was shown in Chapter 3 for the present n-heptane turbulent flames.

Recall that two main observations were made from the conditional means of the fuel consumption rate at the reaction surface (Fig. 4.5b). First, the mean source term of any of the unity Lewis number turbulent flames is very close to that of the corresponding laminar flame. This indicates that, for all fuels, turbulence does not affect significantly the mean fuel consumption rate in the absence of differential diffusion. Second, simulations including differential diffusion consistently exhibit a lower mean source term than the corresponding laminar flame with differential diffusion. Yet, the conditional mean approaches that of the laminar flame without differential diffusion as Ka_δ is increased.

In this section, the unity and non-unity Lewis number cases are investigated separately to isolate the effects of differential diffusion.

4.4.1 Unity Le: Effects of dissipation rate

Several correlations have been proposed in the literature for the fluctuations of the chemical source terms, including curvature and strain rate [98, 2]. However, it was shown by Savard and Blanquart [101] that, in high Karlovitz number unity Lewis flames, the burning rate does not correlate strongly with either strain rate or curvature.

Kolla [55] showed that if the species mass fractions are only a function of the progress variable, the species transport equation can take the following form:

$$\dot{\omega}_c \frac{\partial Y_i}{\partial c} = \frac{\rho\chi}{2}\frac{\partial^2 Y_i}{\partial c^2} + \dot{\omega}_i, \tag{4.12}$$

where Y_i is the species mass fraction, c is the progress variable, and χ is its dissipation rate defined as:

$$\chi = 2\alpha|\nabla c|^2. \tag{4.13}$$

Recently, Savard [99] derived the same premixed flamelet equations by applying a local coordinate transformation to the species and temperature transport equations. These results underscore that the fuel burning rate for unity Lewis number flames in the thin reaction zone regime is a function of a progress variable (*e.g.* the temperature) and its dissipation rate and suggest a linear dependence of the chemical source term on χ. In other words, at a fixed temperature/progress variable, the fluctuations in fuel consumption are strongly correlated with χ.

This is illustrated in Fig. 4.8 presenting the joint probability density functions of the fuel consumption rate *vs.* the dissipation rate evaluated at T_{peak} for different fuels in case B. A strong correlation is observed for the three fuels used in this study, showing a close-to-linear dependence. The correlation coefficients for the different cases are defined as

$$r = \frac{\sum_{i=1}^{n}(X_i - \bar{X})(Y_i - \bar{Y})}{\sqrt{\sum_{i=1}^{n}(X_i - \bar{X})^2}\sqrt{\sum_{i=1}^{n}(Y_i - \bar{Y})^2}} \tag{4.14}$$

and are summarized in Table 4.5. The coefficients are close to unity, especially for cases A and B,

confirming the strong linear relationship between $\dot{\omega}_F$ and χ. Figure 4.9 shows the joint probability density functions of the fuel consumption rate *vs.* the dissipation rate evaluated at T_{peak} for different fuels in case C. Once again, a good correlation and linear dependence are observed for the different fuels but weaker than for case B. This is most likely due to the widening of the reaction zone at increasing Karlovitz numbers. It was shown in Chapter 3 that the reaction zone thicknesses for the n-heptane flames were close to the laminar values in cases A and B and larger in cases C and D. The validity of the flamelet equations, Eq. 4.12, relies on the assumption that the reaction zone is thin. Therefore, a weaker correlation between $\dot{\omega}_F$ and χ is expected in the distributed reaction zone regime.

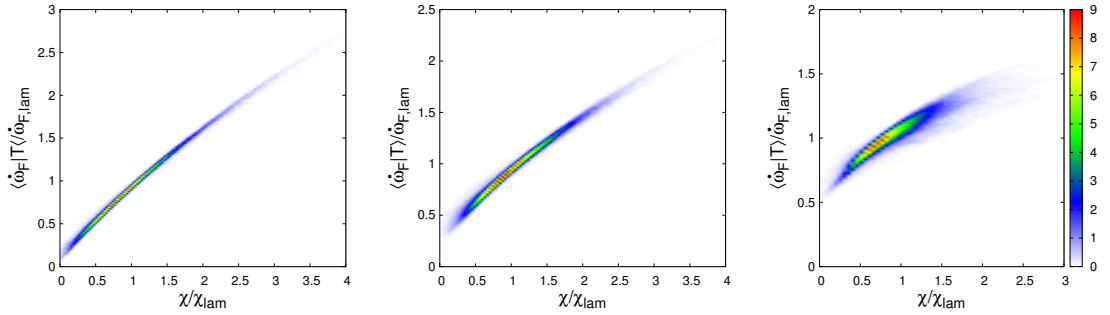

(a) n-C_7H_{16} (b) A_1-CH_3 (c) CH_4

Figure 4.8: Joint probability density functions of the fuel consumption rate and dissipation rate on the isosurface $T = T_{\text{peak}}$ for unity Lewis number cases B.

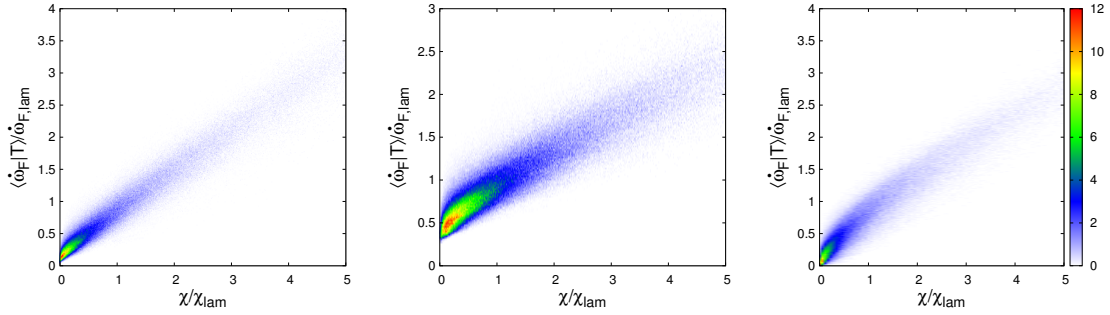

(a) n-C_7H_{16} (b) A_1-CH_3 (c) i-C_8H_{18}

Figure 4.9: Joint probability density functions of the fuel consumption rate and dissipation rate on the isosurface $T = T_{\text{peak}}$ for unity Lewis number cases C.

Given the strong dependence of the source term on the scalar dissipation rate, it is important to analyze its evolution. To provide more information, the PDFs of the logarithm of χ on the

Case	r					
	NC7	$NC7_{\phi=0.7}$	$NC7_{\phi=1.3}$	ACH7	CH4	iC8
A	0.997	–	–	–	–	–
B	0.994	0.993	0.994	0.989	0.925	–
C	0.975	–	–	0.934	–	0.962
D	0.884	–	–	–	–	–

Table 4.5: Correlation coefficient between dissipation rate and fuel consumption rate at $T = T_{\text{peak}}$. Unity Lewis number cases.

reaction surface are shown in Fig. 4.10a. The distribution of dissipation rate of a passive scalar with a uniform mean gradient in homogeneous isotropic turbulence (HIT), taken from Vedula *et al.* [111], is also shown for comparison purposes. When normalized by their respective means and standard deviations, very similar distributions are observed for all fuels and Karlovitz numbers. In fact, the distributions are the same as that from HIT and are close to a log-normal distribution, which is characteristic of turbulent mixing of passive scalars [37, 3, 77]. The standard deviations of the logarithm of χ are shown in Fig. 4.10b. As for the mixing of a passive scalar, the standard deviations increase with increasing Reynolds number (Re_λ is computed using the viscosity at T_{peak}). More specifically, for the present objectives, they do not show strong chemistry effects. Finally, the means of the dissipation rate are shown in Fig. 4.11. For cases A and B, the mean dissipation rate $\langle\chi\rangle$ is close to χ_{lam}. An increase above χ_{lam} is observed for cases C and D. In other words, the mean of the distribution is related to fuel specific, laminar quantities while the standard deviation is entirely due to turbulence.

Now, the two previous results are used to explain burning rates shown in Fig. 4.5b. Assuming that, at a fixed temperature, the fuel consumption rate is solely a function of the dissipation rate, the conditional mean fuel consumption rate can be expressed as

$$\langle\dot{\omega}|T\rangle = \int \dot{\omega}(T,\chi)\text{P}(\chi|T)\text{d}\chi, \tag{4.15}$$

where $\text{P}(\chi|T)$ is the probability density function of the dissipation rate at the given temperature and $\dot{\omega}(T,\chi)$ is the functional dependence of the burning rate on χ. Based on the results shown in

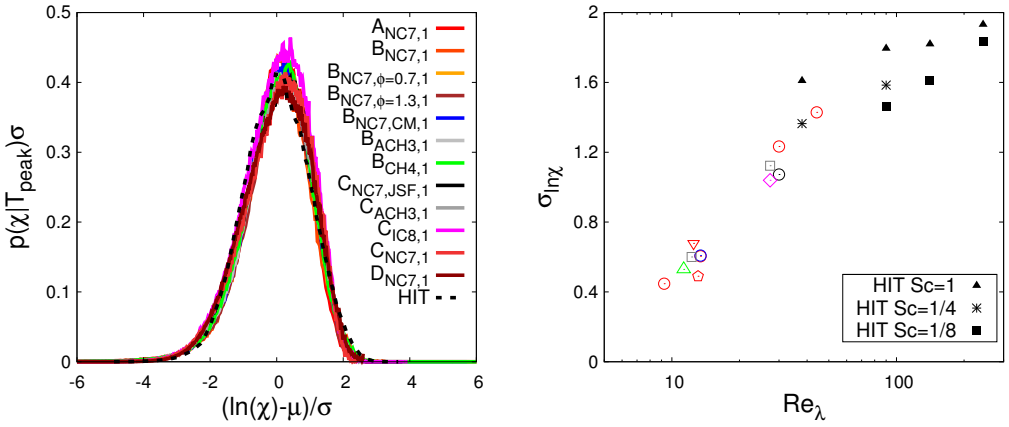

(a) PDF (b) standard deviation

Figure 4.10: a) Probability density functions of the dissipation rate taken on the isosurface of the corresponding temperature of peak source term. b) Standard deviations of the PDFs. The dashed line in a) and HIT data in b) correspond to the PDF of dissipation rate of a passive scalar in homogeneous isotropic turbulence from Vedula *et al.* [111]. Empty symbols correspond to unity Lewis number simulations and the colors refer to different fuels and chemistry models (see Fig. 4.2).

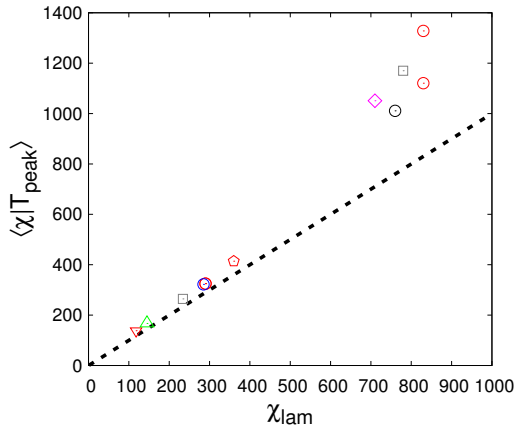

Figure 4.11: Means of the probability density functions of χ at $T = T_{\text{peak}}$ plotted against the corresponding laminar dissipation rate. Empty symbols correspond to unity Lewis number simulations and the colors refer to different fuels and chemistry models (see Fig. 4.2).

Figs. 4.8 and 4.9, this function is approximated by expanding around the laminar dissipation rate

$$\dot{\omega}(T,\chi) = \dot{\omega}(T,\chi_{\text{lam}}) + \beta(\chi - \chi_{\text{lam}}) + \mathcal{O}(\chi^2). \tag{4.16}$$

Substituting Eq. 4.16 into Eq. 4.15, keeping only the linear term (since the dependence of $\dot{\omega}$ on χ is

almost linear), and observing that $\dot{\omega}(T, \chi_{\text{lam}}) \approx \dot{\omega}_{\text{lam}}$ yields

$$\langle \dot{\omega} | T \rangle \approx \dot{\omega}_{\text{lam}} + \beta \left(\langle \chi \rangle - \chi_{\text{lam}} \right). \tag{4.17}$$

Thus, if the first moment of the probability density function is close to the laminar dissipation rate

$$\langle \chi \rangle = \int \chi \mathrm{P}(\chi) \mathrm{d}\chi \approx \chi_{\text{lam}}, \tag{4.18}$$

as seen in Fig. 4.11, then the mean fuel consumption rate should be close to the laminar value and $\langle \dot{\omega} | T \rangle \approx \dot{\omega}_{\text{lam}}$. This was observed in Fig. 4.5b.

It should be noted that, in Eq. 4.16, all the effects of chemistry are contained in $\dot{\omega}(T, \chi_{\text{lam}})$ and β. More specifically, these parameters take different values for different fuels, equivalence ratios, unburnt temperature, etc. Nevertheless, as shown previously, this does not affect the conclusions made here, namely that $\langle \dot{\omega} | T \rangle \approx \dot{\omega}_{\text{lam}}$. In cases C and D, $\langle \chi \rangle$ being larger than χ_{lam} is consistent with the increase in the conditional means of normalized fuel consumption rates at T_{peak} shown in Fig. 4.5b.

4.4.2 Non-unity Le

As opposed to the unity Lewis number cases, the chemical source terms are not solely a function of a progress variable and its dissipation rate when differential diffusion is considered. The correlation between the fuel consumption rate and the dissipation rate is still present but much weaker [99] and does not explain the trends observed in Fig. 4.5b.

The first important observation is that the mean fuel consumption rate is lower than in the corresponding unity Lewis number flame. This is observed for all fuels, equivalence ratios, and mechanisms, but to a lesser extent in the methane flame. This reduction in fuel consumption was previously related to curvature effects. More precisely, Savard and Blanquart [101] showed that, in case $\mathrm{B}_{n\mathrm{C7}}$, low fuel consumption rates are correlated with regions of high curvature, suggesting the presence of focusing/defocusing effects. This is due to the above unity Lewis number of the present

fuels. An increased burning rate has been observed for lighter fuels such as hydrogen [8].

Additionally, Savard and Blanquart [101] showed that the fuel (n-heptane) mass fraction was strongly correlated with curvature, more so than radicals H and OH. Therefore, effects of curvature on the burning rate are felt through the fuel mass fraction. This explains why, in the present study, different fuels with similar (high) Lewis number exhibit similar reductions in mean fuel consumption rates. This result is specific to fuels with significantly non-unity Lewis numbers and contrasts with common observations made in methane flames. For instance, in two-dimensional simulations of methane/air premixed flames, Echekki and Chen [35] reported a stronger correlation between the hydrogen atom mass fraction and curvature. These results can explain the present reduction in the mean fuel consumption rate compared to the laminar flame. Since the Lewis number of the fuel (methane) is very close to unity, focusing/defocusing differential diffusion effects are still present through radicals such as H but to a lesser extent than in high Lewis number fuels.

It was shown in Fig. 4.7a that curvatures get stronger with increasing Ka_δ. Hence, a decrease in the mean fuel consumption rate due to larger curvatures (and thus stronger focusing/defocusing effects) could be expected. This is what happens for moderate Karlovitz numbers up to cases A and B. However, as the Karlovitz number is further increased towards cases C and D, differential diffusion effects are diminished with increasing turbulent mixing (effective Lewis numbers tend towards unity as the Karlovitz number increases [100, 59]). The fuel consumption rates are then less sensitive to curvature and the effective mean values increase towards the unity Lewis number values.

4.4.3 Chemical mechanism

Figure 4.12 presents the mean fuel consumption rates for cases B and C with n-heptane, using different mechanisms. In the laminar flames of case B (Fig. 4.12a), the reduced mechanism predicts consumption rates very similar to the detailed CaltechMech, for both non-unity and unity Lewis number flames. This is expected as the reduced model was derived from the full CaltechMech [11]. In the turbulent flames (Fig. 4.12b), both mechanisms again predict very similar fuel consumption rates. It is important to note that the effect of differential diffusion is significantly larger than the

difference between the two chemical models. The flame-turbulence interaction is thus not affected by the size of the chemical mechanism.

The laminar flames of case C (Fig. 4.12c) do show some slight difference in the fuel consumption rates between the reduced mechanism and the detailed JetSurF mechanism. This could be due to some inherent differences between the models as JetSurF has isomers for all radicals and a large number of reactions dedicated to thermal cracking and β-scissions. Despite these differences, in the turbulent flames (Fig. 4.12d), the fuel consumption rates are very close *once normalized* by their respective laminar peak values. This indicates that, as for case B, there is no effect of the mechanism on the turbulent flame behavior. In summary, in both cases B and C, the reduction in fuel consumption rate in the non-unity Lewis number flames is predicted by all three mechanisms and the rates of the unity Lewis number flames remain within approximately 10% of the laminar values.

4.5 Summary: Controlling parameters

The present results suggest that the mean turbulent flame speed and fuel consumption rates can be predicted with the knowledge of only a few global laminar flame properties. If these properties are predicted accurately with any given chemical model, the results from simulations of turbulent flames are likely to also be accurate.

More precisely, when appropriately normalized, all relevant quantities follow universal behaviors independent of the fuels, equivalence ratios, chemical mechanisms, etc. Some of the quantities are entirely controlled by turbulence and do not require knowledge of the underlying chemistry:

- strain rate scales with τ_η (Fig. 4.6a),
- standard deviation of $\ln(\chi)$ depends on Re_λ (Fig. 4.10b).

Some quantities are entirely controlled by chemical quantities:

- mean of χ follows closely χ_{lam} (Fig. 4.11),

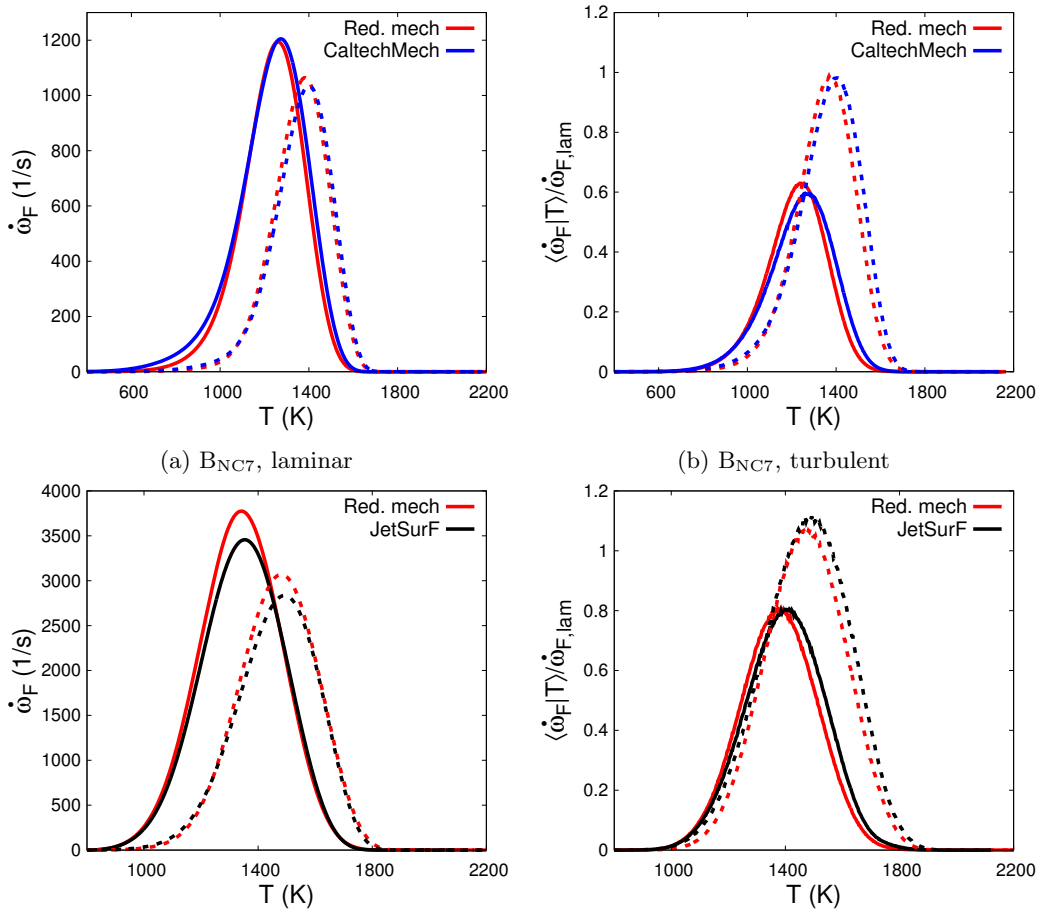

(a) B_{NC7}, laminar

(b) B_{NC7}, turbulent

(c) C_{NC7}, laminar

(d) C_{NC7}, turbulent

Figure 4.12: Conditional means of normalized n-heptane consumption rate for three different mechanisms. Solid lines correspond to non-unity Lewis number cases while dashed lines correspond to unity Lewis number cases. The fuel consumption rates in the turbulent flames are normalized by the peak value in the corresponding laminar flame.

- mean $\dot{\omega}_F$ scales with $\dot{\omega}_{F,\mathrm{lam}}(T_{\mathrm{peak}})$ for unity Lewis numbers (Fig. 4.5b).

Finally, some quantities are controlled by both chemical and turbulent quantities:

- curvature normalized by η_δ is a function of Ka_δ (Fig. 4.7b),
- turbulent surface area is a function of Ka_δ (Fig. 4.5a) (and most likely l/l_F),
- mean $\dot{\omega}_F$ normalized by $\dot{\omega}_{F,\mathrm{lam}}(T_{\mathrm{peak}})$ is only a function of Le_F and Ka_δ (Fig. 4.5b),
- turbulent flame speed normalized by S_L is a function of Ka_δ (Fig. 4.2) (and most likely l/l_F).

In summary, the relevant chemical quantities are the same as used in the Peters/Borghi regime

diagram, namely

- laminar flame speed (S_L),
- laminar flame thickness (l_F),
- reaction zone thickness (δ_F),

with the addition of the fuel Lewis number to capture differential diffusion effects. The peak chemical source term is also used in the various normalizations, but its value can be expressed in terms of the above three quantities.

Chapter 5

Integral Length Scale Effects

In previous chapters, the effects of small-scale turbulence on the flame chemistry at high Karlovitz numbers were investigated. Given that purpose and computational cost considerations, a small integral length scale (roughly equal to the laminar flame thickness) was used. The validity of such an approach relies on two main assumptions. First, the small turbulent scales are universal (even at these low Reynolds numbers). Second, turbulent scales larger than the flame thickness do not impact the chemical processes.

The goal of this chapter is to test these assumptions. More precisely, the objectives are to identify the possible effects of l/l_F on the chemistry, and in doing so to investigate the dependence of A_T/A and I_0 on Ka, Re_t, and l/l_F. These objectives are met by performing simulations with varying integral length scales at a fixed Karlovitz number, and using previous simulations at a fixed l/l_F with varying Ka.

5.1 Computational methodology

The direct numerical simulations performed in this chapter follow the methodology presented in Section 3.1. A total of seven simulations are used, three of them were reported in previous chapters. The parameters for each simulation are provided in Table 5.1. Two simulations are performed using detailed chemistry (DKM) while five are performed using tabulated chemistry (TAB).

5.1.1 Flow configuration

The same flow configuration is used for all the simulations and is illustrated in Fig. 5.1. A slight modification from the configuration of Chapters 3 and 4 is made to account for different domain sizes. The forcing starts at $0.05L_x$ (where L_x is the domain length) and is stopped after a distance of $0.75L_x$. The forcing method used is described in Subsection 3.1.4. The simulations are performed for at least 30 eddy turnover times, τ, and statistics are computed using the last 20 τ to remove any initial transient effects. All simulations are performed on uniform grids with constant Δx spacing and offer sufficient resolution of the small-scale turbulence ($\Delta x \leq 2\eta_u$) [92] and sufficient resolution of the flame ($\Delta x \leq l_F/20$).

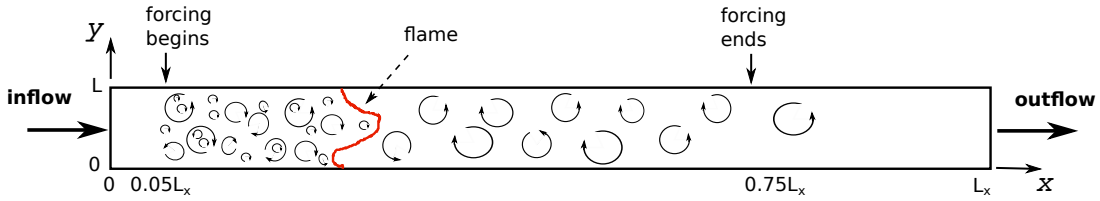

Figure 5.1: Schematic diagram of the flow configuration. The domain is three-dimensional ($L_x \times L^2$) and periodic boundary conditions are used in the y and z directions.

5.1.2 Simulation parameters

For each simulation, the unburnt gas is an n-heptane/air mixture at standard pressure ($P_0 = 1$ atm), unburnt temperature 298K, and equivalence ratio 0.9. Table 5.1 lists the parameters for each simulation. Simulation DKM1 was previously reported in Savard *et al.* [102], and TAB1 and TAB4 were reported in Bobbitt *et al.* [14]. It should be noted that, for $l/l_F = 2$ and 4, the grid is stretched along the streamwise direction in the burnt gases (where the chemical source terms are insignificant). Detailed chemistry simulations (labelled DKM) are performed at two different integral length scales ($l/l_F = 1$ and 4) while keeping the Karlovitz number constant. This allows integral length scale effects to be separated from Karlovitz number effects. The present tabulated chemistry approach (TAB) fixes the dependence of fluid properties and chemical source term on the progress variable to that of a laminar flame with unity Lewis numbers. In doing so, it allows the study of the effects

of integral length scale without differential diffusion effects and without fluctuations in the chemical source term.

It should be noted that, while the Reynolds numbers of the present simulations are still relatively low ($190 < \mathrm{Re}_t < 1150$), flames have been studied experimentally at these conditions. For example, Dunn *et al.* [31] and Zhou *et al.* [120] studied piloted premixed jet flames at similarly high Karlovitz numbers (up to 3500) and low Reynolds numbers (Re_t from 100 to 5200). Sustained flames have even been observed at similar Karlovitz numbers and much larger Reynolds numbers (Re_t up to 80,000) in the recent experiments by Skiba *et al.* [105]. In these experiments and in the present DNS, no global extinction was observed.

Case	DKM1	DKM4	TABn n=1	n=1.5	n=2	n=2.5	n=4
T_u (K)	298				298		
ϕ	0.9				0.9		
S_L (m/s)	0.36				0.27		
l_F (mm)	0.39				0.43		
u'/S_L	18	30	21	25	28	30	33
l/l_F	1.1	4.0	1.0	1.5	2.0	2.5	4.0
Ka_u	220	220	280	300	300	310	280
Ka_δ	7.0	7.7	5.0	5.3	5.4	5.4	5.6
Re_t	190	1150	190	330	490	660	1150
η_u (m)	9.0×10^{-6}				9.0×10^{-6}		
Δx (m)	1.8×10^{-5}				1.8×10^{-5}		
c_{peak}	0.18				0.2		

Table 5.1: Parameters of the simulations. ϕ is the equivalence ratio, S_L is the laminar flame speed, $l_F = (T_b - T_u)/|\nabla T|_{\max}$ is the laminar flame thickness, $l = u'^3/\epsilon$ is the integral length scale, Ka_u is the Karlovitz number in the unburnt gas, Ka_δ is the reaction zone Karlovitz number, $\mathrm{Re}_t = u'l/\nu$ is the turbulent Reynolds number in the unburnt gas, η_u is the Kolmogorov length scale in the unburnt gas, Δx is the grid spacing in the unstretched region, and c_{peak} is the progress variable value at peak progress variable production rate in the turbulent flame.

5.2 Results overview

5.2.1 Qualitative description

Figure 5.2 shows two-dimensional slices of temperature and fuel consumption rate for cases DKM1 and DKM4. The slices are taken at arbitrary spatial and temporal locations after the initial transient, and are scaled to illustrate differences in physical domain sizes.

The smaller integral length scale case presents a relatively continuous flame front and appears to be constrained by the domain size (Fig. 5.2a). Recall that periodicity is imposed in the y and z directions. The larger integral length scale case ($l/l_F = 4$) presents significant qualitative differences (Fig. 5.2c). The flame front now shows discontinuities as pockets of unburnt gases are observed in the products and pockets of burnt gases are observed in the reactants. In contrast to the $l/l_F = 1$ case, the shape of the flame does not appear to be constrained by the domain size.

(a) T, DKM1

(b) $\dot{\omega}_F$, DKM1

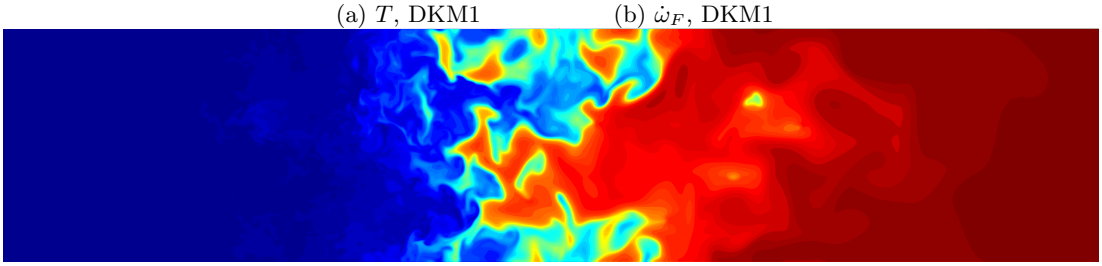

(c) T, DKM4

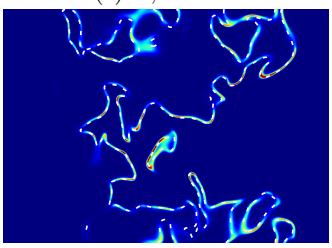

(d) $\dot{\omega}_F$, DKM4

Figure 5.2: Two-dimensional slices centered around the flame of the detailed chemistry cases: (a-c) temperature and (b-d) fuel consumption rate (normalized by the peak value of the corresponding laminar flame). Figures are scaled to illustrate differences in physical length scales. The temperature ranges from 298 to 2200 K. The fuel consumption rate range is satured at [0,2] in each case. The isotherm of peak source term is also shown (white).

5.2.2 Turbulent flame speed

The *instantaneous* turbulent flame speed is defined here as the volume integral of the progress variable production rate:

$$S_T = \frac{1}{\rho_u c_b L^2} \int_V \rho \dot{\omega}_c \, \mathrm{d}V, \tag{5.1}$$

where subscripts u and b denote values taken in the unburnt and burnt gases, respectively. The instantaneous flame speed is computed for each data file saved (approximately one eddy turnover time apart) and then averaged (over time) to obtain the mean turbulent flame speed $\overline{S_T}$. The flame speed obtained from this definition is the same as using the volumetric integral of the fuel burning rate [101, 59].

The burning efficiency introduced in Chapter 4 can be reformulated using the progress variable source term and gradient to approximate the turbulent flame speed as:

$$\frac{S_T}{S_L} \approx \frac{A_T}{A} \frac{\langle \dot{\omega}_c / |\nabla c| \big| c_{\text{peak}} \rangle}{(\dot{\omega}_c / |\nabla c|)_{\text{lam, peak}}}, \tag{5.2}$$

with the burning efficiency:

$$I_0 \approx \frac{\langle \dot{\omega}_c / |\nabla c| \big| c_{\text{peak}} \rangle}{(\dot{\omega}_c / |\nabla c|)_{\text{lam, peak}}} = I_c. \tag{5.3}$$

Equation 5.2 is verified by plotting the instantaneous $A_T/A \cdot I_c$ against the instantaneous normalized turbulent flame speed for each data file used and from all simulations in Fig. 5.3. The turbulent flame surface area A_T, defined as the area of an isotherm $c = c_{\text{peak}}$, is computed using a marching cubes algorithm [62]. Most points fall along a straight line, indicating that, for the present flames, the burning efficiency can be well approximated by Eq. (5.3). Most importantly, this expression holds for the different integral length scales and two different chemical models (DKM and TAB).

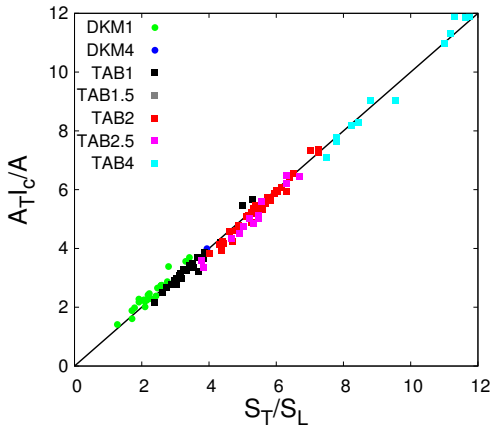

Figure 5.3: Scatter plot of the instantaneous $A_T/A \cdot I_c$ plotted against the instantaneous normalized turbulent flame speed for each data file used. The colors refer to the different cases.

5.3 Effects of integral length scale

Table 5.2 lists the time-averaged turbulent flame speeds normalized by the corresponding unstretched laminar flame speeds, the normalized flame surface areas, and the burning efficiencies. In the following sections, the effects of the integral length scale on the turbulent flame surface area and burning efficiency are studied separately.

Case	$\overline{S_T}/S_L$	$\overline{A_T}/A$	I_0
DKM1	2.28	3.16	0.76
DKM4	3.93	7.5	0.7
TAB1	3.42	3.12	1.08
TAB1.5	5.22	4.60	1.09
TAB2	5.43	4.91	1.08
TAB2.5	6.92	6.08	1.08
TAB4	10.1	9.36	1.09

Table 5.2: Time average normalized turbulent flame speed, normalized turbulent flame surface area at c_{peak}, and burning efficiency for the different cases.

5.3.1 Turbulent flame surface area

To investigate the impact of the integral length scale ratio, the flame surface area (defined as the isosurface $c = c_{\text{peak}}$) to domain cross-section area ratio (A_T/A) is shown in Fig. 5.4 for the different cases.

At a fixed integral length scale ($l/l_F \approx 1$), it was observed in Chapter 3 that, for n-heptane/air flames, the turbulent flame surface area increased with increasing Ka_δ, suggesting increased small-scale wrinkling. This is illustrated in Fig. 5.4a where the values of A_T/A for cases A through D of Ref. [59] (detailed chemistry simulations using both non-unity and unity Lewis numbers) are summarized. Case B is the same as the present DKM1 case.

In the present work, the effects of the integral length scale at a fixed Ka number are shown in Fig. 5.4b. The turbulent flame surface area increases with increasing integral length scale, as noted in previous studies [91, 89, 80]. The almost linear dependence between A_T/A and l is consistent with the analysis of Peters [80] for the corrugated flamelet regime. Using the G-equation, it was argued that $A_T/A \sim l/\lambda_G$ where λ_G is the Taylor length scale for the G-equation.

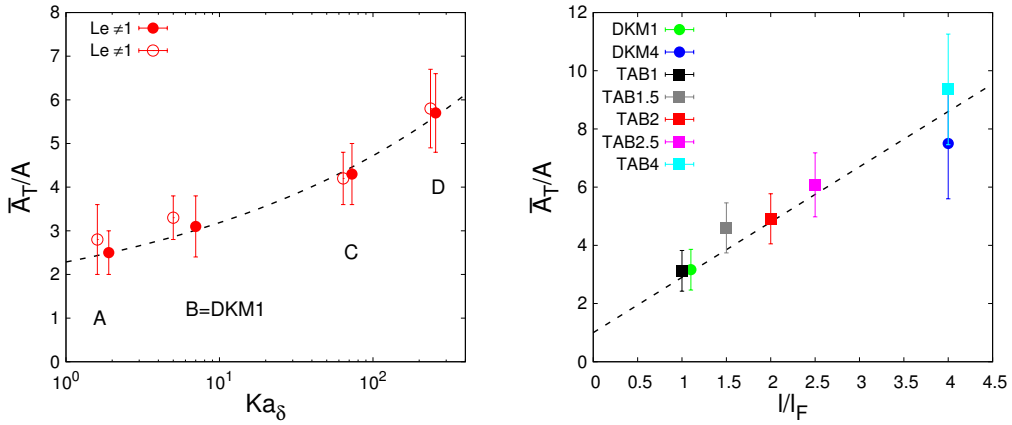

(a) Effects of Karlovitz number

(b) Effects of integral length scale

Figure 5.4: Effects of the reaction zone Karlovitz number from Lapointe *et al.* [59] at $l/l_F \approx 1$ (left) and integral length scale from present study at $\mathrm{Ka}_\delta \approx 5$ (center) on the reaction zone surface area. The error bars indicate the standard deviations.

Finally, it is of interest to study the effects of integral length scale on the distributions of tangential strain rate and curvature at the reaction surface. These quantities are related to both the turbulent flame surface area and chemical source terms as stretching, straining, and curvature can affect the chemical source terms and cause small-scale wrinkling of the flame surface.

The strain rate tangential to the reaction surface is computed as

$$a_t = \nabla \cdot \mathbf{u} - \mathbf{n} \cdot \nabla \mathbf{u} \cdot \mathbf{n}, \tag{5.4}$$

where $\mathbf{n} = -\nabla c/|\nabla c|$ is the normal to the isosurface $c = c_{\mathrm{peak}}$ and the curvature is defined as $\kappa = -\nabla \cdot \mathbf{n}$ and is taken to be positive when the center of curvature is in the burnt gases. Figure 5.5 shows the probability density functions of strain and curvature at the reaction zone, normalized by the Kolmogorov time scale and the laminar reaction zone thickness, respectively. Differences between the distributions are negligible, suggesting no significant effect of the integral length scale on the small-scale wrinkling of the flame front.

In all those results, differential diffusion effects do not have a noticeable effect on the flame surface area and distributions of strain rate and curvature, as the non-unity detailed, unity detailed, and tabulated (unity Lewis number) cases present very similar A_T/A at a fixed Ka_δ. Differential

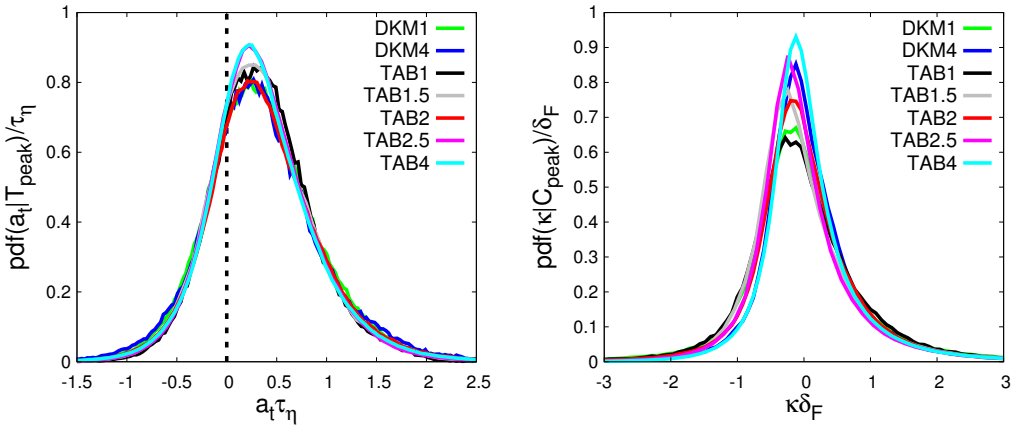

(a) Strain rate (b) Curvature

Figure 5.5: Probability density function of strain rate (left) and curvature (right) on the isosurface $c = c_{\text{peak}}$.

diffusion does, however, have an impact on the chemical source terms.

5.3.2 Unity Lewis number tabulated chemistry

As shown earlier, the burning efficiency in the tabulated chemistry cases is clearly unaffected by changes in the integral length scale (see Table 5.2).

In the present tabulated chemistry cases, the progress variable source term is fixed to its laminar value, *i.e.* $\dot{\omega}_c(c) = \dot{\omega}_{c,\text{lam}}(c)$. The burning efficiency is thus independent of the source term and can be simplified to

$$I_c = \left\langle \frac{1}{|\nabla c|} \middle| c_{\text{peak}} \right\rangle |\nabla c|_{\text{lam}}(c_{\text{peak}}). \tag{5.5}$$

It was reported in previous studies that the surfacic distribution of scalar dissipation rate ($\chi = 2\alpha|\nabla c|^2$) is close to log-normal [37, 3, 77], and thus $\langle \chi|c \rangle \approx e^{\mu+\sigma^2/2}$, where μ and σ are the mean and standard deviation of the logarithm of χ, respectively. Using this observation, Eq. (5.5) can be approximated by

$$I_c \approx \sqrt{\frac{\chi_{\text{lam}}}{e^{\mu+\sigma^2/2}}} \approx \frac{1}{\sqrt{e^{\sigma^2/2}}} = e^{-\sigma^2/4}, \tag{5.6}$$

recognizing that $\chi_{\text{lam}} \approx e^{\mu}$ and that σ represents the effects of turbulence on the dissipation rate [111]. In the present cases, $\sigma \approx 0.6$ and thus $I_0 \approx 1.09$, corresponding to the values listed in Table 5.2.

This suggests that, in the case of a fixed chemical source term (unaffected by turbulence), the burning efficiency increases with the turbulence intensity at the reaction zone.

5.3.3 Non-unity Lewis number detailed chemistry

As opposed to the tabulated chemistry cases, $\dot{\omega}_c$ is influenced by the turbulent flow in the detailed chemistry cases and does not necessarily follow the laminar behavior. Figure 5.6 compares various statistics of the progress variable production rate statistics for the detailed chemistry cases at different integral length scales (DKM1 and DKM4).

First, a lower mean progress variable source term is observed in the non-unity Lewis number case compared to the laminar flame (Fig. 5.6a). This reduction is only observed when differential diffusion effects are included [101, 59] and is related to curvature effects, as shown in Fig. 5.6c. More precisely, low chemical source terms are correlated with regions of high positive curvature. Central to this chapter's objectives, this dependence of the chemical source terms on the reaction zone curvature is independent of the integral length scale, as shown in Fig. 5.6c. Combined with an identical PDF of curvature as shown in Fig. 5.5b, it is not surprising that the conditional mean chemical reaction rates are the same (Fig. 5.6a) for the two integral length scales considered ($l/l_F = 1$ and 4). Not only are the means of the source term identical, but the fluctuations are the same too (Fig. 5.6b). Identical observations were made for the source terms of all major, intermediate, and radical species. Additional comparisons are provided in Appendix D.

The lack of dependence on l/l_F is in clear contrast to the effects of the reaction zone Karlovitz number and of differential diffusion highlighted in previous chapters.

5.4 Summary

Two main observations were made with respect to the impact of the integral length scale. First, the turbulent flame surface area was found to be strongly affected by the large scales, increasing linearly with l/l_F. Second and in constrast, the chemical source terms (and thus the burning efficiency) were essentially unaffected by changes in the integral length scale *at a fixed* Ka_δ. This last observation

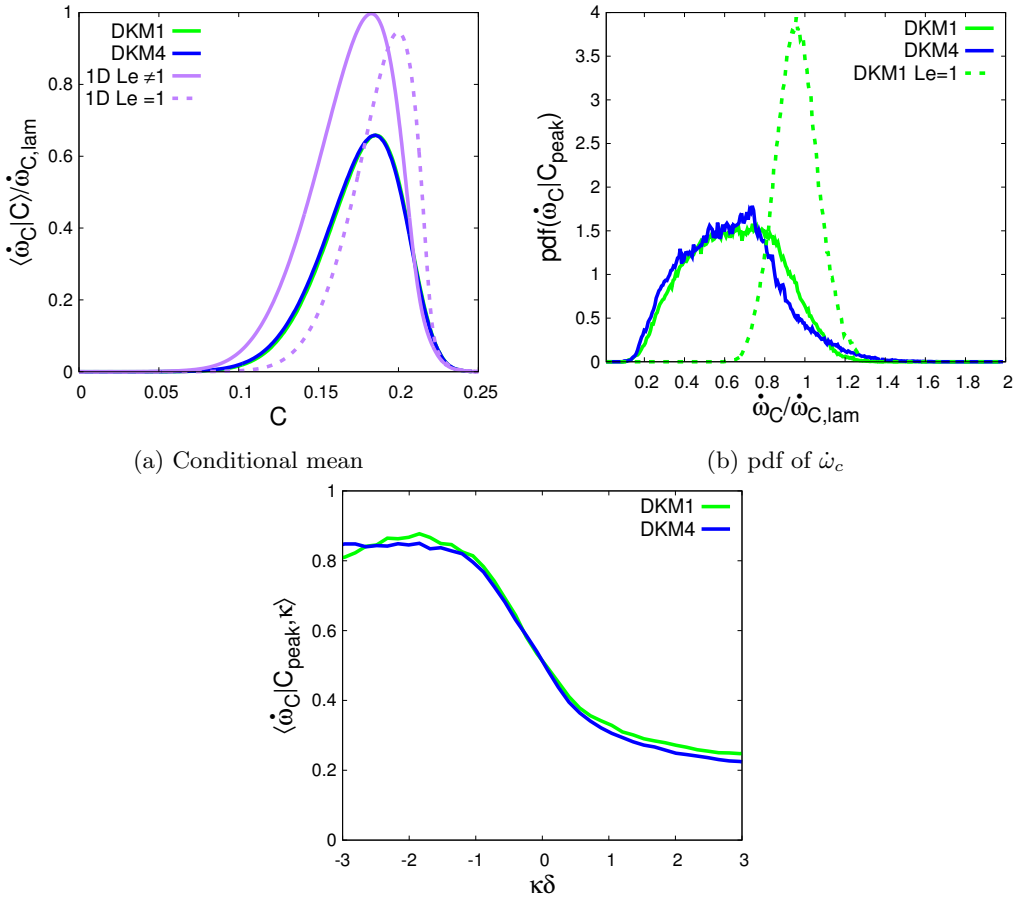

(a) Conditional mean

(b) pdf of $\dot{\omega}_c$

(c) Curvature conditional mean of $\dot{\omega}_c$

Figure 5.6: Conditional mean (a) and probability density function (b) of the normalized progress variable production rate (normalized by the non-unity Lewis number laminar flame). The probability density function is taken at c_{peak}. The PDF of the unity Lewis number detailed chemistry case from Ref. [102] (DKM1, Le=1) is also shown to illustrate the presence of differential diffusion effects. c) Conditional mean on curvature of the progress variable source term at c_{peak}.

is particularly important as it confirms that the chemical source terms are controlled by the small turbulent scales ($\lesssim \delta_F$) and not the large scales. Despite the low Reynolds number of the present simulations, the dissipation scales are universal and their influence on the chemical source terms does not change.

The turbulent flame speed is thus affected by both large and small scales. The large scales modulate the flame surface area while the small scales primarily play a role in modulating the chemical source term (in the presence of differential diffusion) and locally broadening the reaction zone (change in local scalar gradients).

Chapter 6

Filtered Chemical Source Term

In the previous chapters, the physics of high Karlovitz number flames was studied through Direct Numerical Simulations. The focus is now shifted towards assessing the potential of simulating such flames with Large Eddy Simulations. In this chapter, the DNS dataset is used to assess assumptions involved in the sub-filter closure of the chemical source terms.

6.1 Introduction

In traditional chemistry tabulation for low Karlovitz number turbulent flames, the filtered chemical source term of the progress variable, $\tilde{\dot{\omega}}_c$ (where $\tilde{}$ denotes density-weighted spatial filtering), is expressed as a function of the filtered progress variable, $\tilde{c}$, and its variance, $c_v = \widetilde{cc} - \tilde{c}\tilde{c}$ (or, equivalently, the unmixedness $S_c = c_v/[\tilde{c}(c_b - \tilde{c})]$). More precisely, the dependence of $\tilde{\dot{\omega}}_c$ on $\tilde{c}$ and c_v is obtained through the sub-filter probability density function (PDF) of the progress variable:

$$\tilde{\dot{\omega}}_c\left(\tilde{c}, c_v\right) = \int_0^{c_b} \dot{\omega}_c(c) P(c|\tilde{c}, c_v) \mathrm{d}c, \tag{6.1}$$

where $\dot{\omega}_c$ is the unfiltered progress variable source term, $P(c|\tilde{c}, c_v)$ is the sub-filter PDF of c at a given $\tilde{c}$ and c_v, and the progress variable is normalized between 0 and c_b. Two assumptions are involved in Eq. (6.1):

1. None of the fluctuations of $\dot{\omega}_c$ at a given c are necessary ($\dot{\omega}_c \rightarrow \dot{\omega}_c(c)$).

2. Only two quantities are sufficient to express $\tilde{\dot{\omega}}_c$, namely $\tilde{c}$ and c_v ($\tilde{\dot{\omega}}_c \rightarrow \tilde{\dot{\omega}}_c\left(\tilde{c}, c_v\right)$).

Should these two assumptions be valid, there are two unknown functions:

1. The sub-filter PDF, $P(c|\tilde{c}, c_v)$.

2. The unfiltered chemical source term, $\dot{\omega}_c(c)$.

It is the goal of this chapter to investigate these assumptions and assess common expressions for $P(c|\tilde{c}, c_v)$ and $\dot{\omega}_c(c)$. The DNS dataset used is reviewed in Section 6.2, the methodology is described in Section 6.3, assumptions 1 and 2 are assessed in Section 6.4, and the functions $P(c|\tilde{c}, c_v)$ and $\dot{\omega}_c(c)$ are discussed in Section 6.5.

6.2 Review of DNS dataset

Previously described DNS of high Karlovitz number n-heptane flames are used in this chapter to investigate the filtered chemical source terms. The 10 simulations used were previously reported in Chapters 3, 4, and 5. The reader is referred to previous chapters for description of the numerical framework, governing equations, and validation.

6.2.1 Simulation parameters

For each simulation, the unburnt gas is an n-heptane/air mixture at standard pressure ($P_0 = 1$ atm) and with an equivalence ratio of 0.9. The unburnt temperature, T_u, and turbulent RMS velocity, u', were varied to cover a range of reaction zone Karlovitz numbers. Table 6.1 lists the parameters for the simulations.

For each case (A, B, B^4, C, and D), detailed chemistry simulations were performed using both non-unity (no subscript) and unity Lewis numbers (subscript 1) to isolate the effects of differential diffusion. A reduced mechanism consisting of 35 species and 217 reactions was used [101]. Cases B^4 and B_1^4 are used to assess integral length scale effects on the filtered source terms and allow larger filter widths.

Case	A	B	B[4]	C	D
T_u (K)		298		800	
S_L (m/s)		0.36		2.3	
l_F (mm)		0.39		0.25	
u'/S_L	9	18	33	19	45
l/l_F	1.1	1.1	4	1.2	1.2
Ka_u	78	220	220	204	740
Ka_δ	1.9	7.0	7.0	73	256
Re_t	83	190	1150	170	380
Δx (μm)	18	18	18	12	7
Grid ($\times 10^6$)	23	23	675	23	117

Table 6.1: Parameters of the simulations. S_L is the laminar flame speed, $l_F = (T_b - T_u)/|\nabla T|_{\max}$ is the laminar flame thickness, $\mathrm{Ka}_u = \frac{l_F}{S_L}\sqrt{\frac{u'^3}{\nu_u l}}$ is the unburnt Karlovitz number, $\mathrm{Ka}_\delta = \delta_F^2/\eta_\delta^2$ is the reaction zone Karlovitz number evaluated using the reaction zone thickness and the Kolmogorov length scale at the reaction zone, $\mathrm{Re}_t = u'l/\nu$ is the turbulent Reynolds number in the unburnt gas, and Δx is the grid spacing.

6.2.2 Chemical source terms

The effects of intense turbulence and differential diffusion on the chemical source terms of the present n-heptane flames have been reported in Chapters 3, 4, and 5. Findings relevant to the present chapter are briefly reviewed here.

In the unity Lewis number cases, the mean source terms conditioned on the progress variable $\langle \dot{\omega}_c | c \rangle$ are close to their corresponding freely propagating, unstretched laminar flames profiles [101, 59] (as shown in Fig. 6.1a). The progress variable is defined here as $c = Y_{\mathrm{H_2O}} + Y_{\mathrm{H_2}} + Y_{\mathrm{CO}} + Y_{\mathrm{CO_2}}$. In contrast, in the non-unity Lewis number cases, the same source terms exhibit lower values than the corresponding laminar flames (Fig. 6.1b) [101, 59]. Regardless of the mean values, there are large fluctuations in these chemical source terms. This is illustrated in Fig. 6.1c by their probability density functions at c_{peak} for cases B and $\mathrm{B_1}$ (c_{peak} is the progress variable value of peak progress variable production rate in the turbulent flame). In both unity and non-unity Lewis number cases, the PDF illustrates large fluctuations in the unfiltered chemical source terms at a fixed c.

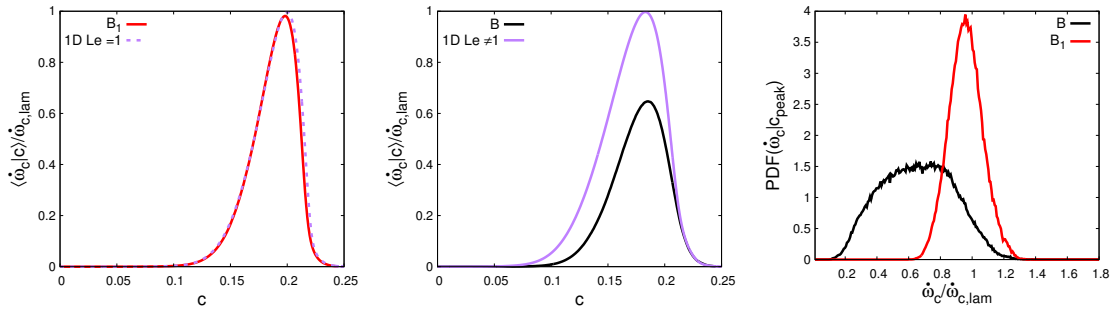

(a) Conditional mean Le = 1 (b) Conditional mean Le ≠ 1 (c) PDF of $\dot{\omega}_c$

Figure 6.1: Conditional means (a-b) and probability density function (c) of the normalized progress variable production rate (normalized by the corresponding laminar flame value). The probability density function is taken at the corresponding progress variable at peak source term.

6.3 Methodology

6.3.1 Filtering of DNS data

In the following sections, spatially filtered quantities are computed from the DNS data sets. Consider a filtering function F. The filtered field $\overline{\phi}$ is defined as:

$$\overline{\phi}(\mathbf{x}) = \iiint F(\mathbf{x}-\mathbf{x}')\phi(\mathbf{x}')d\mathbf{x}'. \tag{6.2}$$

Density-weighted (Favre) filtered fields are denoted as $\tilde{\phi}$:

$$\tilde{\phi} = \frac{\overline{\rho\phi}}{\overline{\rho}}. \tag{6.3}$$

Practically, the filtered field (denoted by an overbar) is computed from a diffusion equation which approximates the convolution in Eq. (6.2) using a Gaussian filter:

$$\overline{\phi} = \phi + \frac{\Delta^2}{24}\nabla^2\phi + \frac{\Delta^4}{1152}\nabla^4\phi, \tag{6.4}$$

where only the first moments of the Gaussian filter are considered. A similar approach was used by Moureau *et al.* [71]. Cases A through D are filtered with filter widths varying from $\Delta = 4\Delta x_{\mathrm{DNS}}$ to $\Delta = 32\Delta x_{\mathrm{DNS}}$. Cases B^4 and B_1^4 are filtered with larger filter widths up to $\Delta = 128\Delta x_{\mathrm{DNS}}$. This

corresponds to filter widths varying from DNS resolution to approximately six times the laminar flame thickness. Filtering the present DNS data with larger filter widths is not possible due to the low turbulent Reynolds numbers of the simulations [112].

6.3.2 LES equations

Combustion modeling using a tabulated chemistry approach is considered for the analysis of subgrid scale closures for LES. The filtered (LES) equations are as follows:

$$\frac{\partial \overline{\rho}}{\partial t} + \nabla \cdot (\overline{\rho}\tilde{\mathbf{u}}) = 0, \tag{6.5}$$

$$\frac{\partial \overline{\rho}\tilde{\mathbf{u}}}{\partial t} + \nabla \cdot (\overline{\rho}\tilde{\mathbf{u}}\tilde{\mathbf{u}}) = -\nabla \overline{p} + \nabla \cdot \overline{\tau} + \nabla \cdot \overline{\tau}^{u}_{\mathbf{u}}, \tag{6.6}$$

$$\frac{\partial \overline{\rho}\tilde{c}}{\partial t} + \nabla \cdot (\overline{\rho}\tilde{\mathbf{u}}\tilde{c}) = \nabla \cdot \left(\overline{\rho}\widetilde{D_c}\nabla \tilde{c}\right) + \nabla \cdot \overline{\tau}_c + \overline{\rho}\tilde{\dot{\omega}}_c, \tag{6.7}$$

where $\overline{\rho}$, $\tilde{\mathbf{u}}$, and $\tilde{c}$ are the resolved quantities and $\overline{\tau}^{u}_{\mathbf{u}}$, and $\overline{\tau}_c$ are subgrid-scale terms. The subgrid-scale terms, along with the filtered chemical source term $\tilde{\dot{\omega}}_c$, represent unresolved phenomena by the LES grid and require closure. The present study focuses solely on the filtered chemical source term.

6.3.3 Comparison metrics

In the next sections, the assumptions and unknown functions previously mentioned in Section 6.1 will be assessed using four different comparison metrics.

The filtered source terms from detailed and tabulated chemistry will be first compared through their conditional means, $\langle \tilde{\dot{\omega}}_c | \tilde{c} \rangle$, and second through their conditional probability density functions $\mathrm{PDF}(\tilde{\dot{\omega}}_c | \tilde{c}_{\mathrm{peak}})$. Both conditional means and PDFs are computed using volumetric weighting. In other words, computational cells whose values of $\tilde{c}$ are within a small range (bin) of the desired value are considered. The mean or probability is then computed by weighting the values of $\tilde{\dot{\omega}}_c$ by the corresponding cell volume.

Third, the source term tabulation will be assessed through the global prediction error made on

the filtered tabulated chemical source term $\tilde{\dot{\omega}}_{\text{table}}$ compared to the filtered detailed chemistry source term $\tilde{\dot{\omega}}_{c,\text{DKM}}$ [73, 51]:

$$\epsilon_{\text{table}} = \sqrt{\frac{\int_\Omega (\tilde{\dot{\omega}}_{\text{table}} - \tilde{\dot{\omega}}_{c,\text{DKM}})^2 \mathrm{d}V}{\int_\Omega \tilde{\dot{\omega}}^2_{c,\text{DKM}} \mathrm{d}V}}. \tag{6.8}$$

This is the most stringent test since local point-wise errors can be made even if the tabulated and exact filtered source terms have similar means and PDFs.

Finally, the performance of the tables will be compared through the time-averaged turbulent flame speed computed as the volumetric integral of the progress variable source term:

$$S_T = \frac{1}{\rho_u c_b L^2} \int_V \overline{\rho} \tilde{\dot{\omega}}_c \, \mathrm{d}V, \tag{6.9}$$

where subscripts u and b denote values taken in the unburnt and burnt gases, respectively. This a very important metric since accurate prediction of the turbulent flame speed is often crucial in the design of practical devices. It is also the most lenient metric since local prediction errors may not have an impact on the global flame speed.

A summary of the metrics used to assess the different assumptions is provided in Table 6.2.

Metrics	$\langle \tilde{\dot{\omega}}_c \vert \tilde{c} \rangle$	PDF$(\tilde{\dot{\omega}}_c \vert \tilde{c}_{\text{peak}})$	ϵ	$\overline{S}_T$
Assumption 1	✓	✓		
Assumption 2			✓	
Function 1	✓		✓	✓
Function 2	✓			

Table 6.2: Comparison metrics used for the different assumptions.

First, the filtered chemical source terms from the detailed chemistry cases will be compared to tabulated chemistry (assumption 1). Second, tabulation of the filtered source terms using $\tilde{c}$ and its variance will be assessed (assumption 2). Third, the filtered source terms will be compared to predictions from commonly used PDF models (function 1). Finally, the possibility of using laminar flames to generate the table will be discussed (function 2).

6.4 Assumptions

6.4.1 Assumption 1: Detailed *vs.* tabulated chemistry

The present chapter is not dedicated to finding what the mean function ($\dot{\omega}_c(c)$) is, nor what the fluctuations are due to, nor how to reproduce them. Instead, the focus is on whether capturing these fluctuations is necessary for LES modeling. That is assumption 1 of the introduction.

To test this assumption, results obtained with detailed chemistry (DKM) are compared to results obtained with tabulated chemistry (TAB) using a table of a single progress variable. For each case A through D, the statistics of the filtered chemical source terms for detailed and tabulated chemistry are obtained as follows:

1. Get the unfiltered source term field $\dot{\omega}_c^{\mathrm{DKM}}(x,y,z)$ from the detailed chemistry simulation.
2. Compute the conditional mean $\langle\dot{\omega}_c^{\mathrm{DKM}}|c\rangle$.
3. Tabulate the source term against the progress variable using the conditional mean $\dot{\omega}_c^{\mathrm{TAB}}(c) = \langle\dot{\omega}_c^{\mathrm{DKM}}|c\rangle$.
4. Use the DKM field of $c(x,y,z)$ to lookup the tabulated source term $\dot{\omega}_c^{\mathrm{TAB}}(c)$ and get the field $\dot{\omega}_c^{\mathrm{TAB}}(x,y,z)$.
5. Perform spatial filtering operation described in Section 6.3 to obtain $\tilde{\dot{\omega}}_c^{\mathrm{DKM}}(x,y,z)$ and $\tilde{\dot{\omega}}_c^{\mathrm{TAB}}(x,y,z)$.
6. Compute conditional means and conditional PDFs $\langle\tilde{\dot{\omega}}_c|\tilde{c}\rangle$ and PDF$(\tilde{\dot{\omega}}_c|\tilde{c}_{\mathrm{peak}})$ for both DKM and TAB.

The possibility of using a table generated from 1D flamelet solutions, as an approximation for the conditional mean $\dot{\omega}_c^{\mathrm{TAB}}(c)$, is discussed in Section 6.5.2.

Figure 6.2 compares the filtered progress variable source term from detailed chemistry DNS, $\tilde{\dot{\omega}}_c^{\mathrm{DKM}}$, to tabulated chemistry, $\tilde{\dot{\omega}}_c^{\mathrm{TAB}}$, at different filter widths. The two conditional means $\langle\tilde{\dot{\omega}}_c|\tilde{c}\rangle$ are shown in Fig. 6.2a for the unity Lewis number case case B_1^4. Case B_1^4 is used since it allows filtering at larger filter widths than case B_1. As shown in Chapter 5, the change in integral length scale does not

significantly affect the source term. Overall, as expected, filtering reduces the magnitude of the peak source term and flattens the profile. The two conditional means are in very good agreement for all filter widths. To further illustrate the effects of filtering, the peak value of the mean filtered progress variable production rate is plotted against filter width in Fig. 6.2b for all Le = 1 cases A through D, covering a range of reaction zone Karlovitz numbers. The same decrease in the peak source term with increasing filter width is observed for all cases, independent of the chemical model (detailed *vs.* tabulated) and Karlovitz number. This result is important as it underscores that the fluctuations in the unfiltered source terms at a given c (Fig. 6.1c) are not essential in predicting the mean filtered source term. It should be noted that $\Delta/\bar{\delta}_F$, where $\bar{\delta}_F$ is the mean reaction zone thickness of the turbulent flame, is preferred over Δ/l_F for the present flames in the thin and distributed reaction zones regimes since thickening of the preheat and reaction zones is observed. Values of $\bar{\delta}_F$ for the present cases were reported in Chapter 3.

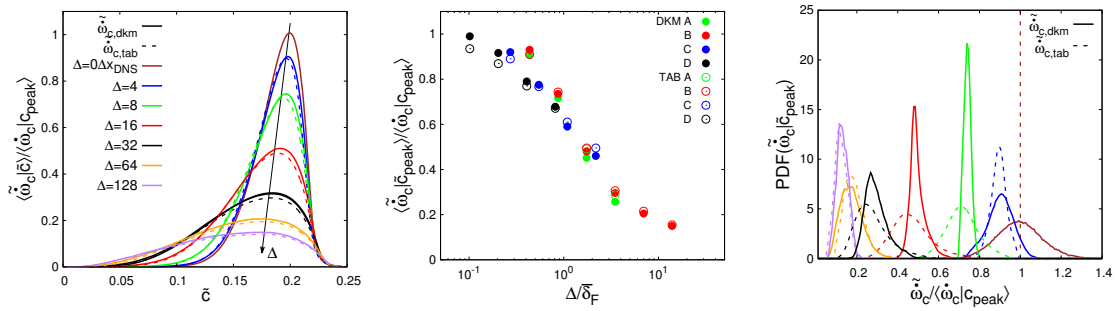

(a) Conditional means (Le=1) (b) Conditional mean at c_{peak} (c) PDF of $\tilde{\dot{\omega}}_c$

(d) Conditional means (Le≠1) (e) Conditional mean at c_{peak} (f) PDF of $\tilde{\dot{\omega}}_c$

Figure 6.2: Conditional means (a-d) and probability density functions (c-f) of the filtered progress variable source term from detailed chemistry DNS (solid lines) compared with filtered tabulated chemistry (dashed lines) for unity Lewis number case B_1^4 (top) and non-unity Lewis number case B^4 (bottom). (b-e) Conditional means of $\tilde{\dot{\omega}}_c$ at $\tilde{c}_{\text{peak}}$ for cases A through D plotted against the normalized filter width $\Delta/\bar{\delta}_F$, where $\bar{\delta}_F$ is the mean reaction zone thickness of the turbulent flame [59].

As reproducing only the conditional mean profiles $\left(\langle\tilde{\dot{\omega}}_c|\tilde{c}\rangle\right)$ may be insufficient, the filtered source terms from detailed and tabulated chemistry are further compared by evaluating their probability density function on the isosurface of $\tilde{c}_{\text{peak}}$, as shown in Fig. 6.2c (this is the second metric discussed in Section 6.3.3). Fluctuations in this filtered source term can come from two different sources: (1) from the unfiltered source term at a fixed c (Fig. 6.1c), and (2) from the spatial filtering procedure. As expected, significant discrepancies are observed at small filter widths $\Delta < l_F$ ($\Delta \leq 16\Delta x_{\text{DNS}}$). The PDF of the tabulated source terms is a delta function at $\Delta = 0$ (as shown by the dashed brown lines in Figs. 6.2c and 6.2f) and gets broader as the filter width is increased. This is due to the spatial filtering procedure. A different behavior is observed for the detailed chemistry source terms. The PDF gets thinner suggesting that the fluctuations due to turbulence-chemistry interactions are averaged out. However, at filter widths $\Delta \gtrsim l_F$ ($\Delta > 16\Delta x_{\text{DNS}}$), the PDFs of $\tilde{\dot{\omega}}_c$ from filtered detailed and tabulated chemistry are in decent agreement. At these larger filter widths, the flow structures affecting the chemical source terms are filtered out and only fluctuations from the spatial filtering procedure remain, reducing the differences between the two combustion models.

A similar behavior is observed in the non-unity Lewis number cases. Figures 6.2d and 6.2f present the conditional means and PDFs of the filtered progress variable source terms from detailed chemistry, and non-unity Lewis number DNS (case B^4) compared to tabulated chemistry at different filter widths. The non-unity Lewis number filtered source terms are normalized by the peak of the mean unfiltered source term (Fig. 6.1b). Once again, the mean filtered source terms are in good agreement (Fig. 6.2d) and significant discrepancies in the PDFs observed at small filter widths are reduced as Δ is increased beyond the laminar flame thickness (Fig. 6.2f). Furthermore, this agreement is observed independently of the Karlovitz number, as illustrated in Fig. 6.2e showing the peak value of the mean filtered progress variable production rate plotted against filter width. As in the unity Lewis number cases (Fig. 6.2b), a similar decrease is observed for all non-unity Lewis number cases.

These results indicate that, while fluctuations due to turbulence affect the DKM filtered source terms at small filter widths, their influence becomes negligible when the filter width is larger than the

flame thickness. This is consistent with the fact that fluctuations in the chemical source terms are due to small turbulent scales of the order of the reaction zone thickness [59], and are thus sub-filter phenomena. In summary, assumption 1 is valid for $\Delta \gtrsim l_F$ when $\dot{\omega}_c(c) = \langle \dot{\omega}_c^{\mathrm{DKM}} | c \rangle$.

6.4.2 Assumption 2: Tabulation using $\tilde{c}$ and c_v

As discussed earlier, a common approach for LES with tabulated chemistry consists of assuming the filtered chemical source term is a function of the filtered progress variable, $\tilde{c}$, and its variance, c_v (or, equivalently, the unmixedness factor S_c) [30, 75, 54]. This is assumption 2 of the introduction. The validity of such a modeling approach for high Ka flames is assessed here by comparing the exact term to the optimal estimator given these two variables.

The optimal estimator is the function (of $\tilde{c}$ and c_v) that minimizes the prediction error made on the chemical source term (L^2-norm)

$$\epsilon_f = \sqrt{\frac{\int_\Omega (f(\tilde{c}, c_v) - \tilde{\dot{\omega}}_{c,\mathrm{DNS}})^2 \mathrm{d}V}{\int_\Omega \tilde{\dot{\omega}}_{c,\mathrm{DNS}}^2 \mathrm{d}V}}, \tag{6.10}$$

where $f(\tilde{c}, c_v)$ is any function of these two variables. It can be shown that the optimal estimator is exactly the conditional mean from the filtered DNS, i.e. $\langle \tilde{\dot{\omega}}_c | \tilde{c}, c_v \rangle$ [70]. The irreducible error associated with assuming that $\tilde{\dot{\omega}}_c$ is only a function of $\tilde{c}$ and c_v is then given by Eq. (6.10) evaluated with $f(\tilde{c}, c_v) = \langle \tilde{\dot{\omega}}_c | \tilde{c}, c_v \rangle$. These prediction errors are shown in Table 6.3. This is illustrated in Fig. 6.3 which shows the probability density function of the point-wise comparison between the predicted (optimal estimator) and the actual filtered DNS source term for B^4 at three different filter widths. The prediction error, ϵ_f, corresponds to the mean square deviation from the solid black line. The scatter around the black diagonal is limited for the three filter widths shown in Fig. 6.3. The correlation coefficients for the different cases are defined as

$$r = \frac{\sum_{i=1}^{n} (X_i - \bar{X})(Y_i - \bar{Y})}{\sqrt{\sum_{i=1}^{n} (X_i - \bar{X})^2} \sqrt{\sum_{i=1}^{n} (Y_i - \bar{Y})^2}} \tag{6.11}$$

and are shown on Fig. 6.3. This indicates a good prediction of the filtered source term.

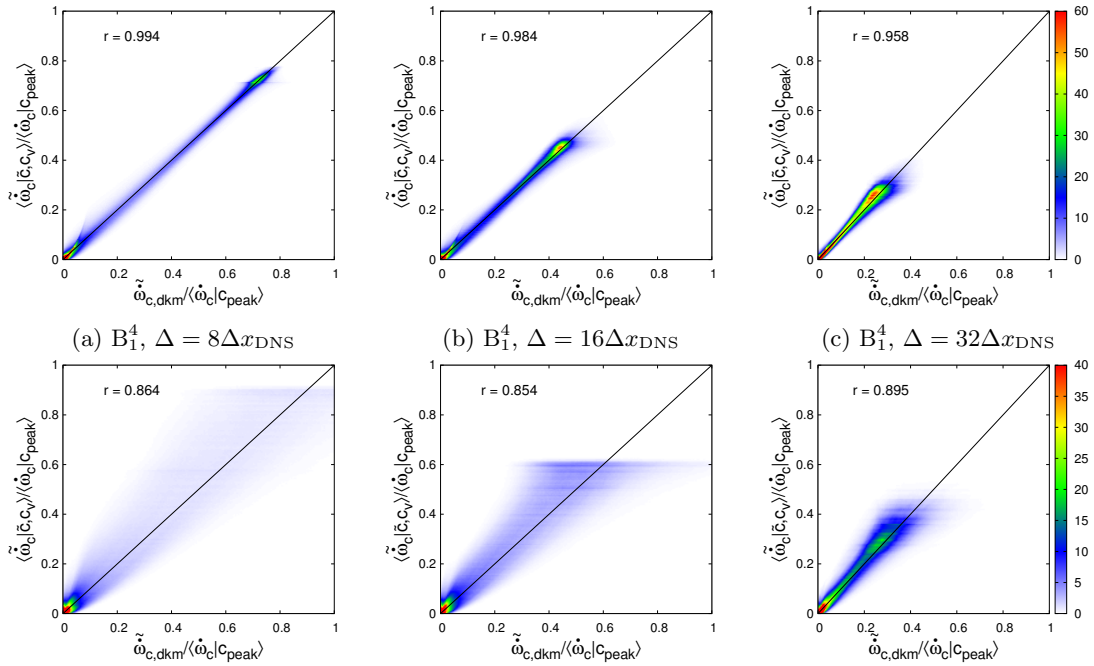

(a) B_1^4, $\Delta = 8\Delta x_{\mathrm{DNS}}$ (b) B_1^4, $\Delta = 16\Delta x_{\mathrm{DNS}}$ (c) B_1^4, $\Delta = 32\Delta x_{\mathrm{DNS}}$

(d) B^4, $\Delta = 8\Delta x_{\mathrm{DNS}}$ (e) B^4, $\Delta = 16\Delta x_{\mathrm{DNS}}$ (f) B^4, $\Delta = 32\Delta x_{\mathrm{DNS}}$

Figure 6.3: Filtered chemical source obtained from the optimal estimator compared to the source term from the filtered detailed chemistry DNS for unity Lewis number case B_1^4 (a-c) and non-unity Lewis number case B^4 (d-f) for three different filter widths. The corresponding correlation coefficient is listed.

For all unity Lewis number detailed chemistry cases and filter widths, the prediction error from the optimal estimator is small (at most 16%). This indicates that, even with large source term fluctuations (Fig. 6.1c), a tabulation approach using only the filtered progress variable and its variance provides a very good estimate of the filtered source term for LES of unity Lewis number flames independent of the filter width. While assumption 2 is clearly valid for these cases, larger errors are observed for the non-unity Lewis number cases. However, these errors decrease as the filter width is increased, suggesting assumption 2 may become appropriate for larger filter widths.

		Le= 1				Le≠ 1			
	Δ	A_1	B_1	C_1	D_1	A	B	C	D
DKM	4	0.06	0.04	0.06	0.11	0.44	0.42	0.34	0.26
	8	0.07	0.06	0.09	0.13	0.38	0.37	0.29	0.23
	16	0.12	0.12	0.12	0.13	0.39	0.36	0.22	0.17
	32	0.15	0.13	0.12	0.11	0.36	0.29	0.15	0.12
	64		0.15				0.26		
	128		0.16				0.29		

Table 6.3: Prediction error from the optimal estimator of the progress variable source term for detailed chemistry simulations for the different cases.

6.5 Unknown functions

6.5.1 Presumed sub-filter PDF

In Sections 6.4.1 and 6.4.2, it was shown that it is not necessary to capture the fluctuations in the unfiltered chemical source terms (i.e. $\dot{\omega}_c \approx \dot{\omega}_c(c)$) and that $\tilde{c}$ and c_v are good tabulation variables for the filtered chemical source term (i.e. $\tilde{\dot{\omega}}_c \approx \tilde{\dot{\omega}}_c(\tilde{c}, c_v)$). In this section, the filtered source terms predicted from β-PDF, and FLF-PDF closures (defined in Appendix E.1) are compared to the filtered DNS in order to determine an appropriate function for $P(c|\tilde{c}, c_v)$.

6.5.1.1 Comparison of the sub-filter PDF

In order to assess the validity of common presumed-PDF models, it is insightful to first evaluate the sub-filter PDF from the filtered DNS. Figure 6.4 presents the sub-filter PDFs of c computed at a fixed $\tilde{c} = 0.12$ for two values of S_c for the different cases.

First, it should be noted that the sub-filter PDFs of the filtered detailed chemistry DNS are not significantly influenced by differential diffusion effects or changes in integral length scale. This is illustrated in Fig. 6.4a. Second, the sub-filter PDFs from the filtered DNS is in better agreement with the FLF-PDF than the β-PDF (Figs. 6.4b and 6.4c). This agrees with the results of Moureau *et al.* [71] at a lower Karlovitz number. However, larger differences are observed here between the FLF-PDF and filtered DNS PDF. This is likely due to the much higher Karlovitz numbers of the present simulations.

Two main reasons can explain these differences: (1) the turbulent flame is significantly thickened

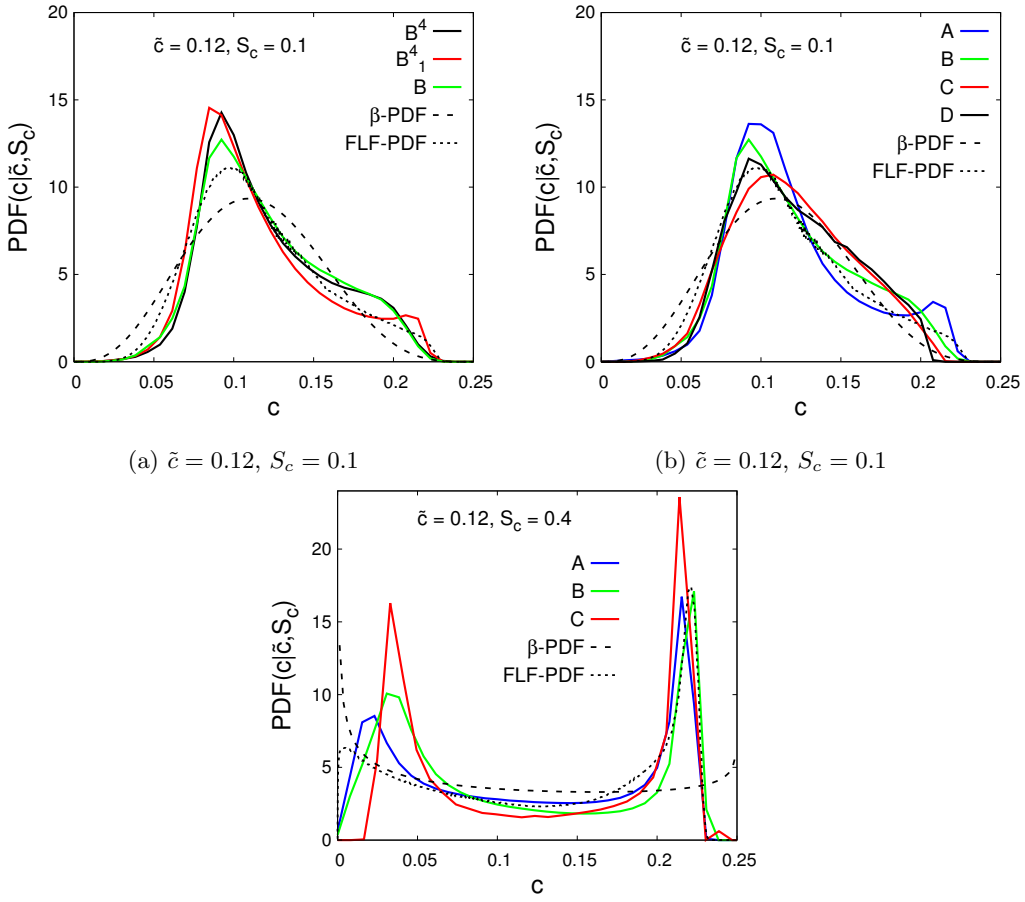

(a) $\tilde{c} = 0.12$, $S_c = 0.1$

(b) $\tilde{c} = 0.12$, $S_c = 0.1$

(c) $\tilde{c} = 0.12$, $S_c = 0.4$

Figure 6.4: Sub-filter probability density function of c at given $\tilde{c}$ and $S_{\tilde{c}}$ comparing filtered detailed chemistry DNS, β-PDF, and FLF-PDF.

and (2) the flow field is highly three-dimensional. While it is difficult to account for the shape of the turbulent flame in 1D laminar flames, the thickening of the preheat zone can be modeled through an enhanced turbulent diffusivity. Consider, for example, the semi-empirical model of Savard and Blanquart [100] for the turbulent diffusivity:

$$D + D_T = D(1 + a\mathrm{Ka}), \tag{6.12}$$

where D is the laminar diffusivity, D_T is the turbulent diffusivity, a is a constant, and Ka is the Karlovitz number. Note that the Karlovitz number is computed using the local, temperature-dependent, viscosity and is varied by increasing u'. It is therefore higher in the unburnt gases and

decreases across the flame, $\mathrm{Ka} = \mathrm{Ka}_u \sqrt{\frac{\nu_u}{\nu}}$. The effect of enhanced diffusivity on the FLF-PDF is studied by performing 1D laminar flame simulations at increasing Karlovitz numbers. The results are illustrated in Fig. 6.5. The left peak of the PDF shifts towards the right as the Karlovitz is increased while the position of the right peak is essentially unchanged. This shift is consistent with the trend observed in the filtered DNS (Fig. 6.4c) and can be associated with a significant thickening of the preheat zone. The height of the left peak is still underpredicted by the modified FLF-PDF. This is likely due to the three-dimensional nature of the flow field.

While the shapes of the predicted PDF differ somewhat from the filtered DNS PDF, the impact of these differences on the filtered source term might be limited. This is investigated next.

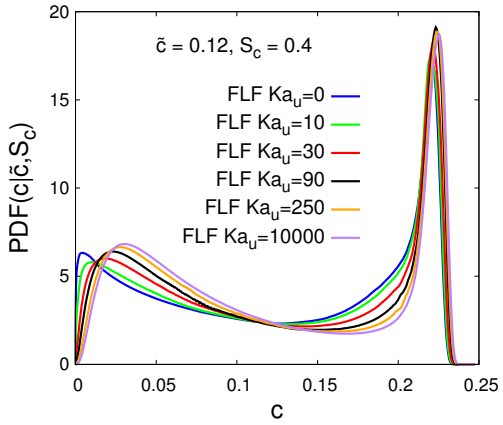

Figure 6.5: Sub-filter probability density function of c at given $\tilde{c}$ and $S_{\tilde{c}}$ comparing FLF-PDF with added diffusivity. The unburnt Karlovitz number is reported in the legend since the Karlovitz number varies across the flame due to viscosity changes.

6.5.1.2 Comparison of source terms

The chemical source terms predicted by the β-PDF and FLF-PDF tables are compared to the filtered DNS source terms. The filtered tabulated source terms are obtained as follows:

1. Get the unfiltered tabulated source term using the conditional mean from the DNS, $\dot{\omega}_c^{\mathrm{TAB}}(c) = \langle \dot{\omega}_c^{\mathrm{DKM}} | c \rangle$.

2. Compute the filtered source term using Eq. (6.1), $\tilde{\dot{\omega}}_c(\tilde{c}, c_v) = \int_0^{c_b} \dot{\omega}_c^{\mathrm{TAB}}(c) P(c|\tilde{c}, c_v) \mathrm{d}c$.

3. Tabulate the filtered source term $\tilde{\dot{\omega}}_c(\tilde{c}, c_v)$ against $\tilde{c}$ and c_v for both the β-PDF and FLF-PDF.

4. Use the filtered DKM fields of $\tilde{c}$ and c_v to look up $\tilde{\dot{\omega}}_c\left(\tilde{c}, c_v\right)$.

Figure 6.6 shows the conditional means of the filtered chemical source terms obtained with the β-PDF and FLF-PDF tables for cases B^4 and B_1^4 (the conditional mean obtained using the optimal estimator is identical to the filtered DNS and is not shown). At small filter widths ($\Delta = 4$ or $8\Delta x_{\mathrm{DNS}}$), the predicted source term is very close to that of the filtered DNS, regardless of the sub-filter PDF used. At higher filter widths ($\Delta \geq 16\Delta x_{\mathrm{DNS}}$), the shape of the conditional mean predicted from the table differs from the filtered DNS. This is the case for both sub-filter PDFs, but the FLF-PDF table is in better agreement. This is consistent with the comparison of the sub-filter PDFs in Section 6.5.1.1. In all cases, the magnitude of the peak filtered source term from the PDF models agrees fairly well with the filtered DNS.

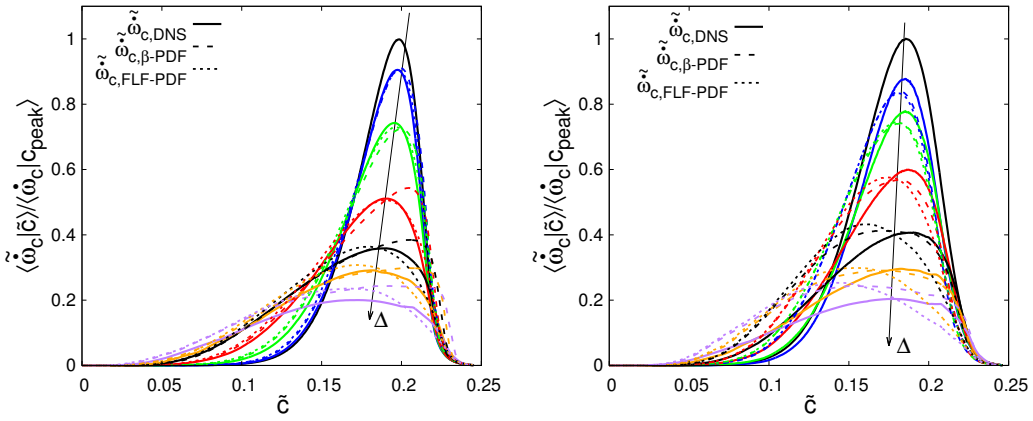

(a) Case B_1^4 (b) Case B^4

Figure 6.6: Filtered progress variable source term (solid lines) (case B^4) compared with predictions from the β-PDF and FLF-PDF tables (dashed lines) using different filter widths $\Delta = 1$, 4, 8, 16, 32, 64, and $128\Delta x_{\mathrm{DNS}}$.

While the conditional means of the chemical source terms $\left(\langle\tilde{\dot{\omega}}_c|\tilde{c}\rangle\right)$ are relatively well predicted by the β-PDF and FLF-PDF, it is not clear that the fluctuations in $\tilde{\dot{\omega}}_c$ will be captured adequately. Since the shape and location of the peaks of the conditional means differ between the filtered DNS, β-PDF, and FLF-PDF, it is not relevant to compare the probability density function of $\tilde{\dot{\omega}}_c$ at $\tilde{c}_{\mathrm{peak}}$ as was done for assumption 1. Instead, as done for assumption 2, the prediction errors from the assumed PDF models, defined in Eq. (6.8), are summarized in Table 6.4. The prediction errors

are larger than for the optimal estimator up to a factor of 2 or 3 for larger filter widths. From these results, it is difficult to determine which PDF is better, as the prediction errors from both β-PDF and FLF-PDF tables are relatively close. It is also difficult to determine if the predictions from these tables are satisfactory since the mean source terms are well predicted but significant point-wise errors are observed.

		Le= 1				Le$\neq$ 1			
	Δ	A_1	B_1	C_1	D_1	A	B	C	D
β	4	0.16	0.23	0.25	0.21	0.68	0.56	0.55	0.54
	8	0.17	0.25	0.24	0.20	0.65	0.52	0.52	0.53
	16	0.25	0.26	0.22	0.18	0.56	0.44	0.46	0.51
	32	0.37	0.36	0.26	0.16	0.40	0.33	0.38	0.47
	64		0.42				0.36		
	128		0.48				0.40		
FLF	4	0.17	0.24	0.26	0.23	0.66	0.55	0.55	0.54
	8	0.18	0.25	0.25	0.22	0.65	0.53	0.54	0.53
	16	0.19	0.25	0.22	0.19	0.58	0.48	0.51	0.52
	32	0.19	0.24	0.20	0.17	0.46	0.40	0.48	0.50
	64		0.26				0.34		
	128		0.27				0.35		

Table 6.4: Prediction error (Eq. (6.8)) from β-PDF, and FLF-PDF tables of the progress variable source term for the different cases.

As a final comparison, the turbulent flame speeds predicted from both β-PDF and FLF-PDF are compared in Table 6.5. This instantaneous flame speed is computed for each data file saved (approximately one eddy turnover time apart) using Eq. (6.9) and then averaged (over time) to obtain the mean turbulent flame speed $\overline{S_T}$. Again, the filtered progress variable and its variance are evaluated from the (filtered) DNS and are used to look up the filtered density and filtered source terms from the β-PDF and FLF-PDF tables. As shown in Table 6.5 and in all cases, both β-PDF and FLF-PDF predict the turbulent flame speed accurately (within a few %). This result remains valid even for the non-unity Lewis number cases. This is in contrast to the large point-wise errors reported in Table 6.4, and suggests that an accurate prediction of the mean filtered source term is sufficient to obtain a good estimate of the turbulent flame speed.

		Le= 1				Le≠ 1			
	Δ	A_1	B_1	C_1	D_1	A	B	C	D
β	4	1.00	1.00	0.99	1.00	0.99	0.98	0.93	0.94
	8	0.99	0.99	0.99	1.00	0.99	0.98	0.93	0.94
	16	1.00	1.00	0.99	1.00	0.99	0.99	0.95	0.95
	32	1.05	1.03	1.02	1.02	1.03	1.08	1.00	0.96
	64		1.02				1.10		
	128		1.05				1.12		
FLF	4	1.05	1.01	1.00	1.02	1.01	1.01	0.97	1.01
	8	1.06	0.99	1.01	1.01	1.01	1.00	0.96	1.01
	16	0.99	1.00	1.00	1.01	1.00	1.01	0.98	1.01
	32	1.01	1.01	1.01	1.00	1.02	1.06	1.01	1.02
	64		1.02				1.08		
	128		1.01				1.09		

Table 6.5: Predicted turbulent flame speeds (S_T from Eq. (6.9)) from β-PDF and FLF-PDF tables for the different cases normalized by the actual flame speed.

6.5.2 Unfiltered chemical source term $\dot{\omega}_c(c)$

Throughout the previous analysis, the mean chemical source terms from the detailed chemistry DNS were used to generate the chemistry tables, in other words $\dot{\omega}_c^{\mathrm{TAB}}(c) = \langle \dot{\omega}_c^{\mathrm{DKM}} | c \rangle$. However, in practice, it is desirable to generate the tables using 1D flamelet solutions. This is the second unknown function $\dot{\omega}_c(c)$.

As shown in Fig. 6.1a, in the unity Lewis number case, the mean progress variable source term is well approximated by the corresponding one-dimensional, unstretched laminar flame. Thus, laminar flames can be readily used to populate chemistry tables for LES. While assuming unity Lewis numbers may be unrealistic for heavy fuels such as n-heptane, it could apply to fuels with close to unity Lewis numbers such as methane.

For fuels with non-unity Lewis numbers, it was shown in previous work [101, 59] that the mean fuel consumption rate (and, similarly, the mean progress variable source term) is lower than in the corresponding unity Lewis number flame (see Fig. 6.1b). This was observed for different fuels, equivalence ratios, and chemical mechanisms in Chapter 4. This reduction in fuel consumption was previously related to curvature effects. Savard and Blanquart [101] showed that, in the present case B, low fuel consumption rates are correlated with regions of high curvature. This is observed for moderate Karlovitz numbers cases A and B. However, as the Karlovitz number is further increased,

as in cases C and D, differential diffusion effects are diminished with increasing turbulent mixing (effective Lewis numbers tend towards unity as the Karlovitz number increases [100, 59]). The chemical source terms are then less sensitive to curvature and the effective mean values increase towards the unity Lewis number values. This is illustrated in Fig. 6.7 presenting the peak values of the mean unfiltered progress variable production rate for cases A through D.

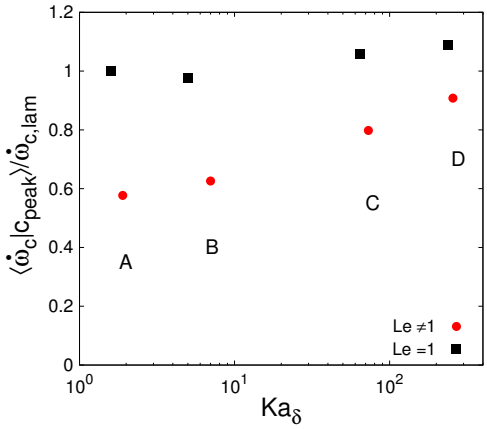

Figure 6.7: Mean progress variable source term at c_{peak} for simulations at varying reaction zone Karlovitz numbers.

This suggests that, for low Karlovitz number flames (flamelet regimes, $\mathrm{Ka}_\delta < 0.1$), the chemical source terms can be tabulated using the non-unity Lewis number unstretched laminar flame. On the other hand, in the limit of high Karlovitz numbers ($\mathrm{Ka}_\delta > 100$), a tabulation using unity Lewis number unstretched laminar flames should produce good results since turbulent mixing reduces differential diffusion effects. In the moderate/high Karlovitz number range, $\mathrm{Ka}_\delta \sim \mathcal{O}(0.1-100)$, the mean chemical source term is not predicted as accurately by 1D unstretched laminar flames.

The mean chemical source term could be obtained by simply scaling the laminar flame source term by a burning efficiency:

$$I_0 = \frac{\langle \dot{\omega}_c^{\mathrm{DKM}} | c_{\mathrm{peak}} \rangle}{\dot{\omega}_{c,\mathrm{lam}}}. \tag{6.13}$$

However, predicting I_0 *a priori* is an active area of research and there does not currently exist a predictive model which includes differential diffusion, turbulent mixing, dissipation rate, strain, and curvature effects in tabulated chemistry of turbulent flames simulations.

6.6 Summary

DNS with detailed chemistry and unity and non-unity Lewis numbers were used to assess the effects of turbulence-chemistry interactions and differential diffusion effects on the sub-filter closure of the chemical source terms.

First, it was observed that filtered source terms from detailed chemistry and tabulated chemistry were in good agreement at sufficiently large filter widths ($\Delta \gtrsim l_F$) for both unity and non-unity Lewis number cases. This seems to indicate that fluctuations in the chemical source terms observed in the detailed chemistry cases do not have a significant influence on the filtered source term and can be neglected in LES.

Second, it was shown using the concept of optimal estimators that a tabulation approach using $\tilde{c}$ and its variance, c_v, can predict accurately the filtered chemical source terms for both detailed and tabulated chemistry filtered DNS.

Third, predictions of the chemical source term from commonly assumed β-PDF and FLF-PDF models were compared to the filtered DNS. Both models lead to non-negligible errors in the local source terms but predicted accurately the turbulent flame speed. This is an important result since accurate prediction of the burning velocity is of importance for many combustion devices.

Fourth, the possibility of using 1D laminar flames to generate the chemistry tables was discussed. It was shown that in the limit of high Karlovitz number, one-dimensional unstretched laminar flames accurately predict the mean progress variable production rate. For heavy hydrocarbon flames ($\mathrm{Le}_F > 1$) at moderate/high Karlovitz numbers, inclusion of strain/curvature effects in flamelet models is necessary to accurately predict the mean chemical source term.

These *a priori* results illustrate the potential of using simple tabulated chemistry approaches based on presumed PDFs for LES of premixed flames in the thin and distributed reaction zones regimes. *A posteriori* studies comparing LES of high Karlovitz number flames will be performed in the next chapter.

Chapter 7

Large Eddy Simulations of Piloted Premixed Jet Flames

In the previous chapters, Direct Numerical Simulations of high Karlovitz number flames were performed and analyzed. The analysis focused on the transition from the thin to distributed reaction zones regimes, potential fuel and chemistry effects, and effects of integral length scale. The main findings were as follows:

- differential diffusion effects are reduced as the Karlovitz number increases but remain present even at high Karlovitz numbers;
- fuel effects are minor and only a few global laminar flame properties appear necessary to predict the overall turbulent flame behavior;
- the chemical source terms are unaffected by changes in Reynolds number at a fixed Ka_δ.

Finally, DNS fields were spatially filtered to gain insight into LES modeling. The results suggested that simple tabulated chemistry approaches based on $\tilde{c}$ and its variance using presumed PDFs may be sufficient to perform predictive LES of high Karlovitz number flames.

In this chapter, Large Eddy Simulations of experimentally-studied high Karlovitz number flames are performed. The goal is to investigate fuel and hydrodynamic effects for a variety of fuels from small alkanes/alkenes (methane/ethylene) to large *n*-alkanes (*n*-heptane) to aromatic fuels (toluene) under a fixed laminar flame speed. These objectives will be achieved by performing Large Eddy Simulations of a modified piloted premixed jet burner (PPJB) [31, 32] combined with matching

experimental results. Any possible fuel effects will be isolated by conducting the experiments and simulations with fuel/air mixtures with the same S_L and by performing LES with models purposely assuming the same structure as laminar flames, building upon the DNS performed and analyzed in the previous chapters.

First, an overview of the experimental setup is provided, followed by a description of the measurement techniques and the modeling strategies used to simulate the turbulent flames. Then, a detailed comparison of boundary conditions and jet development between experiments and simulations is provided. Finally, the effects of fuel and fluid dynamics are analyzed by considering the height of the turbulent flame.

7.1 Piloted premixed jet burner

The present work relies on the original PPJB burner design [31, 32] with modifications to allow studies of fuels with a wide range of molecular weights. A schematic of the burner design used in the experiments is shown in Fig. 7.1. The burner consists of two co-annular premixed flames surrounding and stabilizing the high exit velocity central jet.

The main jet consists of a straight stainless steel tube with an internal diameter of D=5.84 mm and an external diameter of 6.35 mm. Keeping S_L constant, the main jet exit velocity U_{jet} and fuel are varied to investigate finite-rate chemistry and fuel effects.

The main jet is surrounded by a pilot flow coming out of a co-annular tube with internal diameter of D_{pilot}=22.9 mm and outer diameter of 24.1 mm. The nozzle edge of the jet is located 0.6mm above the pilot nozzle. A small step (0.5 mm thick) located 11 mm from the burner exit is used to hold a 5 mm thick brass perforated plate. This plate is composed of 52 holes (1.52 mm in diameter) and serves as anchor for the stoichiometric premixed methane/air flames. The pilot tube has an unburnt exit velocity of 0.75 m/s before the step. The pilot tube is 70 mm in length and externally conical in shape with a 32.4 mm diameter base.

Finally, the outermost co-axial coflow uses hot products to thermally insulate the jet. Hydrogen/air flames at ϕ=0.44 and 0.51 are used to provide coflow temperatures (T_{coflow}) of 1400K and

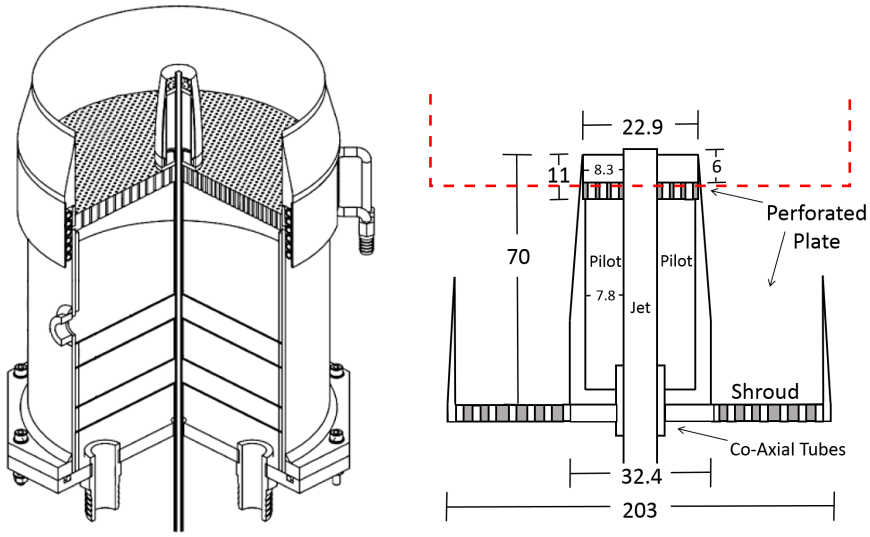

(a) Schematic (b) Cutaway

Figure 7.1: Piloted premixed jet burner (PPJB) schematic and cutaway with dashed lines showing the lower bounds of the computational domain. All measurements are in mm.

1500K respectively. A fuel mixture of 20% hydrogen and 80% ethylene by mole with air at ϕ=0.55 is used to provide a temperature of T_{coflow}=1600K. The coflow flames are stabilized on a perforated plate (outer diameter of 203 mm) with 1800 x 1.52 mm holes. The cold flow exit velocity before the plate is 0.7 m/s. All three streams are at the controlled laboratory air temperatures of 298K before being subsequently burned.

Experiments and simulations are performed at various jet Reynolds numbers,

$$\text{Re}_{\text{jet}} = \frac{U_{\text{jet}} D}{\nu}, \tag{7.1}$$

of 25,000, 37,500, 50,000, and 75,000 for four different fuels: methane, ethylene, n-heptane, and toluene. The equivalence ratio of the main jet was varied to enforce the same laminar flame speed, S_L=10 cm/s, corresponding to methane ϕ=0.59, adiabatic flame temperature T_{ad}=1649K; ethylene ϕ=0.48, T_{ad}=1543K; n-heptane ϕ=0.56, T_{ad}=1629K; and toluene ϕ=0.58, T_{ad}=1720K. Under these conditions, the laminar flame thicknesses of the different fuels are all close to 1 mm (less than 7% difference between the thinnest and thickest flames).

Table 7.1 provides a summary of the conditions investigated. These turbulent premixed flames are characterized by large turbulence intensities and high unburnt Karlovitz numbers. The flames are expected to fall in the broken/distributed reaction zone regime in the typical Peters/Borghi regime diagram, as shown in Fig. 7.2.

U_{jet} (m/s)	Re_{jet}	$\frac{u'}{S_L}$	$\tau_t = \frac{u'}{L_{\text{int}}}$ (ms)	$\frac{L_{\text{int}}}{l_F}$	τ_η (ms)	Ka_u	Ka_δ	$\text{Da}=\frac{\tau_t}{\tau_f}$	Re_t
68.5	25000	65	0.88	7.1	0.0153	524	12	0.0314	3037
100	37500	104	0.48	6.7	0.0071	1132	25	0.0173	4564
133	50000	157	0.32	6.3	0.0039	2079	48	0.0115	6405
200	75000	252	0.18	5.5	0.0018	4533	104	0.0063	9074

Table 7.1: Conditions of the experiments and simulations performed. The turbulence intensity and integral length scale are evaluated from the PIV measurements on the centerline at x/D=15. Flame properties of methane/air are used to compute the Karlovitz and Damköhler numbers.

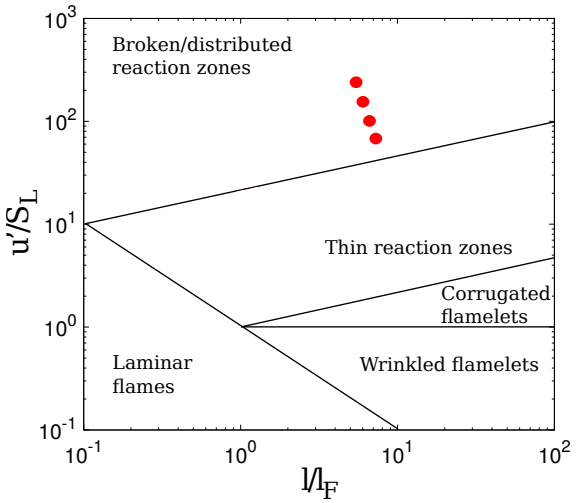

Figure 7.2: Regime diagram showing the present premixed jet flames.

7.2 Experimental approach

The experimental approach is reviewed here for completeness. Experiments were performed by collaborators at the University of Southern California. The author of this thesis did not take part in the experimental investigation.

7.2.1 Fuel vaporization system

A new fuel vaporization system was designed based on existing technology developed for heavy hydrocarbon investigations in laminar flames [47, 49]. This system has a much higher flowrate capable of fully vaporizing up to 20 mL/min of liquid fuel with air flow rates of up to 400 Standard litres per minute (SLPM). The system consists of inline heaters that preheat the air which issues into heated stainless steel chambers. The fuel is then injected in a crossflow configuration into the chambers as a fine mist of droplets from the tip of a Meinhardt liquid nebulizer [49]. The fuel is held in a Chemyx syringe and the flow rate controlled with a high accuracy Nexus syringe pump. Special care has been taken in order to avoid hot spots that can cause fuel decomposition and cold spots that can cause fuel condensation throughout the flow system [47]. The gaseous flow rates are controlled accurately using sonic nozzles.

7.2.2 CH* luminosity

Flame height H_{fl} is commonly used to compare flames in Bunsen and jet burner configurations and will be the main metric here to compare between fuels. For each flame, 100 images of the CH* luminosity are taken using a filter centered at 434 nm with a bandwidth of 17 nm to capture the primary emittance band from CH* which peaks around 431 nm. These images are taken with an Andor Zyla camera using an exposure time of 200 ms and then averaged together. H_{fl} is defined as the location where the line-of-sight chemiluminescence of the flame brush drops to a quarter of the maximum value along the jet centerline, not accounting for the luminosity from the pilot. The error bars on these measurements are $\pm 1D$.

7.2.3 Particle Image Velocimetry (PIV)

A high power Q-switched frequency-doubled laser (Quantel Brilliant Twins) generates light at 532 nm and expands using a plano-cylindrical lens (Thorlabs) into a thin sheet through the jet centerline at 10 Hz. The jet is seeded with 0.3-1 μm aluminum oxide particles that survive the flame. 500 statistically independent coupled Mie scattering images are taken with three "stitched" high resolution SCMOS

cameras (Andor Zyla 5.5) focalized with a F85mm/2.8D Nikkon lens in order to find the velocity field along the entire height of the jet. A laser-line filter at 532 nm removes the flame luminosity signal. Inter-frame times range between 1 μs-20 μs, depending on U_{jet} and the average velocity at the location of interest. The image couples have a resolution of 57.9 μm/pixel and are post-processed with the Davis Flowmaster software (LaVision Research Inc.) with decreasing interrogation window sizes of 64x64 pixels then 16x16 pixels with 50 percent overlap between windows and then averaged to obtain the mean and RMS velocity profiles. Vectors with a peak ratio of less than 1.05 are removed and the universal outlier detection method is used for spurious vector removal.

PIV measurements at 1 mm above the burner surface (boundary conditions) are taken with a finer resolution of approximately 9 μm/pixel using one SCMOS camera and a F200mm/4D Nikon lens. All three streams are seeded simultaneously with tracer particles. A separate Δt is used for the central jet and the pilot/coflow since the exit velocity of the central jet is significantly greater than the pilot and coflow streams. For this data set, 1000 statistically independent images are averaged.

The PIV uncertainty of the jet is dependent on U_{jet} and is estimated to be $\pm 0.05 U_{\text{jet}}$. PIV measurements in the coflow and pilot have a 10% relative uncertainty due to a lower particle seeding density.

7.2.4 Temperature measurements

Temperature measurements along the centerline are taken with a ceramically-shielded thermocouple (Omega, Inc) and corrected for radiation. The thermocouple tip, 200μm in diameter, is inserted into the flame perpendicular to the incoming flow with approximately 1 mm of the leads exposed. The thermocouple measurements have an uncertainty of $\pm$50K everywhere except at the interface between flows. There, the uncertainties reach $\pm$100K due to oscillations in the measured temperature values.

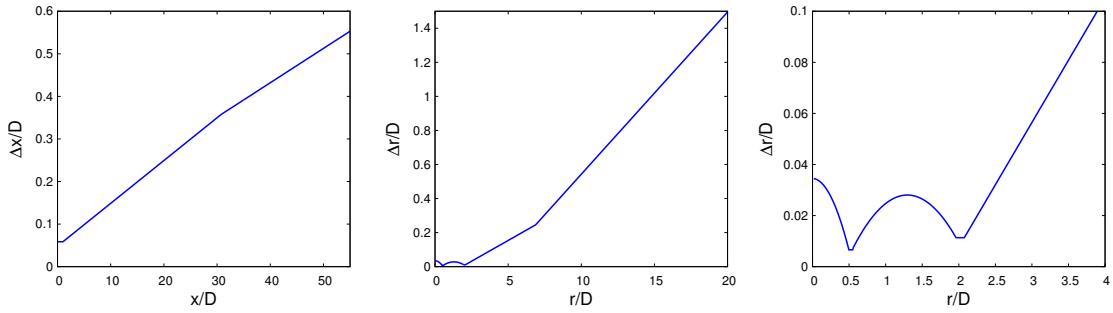

(a) axial (b) radial (c) radial, centerline region

Figure 7.3: Axial and radial spacings for the baseline LES grid.

7.3 Numerical approach

7.3.1 Flow configuration

The size of the computational domain (the lower bound of which is illustrated on Fig. 7.1) is selected to be 0.35m $\times$0.13m $\times 2\pi$ in the axial, radial, and azimuthal directions, respectively. The discretization strategy is similar to that of previous investigations of piloted turbulent jet flames [24, 116]. The grid in the axial direction is finest at the burner exit and stretched downstream. The radial direction uses a non-uniform distribution with two hyperbolic tangent functions to concentrate the points in the shear layers between the different streams. The grid is stretched away from the walls in each stream. The azimuthal direction is discretized with equally spaced points.

The baseline grid has a total 3.28M grid cells. There are 256, 200, and 64 points in the axial, radial, and azimuthal directions, respectively. This corresponds to a resolution ranging from $\Delta/l_F \approx 0.5$ close to the burner exit to $\Delta/l_F \approx 4$ far downstream. The grid size with respect to the Kolmogorov scale in the unburnt gases is $\Delta/\eta_u \approx 30$ for the lowest Reynolds number case to $\Delta/\eta_u \approx 100$ for the highest Reynolds number case. The grid spacings in the axial and radial directions are shown in Fig. 7.3 and the grid itself is shown in Fig. 7.4.

7.3.2 Chemistry tabulation

Following the conclusions of Chapter 6, a tabulated chemistry approach using a presumed PDF is used to perform the present LES. All thermodynamic and flame properties are tabulated using the

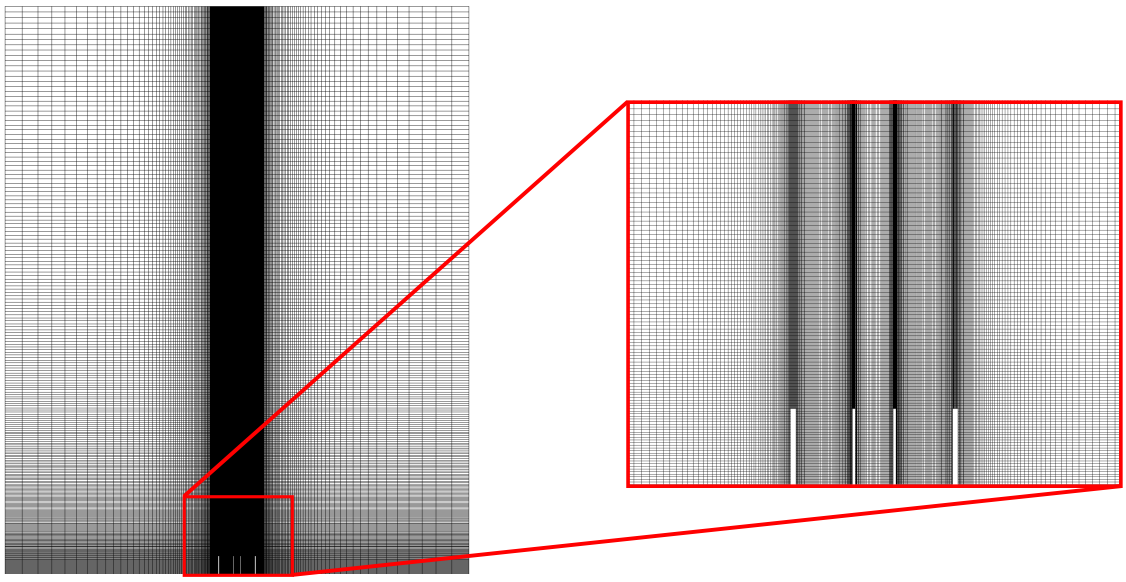

Figure 7.4: Baseline grid used in the Large Eddy Simulations. Inset shows close-up of the burner exit.

filtered progress variable, $\tilde{c}$, its variance, c_v, and the filtered mixture fraction, $\tilde{Z}$, from the solution of one-dimensional, unstretched, laminar premixed flames (i.e. flamelets) [42, 110, 53]. The progress variable is defined as the sum of H_2O, H_2, CO, and CO_2 mass fractions. The mixture fraction is used as an additional tabulation variable to capture mixing/dilution effects between the main jet, pilot, and coflow streams.

The effects of differential diffusion on the chemical source term are taken into account by scaling the laminar source term $\dot{\omega}_{c,\mathrm{lam}}$ by a burning efficiency as discussed in Section 6.5.2. The burning efficiency is estimated from the previous DNS (see Fig. 6.7) and varies with the Karlovitz number. This scaling is only applied to the *n*-heptane and toluene flames. No significant reduction in the burning rate is expected for methane and ethylene since their Lewis numbers are close to unity.

A new chemistry table is generated for each fuel considered by combining individual flamelets with various compositions. While the experimental setup involves three different fuels (one for each stream), the present chemistry tables only consider two. The main jet is represented by a fuel/air flamelet at the given equivalence ratio (for instance, *n*-heptane/air at ϕ=0.56); the pilot stream is represented by a flamelet of methane/air at stoichiometry; and the coflow is represented by a flamelet of lean fuel/air mixture (same fuel as the main jet) which yields the same burnt temperature as the

experimental coflow temperature. The mixture fractions for these three flamelets are evaluated in the unburnt gases using

$$Z = Z_{st} + (1 - Z_{st})(Y_{\mathrm{CH_4}} + Y_{\mathrm{Fuel}}) - Z_{st}\frac{Y_{\mathrm{O_2}}}{0.232} \tag{7.2}$$

and are used as inlet values for the three corresponding streams. Additional flamelets at intermediate mixture fractions are used to populate the table. These flamelets are computed using FlameMaster [84] and the detailed mechanism CaltechMech [12]. This chemical model contains 174 species and 1896 reactions (forward and backward counted separately) and has been validated extensively for all present fuels [13, 76].

These flamelets are filtered with different filter widths, and the filtered fields are then tabulated against the filtered progress variable $\tilde{c}$, its variance c_v, and the filtered mixture fraction $\tilde{Z}$ [40, 75, 71]. This corresponds to the FLF-PDF discussed in Chapter 6. The variance of Z is neglected, and the variance of the progress variable is obtained in the LES using an algebraic model [83, 9]. The resulting flamelet library is discretized with $200 \times 100 \times 200$ grid points in the $\tilde{c}$, c_v, and $\tilde{Z}$ directions, respectively.

7.3.3 Boundary conditions

Inlet boundary conditions are specified for the fuel, pilot, and coflow streams. Constant Dirichlet boundary conditions are used for the scalars. A time-dependent Dirichlet boundary condition is used for the velocity in the fuel stream (main jet). The turbulent velocity profiles are extracted from a separate, fully-developed pipe flow simulation described below. The velocity profiles for the pilot and coflow streams are considered uniform in space and time.

The tabulated chemistry approach requires values of $\tilde{c}$ and $\tilde{Z}$ at the inlets to impose the desired temperature and gas composition. The values are summarized in Table 7.2.

	CH_4		C_2H_4		N-C_7H_{16}		A_1-CH_3	
Scalar	$\tilde{c}$	$\tilde{Z}$	$\tilde{c}$	$\tilde{Z}$	$\tilde{c}$	$\tilde{Z}$	$\tilde{c}$	$\tilde{Z}$
Main jet	0.0	0.0317	0.0	0.315	0.0	0.0357	0.0	0.0419
Pilot	0.266	0.0549	0.266	0.0549	0.266	0.0549	0.266	0.0549
Coflow	0.145	0.0289	0.132	0.0299	0.143	0.0317	0.142	0.0344

Table 7.2: Progress variable and mixture fraction inlet values used with the different fuels to achieve desired composition and $T_{\text{coflow}} = 1500$K.

7.3.4 Turbulent pipe flow

Separate, fully-developed periodic pipe flow simulations are performed to generate the time history of the turbulent inlet velocity profile of the main jet. Simulations are performed for each of the experimentally measured axial mean bulk velocities. Constant density, non-reacting flow is considered with the density and viscosity values of the fuel/air mixture at the unburnt temperature.

The domain is periodic in the stream-wise (axial) direction with a length $10D$. The axial diretion is discretized uniformly with 128 points. The azimuthal direction is discretized uniformly using 64 points. The radial direction is discretized with 64 to 96 points (depending on the Reynolds number) and is stretched towards the pipe centerline using a hyperbolic tangent function with a stretching rate of 2.8. This ensures adequate resolution of the near-wall region.

The same LES closure models used in the turbulent flame LES are used for the pipe flow simulations. The simulations are initialized with a parabolic profile superimposed with random perturbations. After the initial transient, turbulent velocity profiles are recorded over 0.3 seconds in physical time.

7.4 Numerical validation

Boundary conditions at the jet exit are discussed first to assess the consistency between experiments and simulations. They are followed by comparison of the downstream development of the turbulent jet and investigation of the effect of grid resolution. This is done for the methane/air flame at Re_{jet}=50,000 and T_{coflow}=1500K.

7.4.1 Boundary conditions

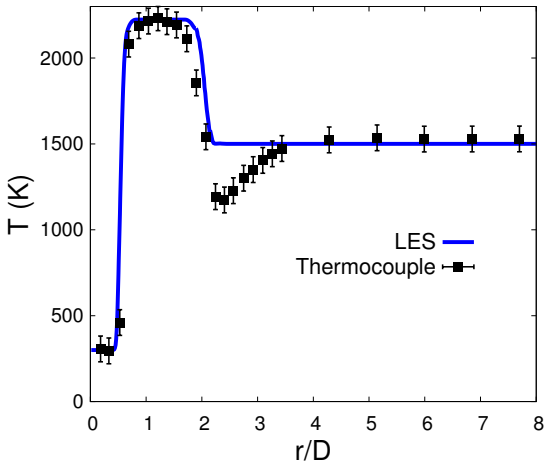

Figure 7.5: Comparison of experimental and numerical temperature profiles at $x = 1$ mm above the jet exit.

As shown in Fig. 7.5, thermocouple measurements indicate that the temperature at the burner exit on the centerline stays close to 298K even with the pilot and coflow ignited. The temperature rises sharply in the pilot and peaks around the T_{ad} of stoichiometric methane/air at 2250K. The temperature then lowers down to reach a constant value of 1500K in the coflow. The numerical and experimental temperature profiles match reasonably well. The dip in temperature between the pilot and the coflow (missing in the simulations) can be attributed to conduction heat transfer from the hot coflow to the pilot nozzle which was not accounted for in the simulations. In a similar configuration, Chen and Ihme [24] showed that this difference in temperature near the burner exit did not affect the downstream evolution of the flame.

Next, the velocity profiles at the jet exit (1 mm above the exit) are compared in Fig. 7.6. The measured velocities on the left and right sides of the burner appear to be reasonably symmetric and consistent. The numerical simulations present a flatter profile with a sharper drop-off, suggesting that the experimental pipe flow is not fully turbulent (Fig. 7.6a). The difference in jet velocity profiles results in different shear layers close to the burner exit. This is consistent with the discrepancies in RMS velocity (u') and entrainment of the pilot (Fig. 7.6b).

In order to assess the effects of boundary conditions, additional simulations were performed by

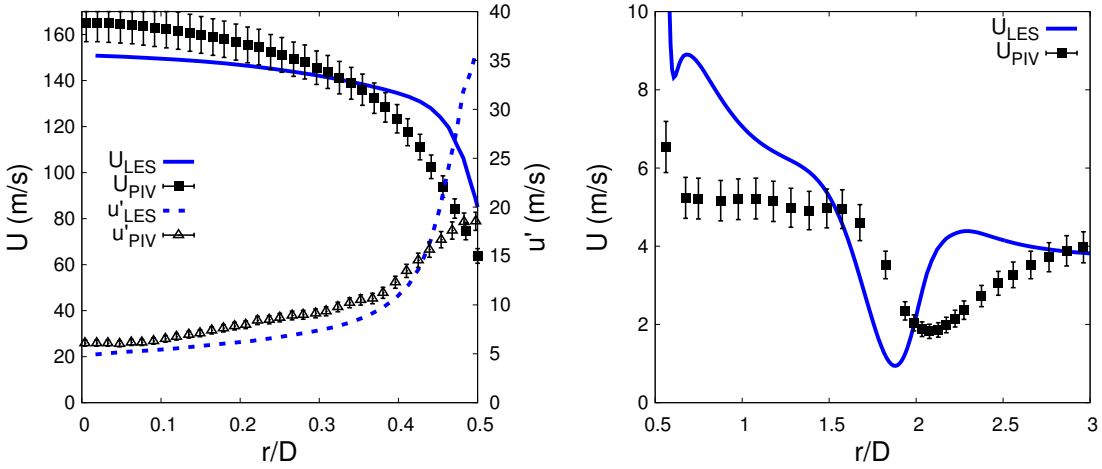

(a) Jet - Axial velocity

(b) Pilot/coflow - Axial velocity

Figure 7.6: Comparison of the velocity profiles measured experimentally and predicted numerically (with fully-turbulent inflow) at $x = 1$ mm above the jet exit.

rescaling the turbulent pipe flow profile with the mean experimental profile. No changes were made to the imposed velocity in the pilot and coflow. Comparison with the previous fully turbulent inlet and experiments are shown in Fig. 7.7. Enforcing the experimentally-measured mean profile in the jet stream leads to a better agreement between rms velocities as well as pilot mean axial velocities.

The effect of these differences in inlet boundary conditions on the downstream development of the jet are investigated in Section 7.4.2.

7.4.2 Jet development

With the boundary conditions assessed, the next step is to investigate the downstream evolution of the turbulent reacting jet. This is done first by comparing mean ($\bar{U}$) and RMS velocity (u') profiles along the jet centerline. Figure 7.8a shows a reasonable agreement between experiment and simulation as the centerline velocity shows the same general decay in mean velocity with a corresponding increase in RMS velocity. This is typical of momentum spreading radially outward as the axial distance increases. The radial profiles of mean and rms velocity upstream show similar jet spreading behavior as seen in Figs. 7.8b and 7.8c. The LES mean radial profiles are slightly wider with higher RMS velocity, a behavior which remains consistent further downstream.

The impact of the jet boundary conditions on the downstream development is investigated by

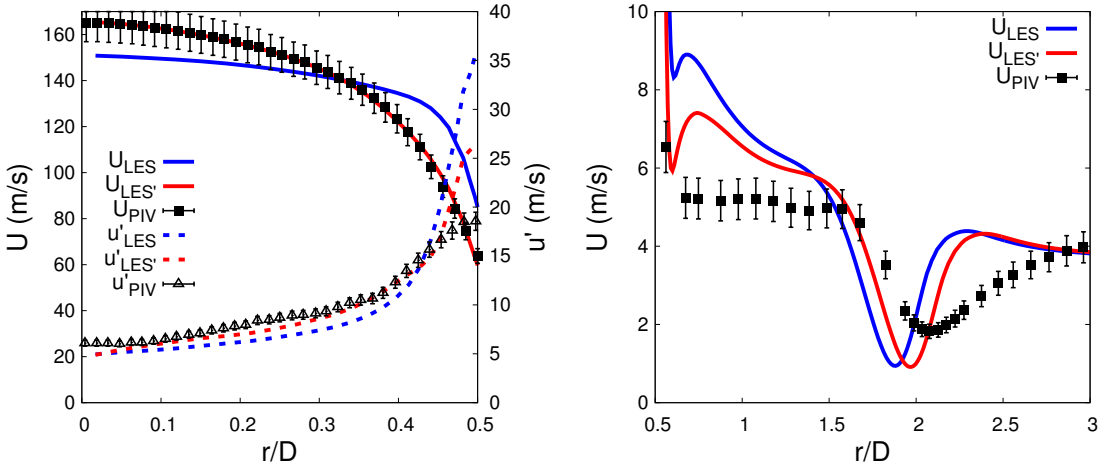

(a) Jet - Axial velocity

(b) Pilot/coflow - Axial velocity

Figure 7.7: Comparison of the velocity profiles measured experimentally and predicted numerically (LES′ with experimental mean inflow in red) at $x = 1$ mm above the jet exit.

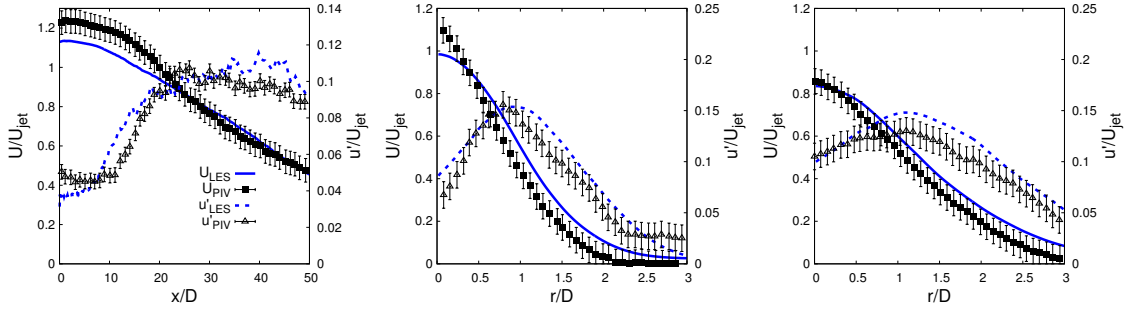

(a) Centerline

(b) $x/D = 15$

(c) $x/D = 25$

Figure 7.8: Axial (left) and radial (center and right) profiles of mean $\bar{U}$ and rms velocities u'. Fully-turbulent pipe flow imposed at the jet inlet.

comparing the profiles obtained when imposing the experimentally-measured mean flow at the jet inlet. As shown in Fig. 7.9, imposing the experimental profile improved the prediction of the mean centerline velocity close to the jet exit but doesn't significantly affect the velocity profiles 15 and 25 diameters downstream of the burner exit. This indicates that the downstream development of the jet isn't very sensitive to small variations in the inlet conditions.

7.4.3 Grid resolution

Grid resolution is assessed by performing simulations with different grids. Starting from the baseline grid described previously (labelled "grid1"), the grid resolution is doubled in each direction separately

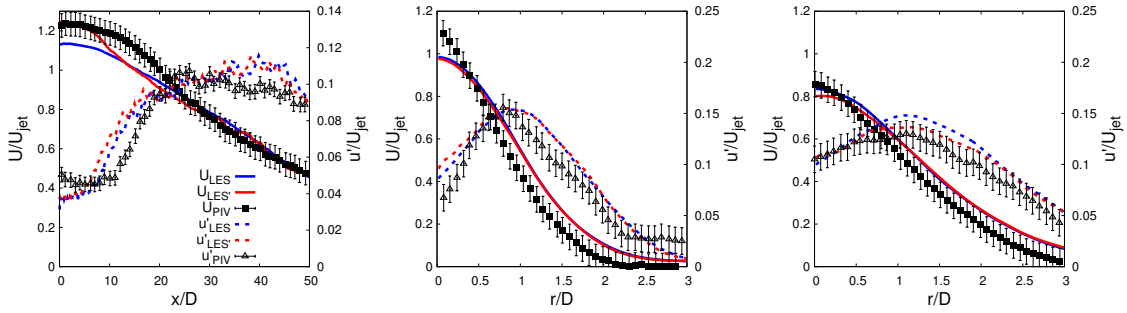

(a) Centerline (b) $x/D = 15$ (c) $x/D = 25$

Figure 7.9: Axial (left) and radial (center and right) profiles of mean $\bar{U}$ and rms velocities u'. Experimentally-measured mean flow imposed at the jet inlet for the LES$'$ case in red.

(grids labelled according to Table 7.3). The effects of grid resolution are assessed by comparing velocity profiles both close to the jet exit and further downstream.

Mesh	nx	nr	nz
Grid1	256	200	64
Grid2	512	200	64
Grid3	256	400	64
Grid4	256	200	128
Grid5	512	400	128

Table 7.3: Different LES grids used to assess effect of grid resolution.

Figure 7.10 shows the velocity profiles closed to the jet exit obtained with the different grids. No difference is observed on the mean jet profile since the experimental profile is imposed in all cases. The rms axial velocity is in better agreement in the shear layer between the jet and coflow ($r/D = 0.5$) with the grids refined in the axial direction (grid2 and grid5). This leads to a slightly better prediction of the entrainment, as seen from the pilot axial velocity in Fig. 7.10b.

Figure 7.11 shows the axial velocity profiles on the centerline and at two locations downstream of the jet exit. The effect of the grid resolution on the downstream evolution of the jet is marginal. All grids predict very similar velocity profiles at $x/D = 15$ and $x/D = 25$. This suggests that, while differences are observed in the shear layers close to the jet exit, the baseline grid resolution is sufficient to adequately capture the downstream development of the jet. Therefore, all subsequent simulations investigating fuel and hydrodynamic effects on flame height are performed using the baseline grid.

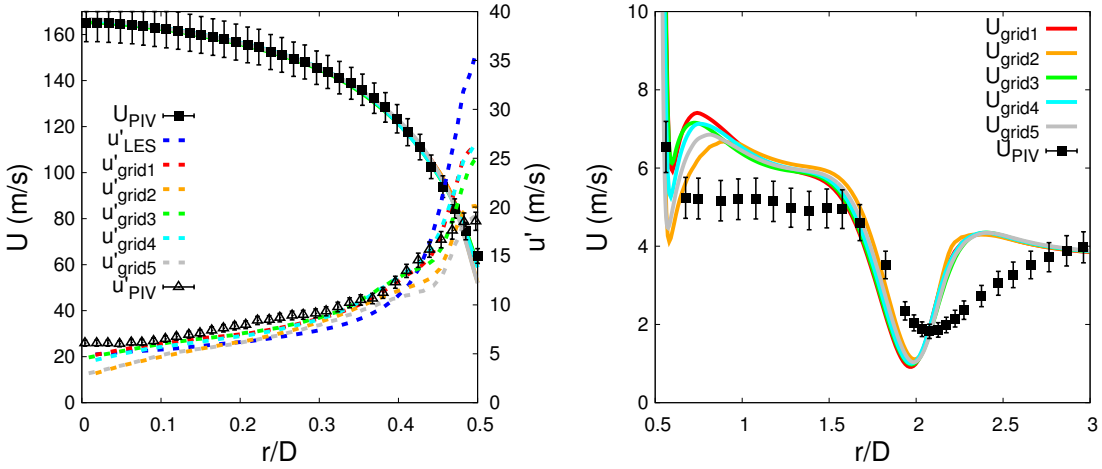

(a) Jet - Axial velocity

(b) Pilot/coflow - Axial velocity

Figure 7.10: Comparison of the velocity profiles measured experimentally and predicted numerically with different grids (with experimental mean inflow) at $x = 1$ mm above the jet exit.

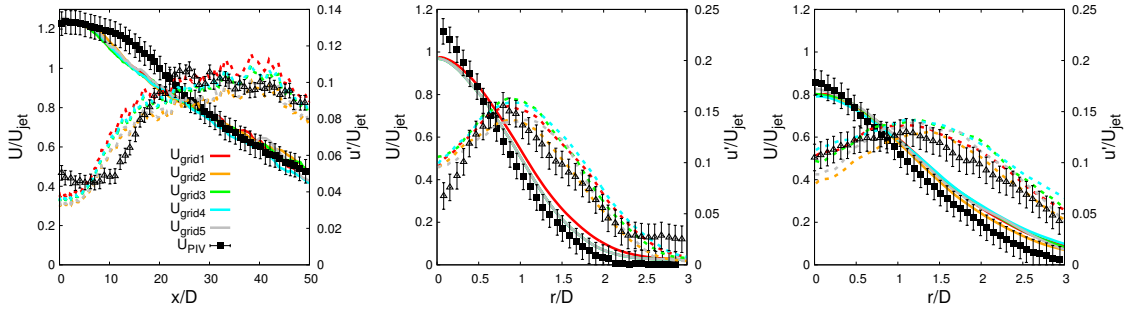

(a) Centerline

(b) $x/D = 15$

(c) $x/D = 25$

Figure 7.11: Axial (left) and radial (center and right) profiles of mean $\bar{U}$ and rms velocities u' obtained with different grids. Experimentally-measured mean flow imposed at the jet inlet.

7.5 Global fuel effects

The stability of flames in the original PPJB configuration [32] was observed to be influenced by ϕ, $\mathrm{Re}_{\mathrm{jet}}$, and T_{coflow}. In this study, ϕ is adjusted to enforce a constant S_L as baseline for comparison between fuels. $\mathrm{Re}_{\mathrm{jet}}$ and T_{coflow} are then varied to investigate possible fuel effects on the flame height, H_{fl}. While a single global quantity, H_{fl} encompasses both hydrodynamic and chemical effects.

First, instantaneous and averaged fields from the simulations are shown to provide the reader with a visual overview of the flames. Then, experimental results are reviewed to highlight the effects of coflow temperature and Reynolds number on the flame heights. Finally, numerical results are compared to experiments at a fixed coflow temperature.

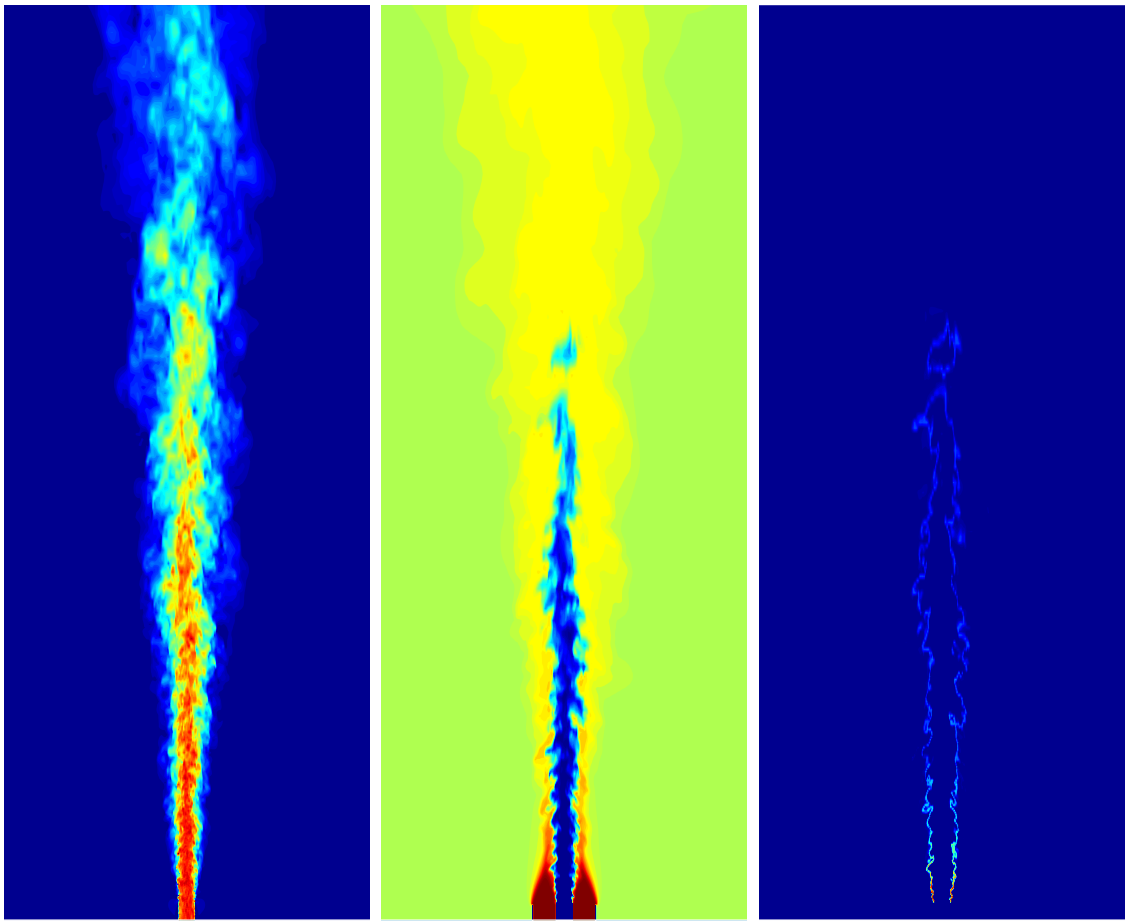

(a) Axial velocity magnitude (b) Progress variable (c) Progress variable source term

Figure 7.12: Instantaneous 2D contours from methane/air flames at $\mathrm{Re_{jet}} = 50,000$ and $T_{\mathrm{coflow}} = 1500\mathrm{K}$. Ranges are [0, 180] m/s for the velocity, [0, 0.27] for the progress variable, and [0, 1200] (1/s) for $\dot{\omega}_c$.

7.5.1 Instantaneous and averaged fields

Instantaneous fields of axial velocity, progress variable, and progress variable source term are shown in Fig. 7.12 for the CH_4/air flame at $\mathrm{Re_{jet}} = 50,000$ and $T_{\mathrm{coflow}} = 1500\mathrm{K}$.

Time-averaged fields of progress variable for the different Reynolds are shown in Fig. 7.13. This comparison highlights the effect of the increasing jet velocity on the progress variable field. As jet velocity is increased, entrainment of the outer streams is enhanced. This is visible in the "neck-region" where the pilot stream is depleted and replaced by the outer coflow. This region moves closer to the burner exit as the velocity is increased.

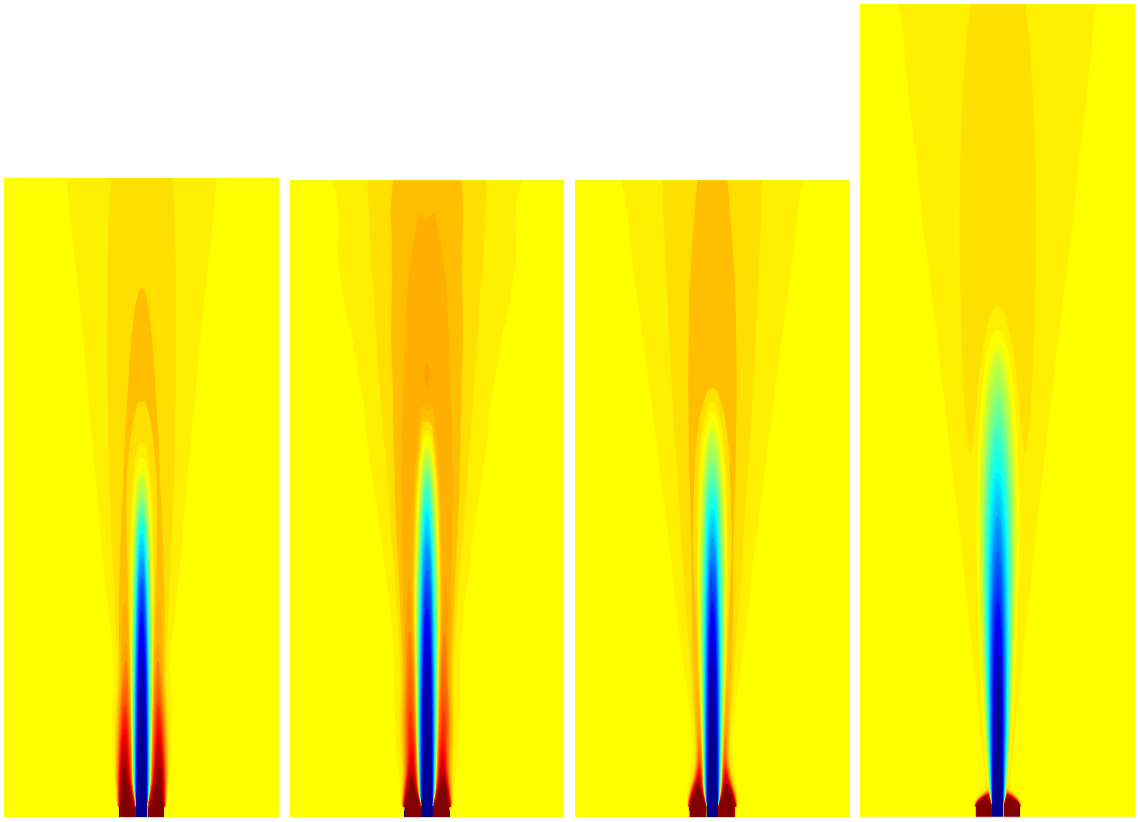

(a) $\mathrm{Re_{jet}} = 25,000$ (b) $\mathrm{Re_{jet}} = 37,500$ (c) $\mathrm{Re_{jet}} = 50,000$ (d) $\mathrm{Re_{jet}} = 75,000$

Figure 7.13: Time-averaged 2D temperature contours from methane/air flames at $T_{\mathrm{coflow}} = 1500$K and different Reynolds numbers. Temperature range is [298, 2200] for all cases. A longer grid is used for the $\mathrm{Re_{jet}} = 75,000$ case.

7.5.2 Flame height

In the present study, the main comparison metric between simulations and experiments to investigate fuel and hydrodynamic effects is the flame height. As mentioned previously, H_{fl} is defined as the location where the line-of-sight chemiluminescence of the flame brush drops to a quarter of the maximum value along the jet centerline, not accounting for the luminosity from the pilot. This is illustrated in Fig. 7.14 for the methane/air flame at $\mathrm{Re_{jet}} = 50,000$ and $T_{\mathrm{coflow}} = 1500$K.

7.5.3 Experimental T_{coflow} effects on H_{fl}

First, the effects of heat loss/heat gain were investigated experimentally by varying T_{coflow}. Three cases were considered: T_{coflow}=1400K, 1500K, and 1600K. When T_{coflow} is lower than the adiabatic

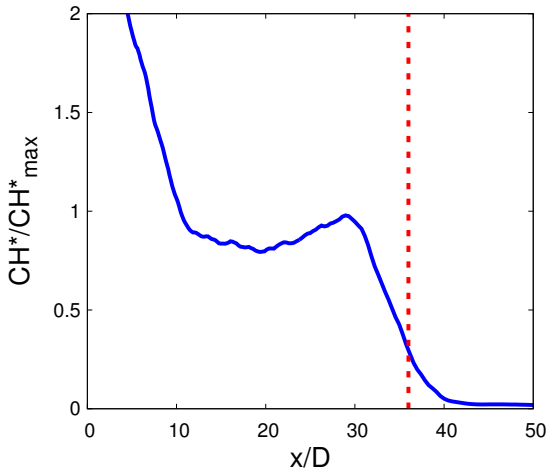

Figure 7.14: Time-averaged line-of-sight integrated centerline chemiluminescence profile from the methane/air flame at $\mathrm{Re_{jet}} = 50,000$ and $T_{\mathrm{coflow}} = 1500\mathrm{K}$. The dashed red line indicates the flame height.

temperature of the main jet, $T_{\mathrm{ad,jet}}$, the flame suffers heat losses (case 1); when T_{coflow} is higher, the flame is super-adiabatically heated (case 2). S_T for the first (resp. second) case is expected to be lower (resp. larger), resulting in a taller flame (resp. shorter flame). Figure 7.15 shows experimental measured flame heights, H_{fl}, plotted against the heat loss experienced by the jet, $T_{\mathrm{ad,jet}} - T_{\mathrm{coflow}}$. The expected behavior is confirmed as H_{fl} increases with increasing $T_{\mathrm{ad,jet}} - T_{\mathrm{coflow}}$. The flame heights of the heavier hydrocarbon/air flames (n-heptane and toluene) align nicely when plotted against $T_{\mathrm{ad,jet}} - T_{\mathrm{coflow}}$. However, fuel-dependent differences are observed. Most notably, methane flames are consistently longer while ethylene flames are consistently shorter.

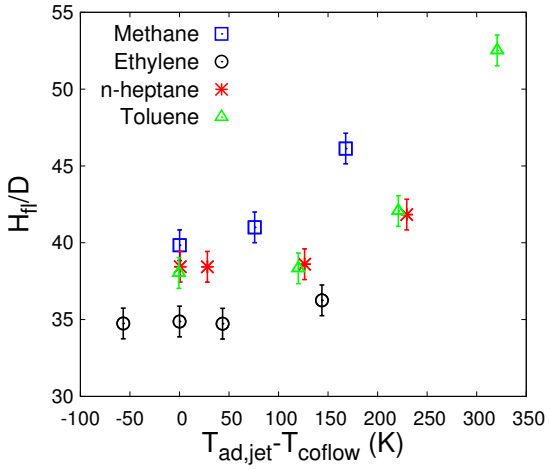

Figure 7.15: Effect of T_{coflow} at a fixed $\mathrm{Re_{jet}}$ on the experimentally-measured flame heights.

7.5.4 Experimental $\mathbf{Re_{jet}}$ effects on $H_{\mathbf{fl}}$

Next, the effects of $\mathrm{Re_{jet}}$ are shown in Fig. 7.16. Now, all experiments were performed at adiabatic conditions ($T_{\mathrm{coflow}} = T_{\mathrm{ad,jet}}$) in order to remove the effects of heat losses. When U_{jet} (equivalently $\mathrm{Re_{jet}}$ in this case) is increased at a fixed S_L, the flame is expected to be longer as seen in the original PPJB experiments [32]. Making the crude assumption of a constant turbulent flame speed, S_T, along the time-averaged flame front and approximating the flame shape as a cone, the following scaling is expected:

$$\frac{H_{\mathrm{fl}}}{D} \approx \frac{U}{2S_T}. \tag{7.3}$$

This is the same scaling obtained in Bunsen flames [60]. This behavior is observed consistently for all fuels, as H_{fl} increases fairly linearly with $\mathrm{Re_{jet}}$. Seemingly, methane has the largest H_{fl}, ethylene has the smallest H_{fl}, and the rest of the fuels fall somewhere in between. More interestingly, all fuels but methane exhibit the same slope (within experimental uncertainties). While this linear increase suggests that the change in turbulent flame speed with Reynolds number is minor, such conclusions cannot be drawn solely from these measurements. The turbulent flame speed will not be constant along the flame surface and global flame height measurements do not provide enough information to characterize the evolution of the turbulent flame speed along the flame surface. This should be the subject of future work.

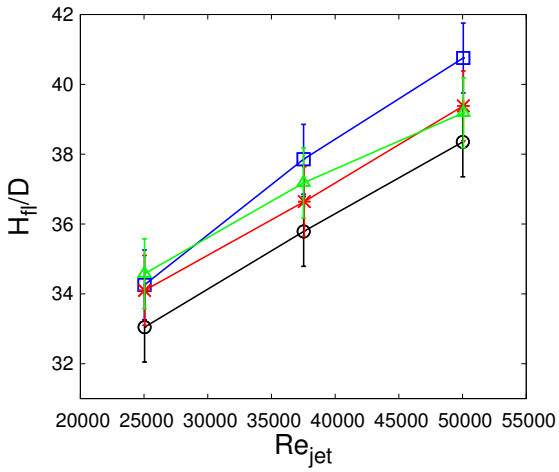

Figure 7.16: Effect of $\mathrm{Re_{jet}}$ at a fixed $T_{\mathrm{ad,jet}} - T_{\mathrm{coflow}}$ on the experimentally-measured flame heights.

7.5.5 Experimental and numerical comparison of H_{fl}

Since differences in H_{fl} were magnified with increasing $\mathrm{Re}_{\mathrm{jet}}$, simulations and experiments are compared at increasing $\mathrm{Re}_{\mathrm{jet}}$ (but not so high that H_{fl} can no longer be defined) of 25,000, 50,000 and 75,000 using a fixed coflow temperature of $T_{\mathrm{coflow}} = 1500$ K. While experiments were performed at varying T_{coflow}, the simulations were only performed at $T_{\mathrm{coflow}} = 1500$ K.

Without surprises, hydrodynamic effects represented by $\mathrm{Re}_{\mathrm{jet}}$ are well captured in the LES. Figure 7.17 shows flame heights against Reynolds number for the four fuels tested. As in the experiments, an approximately linear increase is observed.

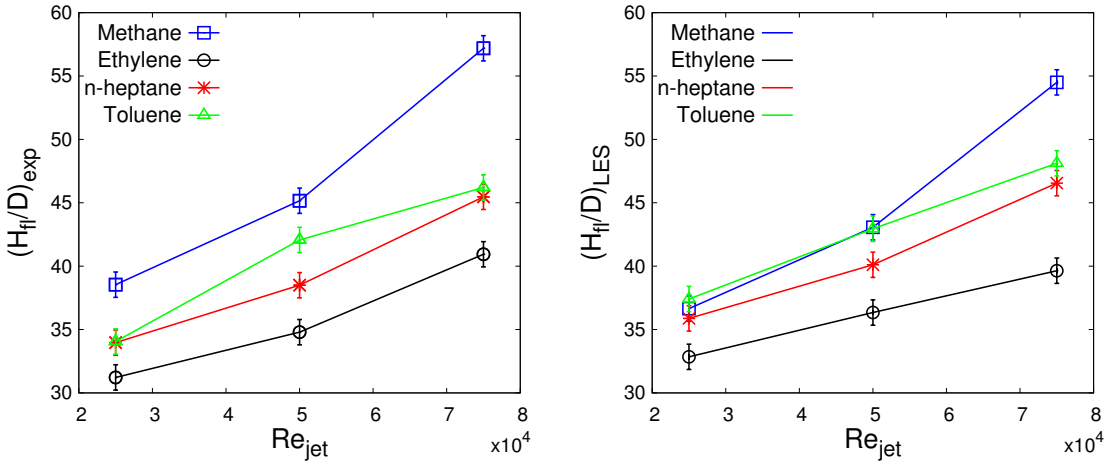

(a) Experiments (b) Large Eddy Simulations

Figure 7.17: H_{fl} at three different $\mathrm{Re}_{\mathrm{jet}}$ for T_{coflow}=1500K.

Finally, as shown in Fig. 7.18, predicted H_{fl} from the LES are within less than 10% of the experimental values, while the effects of Reynolds number amount to more than 30%. The experimental trends of longer flames for methane and toluene than *n*-heptane and ethylene are well reproduced by the simulations. These results are especially interesting given the assumption behind the combustion model used (Section 7.3.2), namely that the structure of the turbulent flame is the same as that of a laminar flame. This suggests that differences in flame lengths between fuels are due to different sensitivies to heat losses (mixing between main jet and coflow) and that this behavior is present in laminar flames.

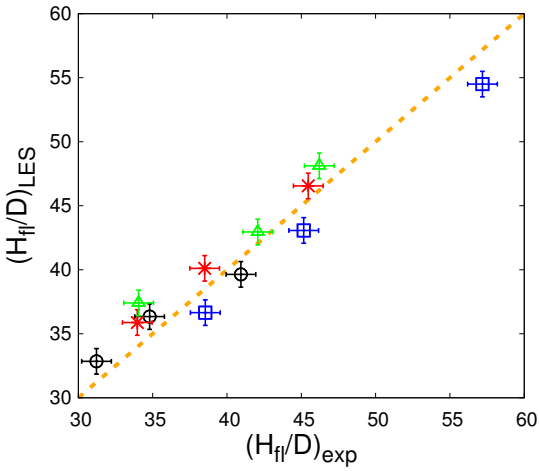

Figure 7.18: Comparison of H_{fl} predicted by the LES and measured experimentally at the three different $\mathrm{Re}_{\mathrm{jet}}$ for T_{coflow}=1500K.

7.6 Summary

The present study investigated fuel and hydrodynamic effects on piloted premixed jet flames. This investigation was carried out at a constant laminar flame speed to isolate these effects. The parameters varied include heat losses, jet Reynolds number, fuel molecular weight, and fuel chemical classification. LES were performed matching the experimental geometry and conditions, and were validated against 2D PIV measurements.

Flame heights defined based on CH* chemiluminescence were used as a metric to compare the different flames. Experimental results indicated that small amounts of heat loss may play a significant role on the jet reactivity as the flame heights scaled with the heat loss from the jet. However, differences between flames with different fuels could still be seen in the absence of heat loss, and these differences were magnified at higher Reynolds numbers. Particularly, methane flames were consistently taller and ethylene flames consistently shorter while other fuels had approximately the same heights. LES reproduced the experimentally observed trends in global flame heights (effects of heat losses and Reynolds number) accurately.

It is important to note that the present LES were performed with a tabulated chemistry approach which assumes that the local flame structure is that of one-dimensional unstretched laminar flames. Hence, fuel and chemistry effects which are not present in laminar flames cannot be captured by the

present approach.

Therefore, the good agreement between simulations and experiments suggests that fuel and chemistry effects in the present turbulent flames are limited to effects present in laminar flames. This is in agreement with the observations made in Chapter 4 from canonical DNS performed with different fuels.

Chapter 8

Conclusions

Direct Numerical Simulations of high Karlovitz number turbulent premixed flames have been performed. The transition from the thin to distributed reaction zones regimes was investigated and different hydrocarbon fuels and chemical models were compared. Effects of integral length scales were investigated. DNS fields were filtered to gain insight into combustion modeling for LES. Finally, LES of experimentally-studied flames were performed.

8.1 Karlovitz number effects

A series of direct numerical simulations of premixed n-heptane/air flames at different Karlovitz numbers have been performed using detailed chemistry. Different unburnt temperatures and turbulence intensities were used and their effects on the flame structure and chemical source terms were investigated. Differential diffusion effects have been systematically isolated by performing simulations with both non-unity and unity Lewis numbers.

First, the increase in turbulence intensity suppressed differential diffusion effects on the flame structure. However, differential diffusion effects on the chemical source terms were still present even at high Karlovitz numbers. The consequences were lower mean fuel consumption and heat release rates in the non-unity Lewis number simulations. As turbulence intensity at the reaction zone was increased (i.e. increase in Ka_δ), these rates are ultimately approaching the respective unity Lewis number values.

Second, the transition to distributed burning was highlighted by measuring the width of the

reaction zone in physical and temperature space. It was shown that the reaction zone's physical width increases with the reaction zone Karlovitz number. However, even at high Karlovitz numbers ($\mathrm{Ka}_\delta \sim 100$), most of the reactions still occur in a thin reaction zone of a thickness comparable to that of a laminar flame.

Third, local extinctions and chemical source terms fluctuations were investigated and quantified through probability density functions at the temperature of peak reactions. Large fluctuations in fuel consumption rate were observed for both non-unity and unity Lewis number simulations, increasing with the reaction zone Karlovitz number.

Throughout the analysis, it was shown that the reaction zone Karlovitz number (evaluated with the appropriate Kolmogorov length scale) was the relevant parameter to characterize the interaction of small-scale turbulence on the chemical source terms. Simulations with similar unburnt Karlovitz numbers but different reaction zone Karlovitz numbers showed distinct fuel consumption and heat release rates.

8.2 Fuel and chemistry effects

Fuels, equivalence ratios, chemical models, and turbulent intensities were systematically varied in DNS of high Karlovitz flames. The analysis focused on turbulent flame speeds, chemical source terms, reaction zone surface areas, and geometry of the reaction zones. Differential diffusion effects have been systematically isolated by performing simulations with both non-unity and unity Lewis numbers.

First and foremost, in the absence of differential diffusion, all fuels still presented similar normalized turbulent flame speeds at a fixed reaction zone Karlovitz number. When differential diffusion effects were included, all fuels presented similar turbulent flame speeds, yet lower than their unity Lewis number counterparts. This is due to the above unity Lewis number of the present fuels. Enhanced burning velocities are expected for light fuels such as hydrogen. Second, distributions of tangential strain rate and curvature on the reaction zone surface were essentially the same when normalized by the Kolmogorov scales at the reaction zone, illustrating that chemistry and transport

effects do not alter the geometry of the reaction zone. Third, differential diffusion effects on the chemical source terms were present even at high Karlovitz numbers. In the unity Lewis number simulations, all fuels presented a mean fuel consumption rate close to the respective laminar value. In the non-unity Lewis number simulations, lower mean burning rates were observed. All three heavy hydrocarbon fuels (n-heptane, iso-octane, and toluene) presented those trends but the mean fuel consumption rate of the methane flame was higher, highlighting the importance of the fuel Lewis number.

In summary, fuel effects in the present high Karlovitz premixed flames were minor. Turbulent flame behavior can be predicted with the knowledge of only a few global laminar flame properties (S_L, l_F, δ_F, Le_i) and turbulence characteristics. Differential diffusion and changes in turbulence intensity at the reaction zone affect the turbulent flame speed significantly more than different fuels, equivalence ratios, and chemical mechanisms. This suggests the potential of reduced combustion models based on laminar flames, such as tabulated chemistry, to model high Karlovitz number premixed flames.

8.3 Integral length scale effects

Additional direct numerical simulations of premixed flames have been performed to investigate the impact of the integral length scale on the structure of the flame and on its propagation.

Two main observations were made with respect to the impact of the integral length scale. First, the turbulent flame surface area was found to be strongly affected by the large scales, increasing linearly with l/l_F. Second and in constrast, the chemical source terms (and thus the burning efficiency) were essentially unaffected by changes in the integral length scale *at a fixed* Ka_δ. This is particularly important as it confirms that the chemical source terms are controlled by the small turbulent scales ($\lesssim \delta_F$) and not the large scales.

The turbulent flame speed is thus affected by both large and small scales. The large scales modulate the flame surface area while the small scales primarily play a role in modulating the chemical source term (in the presence of differential diffusion) and locally broadening the reaction

zone (change in local scalar gradients).

8.4 Filtered chemical source term

DNS data obtained in this thesis was used to assess the effects of turbulence-chemistry interactions and differential diffusion effects on the sub-filter closure of the chemical source terms.

First, it was observed that filtered source terms from detailed chemistry and tabulated chemistry were in good agreement at sufficiently large filter widths ($\Delta \gtrsim l_F$) for both unity and non-unity Lewis number cases. This suggests that fluctuations in the chemical source terms observed in the detailed chemistry cases can be neglected in LES.

Second, it was shown using the concept of optimal estimators that a tabulation approach using $\tilde{c}$ and its variance, c_v, can predict accurately the filtered chemical source terms..

Third, predictions of the chemical source term from commonly assumed β-PDF and FLF-PDF models were compared to the filtered DNS. Both models predicted accurately the turbulent flame speed. This is an important result since accurate prediction of the burning velocity is of importance for many combustion devices.

Fourth, the possibility of using 1D laminar flames to generate the chemistry tables was discussed. It was shown that in the limit of high Karlovitz number, one-dimensional unstretched laminar flames accurately predict the mean progress variable production rate. For heavy hydrocarbon flames ($\mathrm{Le}_F > 1$) at moderate/high Karlovitz numbers, inclusion of strain/curvature effects in flamelet models is necessary to accurately predict the mean chemical source term.

These *a priori* results illustrate the potential of using simple tabulated chemistry approaches based on presumed PDFs for LES of premixed flames in the thin and distributed reaction zones regimes.

8.5 Large Eddy Simulations

Large Eddy Simulations of experimentally-studied piloted premixed jet flames were performed using the tabulated chemistry approach studied previously. The focus was on the investigation of fuel and hydrodynamic effects and the comparison of simulations and experiments.

Velocity profiles and flame heights were compared for different fuels and Reynolds numbers. The velocity profiles were in good agreement and were found to be roughly insensitive to the boundary conditions. The flame heights showed differences between fuels. Methane flames were consistently taller and ethylene flames were consistently shorter. LES predicted accurately the flame heights for the four fuels and three Reynolds numbers tested.

This validates *a posteriori* the conclusions of Chapter 6. Furthermore, since LES used a tabulated chemistry approach assuming a laminar flame structure, the agreement between simulations and experiments suggests that fuel and chemistry effects in the present turbulent flames are limited to effects present in laminar flames.

8.6 Limitations and future directions

The present study of fuel and chemistry effects considered only heavy hydrocarbon fuels with above unity Lewis numbers under thermo-diffusively stable conditions. It would be interesting to extend the analysis to thermo-diffusively unstable conditions, such as lean hydrogen/air flames. Thermo-diffusive instabilities have been shown in previous studies to affect chemical source terms as well as flame surface areas.

Compressibility effects were found to be negligible in the highest Karlovitz number flame (and thus highest Mach number) studied in this thesis. It would be interesting to further increase the Mach number into a regime where compressiblity effects may play a significant role. This includes, for example, flame propagation in closed channels. The compressible code developed in the context of this thesis has already been used successfully to simulate H_2/O_2 flames propagating in an obstructed channel [16]. High local Mach numbers (beyond the validity of the low-Mach number assumption)

were observed and different regimes of flame-turbulence interaction were identified.

The analysis of the filtered DNS focused on assessing common modeling assumptions for the filtered chemical source term. The closure of the sub-filter stresses should also be studied. These terms are known to be of importance, especially when using large filter widths, and appropriate model choices might improve simulations accuracies.

LES and experimental results were compared using only time-averaged velocity and flame height measurements. It would be interesting to compare time-resolved data in order to investigate stochastic effects and their influence on the global flame behavior. Additionally, comparison of species mass fractions and temperature could provide further assessment of the validity of the tabulated chemistry approach used in this work.

Appendices

Appendix A

Karlovitz number effects

A.1 Grid resolution

The grid spacing for all cases is chosen such that $\kappa_{max}\eta > 1.5$ everywhere in the domain, and is limited by the turbulence in the unburnt gases, where η is the smallest. In order to verify the quality of the solution, case B with twice the number of grid points per direction was performed for 13 eddy turnover times (limited by the cost of such a simulation). Figure A.1 compares the fuel burning rate statistics for the nominal (1408×128×128) and refined (2816×256×256) simulations. These differences are marginal for the purpose of the analysis made in this work. Since conditional means and standard deviations are moments of the probability density function, the fact that the pdfs are in excellent agreement indicates that the results would not change noticeably if the refined grid was used instead of the nominal grid. The conclusions are therefore grid independent.

A.2 Mixture-averaged viscosity

In an effort to reduce computational cost, a simplified formula for the evaluation of the mixture-averaged viscosity is preferred over the commonly used Wilke's formula [115]. In the present work, the mixture-averaged viscosity is computed using a similar approach to the mixture-averaged thermal conductivity [64]

$$\mu = \frac{1}{2}\left(\sum_{i=1} X_i\mu_i + \left[\sum_{i=1}\frac{X_i}{\mu_i}\right]^{-1}\right), \tag{A.1}$$

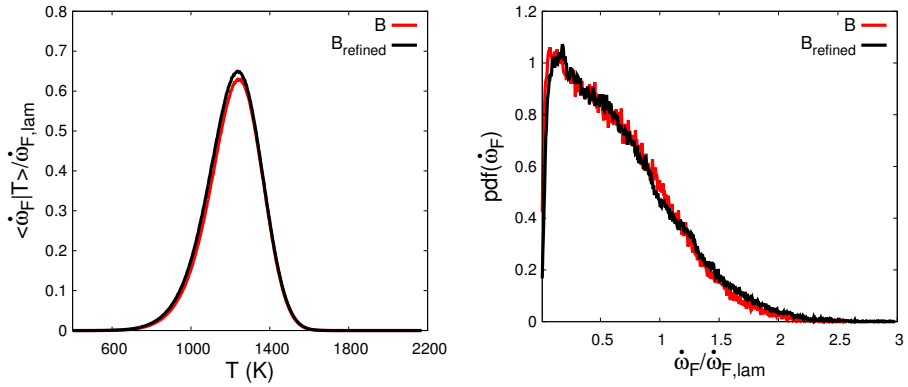

(a) Conditional mean (b) pdf of $\dot{\omega}_F$

Figure A.1: Conditional mean and probability density function of the normalized fuel consumption rates. The probability density function was taken at the corresponding temperature of peak fuel consumption.

where X_i is the species mole fraction and μ_i is the species viscosity. This formulation is linear in the number of species rather than quadratic, which is the case of the common implementation of Wilke's formula.

The mixture-averaged viscosities computed using both Wilke's formula and Eq. (A.1) are compared in Fig. A.2 in the case of the laminar n-heptane/air flame with $T_u = 298$K. The difference between the two methods is always less than 2%. For the present 35 species mechanism, evaluation of the mixture-averaged viscosity is 70 times faster using Eq. (A.1).

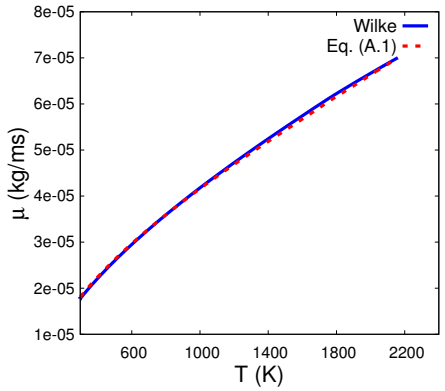

Figure A.2: Mixture-averaged dynamic viscosity of laminar n-heptane/air flame computed using Wilke's formula and Eq. (A.1).

A.3 Surface and volume weighting

Different methods can be used to compute conditional means and conditional probability density functions, among which are surface area weighting and volume weighting. Consider, for example, the computation of conditional means $<y|x>$ or probability density functions $\mathrm{P}(y|x)$. Surface area weighting consists of generating an isosurface at the given value of x and interpolating y onto the isosurface. The mean or probability is then computed by weighting the values of y by the corresponding face area. The creation of the isosurface and the interpolation often lead to an increase in computational cost. In contrast, in volume weighting, computational cells whose value of x are within a small range (bin) of the desired value are considered. The mean or probability is then computed by weighting the values of y by the corresponding cell volume. This method is simpler and computationally cheaper as it only requires binning the data. In the present study, surface area weighting is preferable in the context of model development. For example, a progress variable chemistry tabulation model requires the values of fluid properties and progress variable reaction rate on the progress variables isosurfaces.

The differences between the results obtained with each method are illustrated in Fig. A.3, on the conditional means of fuel consumption rate for case C. In addition to surface area and volume weighting, a third conditional mean was computed using a volumetric (by bin) approach but weighting the values of $\dot{\omega}_F$ by the local value of $|\nabla T|$. In the present simulations, it is observed that, in comparison with surface area weighting, volume weighting decreases the relative importance of large fuel consumption rate regions while increasing that of small fuel consumption rate regions. This results in a significantly lower conditional mean around the peak temperature. At the high turbulence intensities considered here, large temperature gradients are observed in the reaction zone (at high fuel consumption rates). Due to those large gradients, the isosurfaces of temperature get closer together. Thus, there are more isosurfaces in a bin for large fuel consumption rates compared to small fuel consumption rates (small temperature gradients). This is the cause of the decreased weight of large fuel consumption rate regions with volume weighting.

In contrast, volume weighting using the norm of the gradient of temperature gives an extremely

similar result to surface area weighting. It is thus possible to obtain surface area weighted conditional means and probabilities without creating isosurfaces and interpolating 3D fields. This approach was used throughout this work.

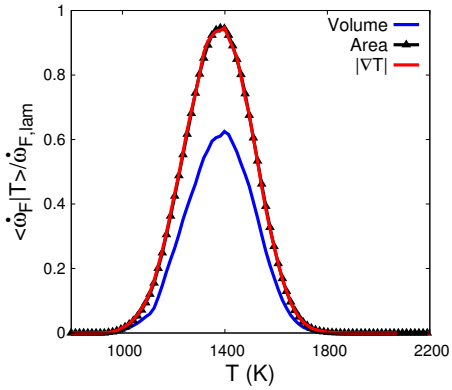

Figure A.3: Conditional means of fuel consumption rate of case C calculated using volume weighting, surface area weighting, and weighting by the norm of the gradient of temperature.

Appendix B

Compressibility effects

B.1 Numerical framework

B.1.1 Governing equations

The governing equations are the compressible Navier-Stokes, total energy, and species transport equations in conservative form:

$$\frac{\partial \rho}{\partial t} + \nabla \cdot (\rho \mathbf{u}) = 0, \tag{B.1}$$

$$\frac{\partial \rho \mathbf{u}}{\partial t} + \nabla \cdot (\rho \mathbf{u}\mathbf{u} + p) = \nabla \cdot \tau + \mathbf{f}, \tag{B.2}$$

$$\frac{\partial \rho e_t}{\partial t} + \nabla \cdot (\mathbf{u}\left(\rho e_t + p\right)) = \nabla \cdot \left(\lambda \nabla T + \sum_{i=1}^{N} h_i \mathbf{j}_i\right) + \nabla \cdot (\tau \cdot \mathbf{u}), \tag{B.3}$$

$$\frac{\partial \rho Y_i}{\partial t} + \nabla \cdot (\rho \mathbf{u} Y_i) = -\nabla \cdot \mathbf{j}_i + \rho \dot{\omega}_i. \tag{B.4}$$

In these equations, $\mathbf{u}$ is the velocity vector, ρ is the fluid density, p is the pressure, τ is the viscous stress tensor, $\mathbf{f}$ is the turbulence forcing term, e_t is the total energy, Y_i is the species mass fraction, $\dot{\omega}_i$ is the species production rate, $\mathbf{j}_i$ is the species diffusion flux, T is the temperature, λ is the

thermal conductivity, h_i is the species enthalpy. The species diffusion term is defined as:

$$\mathbf{j}_i = \rho D_i \frac{Y_i}{X_i} \nabla X_i - \rho Y_i \mathbf{u}_c, \tag{B.5}$$

where $\mathbf{u}_c$ is the correction velocity to ensure conservation of mass:

$$\mathbf{u}_c = \sum_{i=1}^{N} \rho D_i \frac{Y_i}{X_i} \nabla X_i. \tag{B.6}$$

D_i and X_i are the diffusion coefficients and mole fraction of species i. The total energy is $e_t = h - p/\rho + \frac{1}{2}\mathbf{uu}$ with $h = \sum_{i=1}^{N} h_i Y_i$, where h_i is the enthalpy of species n defined as $h_n(T) = \Delta h^0_{f,n} + h_{s,n}(T)$. The equation of state is that of an ideal gas:

$$p = \frac{\rho R T}{\bar{W}}. \tag{B.7}$$

B.1.2 Numerical framework

The governing equations are solved using a compressible formulation of the NGA code, implemented as part of this thesis. As in the low-Mach number formulation, the code uses a second-order accurate spatial discretization on a structured, staggered, cartesian grid (the scalars are stored at cell centers while velocities are stored at cell faces). The staggered grid configuration used with centered differencing and interpolation provides non-dissipative and discrete conservation of mass, momentum, and total energy. The third-order bounded QUICK scheme, BQUICK [45], is used as the transport scheme of the species to ensure that the scalars remain within their physical bounds.

The parts of the code that differ from the low-Mach formulation are described in the following subsections.

B.1.2.1 Evaluation of temperature

Since the system is solved in terms of the conserved variables $(\rho, \rho u, \rho v, \rho w, \rho e_t, \rho Y_i)$ the temperature is not known explicitly and thus an implicit equation must be solved:

$$\frac{\rho RT}{\bar{W}} - \left(-\rho e_t + \rho \sum_{i=1}^{N} h_i(T) Y_i + \frac{1}{2} \rho \mathbf{u}\mathbf{u} \right) = 0. \tag{B.8}$$

B.1.2.2 Time integration

The original, fourth-order accurate, explicit Runge-Kutta time integration scheme is used to solve the discretized system:

$$\begin{aligned} \frac{\partial \mathbf{Q}}{\partial t} &= \mathrm{RHS}(\mathbf{Q}), \\ \mathbf{Q}^{m+1} &= \mathbf{Q}^m + \frac{1}{6}\left(a + 2b + 2c + d\right), \\ a &= \Delta t \mathrm{RHS}(\mathbf{Q}^m), \\ b &= \Delta t \mathrm{RHS}(\mathbf{Q}^m + a/2), \\ c &= \Delta t \mathrm{RHS}(\mathbf{Q}^m + b/2), \\ d &= \Delta t \mathrm{RHS}(\mathbf{Q}^m + c), \end{aligned} \tag{B.9}$$

where $\mathbf{Q}$ is the vector of conserved variables.

The convective and diffusive terms are treated explicitly, which imposes restrictions on the timestep. In contrast, the chemical source terms are treated using a preconditioning strategy based on a diagonal approximation of the chemical Jacobian [103] within the Runge-Kutta steps. In the present turbulent simulations, this allows to use a timestep limited by the acoustic and convective time scales rather than the chemistry.

B.1.2.3 Turbulence forcing

The canonical flow configuration used in the present study lacks generation of turbulence due to large scale flow straining. Consequently, the turbulence is expected to decay. Velocity field forcing is thus necessary to maintain a constant turbulence intensity and achieve a statistically-stationary state.

Linear velocity forcing [81] was chosen for its physical nature and good stability properties. The linear forcing method mimics the missing large scale straining through the addition of a source term to the momentum equation:

$$\mathbf{f} = \frac{\epsilon_{s,0}}{2k_s(x,t)}\left(\rho\mathbf{u}_s(x,y,z,t) - \rho\bar{\mathbf{u}}_s(x,t)\right) + \frac{\epsilon_{d,0} - \mathrm{PD}}{2k_d(x,t)}\left(\rho\mathbf{u}_d(x,y,z,t) - \rho\bar{\mathbf{u}}_d(x,t)\right). \tag{B.10}$$

This source term forces the solenoidal and dilatational velocities, ($\mathbf{u}_s$ and $\mathbf{u}_d$), separately. Using Helmholtz decomposition, the velocity field is expressed as $\mathbf{u} = \mathbf{u}_s + \mathbf{u}_d$ where $\nabla \times \mathbf{u}_d = 0$ and $\nabla \cdot \mathbf{u}_s = 0$. Consequently, $\epsilon_{s,0}$ and $\epsilon_{d,0}$ are the desired dissipation rates and k_s, and k_d are the instantaneous, planar-averaged, kinetic energies. $\mathrm{PD} = -\langle \mathbf{u} \cdot \nabla p \rangle$ is the pressure-dilatation correlation. The split forcing allows the control of the desired dissipation rate and the dilatational to solenoidal dissipation ratio. In contrast, using a single linear forcing term leads to unstable simulations, in which the ratio of dilatational to solenoidal kinetic energies increases without bound. In the present implementation, the velocity field is decomposed by solving a Poisson equation for ϕ, $\nabla^2\phi = \nabla \cdot \mathbf{u}$, which yields the dilatational velocity component $\mathbf{u}_d = \nabla\phi$. The desired dilatational dissipation rate is set to zero, only the solenoidal velocity component is forced.

B.1.2.4 Boundary conditions

Particular care has to be taken when dealing with subsonic inflows and outflows in compressible flows. In the present work, Navier-Stokes Characteristic Boundary Conditions (NSCBC) [88] are used. The implementation follows that of Sutherland and Kennedy [108] and Yoo and Im [119].

The governing equation can be written as:

$$\frac{\partial}{\partial t}\mathbf{Q} + \nabla_n \cdot \mathbf{F_c}^n + \nabla_t \cdot \mathbf{F_c}^t - \nabla \cdot \mathbf{F_d} = \mathbf{S}, \tag{B.11}$$

where n denotes boundary-normal terms and t denotes terms tangent to the boundary. The inviscid

boundary-normal terms are then rewritten, using locally one-dimensional inviscid equations, as:

$$\nabla_n \cdot \mathbf{F_c} = \begin{pmatrix} d_1 \\ ud_1 + \rho d_3 \\ vd_1 + \rho d_4 \\ wd_1 + \rho d_5 \\ \rho u d_3 + \rho v d_4 + \rho w d_5 + (e_t - c_v T)d_1 + \frac{d_2}{\gamma - 1} \\ Y_i d_1 + \rho d_{5+i} \end{pmatrix}, \tag{B.12}$$

where the vector $\mathbf{d}$ is defined as:

$$\mathbf{d} = \begin{pmatrix} \frac{1}{c^2}\left[c^2\mathcal{L}_2 + (\mathcal{L}_5 + \mathcal{L}_1)\right] \\ (\mathcal{L}_5 + \mathcal{L}_1) \\ \frac{1}{\rho c}(\mathcal{L}_5 - \mathcal{L}_1) \\ \mathcal{L}_3 \\ \mathcal{L}_4 \\ \mathcal{L}_{5+i} \end{pmatrix}, \tag{B.13}$$

and the characteristic wave amplitudes in the x-direction are:

$$\mathcal{L} = \begin{pmatrix} \frac{u-c}{2}\left[\frac{\partial p}{\partial n} - \rho c \frac{\partial u}{\partial n}\right] \\ \frac{u}{c^2}\left[c^2\frac{\partial \rho}{\partial n} - \frac{\partial p}{\partial n}\right] \\ u\frac{\partial v}{\partial n} \\ u\frac{\partial w}{\partial n} \\ \frac{u+c}{2}\left[\frac{\partial p}{\partial n} + \rho c \frac{\partial u}{\partial n}\right] \\ u\frac{\partial Y_i}{\partial n} \end{pmatrix}. \tag{B.14}$$

At the inlet, all waves except $\mathcal{L}_1$ are incoming and must be specified while $\mathcal{L}_1$ can be computed from interior data using the formula above with one-sided differencing. The incoming waves are

specified as:

$$\mathcal{L}_2 = \beta_2(T - T_0), \tag{B.15}$$

$$\mathcal{L}_3 = \beta_3(v - v_0), \tag{B.16}$$

$$\mathcal{L}_4 = \beta_4(w - w_0), \tag{B.17}$$

$$\mathcal{L}_5 = \beta_5(u - u_0), \tag{B.18}$$

$$\mathcal{L}_{5+i} = \beta_{5+i}(Y_i - Y_{i,0}). \tag{B.19}$$

At the outlet, all waves except $\mathcal{L}_1$ are outgoing and can be computed from interior data. The incoming wave is specified as:

$$\mathcal{L}_1 = \sigma c \frac{1 - M^2}{2l_x}(p - p_\infty), \tag{B.20}$$

where β's are relaxation coefficients, M is the Mach number at the outlet, σ is a relaxation factor, c is the sound speed, p_∞ is the imposed ambient pressure.

Practically the boundary conditions are implemented as follows:

1. The full RHS of the governing equations is computed in the interior domain.
2. At the boundaries the $\nabla_n \cdot \mathbf{F_c}$ terms are computed using the $\mathcal{L}$s defined above.
3. The $\mathcal{L}$ terms associated with incoming eigenvalues are calculated according to the relations above while the outgoing waves are computed from interior data.

B.1.2.5 Shock treatment

In the present work, centered differences are used to solve the Navier-Stokes equations. In conjunction with the staggered grid formulation, the scheme is accurate and energy conserving. However, it is unstable around very sharp gradients (*e.g.* shocks). In order to alleviate this issue, an artificial dissipation term is added in the vicinity of shocks. The scheme reduces to a first-order updwind scheme at shocks to ensure stability.

A matrix-valued dissipation model is used which adds a different amount of artificial viscosity to

each equation. Switches based on the pressure and density fields are used to determine if artificial dissipation is required. Details on the dissipation model can be found in the work of Jorgenson and Turkel [50].

B.2 Validation

B.2.1 Boundary conditions

B.2.1.1 One-dimensional case

The implementation of the boundary conditions is first tested by investigating a set of propagating acoustic waves. The test case is taken from Baum *et al.* [10]. The gaussian waves are defined as:

$$u = u_0 + \alpha \exp\left[-\left(\beta \frac{x - L/2}{L}\right)^2\right], \tag{B.21}$$

$$p = p_0 + \rho_0 c_0 (u - u_0), \tag{B.22}$$

$$\rho = \rho_0 + \frac{\rho_0 (u - u_0)}{c_0}, \tag{B.23}$$

$$T = \frac{p}{\rho \bar{R}}, \tag{B.24}$$

and propagate towards the outflow boundary condition at the local speed of sound. In order to illustrate the importance of non-reflecting boundary conditions, a Neumann boundary condition is first used at the outflow boundary. The results are presented in Fig. B.1a showing the initial, incoming, and reflected waves. The amplitude of the reflected wave is close to that of the incoming wave. The boundary condition is thus almost perfectly reflecting.

The same simulation is performed using characteristic boundary conditions (NSCBC) at the outflow. The results are shown in Fig. B.1b. The incoming wave gets significantly damped at the boudary, resulting in a much smaller amplitude of the reflected wave. Using a uniform grid of 200 points ($\sim$ 25 points across the initial gaussian), the amplitude of the reflected wave is 1% that of the

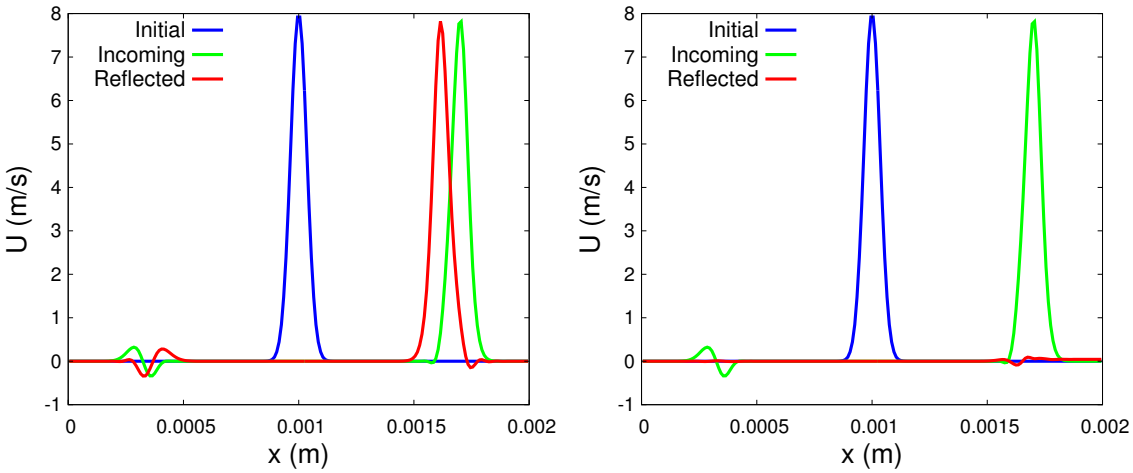

(a) Neumann BC (b) NSCBC

Figure B.1: Propagation of an acoustic wave towards an outflow boundary using Neumann and NSCBC with a uniform grid spacing. The green wave travels to the right while the red wave travels to the left.

incoming wave. Increasing the number of grid points decreases the amplitude of the reflected wave.

B.2.1.2 Two-dimensional case

The boundary conditions are further validated by simulating a two-dimensional vortex propagating through a non-reflecting boundary [119]. This test case has tangential components at the boundary and is more representative of turbulent flow simulations.

The configuration corresponds of a vortex superimposed on a free-stream flow. The initial vortex is prescribed by

$$\begin{pmatrix} u \\ v \end{pmatrix} = \begin{pmatrix} u_\infty \\ 0 \end{pmatrix} + \frac{1}{\rho} \begin{pmatrix} \frac{\partial \psi}{\partial y} \\ -\frac{\partial \psi}{\partial x} \end{pmatrix}, \quad \psi = C \exp\left(-\frac{(x-x_0)^2 + (y-y_0)^2}{2R_c^2} \right), \tag{B.25}$$

where ψ is the stream function for an incompressible non-viscous vortex, C is the vortex strength, R_c is the vortex radius, and (x_0, y_0) is the location of the vortex center. The initial pressure field is initialized as:

$$p = p_\infty - \rho \frac{C^2}{R_c^2} \exp\left(-\frac{(x-x_0)^2 + (y-y_0)^2}{2R_c^2} \right). \tag{B.26}$$

The flow characteristics are

$$M = u_\infty/c = 0.05, \quad R_c/l = 0.1, \quad C/(cl) = -0.0025, \tag{B.27}$$

where c is the speed of sound and l is the domain size in the x and y direction. The domain is 2 mm $\times$ 2 mm and discretized with 200 grid points in each direction.

The isocontours of the vertical velocity component at four different instants are shown in Fig. B.2. Shortly after $t = 80$ μs the vortex has completely exited the computational domain and the maximum vertical velocity component is less than 5% that of initial vortex.

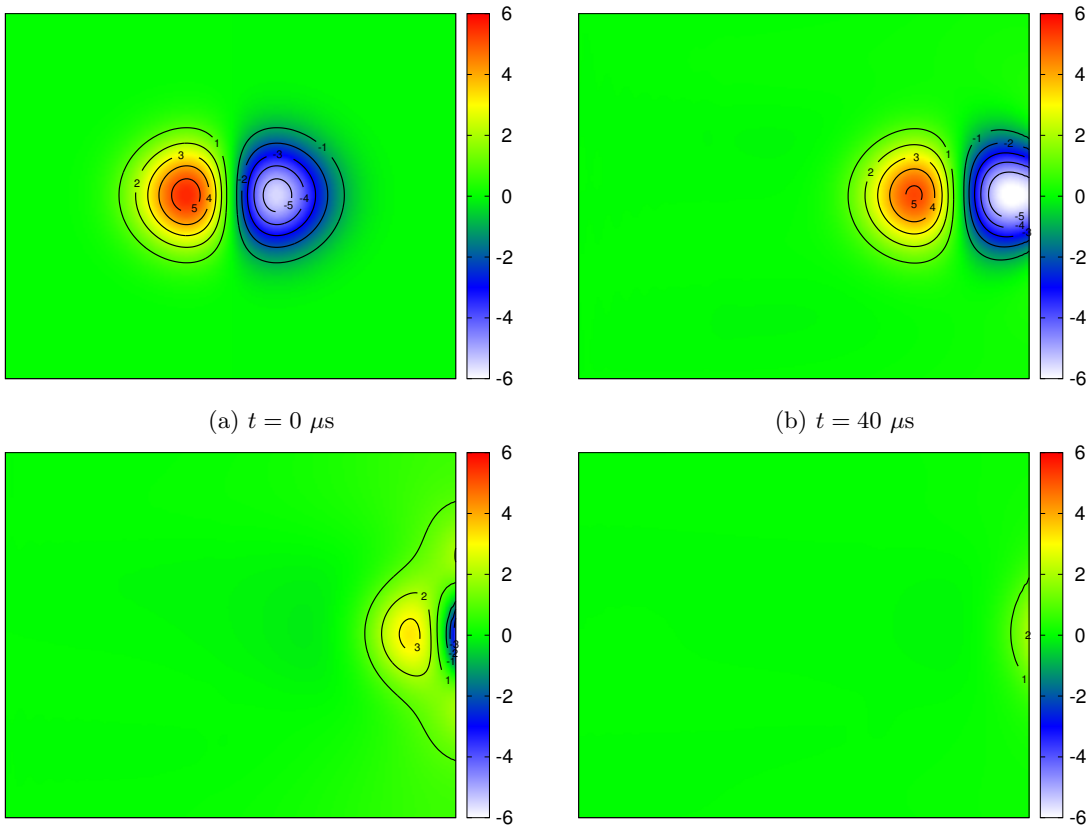

(a) $t = 0$ μs

(b) $t = 40$ μs

(c) $t = 60$ μs

(d) $t = 80$ μs

Figure B.2: Isocontours of v velocity component at four different instants.

B.2.2 One-dimensional laminar flame

The reacting Navier-Stokes equations are validated by performing the simulation of a laminar premixed flame with detailed chemistry. An n-heptane/air flame at $T_u = 800$ K and $p_0 = 1$ atm, described by a 35-species reduced mechanism, is chosen since it will be further studied in the turbulent simulations. The simulation is initialized using the low Mach number solution with a constant pressure everywhere. Initially, weak pressure waves travel towards the inflow and outflow boundaries. After this transient period, a steady propagating flame is obtained. The solution obtained with compressible formulation is shown in Fig. B.3 and compared with that obtained using FlameMaster. Fluid properties (such as density), mass fractions of major and minor species (fuel and H radical shown here), and chemical source terms are in excellent agreement.

B.2.3 Sod's problem

Finally, the artificial dissipation model used to ensure stability around shocks and discontinuities is tested. The Sod shock tube problem is a common test for compressible CFD codes. It is a Riemann problem with initial states:

$$\begin{aligned} \rho_L &= 3, \qquad \rho_R = 1 \\ p_L &= 3, \qquad p_R = 1 \\ u_L &= 0, \qquad u_R = 0. \end{aligned} \tag{B.28}$$

The present numerical simulations are compared to the exact as well as the solution obtained with a Roe solver [95]. The density is shown in Fig. B.4. A good agreement between the current compressible solver, the Roe solver, and the exact solution is observed. The rarefaction wave profile is properly resolved and no oscillations nor excessive smearing are observed around the shock and contact discontinuity.

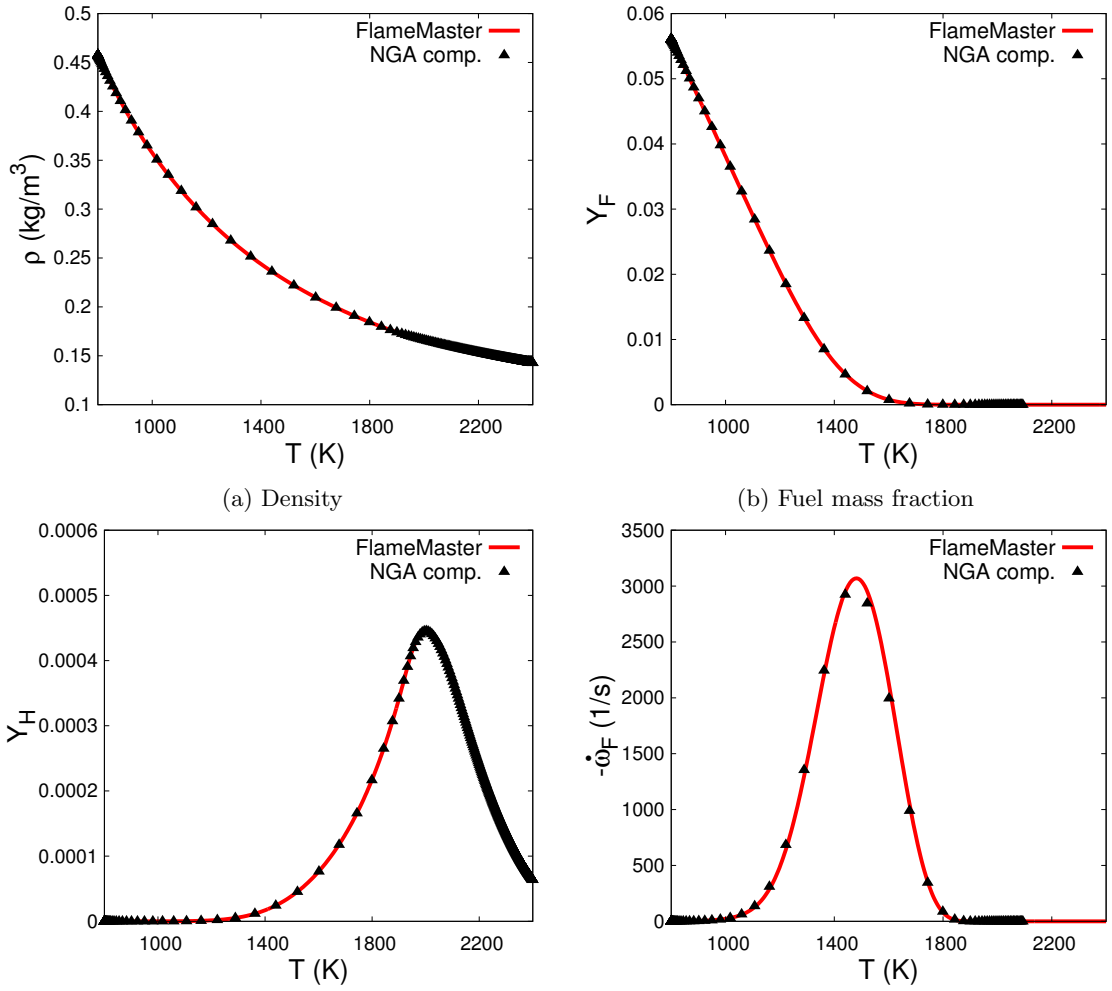

(a) Density

(b) Fuel mass fraction

(c) H mass fraction

(d) Fuel consumption rate

Figure B.3: One-dimensional laminar flame solution with detailed kinetics obtained with the compressible NGA compared to the FlameMaster solution.

B.3 Results

The present work is concerned with the numerical simulations of high Karlovitz number flames. These flames are characterized by large ratios of turbulent rms velocity to laminar flame speed (u'/S_L). In the distributed burning regime, this leads to high-speed subsonic turbulent flows. This is particularly true at high unburnt temperatures which lead to high Mach numbers for the same ratio u'/S_L. It is of interest to assess the importance of compressibility effects and determine if low Mach number codes and combustion models can be used without loss of accuracy.

Case D_1 was chosen for this purpose since it has the largest Mach number in the unburnt gases

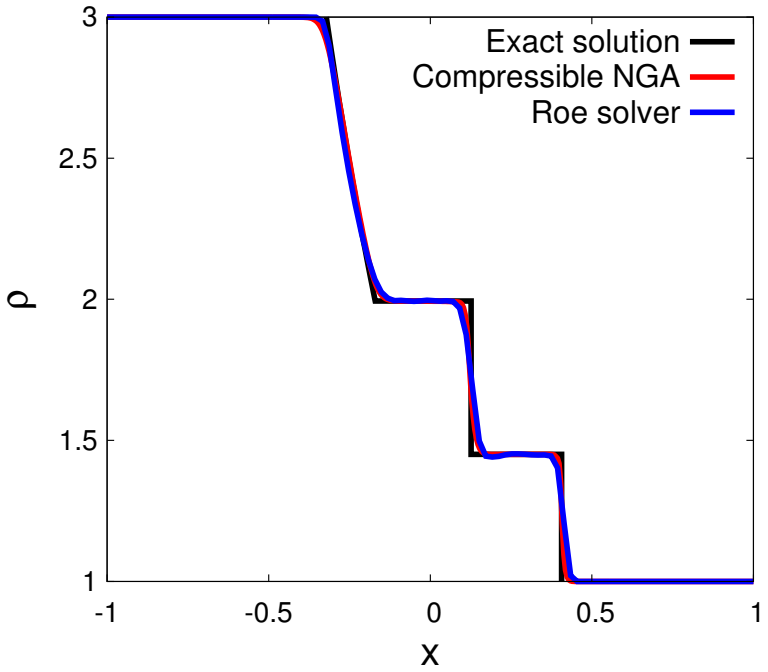

Figure B.4: Exact and numerical solutions to Sod's problem obtained with the present compressible solver and a Roe solver.

among the different DNS cases considered in this work. The turbulent Mach number, $\mathrm{Ma}_t = u'/c$, is approximately 0.25 in the unburnt gases and the maximum Mach number in the domain due to turbulent fluctuations is around 0.9.

Figure B.5 shows two-dimensional slices of instantaneous temperature, Mach number, and fuel consumption rate contours. The contours of temperature and fuel consumption rate are qualitatively similar to those obtained in the low-Mach number simulations. The Mach number is higher in the unburnt gases where smaller eddies and higher turbulent velocities are found. The maximum Mach number in the domain approaches unity. The Mach number decreases through the flame as the speed of sound increases.

In order to compare a bit more quantitatively the compressible and low-Mach number results, the instantaneous pressure fluctuations from both the compressible and low-Mach number simulations are shown in Fig. B.6. No significant differences (other than those due to the unsteadiness of the turbulent flow) are observed. This indicates that hydrodynamic effects dominate both simulations.

The low-Mach number assumption is further verified by computing the budget of the temperature

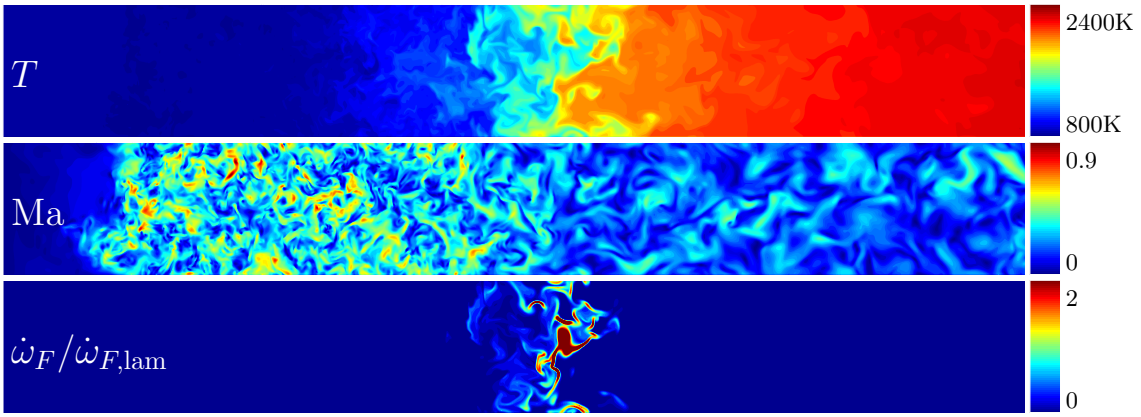

Figure B.5: Two-dimensional slices of the computational domain showing instantaneous temperature, Mach number, and fuel consumption rate contours.

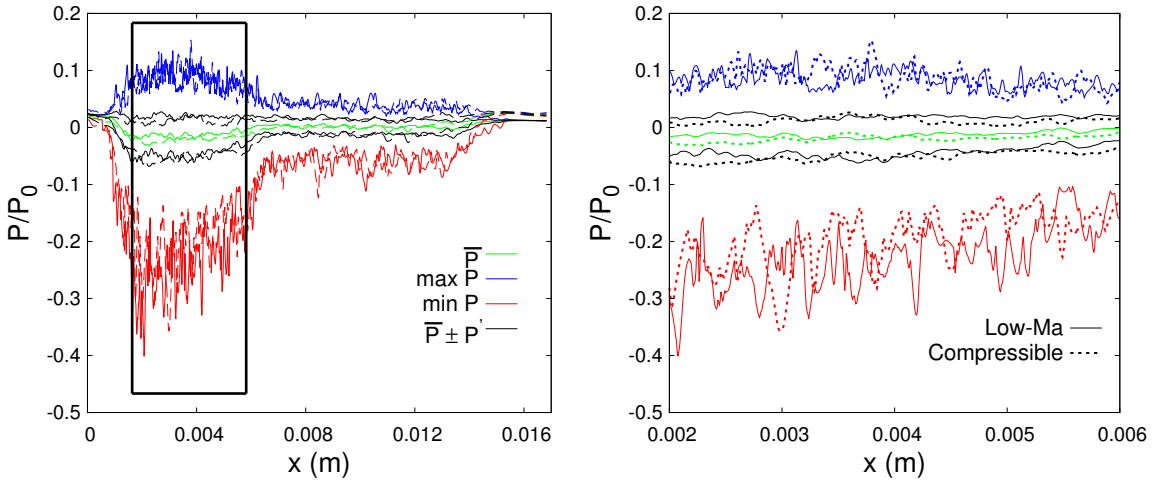

Figure B.6: Instantaneous pressure fluctuations from the compressible and low-Mach number simulations of case D normalized by the background pressure P_0. A constant background pressure has been substracted from P. Mean, maximum, mininum, and rms pressures are shown.

equation:

$$\rho C_p \mathbf{u} \cdot \nabla T = \underbrace{\mathbf{u} \cdot \nabla P}_{\mathcal{O}(M^2)} + \nabla \cdot (\lambda \nabla T) + \underbrace{\tau \cdot \nabla \mathbf{u}}_{\mathcal{O}(M^2)} + \dot{\omega}_T, \tag{B.29}$$

where the convective term is on the left-hand side and the pressure dilatation, diffusion, viscous dissipation, and heat release terms are on the right-hand side. In the low-Mach number temperature equation the $\mathbf{u} \cdot \nabla P$ and $\tau \cdot \nabla \mathbf{u}$ are neglected since they are of order M^2. The conditional means of the different terms are shown in Fig. B.7. Both the pressure dilatation and the viscous dissipation term are negligible compared to the convective, diffusive, and heat release terms.

Compressiblity effects are further assessed by examining the dependence of bulk fluid properties

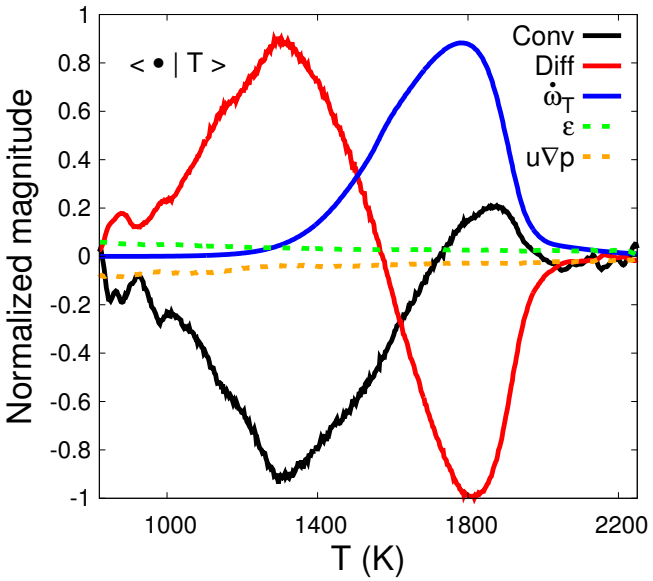

Figure B.7: Conditional means of the terms in the temperature equation from the compressible simulation.

on major species mass fractions. Figure B.8 shows the joint probability density functions of temperature and density *vs.* progress variable. The progress variable is defined here as the sum of the mass fractions of H_2, H_2O, CO, and CO_2. This is a commonly used definition in the simulations of hydrocarbon fuels. Virtually no scatter is observed when the temperature is plotted against the progress variable. All points lie very close to the conditional mean, which follows the laminar flame profile. Some scatter is seen in the jpdf of density but the fluctuations remain within $\sim 10\%$ or less of the mean value and the conditional mean follows closely the laminar flame profile.

Fig. B.6 showed significant pressure fluctuations. The low-Mach number simulation does not incorporate those P fluctations in the chemistry modeling as it assumes a constant thermodynamic pressure. It is thus relevant to investigate if a correlation between pressure and the chemical source terms is present in the compressible simulation. Figure B.9 shows the joint probability density function of fuel consumption rate *vs.* pressure taken on the isosurface of the corresponding temperature of peak source term from the compressible simulation. No strong correlation can be identified.

Finally, Fig. B.10 presents conditional means and probability density functions at $T = T_{\text{peak}}$ of the fuel consumption rate from both the compressible and low-Mach number simulations. Both

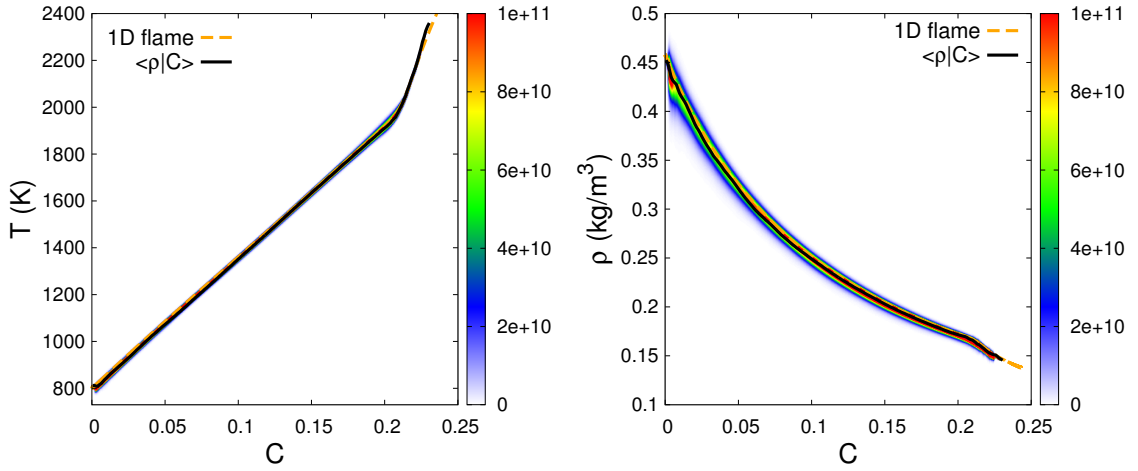

(a) Temperature (b) Density

Figure B.8: Joint probability density functions of temperature and density against progress variable from the compressible simulations.

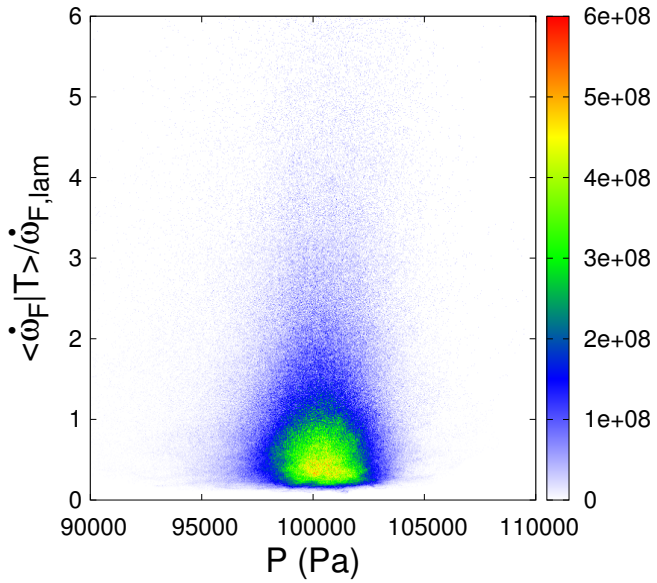

Figure B.9: Joint probability density function of fuel consumption rate against pressure taken on the isosurface of the corresponding temperature of peak source term from the compressible simulation.

simulations present very similar conditional means and distributions.

This confirms that, in the present simulations, compressibility effects are negligible and the low-Mach number assumption is valid. This has implications for the simulation and modeling of high Karlovitz number premixed flames. First, at the subsonic conditions considered in this work, a low-Mach solver is more computationally efficient than a compressible solver since the timestep is

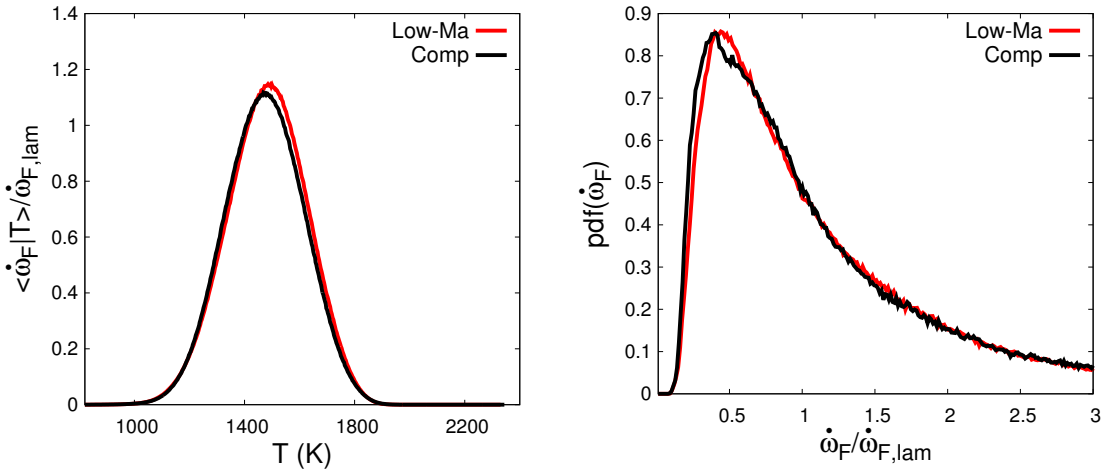

(a) Conditional mean

(b) pdf of $\dot{\omega}_F$

Figure B.10: Conditional means and probability density functions of fuel consumption rates taken on the isosurface of the corresponding peak source term from both compressible and low-Mach number simulations.

not restricted by the acoustic time scale. Second, compressibility effects do not need to be taken into account in the chemistry modeling. In other words, the thermodynamic pressure may be assumed constant in both detailed chemistry and reduced order models and modeling approaches using the assumption of low Mach number can be used. This includes tabulated chemistry based on Flamelet-generated manifolds.

It should be noted that the conclusions drawn here may not hold at higher Mach numbers. Additionally, the present work is not interested in acoustics. Accurate resolution of pressure waves would be necessary to capture those phenomena. Finally, the relatively small integral length scale used in the present work may inhibit the appearance of large scale pressure fluctuations [89]. Investigating this should be the subject of future work.

Appendix C

Fuel and chemistry effects

C.1 Turbulent flame speed correlation

The volumetric integral of the fuel consumption rate in Eq. 6.9 is rewritten as a surface integral along the isocontour $T = T_{\text{peak}}$ and an integral in the normal direction:

$$\int_V \dot{\omega}_F \mathrm{d}V = \int_{T=T_{\text{peak}}} \left(\int \dot{\omega}_F \mathrm{d}n \right) \mathrm{d}A, \tag{C.1}$$

where the local consumption rate $\int \dot{\omega}_F \mathrm{d}n$ can be rewritten using $\mathrm{d}n = \frac{\mathrm{d}T}{|\nabla T|}$:

$$\int \dot{\omega}_F \mathrm{d}n = \int \dot{\omega}_F \frac{\mathrm{d}T}{|\nabla T|}. \tag{C.2}$$

Then, the observation of Savard and Blanquart [101] that the fuel consumption locally scales like its value at $T = T_{\text{peak}}$ is used:

$$\dot{\omega}_F(T) \approx \dot{\omega}_{F,\text{lam}}(T) \frac{\dot{\omega}_F(T_{\text{peak}})}{\dot{\omega}_{F,\text{lam}}(T_{\text{peak}})}, \tag{C.3}$$

and a similar assumption is made for the gradient of temperature:

$$|\nabla T|(T) \approx |\nabla T|_{\text{lam}}(T) \frac{|\nabla T|(T_{\text{peak}})}{|\nabla T|_{\text{lam}}(T_{\text{peak}})}. \tag{C.4}$$

Combining Eqs. 6.9, C.1, C.2, C.3, and C.4, the turbulent flame speed can be approximated as:

$$\frac{S_T}{S_L} \approx \frac{A_T}{A} \frac{\langle \dot{\omega}_F / |\nabla T| \big| T_{\text{peak}} \rangle}{\dot{\omega}_{F,\text{lam}} / |\nabla T_{\text{lam}}|}. \tag{C.5}$$

$\langle \dot{\omega}_F / |\nabla T| \big| T_{\text{peak}} \rangle$ is the conditional mean, at $T = T_{\text{peak}}$, of the fuel consumption rate divided by the temperature gradient (both $\dot{\omega}_F$ and ∇T are computed locally at each grid cell). $A = L^2$ is the domain cross-section, and $\dot{\omega}_{F,\text{lam}} / |\nabla T_{\text{lam}}|$ is computed at $T = T_{\text{peak}}$ in the corresponding laminar flame.

It is important to note that, in contrast to Savard and Blanquart [101], it was not assumed that the temperature gradient at the reaction zone is equal to its laminar counterpart. The improved correlation from assuming Eq. C.4 rather than $|\nabla T|)(T) \approx |\nabla T|_{\text{lam}}(T)$ is seen by comparing Fig. C.1 to Fig. 5.3. The correlation between S_T/S_L and $\frac{A_T}{A} I_0$ is stronger in Fig. 5.3. This is quantified by computing the L^2-norm of the prediction error made on the flame speed,

$$\epsilon_{S_T} = \sqrt{\frac{\sum \left[(S_T/S_L) - (A_T I_0 / A) \right]^2}{\sum (S_T/S_L)^2}}, \tag{C.6}$$

for both Figs. 5.3 and C.1. The error is reduced from 13% to 7% by including the changes in temperature gradient.

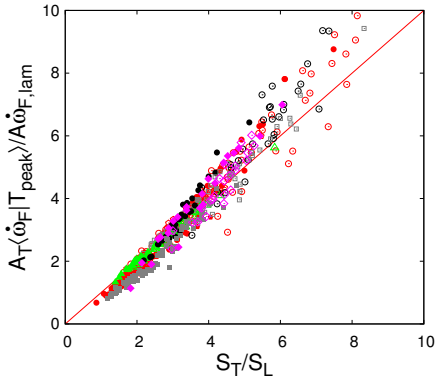

Figure C.1: Scatter plot of the instantaneous $A_T \langle \dot{\omega}_F \big| T_{\text{peak}} \rangle / (A \dot{\omega}_{F,\text{lam}})$ plotted against the instantaneous normalized turbulent flame speed for each snapshot used for all simulations. Filled and empty symbols correspond to non-unity and unity Lewis number simulations, respectively. The colors refer to different fuels and chemistry models (see Fig. 4.2).

C.2 Contours of temperature and fuel consumption

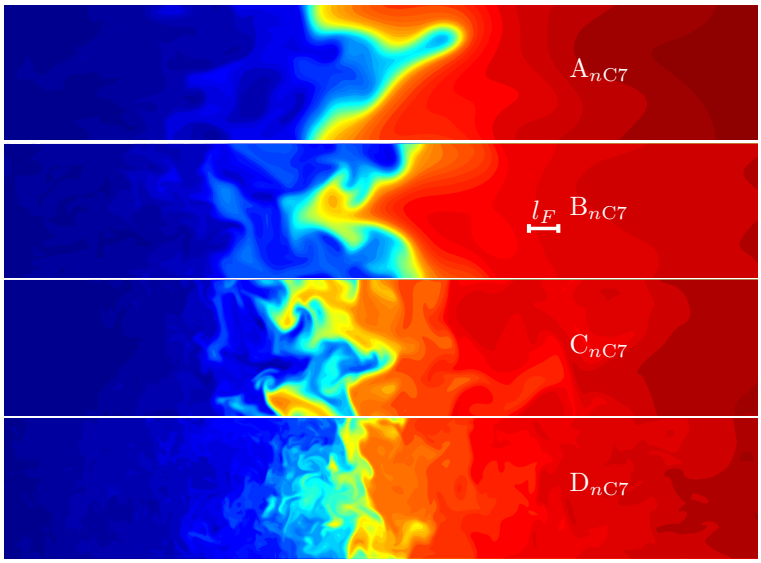

Figure C.2: Two-dimensional slices of a $5L \times L$ region centered around the flame showing temperature for the n-heptane non-unity Lewis number cases. The temperature ranges are [298, 2200] K for A and B and [800, 2400] K for C and D.

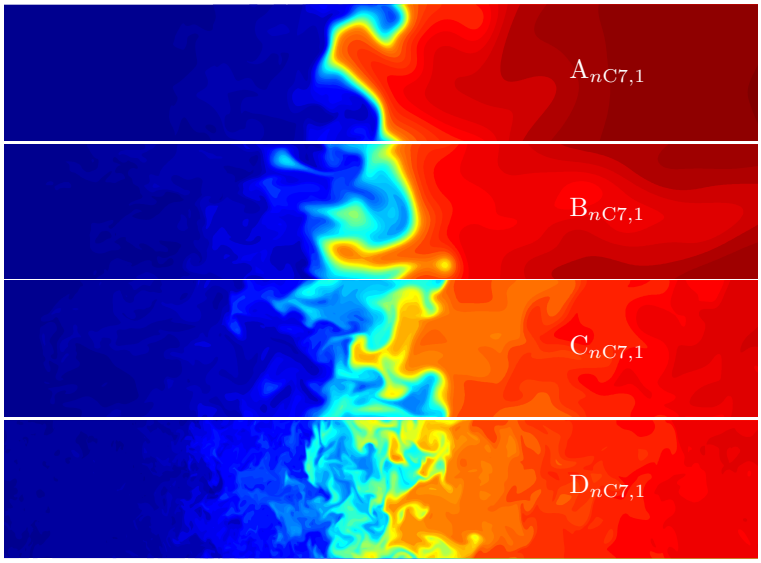

Figure C.3: Two-dimensional slices of a $5L \times L$ region centered around the flame showing temperature for the n-heptane unity Lewis number cases. The temperature ranges are [298, 2200] K for A and B and [800, 2400] K for C and D.

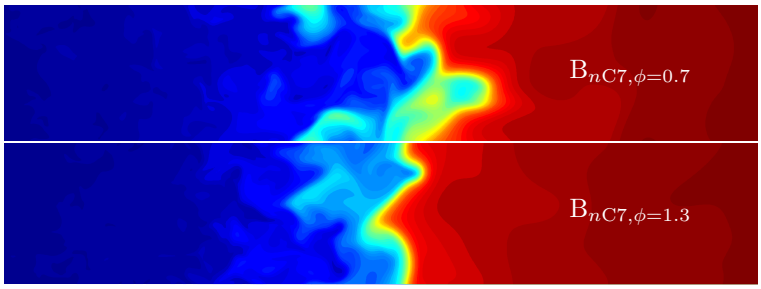

Figure C.4: Two-dimensional slices of a $5L \times L$ region centered around the flame showing temperature for the different equivalence ratios non-unity Lewis number cases. The temperature range is [298, 2200].

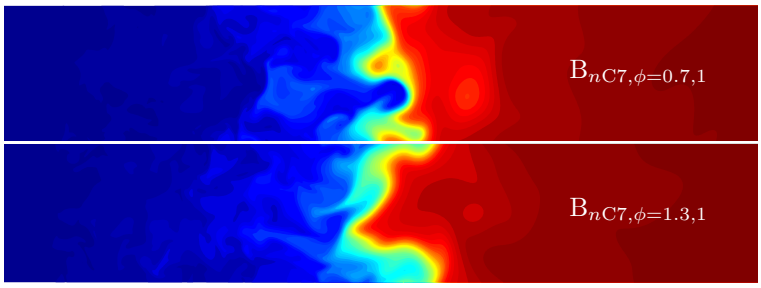

Figure C.5: Two-dimensional slices of a $5L \times L$ region centered around the flame showing temperature for the different equivalence ratios unity Lewis number cases. The temperature range is [298, 2200].

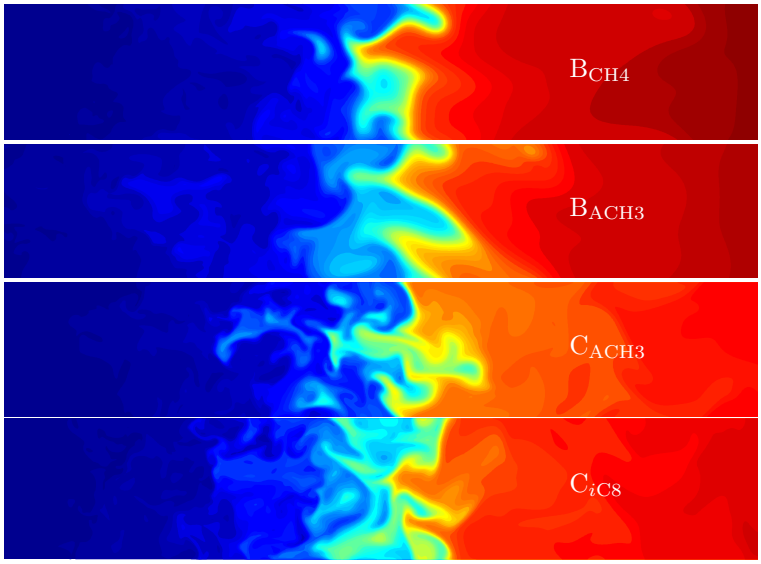

Figure C.6: Two-dimensional slices of a $5L \times L$ region centered around the flame showing temperature for the different fuels non-unity Lewis number cases. The temperature ranges are [298, 2200] K for A and B and [800, 2400] K for C and D.

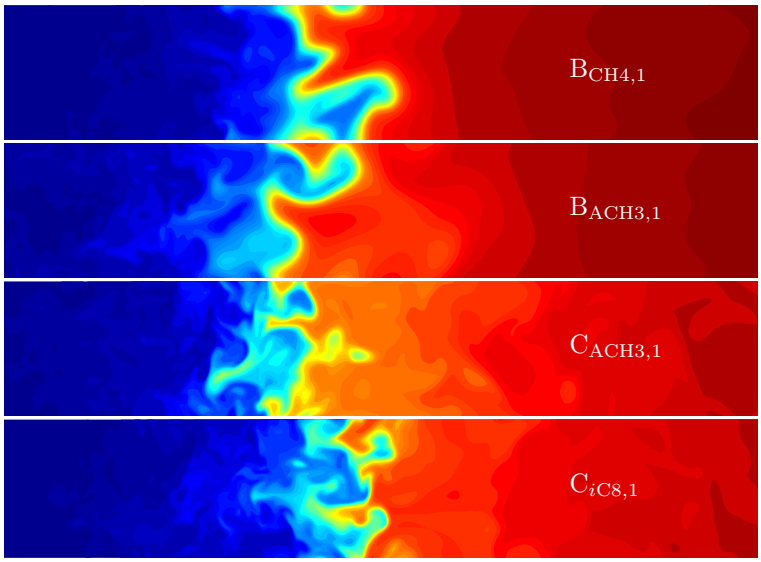

Figure C.7: Two-dimensional slices of a $5L \times L$ region centered around the flame showing temperature for the different fuels unity Lewis number cases. The temperature ranges are [298, 2200] K for A and B and [800, 2400] K for C and D.

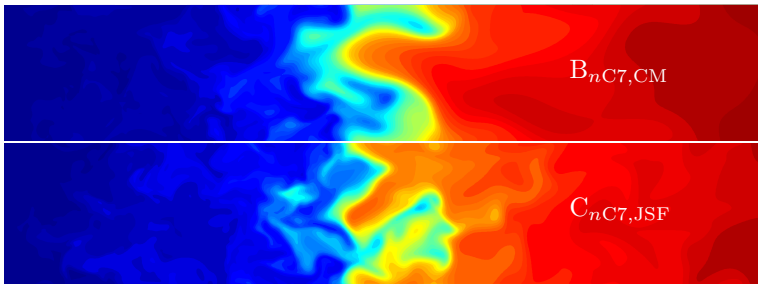

Figure C.8: Two-dimensional slices of a $5L \times L$ region centered around the flame showing temperature for the different mechanisms non-unity Lewis number cases. The temperature ranges are [298, 2200] K for A and B and [800, 2400] K for C and D.

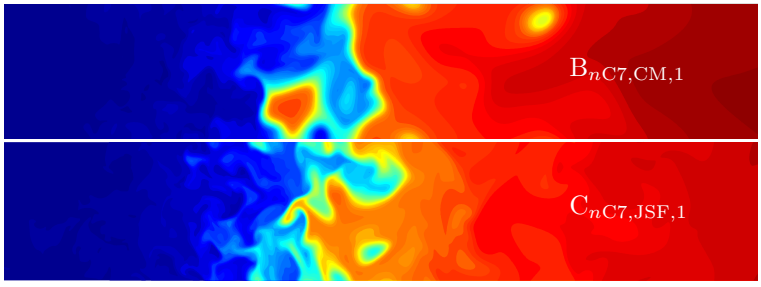

Figure C.9: Two-dimensional slices of a $5L \times L$ region centered around the flame showing temperature for the different mechanisms unity Lewis number cases. The temperature ranges are [298, 2200] K for A and B and [800, 2400] K for C and D.

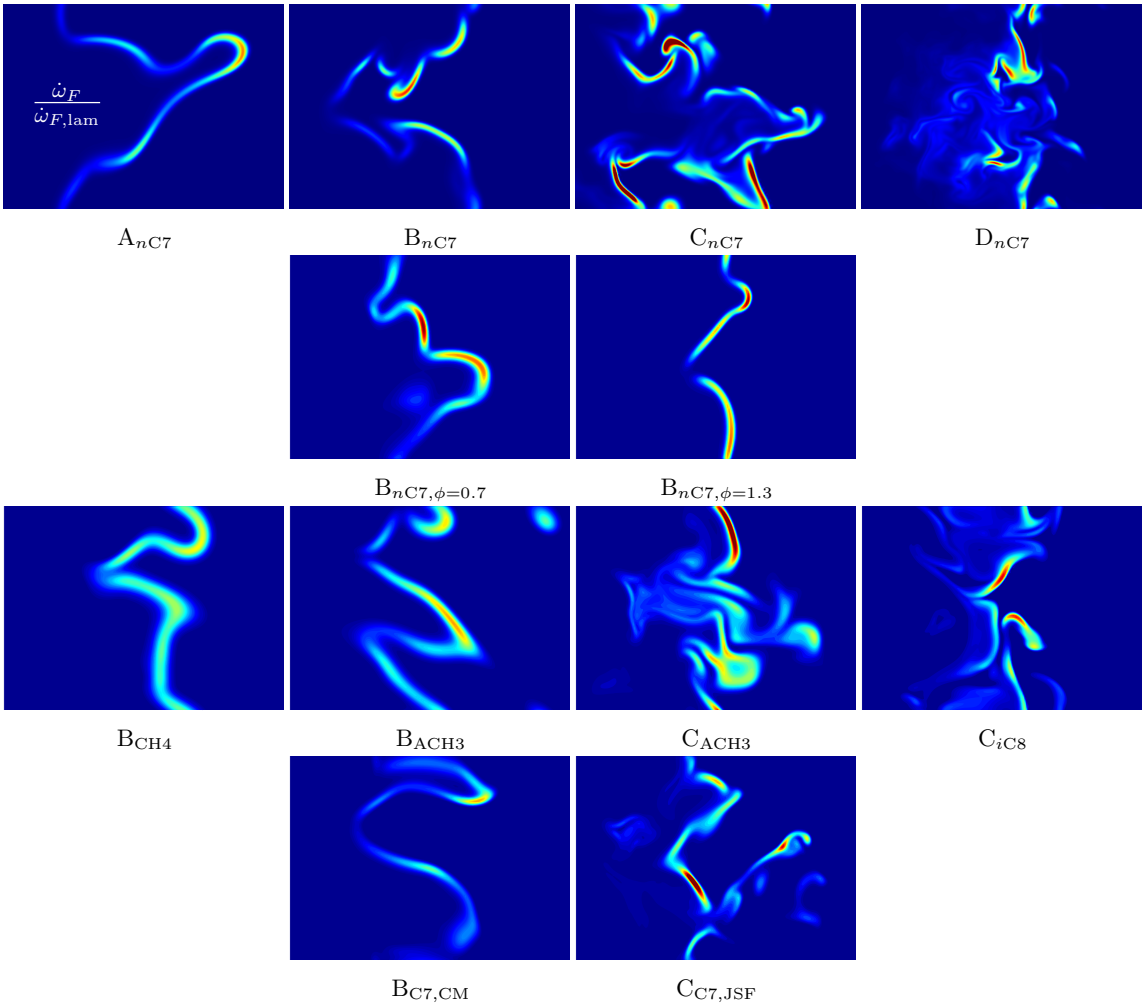

Figure C.10: Two-dimensional slices of a $1.3L \times L$ region centered around the flame showing fuel consumption rate (normalized by the peak value of the corresponding laminar flame). The fuel consumption rate range is satured at [0,2] in each case.

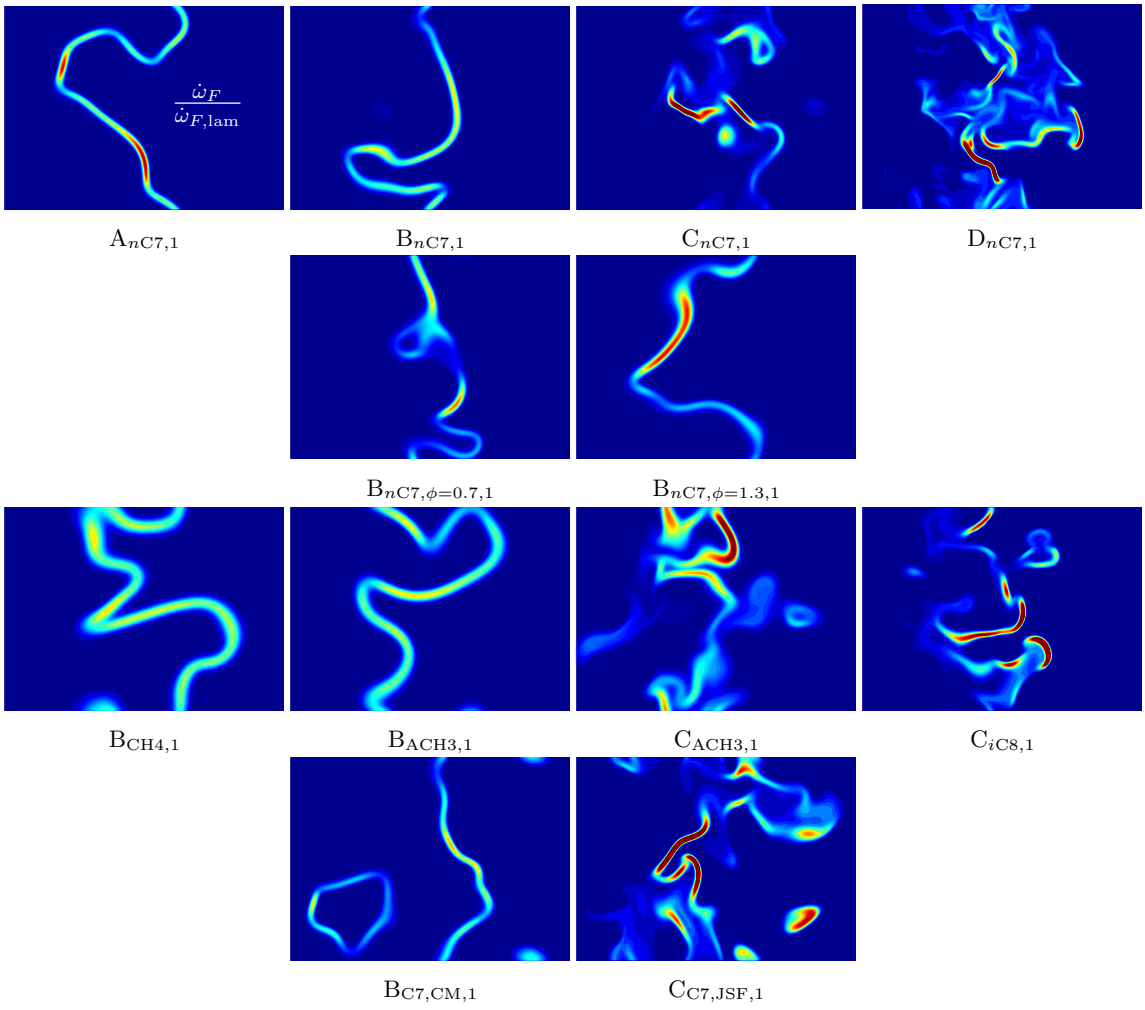

Figure C.11: Two-dimensional slices of a $1.3L \times L$ region centered around the flame showing the fuel consumption rate (normalized by the peak value of the corresponding laminar flame) for unity Lewis number cases. The fuel consumption rate range is satured at [0,2] in each case.

C.3 Contours of fuel consumption and burning efficiency

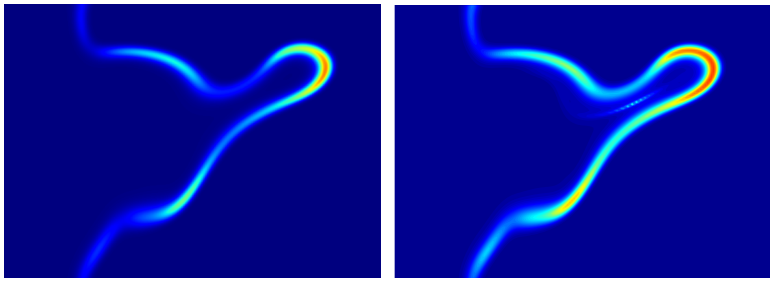

(a) $\dot{\omega}_F/\dot{\omega}_{F,\mathrm{lam}}$ (b) $(\dot{\omega}_F/|\nabla T|)/(\dot{\omega}_{F,\mathrm{lam}}/|\nabla T|_{\mathrm{lam}})$

Figure C.12: Instantaneous 2D slices of a $1.3L \times L$ region centered around the flame showing normalized fuel consumption rate and burning efficiency for case $\mathrm{A}_{n\mathrm{C7}}$.

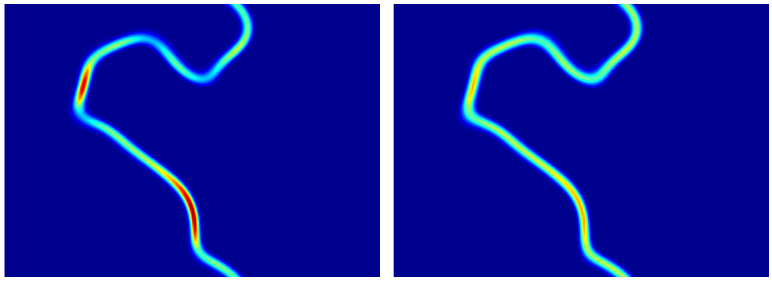

(a) $\dot{\omega}_F/\dot{\omega}_{F,\mathrm{lam}}$ (b) $(\dot{\omega}_F/|\nabla T|)/(\dot{\omega}_{F,\mathrm{lam}}/|\nabla T|_{\mathrm{lam}})$

Figure C.13: Instantaneous 2D slices of a $1.3L \times L$ region centered around the flame showing normalized fuel consumption rate and burning efficiency for case $\mathrm{A}_{n\mathrm{C7},1}$.

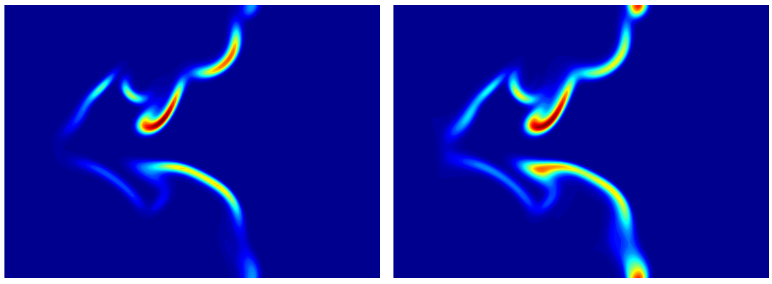

(a) $\dot{\omega}_F/\dot{\omega}_{F,\mathrm{lam}}$ (b) $(\dot{\omega}_F/|\nabla T|)/(\dot{\omega}_{F,\mathrm{lam}}/|\nabla T|_{\mathrm{lam}})$

Figure C.14: Instantaneous 2D slices of a $1.3L \times L$ region centered around the flame showing normalized fuel consumption rate and burning efficiency for case $\mathrm{B}_{n\mathrm{C7}}$.

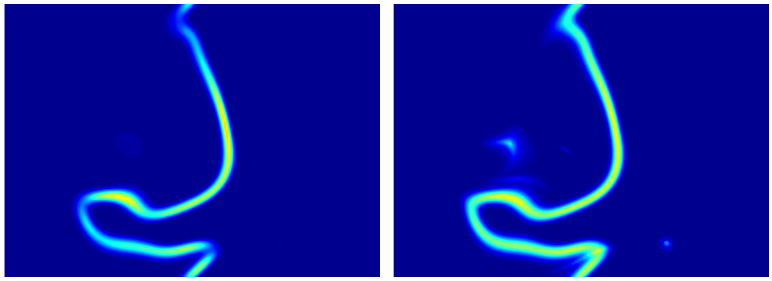

(a) $\dot{\omega}_F/\dot{\omega}_{F,\mathrm{lam}}$ (b) $(\dot{\omega}_F/|\nabla T|)/(\dot{\omega}_{F,\mathrm{lam}}/|\nabla T|_{\mathrm{lam}})$

Figure C.15: Instantaneous 2D slices of a $1.3L \times L$ region centered around the flame showing normalized fuel consumption rate and burning efficiency for case $\mathrm{B}_{n\mathrm{C7},1}$.

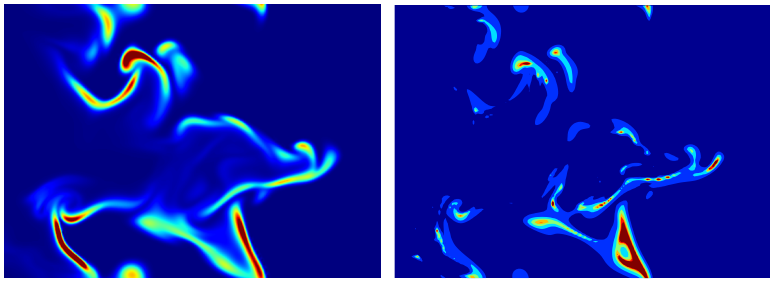

(a) $\dot{\omega}_F/\dot{\omega}_{F,\mathrm{lam}}$ (b) $(\dot{\omega}_F/|\nabla T|)/(\dot{\omega}_{F,\mathrm{lam}}/|\nabla T|_{\mathrm{lam}})$

Figure C.16: Instantaneous 2D slices of a $1.3L \times L$ region centered around the flame showing normalized fuel consumption rate and burning efficiency for case $\mathrm{C}_{n\mathrm{C7}}$.

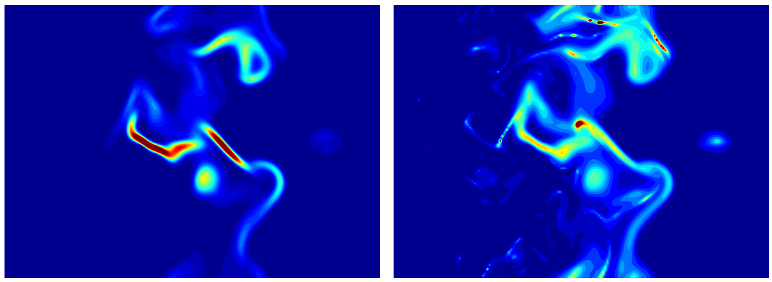

(a) $\dot{\omega}_F/\dot{\omega}_{F,\mathrm{lam}}$ (b) $(\dot{\omega}_F/|\nabla T|)/(\dot{\omega}_{F,\mathrm{lam}}/|\nabla T|_{\mathrm{lam}})$

Figure C.17: Instantaneous 2D slices of a $1.3L \times L$ region centered around the flame showing normalized fuel consumption rate and burning efficiency for case $\mathrm{c}_{n\mathrm{C7},1}$.

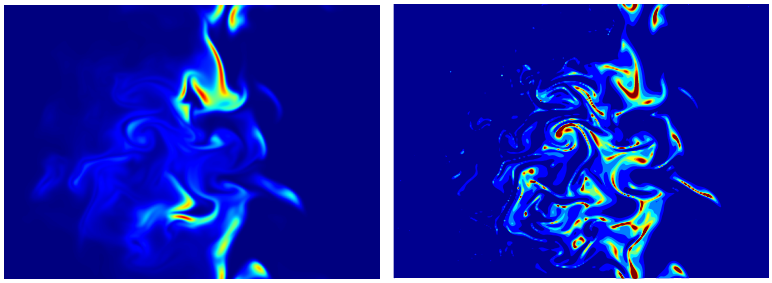

(a) $\dot{\omega}_F/\dot{\omega}_{F,\mathrm{lam}}$ (b) $(\dot{\omega}_F/|\nabla T|)/(\dot{\omega}_{F,\mathrm{lam}}/|\nabla T|_{\mathrm{lam}})$

Figure C.18: Instantaneous 2D slices of a $1.3L \times L$ region centered around the flame showing normalized fuel consumption rate and burning efficiency for case $\mathrm{D}_{n\mathrm{C7}}$.

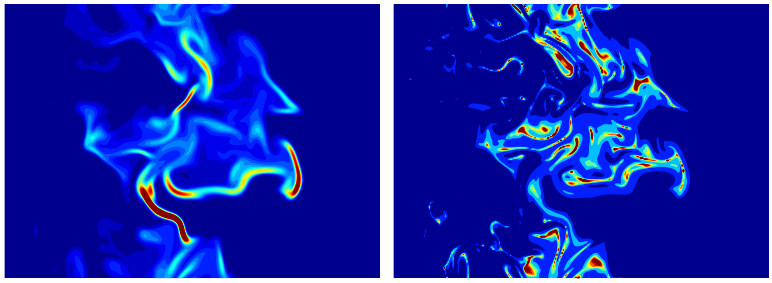

(a) $\dot{\omega}_F/\dot{\omega}_{F,\mathrm{lam}}$ (b) $(\dot{\omega}_F/|\nabla T|)/(\dot{\omega}_{F,\mathrm{lam}}/|\nabla T|_{\mathrm{lam}})$

Figure C.19: Instantaneous 2D slices of a $1.3L \times L$ region centered around the flame showing normalized fuel consumption rate and burning efficiency for case $\mathrm{D}_{n\mathrm{C7,1}}$.

Appendix D

Integral length scale effects

D.1 Energy spectra

Figure D.1 shows the energy and dissipation spectra taken at fixed planes in the unburnt and burnt gases and averaged over time. These correspond to two-dimensional three components velocity spectra computed in a y-z plane.

When normalized by their respective Kolmogorov scales, all spectra taken in the unburnt gases collapse to a single curve. This confirms that, even in the absence of an inertial subrange in the lowest Reynolds number simulations, the dissipation scales in the incoming turbulence are universal.

The spectra taken in the burnt gases appear to collapse to a single curve on the energy spectra. However, the dissipation spectra highlight differences with the unburnt spectra, especially at $l/l_F = 1$ and 2. The relatively small range of scales is due to the decrease of the Reynolds number as temperature (and thus viscosity) increases across the flame. In the present flames at $T_u = 298$ K, the Reynolds number decreases by a factor of ~ 30 from the unburnt to the burnt gases.

D.2 Chemical source terms

In addition to the progress variable production rate shown in the manuscript, the conditional means of the chemical source terms of heat release, fuel, H_2O, C_2H_4, H, and OH are shown in Fig. D.2. In all cases, the source terms are unaffected by changes in the integral length scale. Yet, significant differences between the turbulent flames and the corresponding laminar flames are observed. This

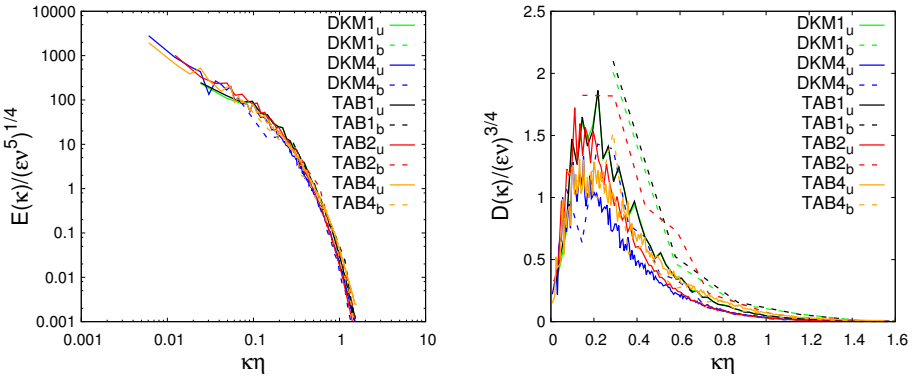

(a) Energy spectra

(b) Dissipation spectra

Figure D.1: Normalized energy and dissipation spectra for the different simulations. Two-dimensional three components spectra taken in y-z planes in the unburnt (subscript u) and burnt (subscript b) gases.

indicates that differential diffusion effects are significant for reactants, products, intermediates, as well as radicals.

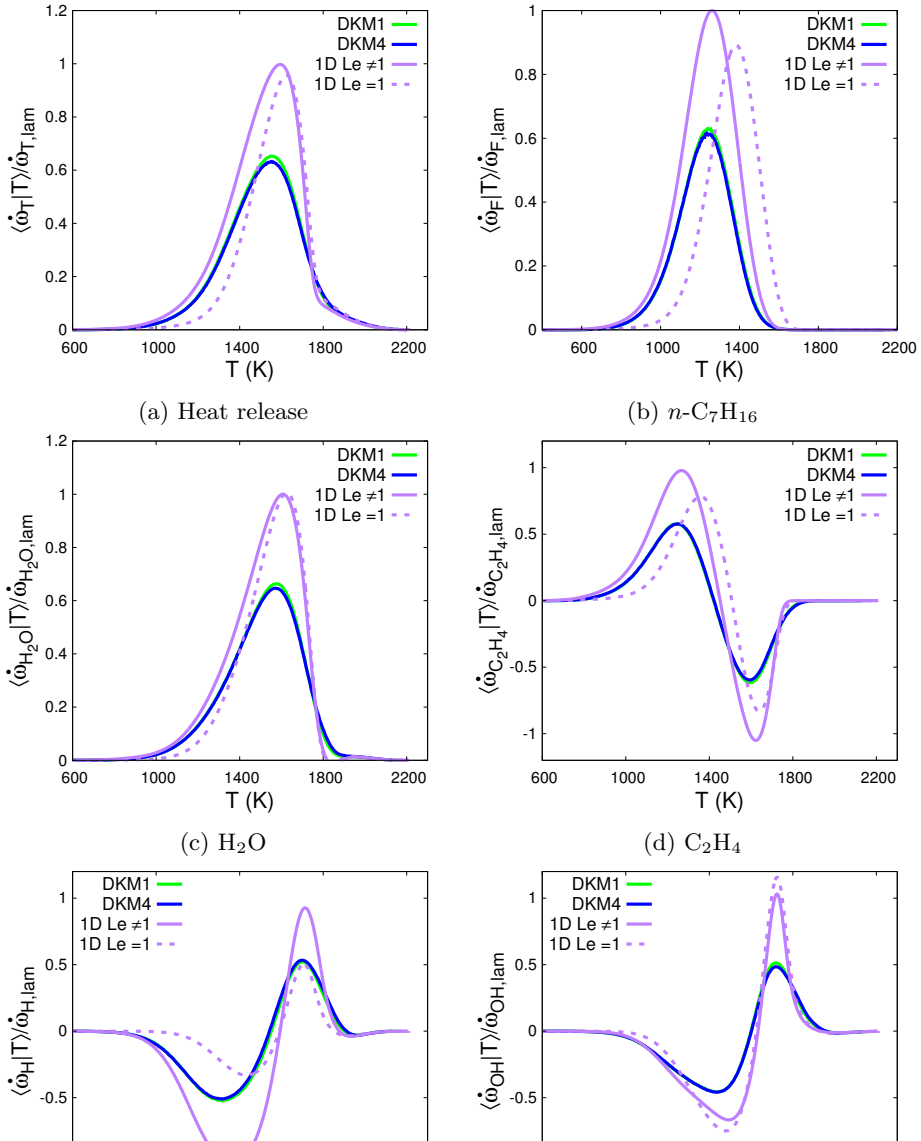

(a) Heat release

(b) n-C_7H_{16}

(c) H_2O

(d) C_2H_4

(e) H

(f) OH

Figure D.2: Conditional means of chemical source terms.

Appendix E

Filtered chemical source term

E.1 Presumed PDF

A common approach in tabulated chemistry combustion models is to presume the shape of the probability density function of the progress variable. A β-function PDF is often assumed [39, 44]. The β-probability density function is defined as:

$$P(c|\tilde{c}, c_v) = \frac{c^{a-1}(1-c)^{b-1}}{\int_0^1 c^{a-1}(1-c)^{b-1}\mathrm{d}c}, \tag{E.1}$$

where a and b are determined from $\tilde{c}$ and its variance:

$$a = \tilde{c}\left(\frac{\tilde{c}(1-\tilde{c})}{c_v} - 1\right), \quad b = a\left(\frac{1}{\tilde{c}} - 1\right), \tag{E.2}$$

for c normalized between 0 and 1.

Another approach consists of using spatially filtered laminar flames to generate the lookup table [40, 75]. A reference one-dimensional flame is filtered at different filter widths and the filtered fields are then tabulated against the filtered progress variable $\tilde{c}$ and its variance. Moureau *et al.* [71] showed that the use of a variable filter size led to better predictions than using the LES grid size as the filter width. This approach is equivalent to convoluting the laminar progress variable source term with a PDF obtained from filtered laminar flames, labeled FLF-PDF. The sub-filter PDF of

the FLF model is

$$P(c|\tilde{c}, S_c) = \frac{\rho(c) F_\Delta \left(\tilde{x}^\Delta(\tilde{c}, \Delta) - x(c) \right)}{\bar{\rho}(\tilde{c}, S_c) |\nabla c|}, \tag{E.3}$$

where $\Delta = \Delta(\tilde{c}, S_c)$ is the filter size that needs to be applied to the laminar flame to match the sub-grid scale scalar variance, and $S_c = c_v/[\tilde{c}(1-\tilde{c})]$ is the unmixedness factor.

Bibliography

[1] U.S. Energy Information Administration. Annual Energy Outlook 2015 available at http://www.eia.gov/forecasts/aeo/, Washington, DC.

[2] A. Amato, M. Day, R.K. Cheng, J. Bell, and T. Lieuwen. Leading edge statistics of turbulent, lean, H_2-air flames. *Proc. Combust. Inst.*, 35:1313–1320, 2015.

[3] R.A. Antonia and K.R. Sreenivasan. Lognormality of temperature dissipation in a turbulent boundary layer. *Phys. Fluids*, 20(11):1800–1804, 1977.

[4] A.J. Aspden, J.B. Bell, M.S. Day, S.E. Woosley, and M. Zingale. Turbulence-flame interactions in type Ia supernovae. *Astrophys. J.*, 689:1173 – 1185, 2008.

[5] A.J. Aspden, J.B. Bell, and S.E. Woosley. Distributed flames in type Ia supernovae. *Astrophys. J.*, 710:1654 – 1663, 2010.

[6] A.J. Aspden, M.S. Day, and J.B. Bell. Lewis number effects in distributed flames. *Proc. Combust. Inst.*, 33:1473 – 1480, 2011.

[7] A.J. Aspden, M.S. Day, and J.B. Bell. Turbulence-flame interactions in lean premixed hydrogen: transition to the distributed burning regime. *J. Fluid Mech.*, 680:287 – 320, 2011.

[8] A.J. Aspden, M.S. Day, and J.B. Bell. Turbulence-chemistry interaction in lean premixed hydrogen combustion. *Proc. Combust. Inst.*, 35:1321–1329, 2015.

[9] G. Balarac, H. Pitsch, and V. Raman. Development of a dynamic model for the subfilter scalar variance using the concept of optimal estimators. *Phys. Fluids*, 20(3):035114 1 – 9, 2008.

[10] M. Baum, T. Poinsot, and D. Thevenin. Accurate boundary conditions for multicomponent reactive flows. *J. Comp. Phys.*, 116:247 – 261, 1995.

[11] F. Bisetti, G. Blanquart, M.E. Mueller, and H. Pitsch. On the formation and early evolution of soot in turbulent non-premixed flames. *Combust. Flame*, 159:317 – 335, 2012.

[12] G Blanquart. CaltechMech, v. 2.3. http://www.theforce.caltech.edu/CaltechMech, 2015.

[13] G. Blanquart, P. Pepiot-Desjardins, and H. Pitsch. Chemical mechanism for high temperature combustion of engine relevant fuels with emphasis on soot precursors. *Combustion and Flame*, 156:588 – 607, 2009.

[14] B. Bobbitt, S. Lapointe, and G. Blanquart. Vorticity transformation in high Karlovitz number premixed flames. *Phys. Fluids*, 28:015101, 2016.

[15] B.D. Bobbitt and G. Blanquart. Investigation of vortex-premixed flame interaction with detailed chemistry. In *Paper 070LT-0343, 8th US National Combustion Meeting*, May 2013.

[16] L.R. Boeck, S. Lapointe, J. Melguizo-Gavilanes, and G. Ciccarelli. Flame propagation across an obstacle: OH-PLIF and 2-D simulations with detailed chemistry. *Proc. Combust. Inst.*, accepted, 2016.

[17] R. Borghi. On the structure and morphology of turbulent premixed flames. *Recent Adv. Aero. Sci.*, pages 117 – 134, 1985.

[18] K.N.C. Bray. Studies of the turbulent burning velocity. *Proc. Roy. Soc. London*, 431:313–323, 1990.

[19] N. Burali, S. Lapointe, B. Bobbitt, G. Blanquart, and Y. Xuan. Assessment of the constant non-unity Lewis number assumption in chemically reacting flows. *Combust. Theor. Model.*, accepted, 2016.

[20] S.M. Candel and T.J. Poinsot. Flame stretch and the balance equation for the flame area. *Combust. Sci. Technol.*, 70:1–15, 1990.

[21] F. Carbone, J.L. Smolke, A.M. Fincham, and F.N. Egolfopoulos. Characteristics of piloted premixed turbulent-jet flames of methane and c_6-c_8 hydrocarbons. *WSSCI Spring 2014 Meeting*, pages paper 14S–03, 2014.

[22] H. Carlsson, R. Yu, and X.-S. Bai. Flame structure analysis for categorization of lean premixed CH4/air and H2/air flames at high Karlovitz numbers: Direct numerical simulation studies. *Proc. Combust. Inst.*, 35:1425–1432, 2015.

[23] P.L. Carroll and G. Blanquart. The effect of velocity field forcing techniques on the nature and evolution of the Karman-Howarth equation. *J. Turbul.*, 15:429 – 448, 2014.

[24] Y. Chen and M. Ihme. Large-Eddy simulation of a piloted premixed jet burner. *Combust. Flame*, 160:2896 – 2910, 2013.

[25] Y.-C. Chen and R.W. Bilger. Experimental investigation of three-dimensional flame-front structure in premixed turbulent combustion: II. lean hydrogen/air bunsen flames. *Combust. Flame*, 138:155 – 174, 2004.

[26] M. Colket, T. Edwards, S. Williams, N.P. Cernansky, D.L. Miller, F. Egolfopoulos, P. Lindstedt, K. Seshadri, F.L. Dryer, C.K. Law, D. Friend, D.B. Lenhert, H. Pitsch, A.F. Sarofim, M. Smooke, and W. Tsang. Development of an experimental database and kinetic models for surrogate jet fuels. In *45th AIAA Aerospace Sciences Meeting and Exhibit, Reno, Nevada, Jan. 8-11*, 2007.

[27] G. Damkohler. Der einfluss der turbulenz auf die flammengeschwindigenkeit in gasgemishcen. *Z. Elektrochem*, 46:601 – 652, 1940.

[28] M. Day, J. Bell, P-T. Bremer, V. Pascucci, V. Beckner, and M. Lijewski. Turbulence effects on cellular burning structures in lean premixed hydrogen flames. *Combust. Flame*, 156:1035 – 1045, 2009.

[29] Olivier Desjardins, Guillaume Blanquart, Guillaume Balarac, and Heinz Pitsch. High order conservative finite difference scheme for variable density low mach number turbulent flows. *J. Comp. Phys.*, 227:7125 – 7159, 2008.

[30] P. Domingo, L. Vervisch, and D. Veynante. Large-Eddy Simulation of a lifted methane jet flame in a vitiated coflow. *Combust. Flame*, 153:415 – 432, 2008.

[31] M. Dunn, A. Masri, and R. Bilger. A new piloted premixed jet burner to study strong finite-rate chemistry effects. *Combust. Flame*, 151:46 – 60, 2007.

[32] M. Dunn, A. Masri, R. Bilger, R. Barlow, and G. Wang. The compositional structure of highly turbulent piloted premixed flames issuing into a hot coflow. *Proc. Combust. Inst.*, 32:1779 – 1786, 2009.

[33] T.D. Dunstan, N. Swaminathan, K.N.C. Bray, and R.S. Cant. Geometrical properties and turbulent flame speed measurements in stationary premixed V-flames using Direct Numerical Simulations. *Flow Turbul. Combust.*, 87:237–259, 2011.

[34] C. Duwig, K.-J. Nogenmyr, C.-K. Chan, and M. J. Dunn. Large-Eddy Simulations of a piloted lean premixed jet flame using finite-rate chemistry. *Combust. Theo. Model.*, 15:537 – 568, 2011.

[35] T. Echekki and J. Chen. Unsteady strain rate and curvature effects in turbulent premixed methane-air flames. *Combust. Flame*, 106:184 – 202, 1996.

[36] T. Edwards. Liquid fuels and propellants for aerospace propulsion: 1903-2003. *J. Prop. Power*, 19(6):1089 – 1107, 1994.

[37] E. Effelsberg and N. Peters. Scalar dissipation rates in turbulent jets and jet diffusion flames. *Symp. (Int.) Combust.*, 22:693–700, 1989.

[38] A. Eucken. The heat-carrying capabilities, the specific heat, and the internal friction of gas. *Physik Z.*, 14:324–333, 1913.

[39] B. Fiorina, O. Gicquel, L. Vervisch, S. Carpentier, and N. Darabiha. Premixed turbulent combustion modeling using tabulated detailed chemistry and PDF. *Proc. Combust. Inst.*, 30:867 – 874, 2005.

[40] B. Fiorina, R. Vicquelin, P. Auzillon, N. Darabiha, O. Gicquel, and D. Veynante. A filtered tabulated chemistry model for LES of premixed combustion. *Combust. Flame*, 157:465 – 475, 2010.

[41] M. Germano, U. Piomelli, P. Moin, and W.H. Cabot. A dynamic subgridscale eddy viscosity model. *Phys. Fluids A: Fluid Dyn.*, 3(7):1760 – 1765, 1991.

[42] O. Gicquel, N. Darabiha, and D. Thevenin. Laminar premixed hydrogen/air counterflow flame simulations using flame prolongation of ILDM with differential diffusion. *Proc. Combust. Inst.*, 28(2):1901 – 1908, 2000.

[43] D.C. Haworth and T.J. Poinsot. Numerical simulations of Lewis number effects in turbulent premixed flames. *J. Fluid Mech.*, 244:405–436, 1992.

[44] F.E. Hernandez-Perez, F.T.C Yuen, C.P.T. Groth, and O.L. Gulder. LES of a laboratory-scale turbulent premixed bunsen flame using FSD, PCM-FPI and thickened flame models. *Proc. Combust. Inst.*, 33:1365 – 1371, 2011.

[45] M. Herrmann, G. Blanquart, and V. Raman. Flux corrected finite volume scheme for preserving scalar boundedness in reacting large-eddy simulations. *AIAA Journal*, 44:2879 – 2886, 2006.

[46] O. Hirschfelder, C.F. Curtiss, and R.B. Bird. *Molecular Theory of Gases and Liquids.* John Wiley and Sons, New York, 1954.

[47] A.T. Holley, X.Q. You, F.N. Egolfopoulos, and H. Wang. Sensitivity of propagation and extinction of large hydrocarbon flames to fuel diffusion. *Proc. Combust. Inst*, 32:1157–1163, 2009.

[48] J. Hult, S. Gashi, N. Chakraborty, M. Klein, K.W. Jenkins, S. Cant, and C.F. Kaminski. Measurement of flame surface density for turbulent premixed flames using PLIF and DNS. *Proc. Combust. Inst.*, 31:1319 – 1326, 2007.

[49] C. Ji, E. Dames, Y.L. Wang, H. Wang, and F.N. Egolfopoulos. Propagation and extinction of premixed C_5-C_{12} n-alkane flames. *Combust. Flame*, 157:277–287, 2010.

[50] P. Jorgenson and E. Turkel. Central difference TVD schemes for time dependent and steady state problems. *J. Comp. Phys.*, 107:297 – 308, 1993.

[51] E. Knudsen, S.H. Kim, and H. Pitsch. An analysis of premixed flamelet models for large eddy simulation of turbulent combustion. *Phys. Fluids*, 22:115109 1 – 24, 2010.

[52] E. Knudsen, H. Kolla, E.R. Hawkes, and H. Pitsch. LES of a premixed jet flame DNS using a strained flamelet model. *Combust. Flame*, 160:2911 – 2927, 2013.

[53] E. Knudsen and H. Pitsch. A general flamelet transformation useful for distinguishing between premixed and non-premixed modes of combustion. *Combust. Flame*, 156:678 – 696, 2009.

[54] E. Knudsen, E.S. Richardson, E.M. Doran, H. Pitsch, and J.H. Chen. Modeling scalar dissipation and scalar variance in large eddy simulation: Algebraic and transport equation closures. *Phys. Fluids*, 24(5):055103 1 – 24, 2012.

[55] H. Kolla. *Scalar disspation rate based flamelet modelling of turbulent premixed flames*. PhD thesis, University of Cambridge, 2009.

[56] H. Kolla, E.R. Hawkes, A.R. Kerstein, N. Swaminathan, and J.H. Chen. On velocity and reactive scalar spectra in turbulent premixed flames. *J. Fluid Mech.*, 754:456–487, 2014.

[57] A. Kolmogorov. The local structure of turbulence in incompressible viscous fluid for very large Reynolds numbers. *Dokl. Akad. Nauk SSSR*, 30:299–303, 1941.

[58] S. Lapointe and G. Blanquart. Fuel and chemistry effects in high Karlovitz premixed flames. *Combust. Flame*, 167:294–307, 2016.

[59] S. Lapointe, B. Savard, and G. Blanquart. Differential diffusion effects, distributed burning, and local extinctions in high Karlovitz premixed flames. *Combust. Flame*, 162:3341 – 3355, 2015.

[60] Chung K Law. *Combustion physics*. Cambridge university press, 2010.

[61] D.K. Lilly. A proposed modification of the germano subgrid-scale closure method. *Phys. Fluids A: Fluid Dyn.*, 4(3):633 – 635, 1992.

[62] W.E. Lorensen and H.E. Cline. Marching Cubes: A high resolution 3D surface construction algorithm. *Computer Graphics*, 21, 1987.

[63] Moshe Matalon and BJ Matkowsky. Flames as gasdynamic discontinuities. *J. Fluid Mech.*, 124:239–259, 1982.

[64] S. Mathur, P.K. Tondon, and S.C. Saxena. Thermal conductivity of binary, ternary and quaternary mixture of rare gases. *Molecular Physics*, 12(6):569–579, 1967.

[65] C. Meneveau, T.S. Lund, and W.H. Cabot. A Lagrangian dynamic subgrid-scale model of turbulence. *J. Fluid Mech.*, 319:353 – 385, 1996.

[66] C Meneveau and T Poinsot. Stretching and quenching of flamelets in premixed turbulent combustion. *Combust. Flame*, 86(4):311–332, 1991.

[67] S.K. Menon, P.A. Boettcher, and G. Blanquart. Enthalpy based approach to capture heat transfer effects in premixed combustion. *Combust. Flame*, 160:1242–1253, 2013.

[68] R. Mercier, V. Moureau, D. Veynante, and B. Fiorina. LES of turbulent combustion: On the consistency between flame and flow filter scales. *Proc. Combust. Inst.*, 35:1359 – 1366, 2015.

[69] P. Moin, K. Squires, W.H. Cabot, and S. Lee. A dynamic subgrid-scale model for compressible turbulence and scalar transport. *Phys. Fluids A: Fluid Dyn.*, 3(11):2746 – 2757, 1991.

[70] A. Moureau, O. Teytaud, and J.-P. Bertoglio. Optimal estimation for Large-Eddy simulation of turbulence and application to the analysis of subgrid models. *Phys. Fluids*, 18(10):105101 1–10, 2006.

[71] V. Moureau, P. Domingo, and L. Vervisch. From Large-Eddy Simulation to Direct Numerical Simulation of a lean premixed swirl flame: Filtered laminar flame-pdf modeling. *Combust. Flame*, 158:1340 – 1357, 2011.

[72] V. Moureau, B. Fiorina, and H. Pitsch. A level set formulation for premixed combustion LES considering the turbulent flame structure. *Combust. Flame*, 156:801 – 812, 2009.

[73] S. Mukhopadhyay, J.A. van Oijen, and L.P.H. de Goey. A comparative study of presumed PDFs for premixed turbulent combustion modeling based on progress variable and its variance. *Fuel*, 144:728 – 740, 2015.

[74] L. Mydlarski and Z. Warhaft. On the onset of high-Reynolds-number grid-generated wind tunnel turbulence. *J. Fluid Mech.*, 320:331 – 368, 1996.

[75] S. Nambully, P. Domingo, V. Moureau, and L. Vervisch. A filtered-laminar-flame PDF subgrid scale closure for LES of premixed turbulent flames. part I: Formalism and application to a bluff-body burner with differential diffusion. *Combust. Flame*, 161:1756 – 1774, 2014.

[76] K. Narayanaswamy, G. Blanquart, and H. Pitsch. A consistent chemical mechanism for oxidation of substituted aromatic species. *Combust. Flame*, 157:1879 – 1898, 2010.

[77] C. Pantano, S. Sarkar, and F.A. Williams. Mixing of a conserved scalar in a turbulent reacting shear layer. *J. Fluid Mech.*, 481:291–328, 2003.

[78] N. Peters. Laminar flamelet concepts in turbulent combustion. *Symp. (Int.) Combust.*, 21:1231 – 1250, 1986.

[79] N. Peters. The turbulent burning velocity for large-scale and small-scale turbulence. *J. Fluid Mech.*, 384:107 – 132, 1999.

[80] N. Peters. *Turbulent Combustion.* Cambridge University Press, 2000.

[81] M.R. Petersen and D. Livescu. Forcing for statistically stationary compressible isotropic turbulence. *Phys. Fluids*, 22:116101 1 – 11, 2010.

[82] C.D. Pierce. *Progress-variable approach for large-eddy simulation of turbulent combustion.* PhD thesis, Stanford University, 2001.

[83] C.D Pierce and P. Moin. A dynamic model for subgrid-scale variance and dissipation rate of a conserved scalar. *Phys. Fluids*, 10(12):3041 – 3044, 1998.

[84] H. Pitsch. Technical report, University of Technology (RWTH), Aachen, 1998.

[85] H. Pitsch. FlameMaster: A C++ computer program for 0D combustion and 1D laminar flame calculations. Available at http://www.itv.rwth-aachen.de/downloads/flamemaster/., 1998.

[86] H. Pitsch. Large-eddy simulation of turbulent combustion. *Ann. Rev. Fluid Mech.*, 38:453 – 482, 2006.

[87] T Poinsot, D Veynante, and S Candel. Quenching processes and premixed turbulent combustion diagrams. *J. Fluid Mech.*, 228:561–606, 1991.

[88] T. J. Poinsot and S. K. Lele. Boundary conditions for direct simulations of compressible viscous flows. *J. Comp. Phys.*, 101:104 – 129, 1992.

[89] A.Y. Poludnenko. Pulsating instability and self-acceleration of fast turbulent flames. *Phys. Fluids*, 27(014106):1 – 25, 2015.

[90] A.Y. Poludnenko and E.S. Oran. The interaction of high-speed turbulence with flames: Global properties and internal flame structure. *Combust. Flame*, 157:995 – 1011, 2010.

[91] A.Y. Poludnenko and E.S. Oran. The interaction of high-speed turbulence with flames: Turbulent flame speed. *Combust. Flame*, 158:301 – 326, 2011.

[92] S.B. Pope. *Turbulent Flows.* Cambridge University Press, 2000.

[93] J. Reveillon and L. Vervisch. Response of the large eddy dynamic model to heat release induced effects. *Phys. Fluids*, 8(8):2248 – 2250, 1996.

[94] L.F. Richardson. *Weather prediction by numerical process*. Cambridge University Press, 1922.

[95] Philip L Roe. Approximate Riemann solvers, parameter vectors, and difference schemes. *Journal of Computational Physics*, 43(2):357–372, 1981.

[96] C. Rosales and C. Meneveau. Linear forcing in numerical simulations of isotropic turbulence: Physical space implementations and convergence properties. *Phys. Fluids*, 17:095106 1 – 8, 2005.

[97] R. Sankaran, E. Hawkes, J. Chen, T. Lu, and C. Law. Structure of a spatially developing turbulent lean methane-air bunsen flame. *Proc. Combust. Inst.*, 31:1291 – 1298, 2007.

[98] R. Sankaran, E. Hawkes, C.S. Yoo, and J. Chen. Response of flame thickness and propagation speed under intense turbulence in spatially developing lean premixed methane-air jet flames. *Combust. Flame*, 162:3294 – 3306, 2015.

[99] B. Savard. *Characterization and modeling of premixed turbulent n-heptane flames in the thin reaction zone regime*. PhD thesis, California Institute of Technology, 2015.

[100] B. Savard and G. Blanquart. An a priori model for the effective species Lewis numbers in premixed turbulent flames. *Combust. Flame*, 161:1547 – 1557, 2014.

[101] B. Savard and G. Blanquart. Broken reaction zone and differential diffusion effects in a high Karlovitz n-C7H16 premixed turbulent flame. *Combust. Flame*, 162:2020 – 2033, 2015.

[102] B. Savard, B. Bobbitt, and G. Blanquart. Structure of a high Karlovitz n-C7H16 premixed turbulent flame. *Proc. Combust. Inst.*, 35:1377–1384, 2015.

[103] B. Savard, Y. Xuan, B. Bobbitt, and G. Blanquart. A computationally-efficient, semi-implicit, iterative method for the time-integration of reactive flows with stiff chemistry. *J. Comp. Phys.*, 295:740–769, 2015.

[104] J.A. Sethian. *Level Set Methods and Fast Marching Methods: Evolving Interfaces in Computational Geometry, Fluid Mechanics, Computer Vision and Materials Science.* Cambridge University Press, 1999.

[105] Aaron W. Skiba, Timothy M. Wabel, Jacob E. Temme, and James F. Driscoll. *Measurements to determine the regimes of turbulent premixed flames.* American Institute of Aeronautics and Astronautics Inc, AIAA, 2015.

[106] G.P. Smith, D.M. Golden, M. Frenklach, N. W. Moriarty, B. Eiteneer, M. Goldenberg, C. T. Bowman, R. K. Hanson, S. Song, W. C. Gardiner, V. V. Lissianski, and Z. Qin. Gri-mech 3.0. Available at http://www.me.berkeley.edu/gri_mech/., Accessed: Jan. 2015.

[107] J. Smolke, S. Lapointe, L. Paxton, G. Blanquart, F. Carbone, A.M. Fincham, and F.N. Egolfopoulos. Experimental and numerical studies of fuel and hydrodynamic effects on piloted turbulent premixed jet flames. *Proc. Combust. Inst.*, accepted, 2016.

[108] J. C. Sutherland and C. A. Kennedy. Improved boundary conditions for viscous, reacting, compressible flows. *J. Comp. Phys.*, 191:902 – 924, 2003.

[109] H. Tennekes and J.L. Lumley. *A First Course in Turbulence.* MIT Press, Cambridge, 1972.

[110] J. A. van Oijen, F. A. Lammers, and L. P. H. de Goey. Modeling of complex premixed burner systems by using flamelet-generated manifolds. *Combust. Flame*, 127:2124 – 2134, 2001.

[111] P. Vedula, P.K. Yeung, and R.O. Fox. Dynamics of scalar dissipation in isotropic turbulence: a numerical and modelling study. *J. Fluid Mech.*, 433:29–60, 2001.

[112] L. Vervisch, P. Domingo, G. Lodato, and D. Veynante. Scalar energy fluctuations in Large-Eddy Simulation of turbulent flames: Statistical budgets and mesh quality criterion. *Combust. Flame*, 157:778 – 789, 2010.

[113] H. Wang, E. Dames, B. Sirjean, D. A. Sheen, R. Tango, A. Violi, J. Y. W. Lai, F. N. Egolfopoulos, D. F. Davidson, R. K. Hanson, C. T. Bowman, C. K. Law,

W. Tsang, N. P. Cernansky, D. L. Miller, and R. P. Lindsted. A high-temperature chemical kinetic model of n-alkane (up to n-dodecane), cyclohexane, and methyl-, ethyl-, n-propyl and n-butyl-cyclohexane oxidation at high temperatures, jetsurf version 2.0, (http://web.stanford.edu/group/haiwanglab/jetsurf/jetsurf2.0/index.html), 2010.

[114] H. Wang, K. Luo, and J. Fan. Direct Numerical Simulation and conditional statistics of hydrogen/air turbulent premixed flames. *Energ. Fuel*, 27:549 – 560, 2013.

[115] C.R. Wilke. A viscosity equation for gas mixtures. *Journal of Chemical Physics*, 18(4):517–519, 1950.

[116] Y. Xuan and G. Blanquart. Effects of aromatic chemistry-turbulence interactions on soot formation in a turbulent non-premixed flame. *Proc. Combust. Inst.*, 35:1911 – 1919, 2015.

[117] Mingfa Yao, Zhaolei Zheng, and Haifeng Liu. Progress and recent trends in homogeneous charge compression ignition (hcci) engines. *Prog. Energ. Combust.*, 35(5):398–437, 2009.

[118] P. Yeung, S. Girimaji, and S. Pope. Straining and scalar dissipation on material surfaces in turbulence: implications for flamelets. *Combust. Flame*, 79:340 – 365, 1990.

[119] C. S. Yoo and H. G. Im. Characteristic boundary conditions for simulations of compressible reacting flows with multi-dimensional, viscous and reaction effects. *Combust. Theo. Model.*, 11:259 – 286, 2011.

[120] B. Zhou, C. Brackmann, Q. Li, Z. Wang, P. Petersson, Z. Li, M. Alden, and X.-S. Bai. Distributed reactions in highly turbulent premixed methane/air flames: Part I. Flame structure characterization. *Combust. Flame*, 162:2937 – 2953, 2015.